Terahertz radiation from intrinsic Josephson junctions in $Bi_2Sr_2CaCu_2O_{8+\delta}$ — dynamics, tunability, and applications

Dissertation
der Mathematisch-Naturwissenschaftlichen Fakultät
der Eberhard Karls Universität Tübingen
zur Erlangung des Grades eines
Doktors der Naturwissenschaften
(Dr. rer. nat.)

vorgelegt von
Fabian Robert Rudau
aus Leonberg

Tübingen
2018

Gedruckt mit Genehmigung der Mathematisch-Naturwissenschaftlichen Fakultät der Eberhard Karls Universität Tübingen.

Tag der mündlichen Qualifikation:	09.02.2018
Dekan:	Prof. Dr. Wolfgang Rosenstiel
1. Berichterstatter:	Prof. Dr. Reinhold Kleiner
2. Berichterstatter:	Prof. Dr. Dieter Kölle

Abstract

Terahertz (THz) radiation offers many new possibilities for applications, e. g., for spectroscopy, high-bandwidth data communication, medical diagnosis, and security screening. However, these potential applications are still largely unused because there are only a few devices available to generate these frequencies. Especially, from 0.3 to 2 THz there is a lack of coherent, compact, low-cost, tunable, and high-power emitters. Devices based on fast electronic circuits usually work at lower frequency and photonic systems at much higher frequencies. Unfortunately, there is no overlap of these technologies. To close this so-called THz gap one can use Josephson junctions which can convert an applied dc voltage into an ac current and, thus, are able to emit electromagnetic waves. According to the Josephson relation, an applied dc voltage of 1 mV translates into a frequency of 483.6 GHz. Especially, intrinsic Josephson junctions (IJJs) occurring in the high-temperature superconductor $Bi_2Sr_2CaCu_2O_{8+\delta}$ (BSCCO) are attractive sources of radiation due to their large frequency range of, in principle, up to 10 THz, and the easy fabrication of hundreds of almost identical junctions stacked on top of each other. The challenging part is to achieve phase synchronization among the junctions to obtain high power emission that scales with the square of the number of junctions. Currently, IJJ stacks with emission powers up to tens of microwatts have been realized, and frequencies ranging from 0.2 to 2.4 THz can be generated. High-precision frequency measurements revealed linewidths down to some megahertz, which is already practical for applications. However, a device that combines all these features does not exist yet. Especially, at higher frequencies above 1 to 2 THz the emission power decreases strongly and the linewidth becomes broad.

The group in Tübingen investigates THz generation from IJJ stacks in close collaboration with the groups of H. B. Wang (Research Institute of Superconductor Electronics, Nanjing University, China & National Institute for Materials Science, Tsukuba, Japan) and V. P. Koshelets (Kotel'nikov Institute of Radio Engineering and Electronics, Moscow, Russia). Within

this collaboration, goals of this thesis were (1) to gain a deeper understanding of the mechanisms of THz generation from IJJ stacks and (2) to find ways how to tune and how to optimize the emission properties of the samples. As a third goal, if possible, some potential applications should be demonstrated.

To understand the physical behavior in more detail and to study the influence of individual parameters on the system a three-dimensional numerical model for large stacks of IJJs was developed. Typically, such stacks with a large number of junctions strongly suffer from Joule heating, such that the temperature distribution becomes highly inhomogeneous and temperature dependencies of all involved physical quantities need to be considered. Based on combined heat diffusion equations and coupled sine-Gordon equations, covering both the thermal physics and the Josephson physics, numerical simulations were done allowing one to have a look into the dynamics of phase synchronization, hot spot formation, and the excitation of standing waves in the stack of junctions acting as a cavity for electromagnetic waves. The overall behavior of the system as well as effects of an external magnetic field were studied and compared to experimental data.

In experiment, a simple array structure was investigated systematically to study the thermal and electric interaction of two nearby IJJ stacks. Moreover, ways to modify and tune the emission properties of BSCCO samples were studied. For instance, it was found that the emission power strongly depends on the position of the hot spot that develops at high-bias currents due to the strong self-heating of the samples. Also, a precise tuning of the emission power is possible by using a focused laser beam that locally heats the sample surface. Furthermore, charge carrier injection was used to change the doping level of the crystal affecting the emission properties.

Since the long-term goal is to build a compact, tunable, and coherent device for a large field of applications at THz frequencies, some first, simple applications are presented which show that BSCCO stacks are suitable candidates as emitters. A compact THz emitter system was built, working at liquid nitrogen temperatures with a commercial 1.5 V battery making it cheap, portable, and easy to handle. Furthermore, spectroscopy experiments were done, showing that it is possible to detect gases like water vapor and ammonia.

Kurzfassung

Terahertzstrahlung bietet viele neue Möglichkeiten für Anwendungen in Bereichen der Spektroskopie, breitbandiger Datenübertragung, medizinischer Diagnostik und bei Sicherheitskontrollen. Viele dieser Anwendungen werden jedoch nicht genutzt, da es nur wenige Bauelemente gibt, die in der Lage sind, Strahlung in diesem Frequenzbereich zu erzeugen. Insbesondere im Bereich zwischen 0,3 und 2 THz mangelt es an günstigen, kompakten, kohärenten und durchstimmbaren Strahlungsquellen mit hoher Intensität. Schnelle Schaltkreise in der Hochfrequenzelektronik arbeiten bei niedrigeren Frequenzen und photonische Systeme, wie beispielsweise Laser, bei höheren Frequenzen. Einen Überlapp der beiden Technologien gibt es jedoch nicht. Um diese sogenannte Terahertzlücke zu schließen, können z. B. Josephsonkontakte eingesetzt werden, die eine angelegte elektrische Gleichspannung in einen Wechselstrom umwandeln können und deshalb in der Lage sind elektromagnetische Strahlung zu emittieren. Bei einer Gleichspannung von 1 mV entsteht so gemäß der Josephsonrelation ein Wechselstrom mit der Frequenz von 483,6 GHz. Besonders intrinsische Josephsonkontakte (IJKs), die im Hochtemperatursupraleiter $Bi_2Sr_2CaCu_2O_{8+\delta}$ (BSCCO) vorkommen, sind attraktive Strahlungsquellen aufgrund des hohen Frequenzbereichs bis zu 10 THz und der einfachen Herstellung von Stapel vieler hunderter, fast identischer Kontakte. Herausfordernd ist jedoch vor allem die Phasensynchronisation der oszillierenden Ströme in allen Kontakten, um eine hohe Ausgangsleistung zu erreichen, die mit dem Quadrat der Anzahl an Kontakten steigt. Momentan ist es möglich Stapel von IJKs mit einer Strahlungsleistung von einigen Zehn Mikrowatt herzustellen und Frequenzen von 0,2 bis 2,4 THz zu erzeugen. Präzise Frequenzmessungen ergaben Linienbreiten hinunter bis zu wenigen Megahertz, was für praktische Anwendungen bereits ausreichend ist. Ein Quelle, die all diese Eigenschaften vereint, existiert jedoch leider noch nicht. Insbesondere bei höheren Frequenzen über 1–2 THz bricht die Strahlungsleistung deutlich ein und die Linienbreite wächst.

Die Untersuchung der Terahertzemission von IJK Stapeln in Tübingen findet in enger Kooperation mit den Arbeitsgruppen von H. B. Wang (Research Institute of Superconductor Electronics, Nanjing Universität, China & National Institute for Materials Science, Tsukuba, Japan) und V. P. Koshelets (Kotel'nikov Institute of Radio Engineering and Electronics, Moskau, Russland) statt. Im Rahmen dieser Kooperation waren die Ziele der vorliegenden Arbeit, (1) ein tieferes Verständnis für die physikalischen Vorgänge in Stapeln von IJKs zu gewinnen und (2) Wege zu finden, wie sich die Strahlungseigenschaften beeinflussen und optimieren lassen. Drittens sollte nach Möglichkeit untersucht werden, inwieweit bereits jetzt schon diese Art von Emitter in praktischen Anwendungen eingesetzt werden können.

Um das physikalische Verständnis zu verbessern und um die Einflüsse verschiedener Parameter auf das System zu untersuchen, wurde ein dreidimensionales numerisches Modell zur Beschreibung großer Stapel von IJKs entwickelt. Da Joulesches Heizen bei Stapeln mit einer großen Zahl von Kontakten für gewöhnlich zu einem starken Selbstheizeffekt und zu einer extrem inhomogenen Temperaturverteilung führt, müssen bei der numerischen Beschreibung die Temperaturabhängigkeiten aller physikalischen Größen berücksichtigt werden. In Simulationen mit einem kombinierten System von Wärmeleitungsgleichungen zur Beschreibung der thermischen Physik und gekoppelten Sinus-Gordon-Gleichungen, welche die Josephsonphysik beinhalten, konnten Phasensynchronisation, die Entstehung von Hotspots und Stehwellen im Stapel, der als Kavität für elektromagnetische Wellen fungiert, beobachtet werden. Das generelle Verhalten des Systems und Effekte eines externen Magnetfelds wurden untersucht und mit Messdaten aus Experimenten verglichen.

Auf der experimentellen Seite wurde die thermische und elektrische Wechselwirkung zweier nebeneinander stehender Stapel als einfache Arraystruktur systematisch untersucht. Weiterhin wurden Möglichkeiten gesucht, wie die Strahlungseigenschaften der Quellen manipuliert und optimiert werden können. Beispielsweise konnte gezeigt werden, dass die Strahlungsintensität stark von der Position des Hotspots abhängt, der bei höheren Strömen aufgrund des starken Selbstheizeffekts entsteht. Außerdem ist es möglich die Strahlungsleistung zu beeinflussen, indem ein Laser auf die Stapeloberfläche fokussiert wird und die Probe lokal heizt. Die Injektion von Ladungsträgern durch das Anlegen hoher Ströme führte zu

einer Änderung der Dotierung des BSCCO-Kristalls und ebenfalls zu einer Veränderung der Strahlungseigenschaften.

Da das eigentliche Ziel dieser Forschung in der praktischen Anwendung von Terahertzstrahlung liegt, werden im Rahmen dieser Arbeit auch einfache Möglichkeiten für Anwendungen präsentiert, die zeigen, dass BSCCO Stapel als Emitter geeignet sind. Es wurde ein kompaktes Emittersystem gebaut, welches zur Kühlung ausschließlich flüssigen Stickstoff benötigt und mit einer gewöhnlichen 1,5 V Batterie arbeitet, was es günstig, mobil und einfach zu verwenden macht. Ebenso konnte bei Spektroskopieexperimenten gezeigt werden, dass es möglich ist, Gase wie beispielsweise Wasserdampf und Ammoniak zu detektieren.

List of publications

This is a cumulative thesis based on nine publications which are listed below. Publications 1 to 4 focus on the physical dynamics of intrinsic Josephson junction (IJJ) stacks, whereas publications 5 to 7 deal with the tunability of the terahertz emission properties. Finally, publications 8 and 9 present applications of terahertz radiation based on IJJ stacks.

All publications are appended at the very end of this thesis and are summarized in chapter 2. They were done in close cooperation with the groups of H. B. Wang[1] and V. P. Koshelets[2].

Electrothermal dynamics of intrinsic Josephson junction stacks

Publication 1 **F. Rudau**, M. Tsujimoto, B. Gross, T. E. Judd, R. Wieland, E. Goldobin, N. Kinev, J. Yuan, Y. Huang, M. Ji, X. J. Zhou, D. Y. An, A. Ishii, R. G. Mints, P. H. Wu, T. Hatano, H. B. Wang, V. P. Koshelets, D. Koelle, and R. Kleiner
Thermal and electromagnetic properties of $Bi_2Sr_2CaCu_2O_8$ intrinsic Josephson junction stacks studied via one-dimensional coupled sine-Gordon equations
Phys. Rev. B **91**, 104513 (2015)

[1] Research Institute of Superconductor Electronics, Nanjing University, Nanjing, China
National Institute for Materials Science, Tsukuba, Japan
[2] Kotel'nikov Institute of Radio Engineering and Electronics, Moscow, Russia

Publication 2 **F. Rudau**, R. Wieland, J. Langer, X. J. Zhou, M. Ji, N. Kinev, L. Y. Hao, Y. Huang, J. Li, P. H. Wu, T. Hatano, V. P. Koshelets, H. B. Wang, D. Koelle, and R. Kleiner
Three-Dimensional Simulations of the Electrothermal and Terahertz Emission Properties of $Bi_2Sr_2CaCu_2O_8$ Intrinsic Josephson Junction Stacks
Phys. Rev. Appl. **5**, 044017 (2016)

Publication 3 B. Gross, **F. Rudau**, N. Kinev, M. Tsujimoto, J. Yuan, Y. Huang, M. Ji, X. J. Zhou, D. Y. An, A. Ishii, P. H. Wu, T. Hatano, D. Koelle, H. B. Wang, V. P. Koshelets, and R. Kleiner
Electrothermal behavior and terahertz emission properties of a planar array of two $Bi_2Sr_2CaCu_2O_{8+\delta}$ intrinsic Josephson junction stacks
Supercond. Sci. Technol. **28**, 055004 (2015)

Publication 4 Y. Huang, H. C. Sun, D. Y. An, X. J. Zhou, M. Ji, **F. Rudau**, R. Wieland, J. S. Hampp, O. Kizilaslan, J. Yuan, N. Kinev, O. Kiselev, V. P. Koshelets, J. Li, D. Koelle, R. Kleiner, B. B. Jin, J. Chen, L. Kang, W. W. Xu, H. B. Wang, and P. H. Wu
Self-Mixing Spectra of Terahertz Emitters Based on $Bi_2Sr_2CaCu_2O_{8+\delta}$ Intrinsic Josephson-Junction Stacks
Phys. Rev. Appl. **8**, 054023 (2017)

Tunability of the terahertz emission properties

Publication 5 X. J. Zhou, J. Yuan, H. Wu, Z. S. Gao, M. Ji, D. Y. An, Y. Huang, **F. Rudau**, R. Wieland, B. Gross, N. Kinev, J. Li, A. Ishii, T. Hatano, V. P. Koshelets, D. Koelle, R. Kleiner, H. B. Wang, and P. H. Wu
Tuning the Terahertz Emission Power of an Intrinsic Josephson-Junction Stack with a Focused Laser Beam
Phys. Rev. Appl. **3**, 044012 (2015)

Publication 6 X. J. Zhou, Q. Zhu, M. Ji, D. Y. An, L. Y. Hao, H. C. Sun, S. Ishida, **F. Rudau**, R. Wieland, J. Li, D. Koelle, H. Eisaki, Y. Yoshida, T. Hatano, R. Kleiner, H. B. Wang, and P. H. Wu
Three-terminal stand-alone superconducting terahertz emitter
Appl. Phys. Lett. **107**, 122602 (2015)

Publication 7 O. Kizilaslan, **F. Rudau**, R. Wieland, J. S. Hampp, X. J. Zhou, M. Ji, O. Kiselev, N. Kinev, Y. Huang, L. Y. Hao, A. Ishii, M. A. Aksan, T. Hatano, V. P. Koshelets, P. H. Wu, H. B. Wang, D. Koelle, and R. Kleiner
Tuning THz emission properties of $Bi_2Sr_2CaCu_2O_{8+\delta}$ intrinsic Josephson junction stacks by charge carrier injection
Supercond. Sci. Technol. **30**, 034006 (2017)

Applications of terahertz radiation from intrinsic Josephson junctions

Publication 8 L. Y. Hao, M. Ji, J. Yuan, D. Y. An, M. Y. Li, X. J. Zhou, Y. Huang, H. C. Sun, Q. Zhu, **F. Rudau**, R. Wieland, N. Kinev, J. Li, W. W. Xu, B. B. Jin, J. Chen, T. Hatano, V. P. Koshelets, D. Koelle, R. Kleiner, H. B. Wang, and P. H. Wu
Compact Superconducting Terahertz Source Operating in Liquid Nitrogen
Phys. Rev. Appl. **3**, 024006 (2015)

Publication 9 H. C. Sun, Z. B. Yang, N. Kinev, O. Kiselev, Y. Y. Lv, Y. Huang, L. Y. Hao, X. J. Zhou, M. Ji, X. C. Tu, C. H. Zhang, J. Li, **F. Rudau**, R. Wieland, J. S. Hampp, O. Kizilaslan, D. Koelle, B. B. Jin, J. Chen, L. Kang, W. W. Xu, R. Kleiner, V. P. Koshelets, H. B. Wang, and P. H. Wu
Terahertz Spectroscopy of Dilute Gases Using $Bi_2Sr_2CaCu_2O_{8+\delta}$ Intrinsic Josephson-Junction Stacks
Phys. Rev. Appl. **8**, 054005 (2017)

Not included in this thesis

Publication I M. Ji, J. Yuan, B. Gross, **F. Rudau**, D. Y. An, M. Y. Li, X. J. Zhou, Y. Huang, H. C. Sun, Q. Zhu, J. Li, N. Kinev, T. Hatano, V. P. Koshelets, D. Koelle, R. Kleiner, W. W. Xu, B. B. Jin, H. B. Wang, and P. H. Wu
$Bi_2Sr_2CaCu_2O_{8+\delta}$ intrinsic Josephson junction stacks with improved cooling: Coherent emission above 1 THz
Appl. Phys. Lett. **105**, 122602 (2014)

Contents

1 Introduction

In the past years, terahertz (THz) research attracted more and more attention due to its huge variety of potential applications. In the electromagnetic spectrum the THz range is located between microwaves and the far infrared from about 0.1 to 10 THz. At these frequencies many dielectric materials such as clothing, paper, plastic, and wood are transparent whereas metals are highly reflective. This property makes THz radiation interesting for transmission and reflection spectroscopy, e. g., for the non-destructive inspection of packages and envelopes to detect weapons, explosives, and drugs which often have characteristic spectra in the THz range and can be easily detected [1]. Because of its low photon energy, THz radiation is non-ionizing and does not damage biological tissues. Therefore, it can be used to scan people at airports or train stations and also could emerge as a key technology in medical diagnosis. Because of its strong absorption at THz frequencies, water can serve as natural contrast agent and allows for the detection of cancer cells which usually have an increased blood supply and, therefore, an increased water content [2]. In terms of spectroscopy, THz radiation offers a new window to investigate molecules and gases. Many molecules have rotational transition frequencies and vibrational modes in the THz range, enabling new detection methods in astronomy which is being done with GREAT[1] installed in SOFIA[2] [3]. Other possible applications are in high-speed data communication with large bandwidths and in material science. Even the analysis of paintings can be done by using THz waves without damaging the artwork [4, 5].

However, the generation of THz radiation is challenging. In particular, in the so-called THz gap from about 0.3 to 2 THz there are only a few devices available that work as oscillators. In case of compact devices, promising candidates are for example photomixers, resonant tunneling diodes (RTDs) [6, 7], and quantum cascade lasers (QCLs) [8–10]. Photomix-

[1] German Receiver for Astronomy at Terahertz Frequencies
[2] Stratospheric Observatory For Infrared Astronomy

ers are widely used for THz time-domain spectroscopy and are utilizing the beat frequency of two optical lasers [11, 12]. RTDs and QCLs are semiconducting devices which even work at room temperature and produce larger emission powers than photomixers but are less tunable in frequency since their emission frequency is mainly determined by the geometry.

Another way to generate THz radiation can be realized by using Josephson junctions (JJs) which is the subject of this thesis. JJs consist of two superconductors which are separated by a non-superconducting barrier. If operated at temperatures below the critical temperature T_c of the superconductors, Cooper pairs can tunnel from one superconductor to the other, which is described by the Josephson effect [13–15]. The current I across the junction only depends on the gauge invariant phase difference

$$\gamma = \phi_2 - \phi_1 - \frac{2\pi}{\Phi_0} \int_1^2 \vec{A} d\vec{l} \tag{1.1}$$

of the two macroscopic wave functions $\psi_m = |\psi_m| \exp(i\phi_m)$ of the superconductors, with $m \in \{1, 2\}$, and the vector potential $\vec{A}$ which is integrated from one superconductor to the other. $\Phi_0 = h/(2e)$ denotes the magnetic flux quantum containing Planck's constant h and the elementary charge e. The current across the junction obeys the 1. Josephson relation

$$I = I_c \sin \gamma \,, \tag{1.2}$$

with I_c being the critical current of the JJ. Up to this current there will be no voltage drop V across the junction and a current of Cooper pairs flows without dissipation. If the critical current of a JJ is exceeded the junction switches to its resistive state resulting in a voltage drop across the junction and in addition to the current of Cooper pairs a dc current of quasiparticles will flow across the barrier. In this state according to the 2. Josephson equation

$$\dot{\gamma} = \frac{2\pi}{\Phi_0} V \tag{1.3}$$

the phase difference γ will start to increase continuously and, therefore, the current of Cooper pairs will start to oscillate across the barrier with a frequency of $f = V/\Phi_0 \approx 483.6\,\mathrm{GHz/mV} \cdot V$. Hence, the junction will emit

electromagnetic radiation with a frequency that can be tuned by varying the bias voltage, and it seems to be easy to cover the whole THz gap with such a device. However, the emission power of a single JJ is typically very low on the order of picowatts, and the emission linewidth is large [16]. Also, the low impedance of a single junction makes it difficult to couple the radiation to the environment efficiently. The fabrication of many artificial JJs in series overcomes these issues and can increase the emission power and sharpen the linewidth [17–20]. Even though, nowadays, one can fabricate microscopic structures very precisely using electron-beam lithography there will always be small differences in the junction parameters making it difficult to synchronize the oscillating currents in the whole array. Moreover, if conventional superconductors are used, e. g. niobium, one is limited to frequencies $f \leq 725\,\mathrm{GHz}$ due to the energy gap of the superconductor of only 1.5 meV [21]. To avoid this problem one can use the high-temperature superconductor $Bi_2Sr_2CaCu_2O_{8+\delta}$ (BSCCO) which has a critical temperature of around 90 K and a large energy gap up to $\sim 50\,\mathrm{meV}$ [21] depending on the doping level of the crystal, which is indicated by δ and describes the number of oxygen atoms per copper atom in a unit cell. For an optimally doped BSCCO crystal with $\delta = 0.16$, in principle, frequencies up to more than 10 THz are accessible. A BSCCO crystal has a layered structure consisting of superconducting copper oxide double layers and insulating bismuth oxide and strontium oxide layers. The superconducting and insulating layers alternate and naturally form JJs [24], as shown in Fig. 1.1(a), and are called intrinsic Josephson junctions (IJJs). Thus, apart from crystal defects, these junctions are identical on an atomic scale and suitable to build large arrays for THz generation.

Figure 1.1(b) shows an example for a current-voltage characteristic (IVC) of a stack of seven IJJs at a bath temperature of $T_\mathrm{b} = 14\,\mathrm{K}$. By increasing the current from zero bias one after the other junction switches to its resistive state and one can trace out the individual branches leading to a total of eight branches including the superconducting one. The main challenge for THz emission is the synchronization of the oscillating currents for all junctions. Recently, for stacks with small lateral dimensions of only several microns synchronized emission was found [25]. A large frequency range from 1 to 11 THz was observed for samples containing at least 100 junctions. The maximum output power was estimated to be around 1 µW. For samples with smaller junction number no emission could be detected,

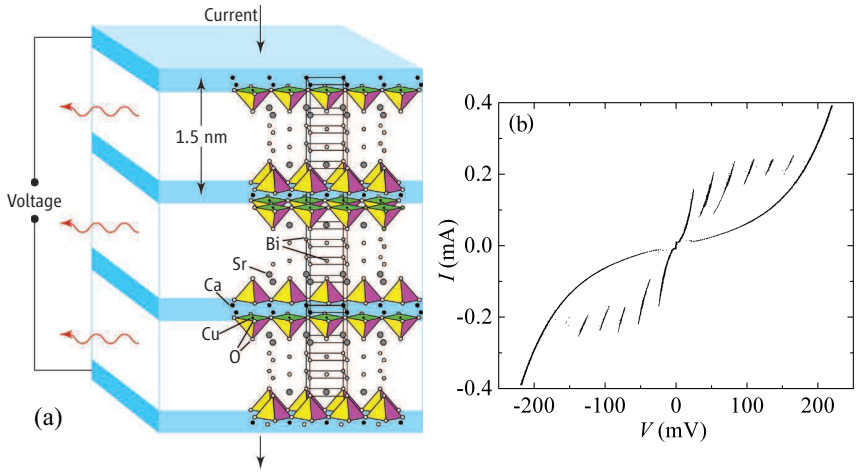

Figure 1.1: (a) BSCCO crystal structure with applied bias current emitting THz radiation (from [22]) and (b) IVC of a stack of seven intrinsic Josephson junctions in BSCCO measured at T_b = 14 K (from [23]).

indicating that one needs to exceed a certain threshold junction number to achieve phase synchronization.

The first successful results were reported by Ozyuzer *et al.* in 2007 [26] for much bigger stacks with a larger number of junctions. They fabricated $300 \times (40 - 100)\,\mu m^2$ sized mesa-type stacks of 1 µm height containing around 670 junctions. From such samples, integrated emission powers up to 0.5 µW were detected at frequencies from 0.35 to 0.85 THz. The emission was found in the resistive state of all junctions when the bias current was decreased again, just before some junctions switched back to their superconducting state. Because the emission frequency was found to be inversely proportional to the stack's width Ozyuzer *et al.* proposed standing waves excited by the Josephson currents inside the stack, acting as a cavity, as synchronization mechanism for the junctions.

A typical IVC of a sample with such a geometry looks as shown in Fig. 1.2(a). Here, for three different bath temperatures T_b the outermost branch was measured where all junctions switched to the resistive state. Only for small input currents (in this case below 2 mA) first some, and

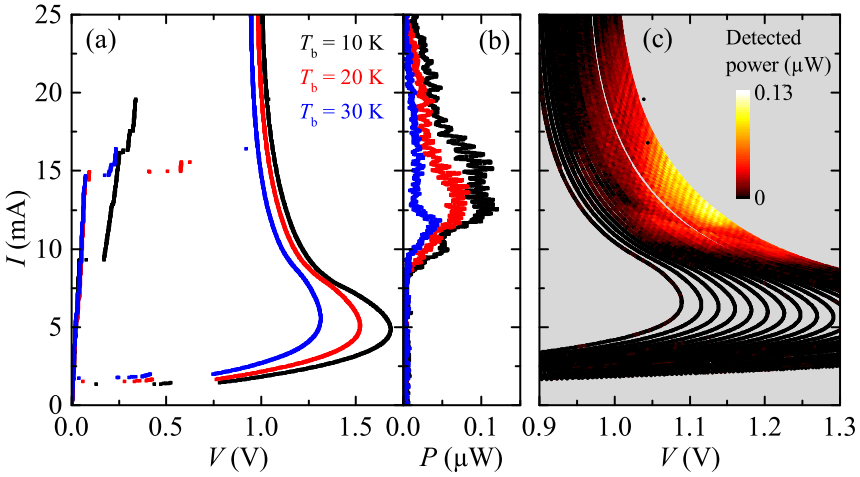

Figure 1.2: (a) IVCs for three different bath temperatures for a $330 \times 50 \times 1.1\,\mu m^3$ mesa structure. (b) shows the bias current vs the detected emission power and (c) a family of IVCs from 10 to 40 K in steps of 1 K of the same sample. The detected emission is color-coded.

by further decrease of the current, all junctions switched back to the superconducting state. Because usually hundreds of IJJs are involved and the thermal conductivity of BSCCO is quite poor, these stacks strongly suffer from Joule heating, leading to a back-bending of the IVC for higher currents. This part of the IVC is called the high-bias regime whereas the lower part with small input power is denoted as the low-bias regime. In the latter one, the temperature distribution in the stack is almost homogeneous with temperatures only slightly larger than the bath temperature. By exceeding a certain current this homogeneous temperature distribution becomes instable and a hot spot develops in the stack, i. e., a region occurs which is heated to temperatures that might even exceed T_c whereas the rest of the stack stays cold. The appearance of the hot spot, which is caused by the strong decrease of the BSCCO *c*-axis resistivity with increasing temperature, is well understood and experimentally confirmed, e. g., by low temperature scanning laser microscopy (LTSLM) and thermal fluorescence

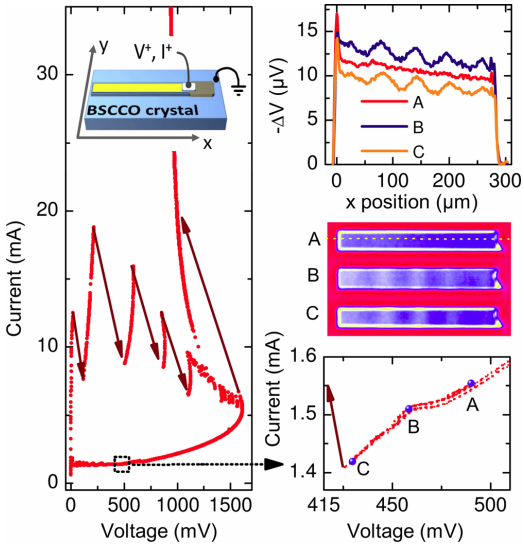

Figure 1.3: LTSLM measurements at three bias currents in the low bias regime at a bath temperature of 25 K for a rectangular $330 \times 40\ \mu m^2$ mesa-type IJJ stack containing around 670 junctions. From [27].

microscopy [27–31]. The phenomenon of a hot spot also can occur in other systems like normal metals and semiconductors and is not only related to BSCCO [32, 33]. For LTSLM imaging, a focused laser beam heats the sample surface pixel-by-pixel and the laser-induced change of the global voltage caused by all the temperature-dependent quantities is measured. Figures 1.3 and 1.4 show examples of LTSLM measurements at low and at high bias, respectively. The current is injected on top of the right end of the stack. At high bias this leads to a formation of the hot spot in the right part of the stack. In such measurements the hot spot looks like a double peak structure because the main signal originates from $d\sigma/dT$ (with σ being the electrical conductivity of BSCCO) and has its largest value at around $T = T_c$ [30]. For this reason, the inner and outer part of the hot spot has a weaker signal and the edge of the hot spot is most pronounced. In Figs. 1.3 and 1.4, one also notices clear standing wave patterns occurring at low and high bias. Such waves can appear over a larger range than the emission

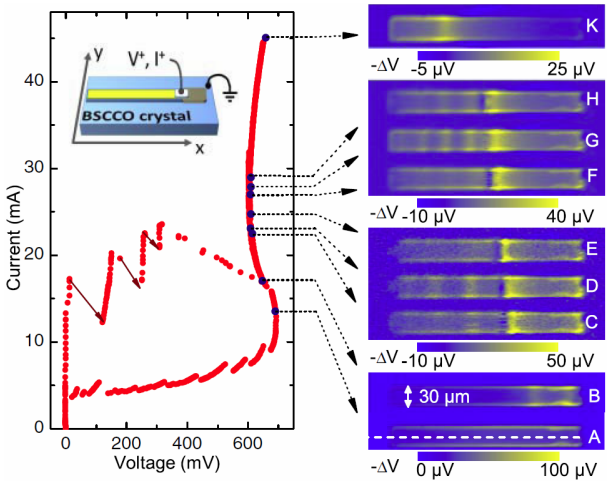

Figure 1.4: LTSLM measurements at different bias points in the high bias regime at a bath temperature of 50 K for a rectangular $330 \times 30\,\mu m^2$ mesa-type IJJ stack containing around 670 junctions. From [27].

in Ozyuzer's measurements was observable, but nevertheless it supports the idea of cavity modes as synchronization mechanism. Note, that in Figs. 1.3 and 1.4 the waves oscillate along the long side of the stack while in Ref. [26] they were proposed to oscillate along the width. Waves along the width of the stack have not been observed by LTSLM yet. However, this might be related to the fact that, especially, in the case of mesa structures there are often strong signals at the edge of the stack caused by a stronger absorption of the laser beam due to the missing gold layer at the sides of the stack, which makes it difficult to distinguish a half wave along the short side from a homogeneous signal.

THz emission can occur both in the low- and high-bias regime. In both regimes the emission power can be on the same order and similar frequency range, tunable by changing bias voltage and bath temperature [26, 34–39]. Most times emission is measured on the outermost branch where all junctions are in their resistive state but, in principle, emission can also be observed on the internal branches when some junctions already switched back to the superconducting state [40]. However, this configuration is

usually more unstable and not reproducible and, thus, not a favorable way to operate the samples. Typically, one observes emission powers on the order of 10 µW at frequencies ranging from 0.3 to 1 THz.

A typical THz emission measurement is shown in Fig. 1.2(b). Here, the emission detected by a Ge bolometer occurs over a large range at high bias and changes with bath temperature. In such kind of plot no systematic change can be noticed. However, when plotting a larger number of IVCs for different bath temperatures into the same graph and using a color-code to indicate the emission intensity, as it was done in Fig. 1.2(c), the picture becomes clearer. A "global" regime appears where the emission takes place, but more interestingly a stripe-like modulation of the emission intensity can be observed. The exact origin of these stripes has not been resolved yet, but it was found that the emission frequency along a given stripe stays constant [41]. Note, that one can also identify a line at around 12 mA where the emission intensity exhibits a small dip. Above this line a hot spot developed.

Also for other sample geometries than mesa structures, emission was observed, such as stand-alone BSCCO stacks contacted by two gold layers (gold-BSCCO-gold (GBG) structure) [42–50] and Z-shaped structures with superconducting electrodes [51, 52]. For the best samples the maximum emission power raised to 82 µW [43], and for arrays of mesas even 610 µW were reported [53], however, the latter result could not be confirmed by other groups yet. The maximum frequency increased to 1.6 THz for rectangular [46] and even up to 2.4 THz for disk-shaped structures [47]. This was mainly achieved due to an improved cooling of the stack by sandwiching the sample between two substrates [45–47], which reduces the back-bending of the IVC and allows for higher voltages and, therefore, higher frequencies. However, the emission power strongly decreases to sub-microwatts at higher frequencies, presumably caused by enhanced damping at higher frequencies.

The appearance of the hot spot at high bias with its large temperature gradients in the stack led to a debate whether or not the hot spot is useful for the emission. Since the hot spot can have temperatures larger than T_c it reduces the superconducting area, i. e., the emitting part of the stack. Also, one would intuitively think that the large temperature gradients will prohibit the ability of the junctions to synchronize. However, it was shown that in presence of a hot spot the linewidth of the emission is on the order of some MHz while it is on the order of GHz at low bias, where

no hot spot develops [54]. Thus, the hot spot seems to enhance the phase synchronization of the junctions and does not have to be avoided. The precise linewidth measurements also revealed that the linewidth becomes smaller with increasing bath temperatures [54]. Such a dependence is quite unusual in general and hard to explain with conventional models.

After Ozyuzer's breakthrough in 2007 a lot of theoretical attempts were made to understand the general behavior of large BSCCO stacks in more detail. The influence of the hot spot was analyzed [29, 30, 55] as well as the phase dynamics were explored [56–78].

The phase dynamics of a single JJ can be described by the RCSJ model (resistively and capacitively shunted junction) for small, point-like JJs [79, 80]. Here, the phase difference along the junction is constant and, thus, the current distribution is homogeneous. Obviously, by definition for long JJs this is not an appropriate assumption, and one has to take changes of the phase difference along the junction into account. Modeling a network of RSCJ-like junctions in parallel, that are inductively coupled to each other, leads to the sine-Gordon equation, which includes spatial variations of the phase difference along the barrier. Several excitations of the phase are possible. First, there can be plasma oscillations which are small changes of the phase difference propagating along the barrier. A second type of excitations are solitons (also called fluxons or Josephson vortices). Here, the phase difference changes by 2π corresponding to a flux change of Φ_0. Such solitons can move without deformation and can collide with, e. g., antisolitons (i. e. solitons with opposite change of phase). In such a case, they either move through each other or annihilate resulting in a plasma oscillation. When introducing a finite length of the junction, solitons can also enter or leave the junction at the edges generating radiation (working principle of flux-flow oscillators) or building standing waves inside the junctions when they are reflected at the edges. Resonant modes also appear if the wavelength (or higher harmonics thereof), associated to the frequency generated by ac Josephson effect, matches the length of the junction. Then, so-called Fiske-steps can be observed on the IVC [81]. Already for a single JJ the interplay of all these effects can lead to a rich amount of dynamics.

In the case of large BSCCO IJJ stacks for THz generation, there are usually hundreds of long JJs in series that are coupled to each other. In principle, the coupling can be inductively caused by in-plane currents that generate magnetic fields in the adjacent layers and capacitively due to charging effects of the superconducting layers. For nearly optimal-doped

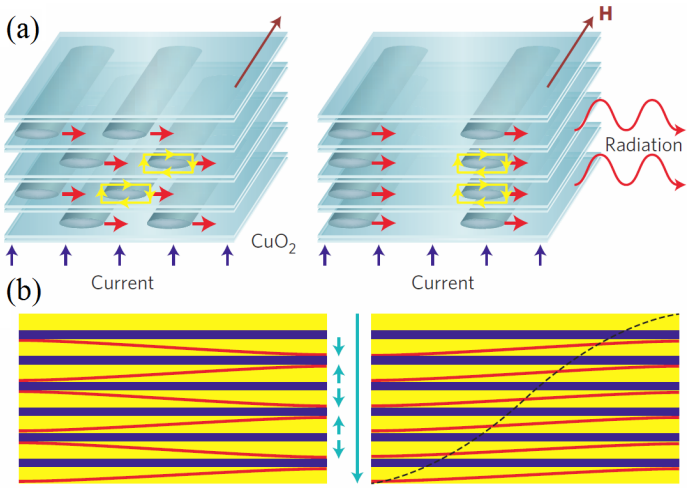

Figure 1.5: (a) Two configurations of Josephson pancake vortices. On the left a triangular arrangement, on the right a rectangular one is shown. The resulting resonant modes for each configuration are depicted in (b). Figure from [21].

BSCCO, the c-axis London penetration depth λ_{ab} is about 200 nm [21], which is much larger than the distance of the superconducting layers of 1.5 nm, and inductive coupling is very strong. Capacitive coupling occurs if electric charges are created in a layer and their electric field penetrates into the neighboring junctions. Especially, in cuprate superconductors this effect can become important, since the charge screening length is larger or at least comparable to the interlayer distance leading to a dynamical breaking of the charge neutrality of the superconducting layers [82, 83]. For large BSCCO stacks the inductive coupling is assumed to be much larger compared to the capacitive one, however, capacitive coupling needs to be considered if, e. g., no in-plane currents are present [65, 84]. Most of the existing theoretical models, attempting to describe large BSCCO stacks, are based on inductively coupled sine-Gordon equations. The challenge is to choose the correct boundary conditions and to analyze whether found solutions are stable.

Calculations based on coupled sine-Gordon equations by Sakai *et al.* [85] and Kleiner [86] revealed that in a stack of N junctions one can have N different mode velocities, each of them corresponding to a certain resonant mode where a different number of junctions oscillate in-phase. The highest mode velocity c_1 belongs to the mode where all junctions oscillate in-phase which is, of course, the favorable one for THz generation. This situation corresponds to a rectangular arrangement of Josephson vortices, as shown on the right handside of Fig. 1.5(a). Although, the triangular lattice is actually energetically preferred due to the repulsive interaction of vortices in adjacent junctions the favorable rectangular lattice can be realized because of the large difference of the mode velocities.

The number of junctions considered affects the numerical result. Due to limited computing power often only stacks with some tens of junctions are treated numerically, which is obviously not the case in the real experiment where hundreds of junctions are involved. Nevertheless, interesting solutions of the phase dynamics were found to describe the mechanisms of synchronization and to efficiently couple the ac Josephson currents to a cavity mode. For instance, Krasnov [73] states that the ac Josephson effect itself does not automatically lead to radiation due to its non-dissipative property. He argues that there needs to be an additional power conversion mechanism that pumps the energy from the ac Josephson currents into the radiation. In his simulations, he found configurations of self-oscillating bound vortex-antivortex pairs (called breathers) that efficiently do this via the Lorentz force and can excite cavity modes. This mechanism is more robust than, e. g., Fiske resonances and allows for tunability and emission at various temperatures.

Another solution was reported in a series of publications by Lin and Hu [60, 61, 63, 65, 66, 68]. They found stable configurations of so-called π-kinks. Here, the phase difference consists of the usual part that evolves linearly in time, a second term for plasma oscillations and a third static part that describes the interlayer coupling. One finds solutions where the static part of the phase changes by π (in general plus any multiple of 2π) along the junction. In adjacent junctions the phase can also change by π along the c-axis with any periodicity of, e. g., two or four layers. Such a configuration would provide an efficient coupling of ac Josephson currents to cavity modes. On the IVC there appear current steps at which the π-kink states appears. By simulating the radiation power one finds that whenever a π-kink has formed the radiation power is enhanced

strongly. However, calculations of the radiation power highly depend on the boundary conditions, making it difficult to make precise estimations. Nevertheless, calculations show a radiation power of 2000-8000 W/cm^2 at different current steps, which is comparable to experimental data. Interestingly, although, the phase difference is non-uniform along the *c*-axis, in the π-kink-configuration the electric and magnetic fields are uniform making coherent radiation possible. The formation of π-kinks leads to a similar mechanism for phase synchronization as the modulation of the Josephson critical current density along the layer as it was proposed by Koshelev and Bulaevskii [57]. However, the modification of the critical current density must be done in advance during the fabrication process, whereas the formation of π-kinks can happen without special preparation. Lin and Hu also proposed that in-plane damping could be an important parameter that is responsible for phase synchronization. They show that if in-plane dissipation is considered, uniform cavity modes along the *c*-axis are favored and emission can occur [87].

Which mechanism exactly is realized in experiment is not clear yet. Most of the theoretical investigations are based on spatially homogeneous electric properties. However, due to the strong self-heating effect, quantities that are temperature-dependent strongly vary in space. Thus, to reproduce the experimental data as close as possible, all temperature-dependencies need to be considered. Especially, at high bias the thermal physics becomes crucial. In the simplest case, one can use the RCSJ model to describe the Josephson physics of an IJJ stack. This attempt was done by Gross *et al.* [55] and the IJJ stack was modeled as two columns of point-like JJs coupled to a thermal bath. The two columns can have different temperatures to allow the development of a hot spot. To reduce the numerical effort and calculation time the junctions are grouped to segments, assuming that in one segment the junctions behave identically, i. e., a segment is like one giant junction. Therefore, a scaling must be implemented to make the result independent of the chosen segmentation. To take the thermal physics into account, the heat diffusion equation was solved simultaneously to the RCSJ model taking the electric currents from the Josephson equations as input and providing the temperature distribution as input for all the temperature-dependent quantities in the RCSJ model. With this model it was tried to reproduce the unusual linewidth dependence on the bath temperature, i. e., that the linewidth decreases with increasing bath temperature as it was observed in Ref. [54]. By introducing a gradient of

the junction size along the c-axis, corresponding to a gradient in the critical current, it was possible to reproduce this observation. In reality such gradients can easily appear by fabrication (slope of the stack edge caused by milling), crystal inhomogeneities or doping. Although, the results look promising one needs to take into account that the RCSJ model is only valid for JJs where the phase difference stays constant along the junction, i. e., the Josephson length λ_J is assumed to be much larger than the lateral sizes of the junction. Because this is not the case for IJJ stacks used for THz generation coupled sine-Gordon equations need to be solved [84, 86, 88]. Heat diffusion together with coupled sine-Gordon equations were solved in publications 1 and 2 which are part of this thesis and are explained in more detail in section 2.1.1. In short, first one-dimensional coupled sine-Gordon equations were used to simulate a two-dimensional model of the stack. The appearance of resonant modes was observed leading to phase synchronization both at low- and high bias. In publication 2, this model was extended to three dimensions by using two-dimensional coupled sine-Gordon equations. More complex standing wave patterns were found that are not always compatible with the excitation of cavity modes or simple superpositions of those. Instead, vortex physics seems to play an important role for the formation of standing wave patterns.

Simulations that reproduce the experimental data well are a powerful tool to design sample geometries and to make predictions for experiments. Especially, for the development of suitable array structures simulations might become helpful. Then, however, also electromagnetic fields in the base crystal, inhomogeneities and defects of the crystals need to be considered as well. Moreover, fabrication techniques like argon ion milling also can create some gradients of doping or critical current density in the stack which need to be implemented in the model. Another issue that is widely ignored in most theoretical investigations is the d-wave symmetry of the superconducting wave function in BSCCO, which affects both the in- and out-of-plane currents and resistances. Thus, in experiment, the orientation in which the stack is pattered on the BSCCO crystal could affect the dynamics of the sample.

For the practical application of THz radiation from IJJ stacks, it is important to know for which direction the radiation power is strongest, which mainly depends on the kind of mode that is excited inside the stack. A wave oscillating along the short side will emit in a different direction than a wave oscillating along the long side. The exact calculation of radiation

patterns for different modes is quite challenging, since one has to consider effects of retardation, refraction and influences by neighboring structures, e. g., the substrate or a base crystal. Moreover, in general the development of a hot spot leads to a breaking of the symmetry and, furthermore, oscillating in-plane currents can occur that affect the direction of radiation. Nevertheless, for different cavity modes the angular dependence was calculated [89–92]. One finds that for most cavity modes the strongest emission occurs neither parallel nor perpendicular to the crystal layers but in some angle which depends on the cavity mode and the sample geometry. However, there are also cavity modes that lead to emission which is strongest in c-direction, e. g., the $(1,1)$ and the $(1,2)$ mode for rectangular mesas. In experiments, one also finds that the emission is not always strongest in c-direction, see for example Refs. [42, 91, 93]. Unfortunately, systematic measurements of the angular dependence for different cavity modes are missing, especially in the near-field of the stack. Such measurements by using, e. g., THz microscopy utilizing a detector junction that can be scanned across the stack or large arrays of detectors would be interesting to improve the general understanding of the emission characteristics. It is well possible that the angular dependence changes with bias current and voltage and the sample emits in different directions along the IVC. Such investigations are necessary to make BSCCO IJJ stacks ready for the practical application and to find a way to stabilize a certain mode to always operate the sample at its optimum. A way to stabilize a certain cavity mode was shown in publication 2. There, a small external magnetic field was applied along the long side of the stack leading to an additional phase gradient along the short side. In simulations this favored the appearance of the $(1,0)$ mode, i. e., one half-wave along the short side and no oscillation along the long side of the stack. By applying a small magnetic field of 5.9 mT along the long side, in experiment the emission power increased by almost a factor of 3, caused by the fact that in case of the $(1,0)$ mode all currents are oscillating in-phase at every time and, thus, electric and magnetic fields cannot cancel each other as it can partially happen for other modes.

Apart from that, there are a lot of other parameters that also can affect the emission properties. The position of the electrode [94] and the position of the hot spot can make a big difference, as it was shown in publication 6. Also the thickness of the electrode has influence and was analyzed in Ref. [95]. The shape of the stack can change the polarization of the emission.

For rectangular stacks the radiation is usually linearly polarized [26] but one can also generate circularly polarized radiation by using a truncated edge square mesa structure. This was predicted theoretically and is already confirmed in experiment. Such geometry can be realized by just heating an edge of a square-shaped sample by a focused laser beam as it was proposed by Asai and Kawabata [96] or just by fabricating a structure with a truncated edge [97, 98].

On the theoretical side, it was also proposed to manipulate the stack by a focused laser beam which locally heats the sample surface. It was predicted that this can excite strong plasma waves and enhance the emission power up to the order of milliwatts [99]. This was the motivation for publication 5. Although, in experiment such a large effect could not be confirmed, it was possible to show that one can precisely tune the emission power in a smaller range.

The electronic properties of cuprate superconductors strongly depend on their doping level. The doping may have a big influence on the emission properties as well. Usually, optimally doped or slightly underdoped crystals are used without knowing if this is the best choice. In publication 7, it was shown that already small changes of the doping level can change the emission properties. Precise and systematic measurements still need to be done, but the presented measurements already show that the doping level is an important parameter for THz emission as well.

The results of this thesis strongly encourage the continuation of THz research based on IJJs. The rich dynamics of IJJ stacks still provide many aspects that can be investigated both in simulations and experiment. Some of the observed results and ways to tune and manipulate the emission properties may help to improve the samples. Optimal conditions still need to be found and there are still open questions, especially, in terms of phase synchronization of several stacks. The developed numerical model may shine some light on the mechanics of IJJ stacks and may help to build improved sample geometries. As it is shown in publication 8 and 9, already simple applications can be realized. Most likely, applications involving THz radiation will become more and more important in different fields of science — perhaps also with the use of BSCCO IJJ stacks.

2 Summary of publications and contributions

In this chapter the appended publications are summarized. At the end of each summary own contributions are described.

2.1 Electrothermal dynamics of intrinsic Josephson junction stacks

This section contains publications 1 to 4 that contribute to the general understanding of the electrothermal dynamics of intrinsic Josephson junction stacks.

2.1.1 **Publication 1:** Thermal and electromagnetic properties of $Bi_2Sr_2CaCu_2O_8$ intrinsic Josephson junction stacks studied via one-dimensional coupled sine-Gordon equations

&

Publication 2: Three-Dimensional Simulations of the Electrothermal and Terahertz Emission Properties of $Bi_2Sr_2CaCu_2O_8$ Intrinsic Josephson Junction Stacks

Despite of several years of research still not all the details of the mechanisms generating coherent THz radiation from IJJ stacks are understood. Especially, the large temperature gradients inside the stack in the presence of a hot spot and the many properties which depend on temperature make it difficult to develop a good intuition and to make predictions for the physical behavior of the system. Therefore, simulations of the system are a useful tool to study the influence of different parameters on the system as

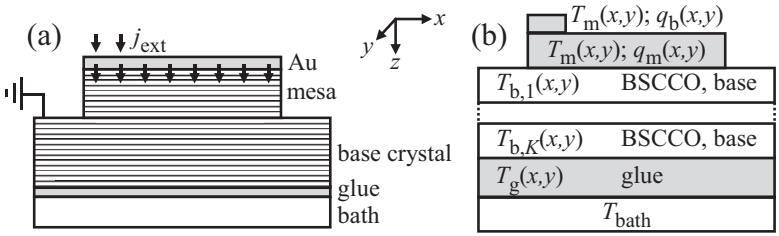

Figure 2.1: Model for numerical simulations. (a) Electric current flow through the mesa into the base crystal. (b) Thermal description of the sample. Figure from publication 2. © by the American Institute of Physics.

well as the behavior in general. In the past, already many attempts were made to simulate stacks of IJJs. But these simulations of the electrodynamics were either based on a homogeneous temperature distribution, or only resistive dc currents were taken into account to calculate the temperature distribution neglecting the superconducting properties. A combined calculation of electrodynamics and heat diffusion has only been done using the RCSJ model which is only valid for point-like JJs and, therefore, not suitable for large IJJ stacks. Instead, coupled sine-Gordon equations should be solved simultaneously together with heat diffusion equations. This was done in publication 1 where one-dimensional sine-Gordon equations were used representing a two-dimensional model of the system where the width of the stack is ignored. The current distribution calculated from the sine-Gordon equations is given as input to the heat diffusion equations which vice versa provide the local temperature for all temperature-dependent parameters in the sine-Gordon equations. In this way, it is possible to self-consistently solve the system of differential equations until a stable solution has developed. In publication 2, this model was extended to three dimensions using coupled sine-Gordon equations also considering the width of the stack. In both cases, the model depicted in Fig. 2.1 is as follows (for the 2D model dependencies on y can be ignored).

A mesa having a length L_s along x, a width W_s along y, and thickness D_m along z is placed on top of a base crystal and consists of N junctions each having a thickness $s = d_s + d_i$ (superconducting layers $d_s = 0.3\,\mathrm{nm}$ and insulating layers $d_i = 1.2\,\mathrm{nm}$). The length and width of the stack is discretized to, e. g., 50 and 9 grid points, respectively. A gold layer covers

the mesa surface and is treated as ideal electric conductor. For the electric circuit the base crystal serves as ground terminal while for the thermal equations heat diffusion through the base crystal is considered, i. e., the base crystal consists of several layers with different temperatures and its bottom surface is set to bath temperature. Inside the mesa no temperature gradients along z are taken into account but, of course, the temperature can vary along x and y. To obtain the temperature distribution, the heat diffusion equation

$$c\dot{T} = \nabla(\kappa\nabla T) + q_\mathrm{m} + q_\mathrm{b} \tag{2.1}$$

is solved with the specific heat capacity c, the thermal conductivity κ, and the power densities q_m and q_b for heat generation in the mesa and the bond wire, respectively. $\nabla = (\partial/\partial x, \partial/\partial y)$ denotes spatial derivatives.

Treating all of the hundreds of junctions individually can be a big numerical effort in terms of calculation time. Therefore, the N junctions are grouped to M segments each containing $G = N/M$ junctions. It is assumed that all junctions in a given segment behave identically. The bias current enters the mesa through a bond wire which is attached on top of the gold layer. The current distributes inside the stack according to the local BSCCO resistivity $\rho(x,y) = (\rho_{ab}, \rho_{ab}, \rho_c)$ and leaves the mesa into the base crystal. All parameters (electric and thermal conductivities, critical current density and Cooper pair density, London penetration depth, etc.) are considered to be temperature-dependent. Taking all dependencies into account, this leads to a sine-Gordon equation for the Josephson phase differences $\gamma_m(x,y)$ for the mth segment

$$\begin{aligned} Gsd_\mathrm{s}\nabla\left(\frac{\nabla\dot{\gamma}_m}{\rho_{ab}}\right) + d_\mathrm{s}\nabla\left(j^\mathrm{N}_{x,m+1} - j^\mathrm{N}_{x,m}\right) + G\lambda_\mathrm{k}^2\nabla(n_\mathrm{s}\nabla\gamma_m) \\ = 2j_{z,m} - j_{z,m+1} - j_{z,m-1} \end{aligned} \tag{2.2}$$

containing the out-of-plane current densities

$$j_{z,m} = \beta_{c0}\ddot{\gamma}_m + \frac{\dot{\gamma}_m}{\rho_{c,m}} + j_\mathrm{c}\sin(\gamma_m) + j^\mathrm{N}_{z,m}\,. \tag{2.3}$$

The index m runs from 1 to M numbering the individual segments. n_s denotes the Cooper pair density, $\beta_{c0} = 2\pi j_{c0}\rho_{c0}^2\varepsilon\varepsilon_0 s/\Phi_0$ the 4.2 K-value of the Stewart-McCumber parameter containing the magnetic flux quantum

Φ_0, the critical Josephson current density $j_c(4.2\,\mathrm{K}) \equiv j_{c0}$ and the c-axis resistivity $\rho_c(4.2\,\mathrm{K}) \equiv \rho_{c0}$. ε_0 denotes the vacuum permittivity and ε the BSCCO dielectric constant. $\lambda_k = [\Phi_0 d_s/(2\pi\mu_0 j_{c0}\lambda_{ab0}^2)]^{1/2}$ is a characteristic length for the interlayer coupling due to kinetic inductances. Geometric inductances are assumed to be much smaller and are neglected. In the equation for λ_k the magnetic permeability μ_0 and the 4.2 K-value of the in-plane London penetration depth $\lambda_{ab}(4.2\,\mathrm{K}) \equiv \lambda_{ab0}$ are contained. Additional in- and out-of-plane Nyquist noise currents $j_{x,m}^N$ and $j_{z,m}^N$ are included to avoid only weakly stable solutions. To make the solutions independent of the total segment number M, for a fixed junction number N a scaling is implemented in the model which rescales the plasma frequency ω_{pl} and λ_k such that the highest mode velocity c_1 stays independent of the number of segments.

Results of the 2D model

This section summarizes the results of publication 1 where the width of the stack was not considered yet. Calculated IVCs for different bath temperatures are shown in Fig. 2.2(a). The dots correspond to the final solution of the full model, the solid lines originate from the first initialization step where only c-axis dc currents were taken into account. These data points coincide at high-bias, showing that dissipation in c-axis by quasiparticles is the dominant effect for self-heating and the back-bending of the IVCs. An example for a simulated temperature distribution is shown in Fig. 2.2(b) for a bias current of $I = 0.6\,I_{c0}$ and $T_b = 20\,\mathrm{K}$. Here, a hot spot appears in the left part of the stack having temperatures even higher than T_c while the right part of the stack stays at temperatures below T_c. In experiment, the hot spot usually appears at the position where the current is injected. This is modeled by an extra heat source at the position of the bond wire which allows to move the hot spot to a desired location. Figure 2.2(b) also shows the time-averaged and along the c-axis averaged, dissipated in- and out-of-plane power densities $\langle q_x \rangle$ and $\langle q_z \rangle$. Along the c-axis, as expected, most of the power is dissipated in the hot spot while in the ab-plane a standing wave has developed in the cold part of the stack, which is a sign of successful phase-locking of the junctions. The dynamics of phase synchronization can be also seen by looking at the time-evolution of the Josephson currents $j_c \sin\gamma_m$ in c-direction. Figure 2.3(a) shows two snapshots at different times differing by roughly half of an

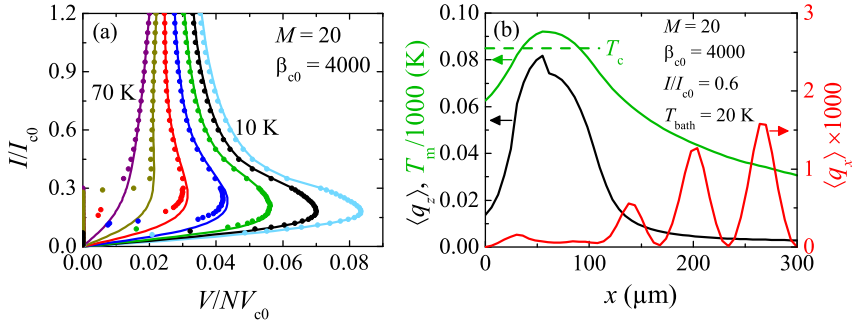

Figure 2.2: (a) Simulation of IVCs for different bath temperatures from 10 K to 70 K in steps of 10 K for 20 segments and $N = 700$. Solid lines represent the results after the first initialization step (only c-axis dc currents), dots show the final results including superconductivity and in-plane currents. The normalization values are $I_{c0} = 30$ mA and $V_{c0} = 30$ mV. (b) Simulation results for the temperature distribution (green), the time-averaged and over all segments averaged dissipated out-of-plane power (black) and the similarly averaged dissipated in-plane power (red) for 20 segments and $T_b = 20$ K.
Figures modified from publication 1. © by the American Institute of Physics.

oscillation period for the low-bias and Fig. 2.3(b) for the high-bias regime. One can clearly see that in both cases resonant modes were excited in the cold part of the stack and the junctions started to synchronize. This supports the idea that the synchronization of the junctions is caused by the excitation of cavity modes in the stack. It is worth to mention that no special synchronization mechanism is implemented in the model that induces phase synchronization and that the resonant modes appear by themselves due to self-organization of pairs of vortices and antivortices oscillating back and forth. The appearance of resonant modes and in-plane standing waves strongly indicate successful phase synchronization and emission from the stack. To quantify this one can calculate the Fourier transform of the time trace of the spatially averaged dissipated in-plane power $q_x(x,t)$. Taking the value q_{xp} at twice of the Josephson frequency of this function indicates how much power is dissipated by in-plane currents

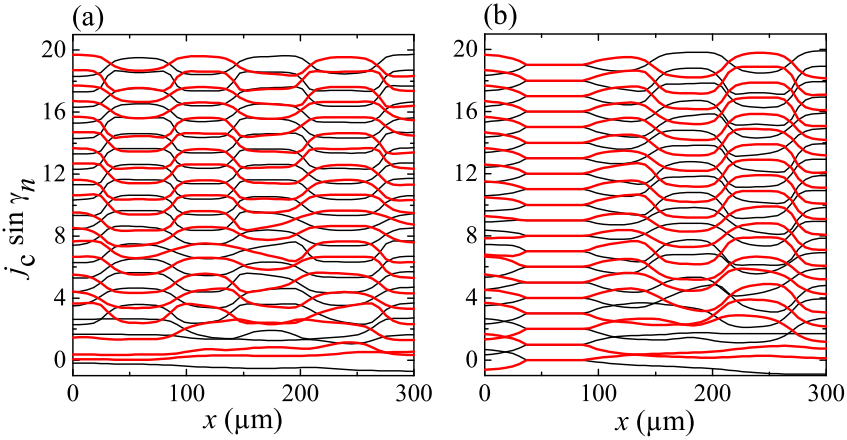

Figure 2.3: Snapshots of the *c*-axis supercurrents at two different times differing by roughly half of an oscillation period for 20 segments and $N = 700$. (a) For $T_b = 50$ K and $I = 0.3\, I_{c0}$ a resonant mode has been excited. (b) For $T_b = 20$ K and $I = 0.6\, I_{c0}$ a resonant mode coexists together with a hot spot (located where the Josephson currents are zero).
Figures modified from publication 1. © by the American Institute of Physics.

oscillating at the Josephson frequency and can be denoted as "strength" of the evolved wave. Although, this quantity describes the dissipated and not the emitted power one can imagine that these quantities are correlated and q_{xp} is used as color-code for the calculated IVCs, see Fig. 2.4(a). One observes that resonances are not excited at all bias currents and mainly occur in a broad region between $V/NV_{c0} \approx 0.02$ and 0.05 depending on the bath temperature. The general plot looks similar to what is observed in plots of families of IVCs obtained from experimental data where the detected emission power is used as color-code, see Fig. 2.4(b). Due to the fact that dissipated and emitted power are compared, of course, there have to be differences but the overall picture looks similar. Especially, the facts that no resonant modes are excited at voltages above $V/NV_{c0} \approx 0.05$ as well as at higher bath temperatures in the high-bias regime, where the whole sample is hot are very comparable to the experiment, where also

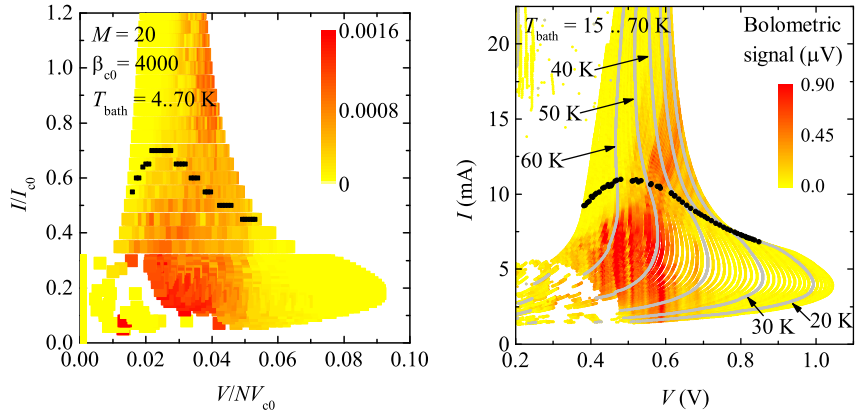

Figure 2.4: (a) Family of simulated IVCs for different bath temperatures from 4 to 70 K in steps of 2 K for 20 segments and $N = 700$. The dissipated in-plane power q_{xp} is used as color-code. Black dots indicate bias points above (below) which the maximum temperature of the stack was above (below) $T_c = 85$ K. For comparison in (b) a family of measured IVCs is shown with subtracted contact resistance from 15 to 70 K in steps of 0.5 K of a $165 \times 60\ \mu m^2$ sized IJJ stack consisting of 480 IJJs. The color-scale represents the detected power by a Ge bolometer. Black dots show bias points above which a hot spot has developed.
Figures modified from publication 1. © by the American Institute of Physics.

no emission was detected at these bias points. However, the stripe-like modulation of the detected power in Fig. 2.4(b) cannot be observed in the simulated data which might be caused by the low number of simulated bias points or because the appearance of the stripes is related to extrinsic effects not occurring inside the sample.

The simulations presented in Figs. 2.2 to 2.4 are based on calculations with $M = 20$, i. e., the 700 IJJs are grouped to 20 segments each containing 35 junctions. To clarify the scaling with M, IVC families for $M = 10$, 20, 35, 50, and even 350 were calculated and compared to each other, again, by inspecting the dissipated in-plane power. Some small differences are noticeable, e. g., for $M = 10$ a regime at high bias appeared where no

resonant modes could be excited any more but for higher values of M the overall picture stays the same, see Fig. 2.5.

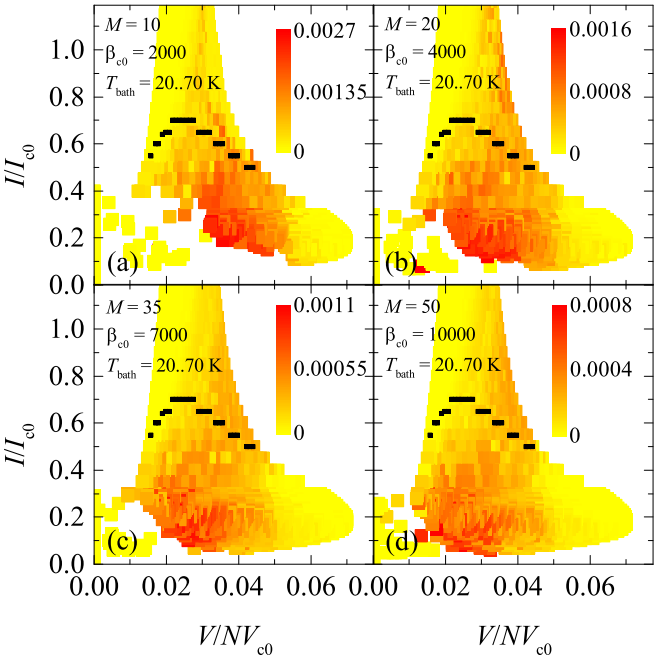

Figure 2.5: (a) to (d) Simulated IVC families for four values of M at T_{bath} from 20 K to 70 K in steps of 2 K. The dissipated in-plane power q_{xp} is used as color scale. The product $\beta_{\mathrm{c0}}G = 1.4 \times 10^5$ is kept constant. Black symbols denote the line above which a hot spot is present.
Figure from publication 1. © by the American Institute of Physics.

Results of the 3D model

In case of the three-dimensional model, now considering also the width of the stack, more complex standing wave patterns become possible. Looking again at the dissipated in-plane power (now called $q_{\parallel}(x, y)$) averaged over time and the height of the stack, again standing waves develop at high-

and low-bias, see Figs. 2.6(c)-(g). Among modes which oscillate along x [$(0,n)$ mode] or along y [$(m,0)$ mode], with n and m being positive integers, also unexpected mixed modes developed by a competition of two others, see Figs. 2.6(d) and (f). Such mixed modes are hard to explain by a simple superposition of usual cavity modes but can be understood by vortex-antivortex pairs that enter the stack at the sides and oscillate back and forth colliding in the center of an antinode of the wave pattern. By analyzing which kind of mode has developed at each bias current, it is possible to indicate this information by the symbol's shape in an IVC family, see Fig. 2.6(a). The strength of a given mode calculated by the value of the Fourier transform of the time- and spatially averaged $q_{\|}(x,y)$ at twice the Josephson frequency is used as color-code and shows whether a mode has developed and, if so, how strong the mode oscillates for a given bias current. One notices that the appearance of different modes happens rather randomly and no clear systematic trend is present. Although, both the $(0,n)$ and the $(m,0)$ modes are expected to radiate, however, to different radiation directions and with different planes of polarization, the $(1,0)$ mode should radiate stronger than $(0,n)$ modes with $n > 1$, because in the case of the $(1,0)$ mode all in-plane currents oscillate in-phase at every timestep and their contributions to the electromagnetic field cannot cancel each other. Therefore, it would be beneficial to favor the appearance of the $(1,0)$ mode to enhance the emission power. This can be realized by applying a static, external magnetic field parallel to the long side of the stack, which adds a small gradient to the phase $\gamma(x,y)$ along the y-axis and, thus, also to the Josephson current. Figure 2.6(b) shows the simulation result for an applied magnetic flux of $\Phi_x = 0.05\,\Phi_0$ per junction which corresponds to a magnetic field of about 1 mT. For a wide range of bias currents and bath temperatures in the high-bias regime the applied field leads to a stabilization of the $(1,0)$ mode. As mentioned above this should lead to an enhanced emission power. This idea was tested in experiment and an external magnetic field of $B_x = 5.9\,\mathrm{mT}$ ($0.32\,\Phi_0$ per junction) was applied parallel to the long side of the stack. Families of IVCs of a $330 \times 75\,\mu\mathrm{m}^2$ sized GBG structure were measured at bath temperatures from 10 to 45 K. Each IVC was measured for $B_x = 0$ and 5.9 mT before the next bath temperature was set. The result is shown in Fig. 2.7. A clear enhancement at many bias currents and bath temperatures was observed. At high-bias the maximum emission power increased up to a factor of 2.7. At low bias even emission at the maximum voltage occurred which is rather unusual

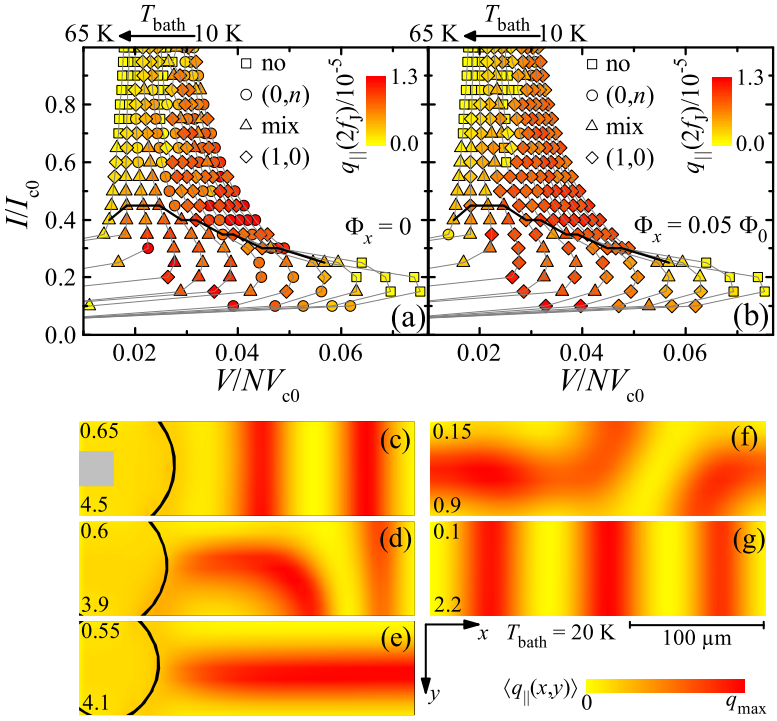

Figure 2.6: (a) shows a family of simulated IVCs for different bath temperatures from 10 to 65 K for no external magnetic field. Different wave patterns can be excited indicated by the shape of the symbol. The dissipated in-plane power is used as color-code. (b) shows a similar calculation, but with an applied external magnetic flux along the *x*-axis of 0.05 Φ_0. (c)-(g) show excited wave patterns for different bias points. The applied current in units of I_{c0} is displayed in the top left corner of each plot, in the bottom left the value for q_{max}. The grey square in (c) indicates, where the bias current is injected.
Figures modified from publication 2. © by the American Institute of Physics.

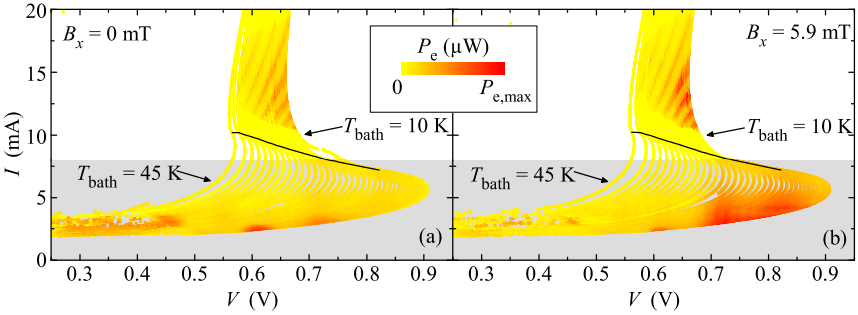

Figure 2.7: Experimental data for a GBG structure: terahertz emission power (color scale) for a large number of IVCs measured at bath temperatures between 10 and 45 K for an external magnetic field of (a) $B_x = 0$ and (b) $B_x = 5.9$ mT. In both (a) and (b) $P_{e,max} = 27.5$ μW for $I > 8$ mA and $P_{e,max} = 0.21$ μW for $I < 8$ mA. Black lines in (a) and (b) indicate the bias currents above which a hot spot is present.
Figures modified from publication 2. © by the American Institute of Physics.

for IJJ stacks, especially, at lower temperatures around 10 K. On the other hand, the emission in the range of 0.3 to 0.5 V which occurred for zero magnetic field seemed to be suppressed by the applied field. For other field orientations, e. g., along the short side of stack or perpendicular to the crystal layers the effect was not observed and even led to strong reduction of the emission power.

Contributions to publication 1

The numerical model to simulate the physics of IJJ stacks was developed by R. Kleiner. He also developed the code written in C. Code optimization and bug fixing was done by me. The experimental data shown in the publication to test and confirm the theoretical model was measured by me. A lot more experimental data to test, verify, and optimize the simulations was provided by me as well, however, most of them did not directly enter the publication. I also developed the measurement software, evaluated both the numerical as well as the experimental data and was involved in preparing and writing the manuscript.

Contributions to publication 2

Publication 2 is a direct follow-up on publication 1. The numerical model introduced in publication 1 was further developed and extended to three dimensions by R. Kleiner. Code optimization, bug fixing, and first tests to run the code in parallel on multiple processors was done by me to improve the performance of the simulations. The experimental data were measured by R. Wieland and me. I developed the measurement software to systematically acquire the experimental data. Together with my co-authors, I analyzed and evaluated the numerical and measured data and was involved in writing the manuscript.

2.1.2 **Publication 3:** Electrothermal behavior and terahertz emission properties of a planar array of two $Bi_2Sr_2CaCu_2O_{8+\delta}$ intrinsic Josephson junction stacks

The maximum output power for single IJJ stacks is still below 100 µW, although several attempts were made, e. g., by fabricating even higher stacks with a larger number of junctions. But due to the poor thermal conductivity the overheating of the stacks becomes more and more severe and at some point the emission power does not increase further. Thus, a promising approach is to build planar arrays of stacks because here the generated heat is distributed over the substrate and cooling can be done more efficiently. However, one has to find a way how the emission of the several stacks can be synchronized. So far, there is only one publication by Benseman *et al.* [53] where this was achieved successfully and a total emission power of 610 µW was reported. This shows that, in principle, it should be possible to build large arrays of IJJ stacks. However, exact conditions for synchronization of several stacks and suitable sample geometries are unknown.

In this publication, the electrothermal behavior of an array of two IJJ stacks was investigated by a combination of transport, THz emission, LT-SLM, and high-resolution frequency measurements. We started with one Z-shaped IJJ stack (for fabrication details see Ref. [51]) having a size of $330 \times 60 \times 0.7\,\mu m^3$ corresponding to about 480 IJJs. After the characterization of the pristine sample, in a first step, the stack was separated into two halves by a focused ion beam (FIB) cut having a width of about 200 nm. At this point, the electrodes were still connected and the sample can be

treated as a simple array structure with two stacks in parallel. Later on, the electrodes were split as well allowing to bias both stacks independently.

In every configuration, emission at high and at low bias as well as hot spot formation was observed. Depending on the bias conditions the hot spot appeared either in the center of one of the stacks or with its center in the slit. Although, the latter configuration is presumably the favorable one to synchronize the stacks it could not be achieved in this configuration. Even with precise setting of the individual voltages of the two stacks while monitoring the emission frequency line using a superconducting integrated receiver (SIR) synchronized emission did not occur. Thus, probably other samples geometries are more appropriate or additional synchronizing elements are needed, e. g., a base crystal or an extra cavity surrounding the stacks. In addition, the temperature distribution, the hot spot position, and the individual voltages must be controlled precisely to make sure that all stacks are as close as possible in the same configuration. Also an external magnetic field presumably helps to make sure that the same cavity mode is excited in all stacks.

Contributions

The first measurements for this publication of the pristine sample and the sample after the first FIB cut were performed by B. Gross before I started my PhD. Data from the finally cut stack with separated electrodes (section 3.3 in the publication) was measured by B. Gross and me. Together, we evaluated and analyzed the data and wrote a first draft of the manuscript.

2.1.3 **Publication 4:** Self-Mixing Spectra of Terahertz Emitters Based on $Bi_2Sr_2CaCu_2O_{8+\delta}$ Intrinsic Josephson-Junction Stacks

There are several ideas how synchronization in IJJ stacks might work, but in experiment the synchronization mechanism itself is difficult to investigate. One can try to image standing wave patterns by LTSLM and assign them to cavity modes but a direct way to measure the properties of the phase synchronization mechanism seems to be hard to realize.

In this publication, we evaluated the quality of synchronization of IJJ stacks at different bias points by measuring the frequencies occurring in the global voltage signal, correlated this information to transport and

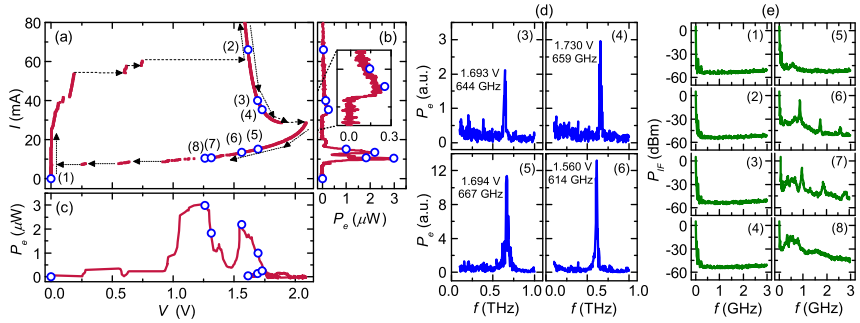

Figure 2.8: (a) IVC for T_b = 40 K and the detected emission vs. (b) bias current and vs. (c) bias voltage. Graph (d) shows Fourier spectra of the emitted radiation and (e) the self-mixing spectra for the labeled bias points.
Figures modified from publication 4. © by the American Institute of Physics.

emission measurements, and analyzed which parameters affect the synchronization in which way. Since JJs are non-linear elements they act as mixers for electromagnetic radiation and produce difference frequencies if groups of junctions oscillate at different frequencies. Thus, the appearance of difference frequencies is a sign for a not completely phase-locked configuration of the stack. In contrast, the absence of difference frequencies indicate that all junctions oscillate at the same frequency. In our case, difference frequencies in the range of some gigahertz were measured using a spectrum analyzer.

Two GBG structures were studied. The emission from sample 1 was detected using a Golay cell while in the case of sample 2 a YBCO grain boundary junction was used as detector. The emission from sample 1 mainly occurred at low bias while at high bias only weak emission peaks were observed. For this reason, sample 2 was also studied which showed stronger emission power at high bias.

Figure 2.8 shows data for sample 1 at T_b = 40 K. At bias points (2) to (4) the intermediate frequency (IF) spectra, shown in Fig. 2.8(e), look almost identical to (1) without bias. This is not surprising for bias point (2) because here, most likely, the whole stack has reached temperatures above

T_c and THz emission disappeared. At bias point (3) and (4) the IF spectra is flat indicating either good phase-lock or because of the weak emission signal the IF signal for this bias is hidden in the background. However, sample 2 also showed flat IF spectra for strong emission power at high bias indicating that phase-lock seems to work well in the presence of a hot spot. At bias point (5) which is already in the low-bias regime a peak appears in the IF spectra. The peaks become even more prominent for the remaining points (6) to (8), meaning that although the THz emission power is quite strong, the synchronization of the junctions seems to be incomplete. The data agree with the earlier high-precision frequency measurements using a SIR [54]. There, it was observed that the linewidth can be two orders of magnitude smaller at high bias in the presence of a hot spot than at low bias, which also suggests that the conditions for phase synchronization are fulfilled better at high bias.

Interestingly, the sample also emitted at very high bath temperatures of $T_b = 80\,\mathrm{K}$ with a frequency of 200 GHz also having a flat IF spectrum without peaks. This indicates again a good phase-locking and is again in agreement with earlier observations that synchronization works better at elevated temperatures.

In conclusion, by the observation of IF spectra due to self-mixing products combined with transport and emission measurements one can quickly and easily study the ability of the sample to achieve good phase-locking for different bias conditions.

Contributions

The measurements in this publication were performed by the group of H. B. Wang together with the group of V. P. Koshelets. Together with my co-authors, I evaluated and interpreted the data. Further, I supplied ideas and comments leading to the final publication.

2.2 Tunability of the terahertz emission properties

In this section, ways to tune and manipulate the terahertz emission properties are presented.

2.2.1 **Publication 5:** Tuning the Terahertz Emission Power of an Intrinsic Josephson-Junction Stack with a Focused Laser Beam

Publication 5 was motivated by a theoretical work of Asai and Kawabata [99] who proposed to locally heat the IJJ stack using a focused laser beam. Their calculations show that this can strongly excite Josephson plasma waves inside the stack which might increase the emission power up to the level of milliwatts.

To experimentally investigate their proposal a new measurement setup was built with which it is possible to detect the emitted power while scanning across the sample surface using a focused laser beam. The arriving power of the laser beam which is fed to the sample surface using a glass fiber was estimated to be on the order of 2 to 5 mW. However, a lot of its intensity is reflected at the top gold layer of the IJJ stack and, thus, probably only some tenth of a milliwatt were absorbed by the stack changing the local temperature of the stack probably by less than 1 K.

Figures 2.9(a)-(c) show the IVC and the detected power P_e for a bath temperature of 22 K. For each bias current a linescan is plotted in Fig. 2.9(a) showing that a hot spot developed in the left part of the stack for currents larger than roughly 8 mA and grows in size for increasing bias currents. Figure 2.9(d) shows how P_e varied for different laser positions x_L along the center of the stack for $I = 28\,\mathrm{mA}$ and $T_b = 22\,\mathrm{K}$. Especially, if the laser spot is set to a position close to or inside the hot spot the emitted power increased strongly. Also, for almost all bias currents in the emitting regime an enhancement was observed, see Fig. 2.9(e), with a maximum enhancement of 75 %. However, it was also observed that the change of the emitted power ΔP_e and the global voltage change ΔV_{dc} caused by a rise of the stack temperature due to the laser heating are proportional to each other irrespectively of the laser position. This proportionality was unexpected and led to the conclusion that the tunability of the emission

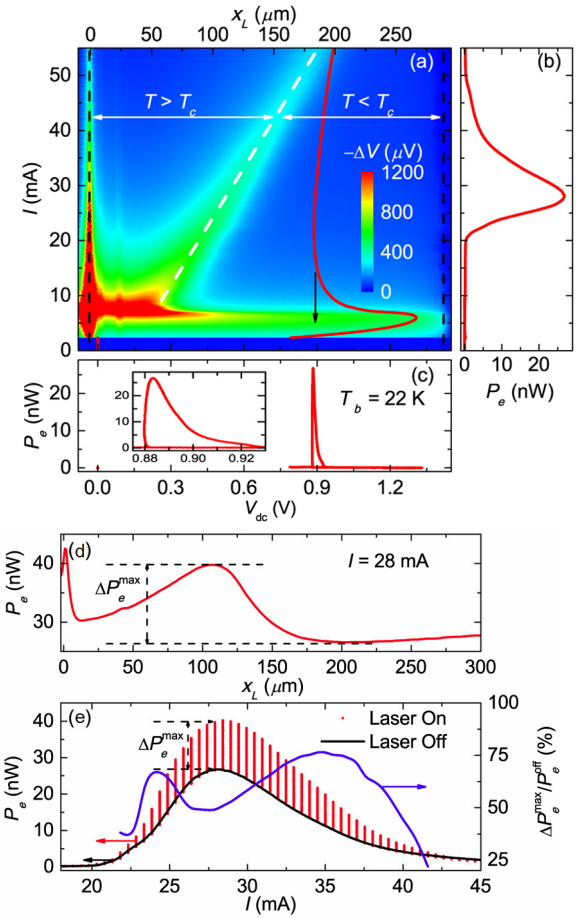

Figure 2.9: (a) IVC for T_b = 22 K and a family of LTSLM linescans along the center of the stack for different bias current. Detected emission vs. (b) bias current and (c) voltage. The inset in (c) shows a zoom to the voltage scale. (e) shows the detected emission for different laser spot positions at I = 28 mA and (e) the maximum enhancement of the emission power caused the laser spot for different bias currents.
Figures modified from publication 5. © by the American Institute of Physics.

power is rather correlated with a rise of the average stack temperature equivalent with a rise of the bath temperature of 0.2 K than with induced local inhomogeneities leading to strong plasma waves as it was predicted by Asai and Kawabata. The predicted effect also would have needed to be much more pronounced when the laser was focused to the cold part of the stack where in our measurements no significant change was observed.

In conclusion, the theoretical predictions could not be confirmed but it was possible to show that one can still precisely tune the emission power by a focused laser beam which might be an useful tool to optimize the emission properties of IJJ stacks.

Contributions

The measurements in this publication were performed by the group of H. B. Wang. I contributed to the evaluation and interpretation of the experimental data and supplied ideas and comments to improve the manuscript. In addition, I was involved in writing and correcting the manuscript.

2.2.2 **Publication 6:** Three-terminal stand-alone superconducting terahertz emitter

The observation of the hot spots in large stacks of IJJs led to a intense debate whether or not the hot spot is helpful for the THz emission properties of IJJ stacks. Since the hot spot can have temperatures higher than T_c it reduces the superconducting part of the stack that is able to emit THz radiation. However, it was observed that in presence of a hot spot the linewidth of the radiation can be as narrow as some MHz whereas it is on the order of GHz when no hot spot is present. Thus, the hot spot seems to play an important role for the phase-locking of the junctions and should not be avoided. Therefore, also the precise control and the manipulation of the hot spot might be important, e. g., the position of the hot spot. Usually, the hot spot arises close to the position where the bias current is injected. If there are two terminals to inject the current one can set the hot spot next to either of these terminals by applying the current to one or the other terminal. By applying the current to both terminals simultaneously and choosing some current ratio it is possible to move the hot spot between the terminals. The way the hot spot position affects the emission properties was investigated in this publication. A new sample geometry was designed

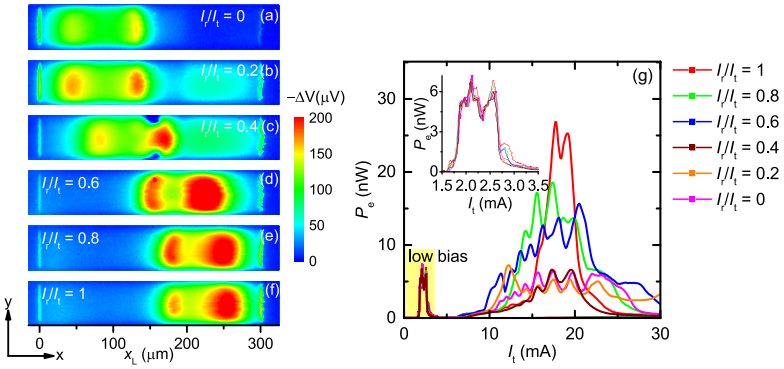

Figure 2.10: (a)-(f) LTSLM images for different current ratios I_r/I_t from 0 to 1 in steps of 0.2 for a fixed total current of I_t = 16 mA and a bath temperature of 20 K. (g) shows the emitted power vs. the total current for the same current ratios. The inset shows a zoom of the low-bias regime.
Figures from publication 6. © by the American Institute of Physics.

where a GBG stack has three terminals, two to inject the current and one terminal as ground. The sample was mounted in a setup with which it is possible to simultaneously detect the emitted power and to take LTSLM images of the stack surface to determine the hot spot position.

Figures 2.10(a)-(f) show, for $T_b = 20\,\mathrm{K}$ and a total current $I_t = I_l + I_r = 16\,\mathrm{mA}$, the position of the hot spot for different current ratios I_r/I_t from 0 to 1 in steps of 0.2 where one can see the hot spot moving from one side to the other. Figure 2.10(g) shows the emitted power for the same current ratios. Here, big changes of the emission power were observed from one ratio to the other. Note, that at low bias no change of the emitted power happens. This is not surprising because here no hot spot is present and, therefore, different current ratios do not affect the current distribution inside the stack as much as in the high-bias regime. Measurements of similar samples in Tübingen even showed that in the hot spot regime already much smaller changes of the current ratio of 0.02 lead to drastic changes of the emission power of the sample. It should also be mentioned that both the LTSLM images as well as the emission properties do not behave symmetrically according to the current ratio. For instance, the emission profile for $I_r/I_t = 1$ is completely different from the symmetric

case $I_r/I_t = 0$. This is probably related to asymmetries of the gap between the terminals leading to a different contact resistance and different thermal coupling of the left and right terminal but could, in principle, also be caused by inhomogeneities of the BSCCO crystal, e. g., defects or even small cracks. Nevertheless, these measurements show that already small modifications of the current distribution inside the stack can lead to strong changes of the emission properties.

Contributions

The experimental data was obtained by the group of H. B. Wang. At the same time, I also did these kind of measurements to systematically investigate and to understand the described effect in more detail. However, this data did not enter the publication directly. With my co-authors I evaluated and analyzed the experimental data and was involved in the interpretation of the results. Finally, I took part in writing the manuscript.

2.2.3 **Publication 7:** Tuning THz emission properties of $Bi_2Sr_2CaCu_2O_{8+\delta}$ intrinsic Josephson junction stacks by charge carrier injection

The properties of high-T_c superconductors strongly depend on its doping level, i. e., the amount of oxygen per unit cell of the crystal. Mostly, optimally doped or slightly underdoped crystals are used to fabricate IJJ stacks for THz generation but in fact it is not clear whether this is the best choice. To investigate the dependence of the electromagnetic and thermal properties on the doping level one has to systematically change the doping level and evaluate how the sample properties change.

In this publication, this was done by charge carrier injection which is a technique to change the doping level *in situ* to higher as well as to lower levels by applying large currents to the sample. This method can change the doping level, however, it does not change the oxygen content of the crystal and is probably related to the filling and unfilling of charge traps in the insulating layers inducing a change of the Cooper pair density in the superconducting layers [100]. Thus, in the experiment one needs to reach a certain threshold voltage at which the (un-)doping process starts. The change of charge carrier concentration is persistent if the sample is kept at low temperature.

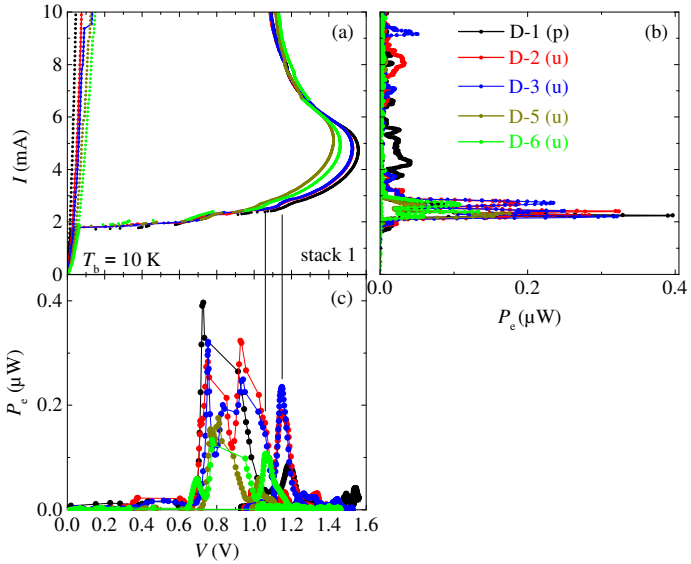

Figure 2.11: (a) shows the IVCs and the procedure of undoping for several steps D-1 to D-6. (b) and (c) show the detected emission power for the different doping levels vs. bias current and vs. bias voltage, respectively. Figures modified from publication 7. © by the Institute of Physics.

Although, this technique is mostly used for stacks with small lateral dimensions and small number of junctions, in publication 7 it was possible to show that one can also use charge carrier injection for large BSCCO stacks, in our case with lateral dimensions of $330 \times 50\,\mu m^2$ containing 930 junctions. On purpose, (un-)doping was only performed over a small range changing the critical temperature by less than 1 K to study if already small changes in the charge carrier concentration affect the THz emission properties of the samples. Currents on the order of 100 mA to 150 mA had to be applied to start the (un-)doping process. After each (un-)doping process the sample's emission properties were measured before the next doping step was performed. Figure 2.11 shows the IVCs and the THz emission properties of a three-terminal GBG structure after subsequent undoping steps for a fixed bath temperature of $T_b = 10\,K$. The resistive branch changed after each doping step indicating that the *c*-axis resistivity

was affected. In its pristine state (D-1), the sample emitted in the range of 4 to 6 mA and showed a strong emission peak at low bias around 2 mA. However, at 2 mA some junctions already switched back to their superconducting state making it difficult to compare this configuration with other doping states. The emission peak between 6 to 8 mA vanishes for the next doping steps and emission appears at higher bias currents. One can also observe a resonance step on the IVCs at around 1 V where a cavity mode seems to be excited. The voltage where this bump appears changes with doping indicating that also the mode velocity is affected by the change of doping.

The emission can not only become weaker or stronger but can even totally vanish for tiny changes of the doping level. On the other hand, this should make it possible to change non-emitting samples to emitting ones by a small treatment of carrier injection or any other way that affects the doping level which would be a way to recover "bad" samples.

Contributions

The idea to use charge carrier injection experiments for our samples to systematically change the THz emission properties by changing the doping level came up by O. Kizilaslan. The experimental data was measured by O. Kizilaslan, R. Wieland, and me. Together, we evaluated and interpreted the measured data. Finally, I was involved in writing and preparing the manuscript.

2.3 Applications of terahertz radiation from intrinsic Josephson junctions

In this section, some simple applications are presented that show that IJJ stacks are, in principle, ready to be used and integrated into other systems.

2.3.1 **Publication 8:** Compact Superconducting Terahertz Source Operating in Liquid Nitrogen

The long-term goal of THz research is to build a low-cost, portable, compact, tunable, coherent, and powerful device which can be used for a large field of applications. This publication focuses on low costs, easy handling, and portability.

A small, compact THz radiation system was designed which operates at liquid nitrogen temperatures. A sandwiched GBG structure was used as emitter with optimized cooling efficiency (for details see Ref. [45]). The radiation was collected and fed into a metallic tube acting as a waveguide and was detected by a Si bolometer. Operating the sample at liquid nitrogen temperatures, see Fig. 2.12, the emitted power was in the range of a tenth of a microwatt and was tunable from 0.266 to 0.364 THz by varying the bias voltage. The linewidth of the radiation was determined to be not larger than 7.5 GHz since this is the resolution limit of the interferometer used to obtain the frequency spectra. However, one should keep in mind that high-resolution measurements of other IJJ stacks showed that the linewidth can be as narrow as some MHz, at least in the presence of a hot spot. For a proof of principle, it was also demonstrated that the device can be powered by a commercial 1.5 V battery which makes it portable and easy to handle, similar to a standard torch. In principle, such a system is ready for practical applications in the lower THz range at relatively low costs since no liquid helium and no sophisticated electronics is required.

Contributions

The measurements in this publication were performed by the group of H. B. Wang. Data analysis and evaluation was done together by my coauthors and me. I also supplied ideas and comments to improve the manuscript.

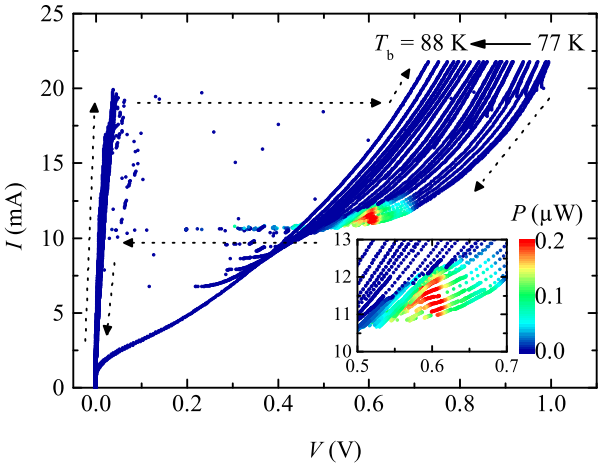

Figure 2.12: IVCs for different bath temperature from 77 K to 88 K. The detected emission power is color-coded. The inset shows a zoom of the emitting region.
Figure modified from publication 8. © by the American Institute of Physics.

2.3.2 **Publication 9:** Terahertz Spectroscopy of Dilute Gases Using $Bi_2Sr_2CaCu_2O_{8+\delta}$ Intrinsic Josephson-Junction Stacks

Spectroscopy is one of the main applications for all kinds of radiation. Many molecules have rotational and vibrational frequencies in the THz range and can be detected easily. In this publication, we demonstrate that clear absorption dips of water and ammonia vapor can be observed with two different setups using THz radiation from IJJ stacks.

In the first setup, the sample is mounted inside a cryocooler which can operate at temperatures down to 30 K. The radiation is collected and reflected by a parabolic mirror and passes a gas chamber. The transmitted radiation is then detected by a Golay cell. By varying the bias voltage across the stack it is possible to tune the emitted frequency and record transmission spectra for different gases inside the chamber.

After measuring the transmitted radiation of the evacuated gas chamber as reference it was filled with, e. g., ammonia vapor. By comparing the detected signals with and without vapor one finds two absorption dips at roughly 557 GHz and 572.5 GHz, see Fig. 2.13(b) and (c). The latter frequency corresponds to the well-known rotational transition frequency of ammonia molecules. The first one arose from remaining water in the ammonia vapor since it was votalized from ammonia water. The same experiment was also done with pure water vapor leading to only one dip at 557 GHz, as expected. Doppler broadening can be suppressed by reducing the gas pressure in the chamber leading to absorption linewidths of 1 GHz limited by noise of the setup. However, this resolution is already comparable to the one of standard THz time-domain spectroscopy setups.

For a high-resolution measurement of the spectra another setup was used consisting of a SIR as detector which has a frequency resolution of less than 100 kHz. Using this setup, the absorption linewidths could be measured down to 4 to 5 MHz at lowered gas pressures, see Fig. 2.13(e) and (f). Note, that the linewidth of the radiation itself was around 60 MHz.

This publication shows that IJJ stacks are already suitable for some kinds of spectroscopy experiments. Especially, the first presented measurement setup might be a reasonable alternative to more expensive and sophisticated setups.

Contributions

The measurements in this publication were performed by the group of H. B. Wang. Together, we evaluated and analyzed the data. I contributed ideas and comments to improve the manuscript leading to the final publication.

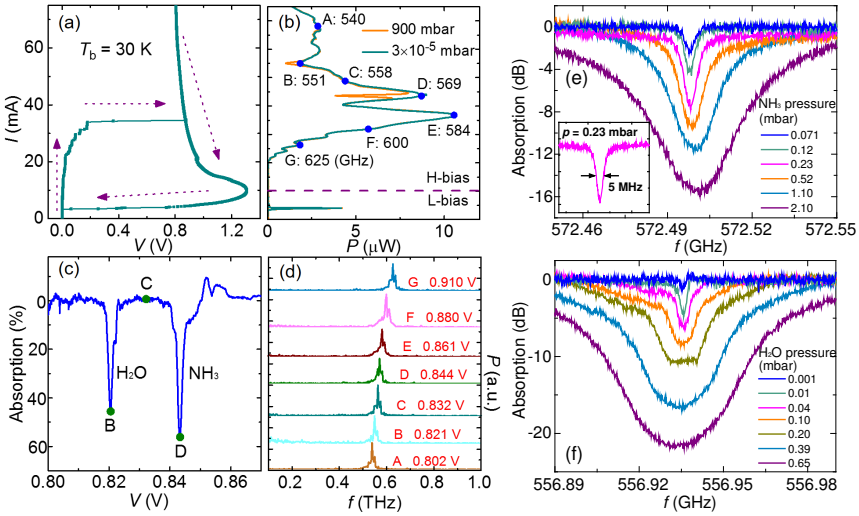

Figure 2.13: (a) IVC for T_b = 30 K. Graph (b) shows the detected emission vs. bias current for two different gas pressures. In (c) the absorption calculated from the ratio of the emission signal for the different gas pressures is plotted. (d) shows Fourier spectra of the emitted radiation at the bias points A-G indicated in (b). THz absorption spectra measured with the SIR are plotted in (e) for ammonia and in (f) for water vapor for different gas pressures.
Figure modified from publication 9. © by the American Institute of Physics.

3 Summary and outlook

This thesis attempted to pursue three goals. First of all, in publication 1 and 2 by the development of a numerical model for IJJ stacks based on combined heat diffusion and coupled sine-Gordon equations the physical dynamics inside the stack have been studied to improve the general understanding of the samples. Starting with the calculation of IVCs, the typical back-bending and the formation of a hot spot in the high-bias regime were reproduced. Self-organized phase synchronization and the excitation of several kinds of resonant modes could be observed in a broad range of bias currents and bath temperatures, both at low and at high bias. By analyzing the dissipated in-plane power it was possible to quantify the strength of the excited waves and to compare this value to the experimentally detected power. In general, results comparable to experiment were observed, however, some differences like the stripe-like modulation of the emission power observed in experiment remain. By applying an external magnetic field it was possible to stabilize the $(1,0)$ mode both in simulations and in experiment. In experiment, this led to an enhancement of the emission power by up to a factor of 2.7.

The possibility of phase synchronization of an array structure realized by dividing a normal-sized IJJ stack into two parallel, electrically independent stacks was investigated in publication 3. Phase synchronization was not observed leading to the conclusion that probably an additional synchronizing element is needed realized, for example, via mesa structures interacting via the common base crystal. In publication 4, a new method was presented to systematically analyze the quality of phase synchronization of a single IJJ stack by measuring the self-mixing spectra. This technique might become a useful tool to quickly check the quality of fabricated samples.

Second, ways to tune the emission properties of BSCCO stacks were studied. In publication 6, it was shown that one can tune the output power not only by changing the bias voltage or bath temperature. The precise control of the hot spot position and, therefore, the current distribution can lead to drastic changes of the emission power. The fact that the emission power

is this sensitive to the current distribution might also explain why the reported emission power of different samples varies strongly. Furthermore, it was shown in publication 5 that the use of a focused laser beam as local heat source can be used as precise tool to adjust the emission power. Also, the choice of the doping level of the BSCCO crystals can drastically change the emission properties (publication 7). In future, all these observations might help to optimize the bias conditions and to operate the samples at maximum emission power.

In the third part, some possibilities for the application of THz radiation were investigated. In publication 9, spectroscopy experiments for water vapor and ammonia were presented. Furthermore, in publication 8 it was shown that it is possible to build a small, portable, and low-cost THz emitter only requiring liquid nitrogen as coolant. Such a system is ready for practical applications in the lower THz range can be easily attached to other devices.

In future, the focus of THz research based on BSCCO is likely to move to the fabrication and investigation of arrays of IJJ stacks. Presumably, this is the only way to achieve a significant boost of the emission power. However, one needs to find a proper synchronization mechanism for such structures. The fact that the synchronized operation of an array of three stacks was only achieved once by one group shows that this will be a challenging task. Maybe, one has to return to sample geometries involving a base crystal as synchronizing element instead of fabricating stand-alone stacks which only can synchronize by radiation. Further, having the ability to control the temperature distribution and current distribution precisely as well as making sure that in each stack the same cavity mode is excited might be a key element. The former could be achieved by multiple injection points for the bias current, the latter one by applying external magnetic fields.

One could also think of designing array structures that do not consist of individual stacks next to each other but of normal-sized structures that are electrically connected. For example, such structures may consist of stacks arranged in a star shape connected in the center. Simulations using the model described in publications 1 and 2 already indicated that such structures may be synchronized via currents flowing through a common hot spot in the center.

Another big step forward would be the development of new fabrication techniques. If one could achieve to grow high-quality BSCCO thin films,

e. g., by pulsed laser deposition one would be much more flexible in designing and fabricating new sample geometries in a reproducible way which is currently an issue when thinking of using BSCCO stacks on a large-scale operation.

For the investigation of single stacks there are still a lot of issues to be analyzed in more detail. The systematic analysis of the influence of the doping level on the emission properties is one of them. Furthermore, there exist no systematic studies on how to properly match the impedance of a IJJ stack to the environment to couple out the THz radiation efficiently. This will become important at latest when attaching the stack to other optical elements or integrating it into other circuits.

List of acronyms

ac	Alternating current
BSCCO	Bismuth strontium calcium copper oxide, $Bi_2Sr_2CaCu_2O_{8+\delta}$
dc	Direct current
FIB	Focused ion beam
GBG	Gold-BSCCO-Gold
IF	Intermediate frequency
IJJ	Intrinsic Josephson junction
IVC	Current voltage characteristic
JJ	Josephson junction
LTSLM	Low temperature scanning laser microscopy
RCSJ	Resistively and capacitively shunted junction
SIR	Superconducting integrated receiver
YBCO	Yttrium barium copper oxide, $YBa_2Cu_3O_7$

Bibliography

[1] J. F. Federici *et al.*, "THz imaging and sensing for security applications – explosives, weapons and drugs", Semicond. Sci. Technol. **20**, S266 (2005).

[2] C. Yu *et al.*, "The potential of terahertz imaging for cancer diagnosis: A review of investigations to date", Quant. Imaging. Med. Surg. **2**, 33 (2012).

[3] S. Heyminck *et al.*, "GREAT: the SOFIA high-frequency heterodyne instrument", Astron. Astrophys. **542**, L1 (2012).

[4] E. Abraham *et al.*, "Non-invasive investigation of art paintings by terahertz imaging", Appl. Phys. A **100**, 585 (2010).

[5] J. Dong *et al.*, "Global mapping of stratigraphy of an old-master painting using sparsity-based terahertz reflectometry", Sci. Rep. **7**, 15098 (2017).

[6] E. R. Brown *et al.*, "Oscillations up to 712 GHz in InAs/AlSb resonant-tunneling diodes", Appl. Phys. Lett. **58**, 2291 (1991).

[7] M. Asada *et al.*, "Resonant Tunneling Diodes for Sub-Terahertz and Terahertz Oscillators", Jpn. J. Appl. Phys. **47**, 4375 (2008).

[8] J. Faist *et al.*, "Quantum Cascade Laser", Science **264**, 553 (1994).

[9] R. Köhler *et al.*, "Terahertz semiconductor-heterostructure laser", Nature **417**, 156 (2002).

[10] B. S. Williams, "Terahertz quantum-cascade lasers", Nat. Photonics **1**, 517 (2007).

[11] E. R. Brown *et al.*, "Photomixing up to 3.8 THz in low-temperature-grown GaAs", Appl. Phys. Lett. **66**, 285 (1995).

[12] M. Tani *et al.*, "Generation of terahertz radiation by photomixing with dual- and multiple-mode lasers", Semicond. Sci. Technol. **20**, S151 (2005).

[13] B. D. Josephson, "Possible new effects in superconductive tunnelling", Physics Letters **1**, 251 (1962).

[14] B. D. Josephson, "Coupled Superconductors", Rev. Mod. Phys. **36**, 216 (1964).

[15] B. D. Josephson, "Supercurrents through barriers", Adv. Phys. **14**, 419 (1965).

[16] A. I. Larkin and Y. I. Ovchinnikov, "Radiation line width in the Josephson effect", Sov. Phys. JETP **26**, 1219 (1968).

[17] P. Barbara *et al.*, "Stimulated Emission and Amplification in Josephson Junction Arrays", Phys. Rev. Lett. **82**, 1963 (1999).

[18] F. Song *et al.*, "Coherent emission from large arrays of discrete Josephson junctions", Appl. Phys. Lett. **95**, 172501 (2009).

[19] F. Song *et al.*, "Compact tunable sub-terahertz oscillators based on Josephson junctions", Appl. Phys. Lett. **98**, 142506 (2011).

[20] M. A. Galin *et al.*, "Towards local oscillators based on arrays of niobium Josephson junctions", Supercond. Sci. Technol. **28**, 055002 (2015).

[21] U. Welp *et al.*, "Superconducting emitters of THz radiation", Nat. Photonics **7**, 702 (2013).

[22] R. Kleiner, "Filling the Terahertz Gap", Science **318**, 1254 (2007).

[23] S.-O. Katterwe, "Properties of small $Bi_2Sr_2CaCu_2O_8$ intrinsic Josephson junctions: confinement, flux-flow and resonant phenomena", PhD thesis (Department of Physics, Stockholm University, 2011).

[24] R. Kleiner *et al.*, "Intrinsic Josephson effects in $Bi_2Sr_2CaCu_2O_8$ single crystals", Phys. Rev. Lett. **68**, 2394 (1992).

[25] E. A. Borodianskyi and V. M. Krasnov, "Josephson emission with frequency span 1–11 THz from small $Bi_2Sr_2CaCu_2O_{8+\delta}$ mesa structures", Nat. Commun. **8**, 1742 (2017).

[26] L. Ozyuzer *et al.*, "Emission of Coherent THz Radiation from Superconductors", Science **318**, 1291 (2007).

[27] H. B. Wang *et al.*, "Hot Spots and Waves in $Bi_2Sr_2CaCu_2O_8$ Intrinsic Josephson Junction Stacks: A Study by Low Temperature Scanning Laser Microscopy", Phys. Rev. Lett. **102**, 017006 (2009).

[28] S. Guénon *et al.*, "Interaction of hot spots and terahertz waves in $Bi_2Sr_2CaCu_2O_8$ intrinsic Josephson junction stacks of various geometry", Phys. Rev. B **82**, 214506 (2010).

[29] A. Yurgens, "Temperature distribution in a large $Bi_2Sr_2CaCu_2O_{8+\delta}$ mesa", Phys. Rev. B **83**, 184501 (2011).

[30] B. Gross *et al.*, "Hot-spot formation in stacks of intrinsic Josephson junctions in $Bi_2Sr_2CaCu_2O_8$", Phys. Rev. B **86**, 094524 (2012).

[31] T. M. Benseman *et al.*, "Direct imaging of hot spots in $Bi_2Sr_2CaCu_2O_{8+\delta}$ mesa terahertz sources", J. Appl. Phys. **113**, 133902 (2013).

[32] E. Spenke, "Zur technischen Beherrschung des Wärmedurchschlages von Heißleitern", Wissenschaftliche Veröffentlichungen aus den Siemens-Werken, 92 (1936).

[33] A. Vl. Gurevich and R. G. Mints, "Self-heating in normal metals and superconductors", Rev. Mod. Phys. **59**, 941 (1987).

[34] K. Kadowaki *et al.*, "Direct observation of tetrahertz electromagnetic waves emitted from intrinsic Josephson junctions in single crystalline $Bi_2Sr_2CaCu_2O_{8+\delta}$", Physica C **468**, 634 (2008).

[35] K. E. Gray *et al.*, "Emission of Terahertz Waves From Stacks of Intrinsic Josephson Junctions", IEEE Trans. Appl. Supercond. **19**, 886 (2009).

[36] L. Ozyuzer *et al.*, "Terahertz wave emission from intrinsic Josephson junctions in high-T_c superconductors", Supercond. Sci. Technol. **22**, 114009 (2009).

[37] H. B. Wang *et al.*, "Coherent Terahertz Emission of Intrinsic Josephson Junction Stacks in the Hot Spot Regime", Phys. Rev. Lett. **105**, 057002 (2010).

[38] T. M. Benseman *et al.*, "Tunable terahertz emission from $Bi_2Sr_2CaCu_2O_{8+\delta}$ mesa devices", Phys. Rev. B **84**, 064523 (2011).

[39] H. Minami *et al.*, "Terahertz Radiation Emitted from Intrinsic Josephson Junctions in High-T_c Superconductor $Bi_2Sr_2CaCu_2O_{8+\delta}$", IEICE Trans. Elect. **E95.C**, 347 (2012).

[40] M. Tsujimoto *et al.*, "Broadly Tunable Subterahertz Emission from Internal Branches of the Current-Voltage Characteristics of Superconducting $Bi_2Sr_2CaCu_2O_{8+\delta}$ Single Crystals", Phys. Rev. Lett. **108**, 107006 (2012).

[41] F. Rudau *et al.*, "Thermal and electromagnetic properties of $Bi_2Sr_2CaCu_2O_8$ intrinsic Josephson junction stacks studied via one-dimensional coupled sine-Gordon equations", Phys. Rev. B **91**, 104513 (2015).

[42] T. Kashiwagi *et al.*, "High Temperature Superconductor Terahertz Emitters: Fundamental Physics and Its Applications", Jpn. J. Appl. Phys. **51**, 010113 (2012).

[43] D. Y. An *et al.*, "Terahertz emission and detection both based on high-T_c superconductors: Towards an integrated receiver", Appl. Phys. Lett. **102**, 092601 (2013).

[44] S. Sekimoto *et al.*, "Continuous 30 μW terahertz source by a high-T_c superconductor mesa structure", Appl. Phys. Lett. **103**, 182601 (2013).

[45] M. Ji *et al.*, "$Bi_2Sr_2CaCu_2O_8$ intrinsic Josephson junction stacks with improved cooling: Coherent emission above 1 THz", Appl. Phys. Lett. **105**, 122602 (2014).

[46] T. Kashiwagi *et al.*, "Generation of electromagnetic waves from 0.3 to 1.6 terahertz with a high-T_c superconducting $Bi_2Sr_2CaCu_2O_{8+\delta}$ intrinsic Josephson junction emitter", Appl. Phys. Lett. **106**, 092601 (2015).

[47] T. Kashiwagi *et al.*, "A high-T_c intrinsic Josephson junction emitter tunable from 0.5 to 2.4 terahertz", Appl. Phys. Lett. **107**, 082601 (2015).

[48] X. J. Zhou *et al.*, "Tuning the Terahertz Emission Power of an Intrinsic Josephson-Junction Stack with a Focused Laser Beam", Phys. Rev. Appl. **3**, 044012 (2015).

[49] X. Zhou *et al.*, "Three-terminal stand-alone superconducting terahertz emitter", Appl. Phys. Lett. **107**, 122602 (2015).

[50] F. Rudau *et al.*, "Three-Dimensional Simulations of the Electrothermal and Terahertz Emission Properties of $Bi_2Sr_2CaCu_2O_8$ Intrinsic Josephson Junction Stacks", Phys. Rev. Appl. **5**, 044017 (2016).

[51] J. Yuan *et al.*, "Terahertz emission from $Bi_2Sr_2CaCu_2O_{8+\delta}$ intrinsic Josephson junction stacks with all-superconducting electrodes", Supercond. Sci. Technol. **25**, 075015 (2012).

[52] B. Gross *et al.*, "Electrothermal behavior and terahertz emission properties of a planar array of two $Bi_2Sr_2CaCu_2O_{8+\delta}$ intrinsic Josephson junction stacks", Supercond. Sci. Technol. **28**, 055004 (2015).

[53] T. M. Benseman *et al.*, "Powerful terahertz emission from $Bi_2Sr_2CaCu_2O_{8+\delta}$ mesa arrays", Appl. Phys. Lett. **103**, 022602 (2013).

[54] M. Li *et al.*, "Linewidth dependence of coherent terahertz emission from $Bi_2Sr_2CaCu_2O_8$ intrinsic Josephson junction stacks in the hot-spot regime", Phys. Rev. B **86**, 060505(R) (2012).

[55] B. Gross *et al.*, "Modeling the linewidth dependence of coherent terahertz emission from intrinsic Josephson junction stacks in the hot-spot regime", Phys. Rev. B **88**, 014524 (2013).

[56] L. N. Bulaevskii and A. E. Koshelev, "Radiation due to Josephson Oscillations in Layered Superconductors", Phys. Rev. Lett. **99**, 057002 (2007).

[57] A. E. Koshelev and L. N. Bulaevskii, "Resonant electromagnetic emission from intrinsic Josephson-junction stacks with laterally modulated Josephson critical current", Phys. Rev. B **77**, 014530 (2008).

[58] A. E. Koshelev, "Alternating dynamic state self-generated by internal resonance in stacks of intrinsic Josephson junctions", Phys. Rev. B **78**, 174509 (2008).

[59] S. Lin *et al.*, "Computer simulation on terahertz emission from intrinsic josephson junctions of high-T_c superconductors", Phys. Rev. B **77**, 014507 (2008).

[60] S. Lin and X. Hu, "Possible Dynamic States in Inductively Coupled Intrinsic Josephson Junctions of Layered High-T_c Superconductors", Phys. Rev. Lett. **100**, 247006 (2008).

[61] X. Hu and S. Lin, "Three-dimensional phase-kink state in a thick stack of Josephson junctions and terahertz radiation", Phys. Rev. B **78**, 134510 (2008).

[62] T. Koyama *et al.*, "In-phase electrodynamics and terahertz wave emission in extended intrinsic Josephson junctions", Phys. Rev. B **79**, 104522 (2009).

[63] S. Lin and X. Hu, "Phase dynamics in intrinsic Josephson junctions and their electrodynamics", Phys. Rev. B **79**, 104507 (2009).

[64] X. Hu and S. Lin, "Cavity phenomena in mesas of cuprate high-T_c superconductors under voltage bias", Phys. Rev. B **80**, 064516 (2009).

[65] X. Hu and S.-Z. Lin, "Phase dynamics in a stack of inductively coupled intrinsic Josephson junctions and terahertz electromagnetic radiation", Supercond. Sci. Technol. **23**, 053001 (2010).

[66] S.-Z. Lin and X. Hu, "Kink State in a Stack of Intrinsic Josephson Junctions in Layered High-T_c Superconductors and Terahertz Radiation", J. Supercond. Novel Magn. **23**, 1025 (2010).

[67] S.-Z. Lin and X. Hu, "Response and amplification of terahertz electromagnetic waves in intrinsic Josephson junctions of layered high-T_c superconductor", Phys. Rev. B **82**, 020504(R) (2010).

[68] S.-Z. Lin and X. Hu, "Stability of the kink state in a stack of intrinsic Josephson junctions", Physica C **470**, S201 (2010).

[69] A. E. Koshelev, "Stability of dynamic coherent states in intrinsic Josephson-junction stacks near internal cavity resonance", Phys. Rev. B **82**, 174512 (2010).

[70] V. M. Krasnov, "Coherent flux-flow emission from stacked Josephson junctions: Nonlocal radiative boundary conditions and the role of geometrical resonances", Phys. Rev. B **82**, 134524 (2010).

[71] S.-Z. Lin and X. Hu, "Radiation of Terahertz Electromagnetic Waves from Build-In Nano Josephson Junctions of Cuprate High-T_c Superconductors", J. Nanosci. Nanotechnol. **11**, 2916 (2011).

[72] S.-Z. Lin *et al.*, "Synchronization in a one-dimensional array of point Josephson junctions coupled to a common load", Phys. Rev. B **84**, 104501 (2011).

[73] V. M. Krasnov, "Terahertz electromagnetic radiation from intrinsic Josephson junctions at zero magnetic field via breather-type self-oscillations", Phys. Rev. B **83**, 174517 (2011).

[74] H. Asai *et al.*, "Three-dimensional numerical analysis of terahertz radiation emitted from intrinsic Josephson junctions with hot spots", Phys. Rev. B **85**, 064521 (2012).

[75] F. Liu *et al.*, "Cavity phenomenon and terahertz radiation of a tall stack of intrinsic Josephson junctions wrapped by a dielectric material", Supercond. Sci. Technol. **26**, 025003 (2012).

[76] H. Asai and S. Kawabata, "An effect of temperature distribution on terahertz phase dynamics in intrinsic Josephson junctions", Physica C **494**, 121 (2013).

[77] S.-Z. Lin and A. E. Koshelev, "Synchronization of Josephson oscillations in a mesa array of $Bi_2Sr_2CaCu_2O_{8+\delta}$ through the Josephson plasma waves in the base crystal", Physica C **491**, 24–29 (2013).

[78] S.-Z. Lin, "Mutual synchronization of two stacks of intrinsic Josephson junctions in cuprate superconductors", J. Appl. Phys. **115**, 173901 (2014).

[79] W. C. Stewart, "Current-Voltage Characteristics of Josephson Junctions", Appl. Phys. Lett. **12**, 277 (1968).

[80] D. E. McCumber, "Effect of ac Impedance on dc Voltage-Current Characteristics of Superconductor Weak-Link Junctions", J. Appl. Phys. **39**, 3113 (1968).

[81] D. D. Coon and M. D. Fiske, "Josephson ac and Step Structure in the Supercurrent Tunneling Characteristic", Phys. Rev. **138**, A744 (1965).

[82] T. Koyama and M. Tachiki, "*I-V* characteristics of Josephson-coupled layered superconductors with longitudinal plasma excitations", Phys. Rev. B **54**, 16183 (1996).

[83] M. Machida *et al.*, "Collective dynamics of Josephson vortices in intrinsic Josephson junctions: exploration of in-phase locked superradiant vortex flow states", Physica C **330**, 85 (2000).

[84] R. Kleiner *et al.*, "Stacked long Josephson junctions in zero magnetic field: A numerical study of coupled one-dimensional sine-Gordon equations", Phys. Rev. B **62**, 4086 (2000).

[85] S. Sakai *et al.*, "Theory and experiment on electromagnetic-wave-propagation velocities in stacked superconducting tunnel structures", Phys. Rev. B **50**, 12905 (1994).

[86] R. Kleiner, "Two-dimensional resonant modes in stacked Josephson junctions", Phys. Rev. B **50**, 6919 (1994).

[87] S.-Z. Lin and X. Hu, "In-plane dissipation as a possible synchronization mechanism for terahertz radiation from intrinsic Josephson junctions of layered superconductors", Phys. Rev. B **86**, 054506 (2012).

[88] R. Kleiner *et al.*, "Stacked long Josephson junctions in external magnetic fields – a numerical study of coupled one-dimensional sine-Gordon equations", Physica C **362**, 29 (2001).

[89] R. A. Klemm and K. Kadowaki, "Angular Dependence of the Radiation Power of a Josephson STAR-emitter", J. Supercond. Novel Magn. **23**, 613 (2010).

[90] R. A. Klemm and K. Kadowaki, "Output from a Josephson stimulated terahertz amplified radiation emitter", J. Phys.: Condens. Matter **22**, 375701 (2010).

[91] R. A. Klemm *et al.*, "Cavity mode waves during terahertz radiation from rectangular $Bi_2Sr_2CaCu_2O_{8+\delta}$ mesas", J. Phys.: Condens. Matter **23**, 025701 (2011).

[92] R. A. Klemm *et al.*, "Terahertz Emission From Thermally Managed Square Intrinsic Josephson Junction Microstrip Antennas", IEEE J. Sel. Topics Quantum Electron. **23**, 1 (2017).

[93] M. Tsujimoto *et al.*, "Geometrical Resonance Conditions for THz Radiation from the Intrinsic Josephson Junctions in $Bi_2Sr_2CaCu_2O_{8+\delta}$", Phys. Rev. Lett. **105**, 037005 (2010).

[94] K. Delfanazari *et al.*, "Effect of Bias Electrode Position on Terahertz Radiation From Pentagonal Mesas of Superconducting $Bi_2Sr_2CaCu_2O_{8+\delta}$", IEEE Trans. THz Sci. Technol. **5**, 505 (2015).

[95] I. Kakeya *et al.*, "Effect of thermal inhomogeneity for terahertz radiation from intrinsic Josephson junction stacks of $Bi_2Sr_2CaCu_2O_{8+\delta}$", Appl. Phys. Lett. **100**, 242603 (2012).

[96] H. Asai and S. Kawabata, "Control of circularly polarized THz wave from intrinsic Josephson junctions by local heating", Appl. Phys. Lett. **110**, 132601 (2017).

[97] A. Elarabi *et al.*, "Polarization Enhancement of Terahertz Radiation Generated by Intrinsic Josephson Junctions in a Truncated Edge Square $Bi_2Sr_2CaCu_2O_{8+\delta}$ Mesa", Physics Procedia **81**, 133 (2016).

[98] A. Elarabi *et al.*, "Monolithic Superconducting Emitter of Tunable Circularly Polarized Terahertz Radiation", Phys. Rev. Appl. **8**, 064034 (2017).

[99] H. Asai and S. Kawabata, "Intense terahertz emission from intrinsic Josephson junctions by external heat control", Appl. Phys. Lett. **104**, 112601 (2014).

[100] Y. Koval *et al.*, "Tuning superconductivity by carrier injection", Appl. Phys. Lett. **96**, 082507 (2010).

Appended publications

Publication 1

Thermal and electromagnetic properties of $Bi_2Sr_2CaCu_2O_8$ intrinsic Josephson junction stacks studied via one-dimensional coupled sine-Gordon equations

F. Rudau,[1] M. Tsujimoto,[1,2] B. Gross,[1] T. E. Judd,[1] R. Wieland,[1] E. Goldobin,[1] N. Kinev,[3] J. Yuan,[4] Y. Huang,[4,5] M. Ji,[4,5] X. J. Zhou,[4,5] D. Y. An,[4,5] A. Ishii,[4] R. G. Mints,[6] P. H. Wu,[5] T. Hatano,[4] H. B. Wang,[4] V. P. Koshelets,[3] D. Koelle,[1] and R. Kleiner[1]

[1]*Physikalisches Institut and Center for Collective Quantum Phenomena in LISA$^+$, Universität Tübingen, D-72076 Tübingen, Germany*

[2]*Kyoto University, Kyoto, Japan*

[3]*Kotel'nikov Institute of Radio Engineering and Electronics, Moscow, Russia*

[4]*National Institute for Materials Science, Tsukuba 3050047, Japan*

[5]*Research Institute of Superconductor Electronics, Nanjing University, Nanjing 210093, China*

[6]*The Raymond and Beverly Sackler School of Physics and Astronomy, Tel Aviv University, Tel Aviv 69978, Israel*

(Received 27 November 2014; revised manuscript received 5 March 2015; published 16 March 2015)

We used one-dimensional coupled sine-Gordon equations combined with heat diffusion equations to numerically investigate the thermal and electromagnetic properties of a 300 μm long intrinsic Josephson junction stack consisting of $N = 700$ junctions. The junctions in the stack are combined with M segments where we assume that inside a segment all junctions behave identically. Most simulations are for $M = 20$. For not too high bath temperatures there is the appearance of a hot spot at high-bias currents. In terms of electromagnetic properties, robust standing-wave patterns appear in the current density and electric field distributions. These patterns come together with vortex/antivortex lines across the stack that correspond to π-kink states, discussed before in the literature for a homogeneous temperature distribution in the stack. We also discuss scaling of the thermal and electromagnetic properties with M, on the basis of simulations with M between 10 and 350.

DOI: 10.1103/PhysRevB.91.104513 PACS number(s): 74.50.+r, 74.72.−h, 85.25.Cp

I. INTRODUCTION

In 2007 it was shown [1] that stacks of intrinsic Josephson junctions (IJJs) [2] in the high-temperature superconductor $Bi_2Sr_2CaCu_2O_8$ (BSCCO) are sources of coherent radiation at THz frequencies, with the possibility to tune the emitted frequency f_e by an applied dc voltage V, following the relation $f_e = V/\Phi_0$. Here Φ_0 is the flux quantum and $\Phi_0^{-1} = 483.6$ GHz/mV. In Ref. [1] stacks of about 1 μm in thickness (corresponding to 666 IJJs), a length L_s of about 300 μm, and a width W of some 10 μm have been realized as mesa structures on top of BSCCO single crystals, contacted by Au layers. These mesas emitted radiation at frequencies between 0.5 and 0.8 THz, with an integrated output power on the order of 1 μW. The emission frequency was found to scale reciprocally with W, indicating that cavity modes, formed along the width of the stack, are responsible for synchronization.

THz radiation emitted from such IJJ stacks became a hot topic in recent years, both in terms of experiment [3–28] and theory [29–68]. For recent reviews, see Refs. [69–71]. IJJ stacks, containing typically 500–2000 junctions, have been realized as mesa structures but also as bare IJJ stacks contacted by Au layers [22,28,69,72] and as all-superconducting Z-shaped structures [14]. Emission frequencies are in the range 0.4–1 THz. For the best stacks, emission powers in the range of tens of μW have been achieved [22,23,72], and arrays of stacks showed emission with a power up to 0.61 mW [24].

A crucial point in the physics of the huge IJJ stacks is overheating [3,5,7–9,18,23,26,49,54,56,62,66,67]. For sufficiently low bias currents, the temperature rises only slightly to values above the bath temperature T_{bath} and the voltage across the stack V increases with increasing bias current I. With increasing I and input power the current-voltage characteristics (IVCs) start to back-bend and, at some bias current in the back-bending region, a hot spot forms suddenly in the stack [3,7,9,18,23,26,27], creating a region which is heated to temperatures above the critical temperature T_c. The reason is the strong increase of the BSCCO c-axis resistivity ρ_c with decreasing temperature together with the poor BSCCO thermal conductivity [49,62,73]. Similar effects also occur in other systems [74,75]. In the IJJ stacks one can thus distinguish a low-bias regime where the temperature in the mesa varies only weakly and a high-bias regime where the hot spot has formed, leaving the "cold" part of the mesa for THz generation via the Josephson effect. The formation of the hot spot also affects the THz emission properties of the stack. For example, it has been found that the linewidth of radiation is much more narrow in the high-bias regime than at low bias [15]. This can be reproduced by simple model calculations based on arrays of pointlike junctions [73]. On the other hand several other properties such as the emission frequency seem to be basically independent of the hot spot position. This has lead to some debate as to whether the hot spot is helpful or just coexists with the electromagnetic properties [26,27,72].

In terms of theory many calculations of electrodynamics have been based on a homogeneous temperature distribution within a stack, while calculations of the thermal properties were based on solving the heat diffusion equations in the absence of Josephson currents [49,54,62]. Some attempts have been made to combine both electrodynamics and thermodynamics, either by using arrays of pointlike IJJs [67,73] or by incorporating temperature-induced effects into an effective model describing the whole stack as a single "giant" junction [56,65,66]. As we will see the latter approach has inconsistencies.

In this paper we report on simulations where we solve the one-dimensional coupled sine-Gordon equations in

combination with the heat diffusion equations. In our approach we group the junctions in the stack to segments. We still assume that all junctions in a segment behave like a giant junction. We find many thermodynamic and electromagnetic properties that have been seen in experiment and also in the previous theoretical calculations, but also there are new features. Despite the good agreement with several experimental observations we cannot emphasize strongly enough that our approach is still far from the 3D case where all junctions in the stack are addressed individually and where in-plane variations of the thermal and electromagnetic properties are taken into account in 2D.

The reminder of the paper is organized as follows. In Sec. II and in the Appendix we introduce the geometry considered, together with the basic equations, the simplifications made, and the numerical procedures used. In Sec. III we present our results, starting with integral properties such as IVCs, then turning to local properties and finally commenting on scaling issues and some special properties such as the role of the hot spot position and the observability of low-temperature scanning laser microscopy (LTSLM) signals. We conclude and summarize in Sec. IV.

II. MODEL

A. Geometry and basic equations

We consider an IJJ stack (mesa) consisting of N IJJs; cf. Fig. 1(a). The thickness of the superconducting layers (CuO_2 planes) is [2] $d_s = 0.3$ nm and the thickness of the insulating layers between the CuO_2 planes is $d_i = 1.2$ nm. The stack has a length L_s along x and a width W along y. The mesa thickness is $D_m = Ns$, where $s = d_s + d_i$. All electrical and thermal properties shall be homogeneous along y. The mesa is covered by a gold layer of thickness D_{Au} and is patterned on a base crystal of length $L_b > L_s$ and thickness D_b. The base crystal is mounted by a glue layer of thickness D_g to a sample holder which is kept at a bath temperature T_{bath}. A bias current I is injected via a bond wire into the Au layer and leaves the mesa into the base crystal. Note that the electrical and thermal parameters (resistivities, critical current densities, thermal conductivities, etc.) introduced below depend on temperature, and thus, for an inhomogeneous temperature distribution, on x. Their spatial variation, as well as $T(x)$, can be found by self-consistently solving the thermal equations (requiring Joule heat dissipation as an input from the electric circuit) and the electrical equations [requiring $T(x)$, as determined from the thermal circuit, as an input].

For the thermal description [cf. Fig. 1(b)] we assume that the mesa plus the contacting Au layer and the bond wire have a temperature $T_m(x)$ which is constant along z but can vary along x. The effective thickness of this layer is $D_{m,\mathrm{eff}}$. The BSCCO base crystal is split into K segments. The segment interfacing the mesa also has the thickness $D_{m,\mathrm{eff}}$; the other layers have a (much larger) thickness $(D_b - D_{m,\mathrm{eff}})/(K-1)$. The temperature in the center (along z) of the kth segment of the base crystal is $T_{b,k}(x)$, and the temperature in the center of the glue layer is $T_g(x)$. The whole ensemble is coupled in the z direction to the bath which is defined to have a constant temperature T_{bath}.

Generally speaking, we solve the heat flow equation

$$c\dot{T} = \nabla(\kappa \nabla T) + q \tag{1}$$

with the specific heat c, the (anisotropic) thermal conductivity κ, and the power density for heat generation q. The dot denotes the derivative with respect to time. Equation (1) needs to be specified for the layered geometry of Fig. 1(b). Details are given in the Appendix. In brief, we solve in the kth layer [k runs from 0 to $K+1$ and includes the mesa ($k=0$) and the glue layer ($k = K+1$)]:

$$c_k \dot{T}_k = \frac{d}{dx}\left(\kappa_{\parallel,k}\frac{d}{dx}T_k\right) + \frac{2}{D_k}(j_{\mathrm{in},k} - j_{\mathrm{out},k}) + q_k, \tag{2}$$

where $j_{\mathrm{in},k}$ and $j_{\mathrm{out},k}$, respectively, denote the heat current densities into and out of the layer k. $\kappa_{\parallel,k}$ is the in-plane thermal conductivity of layer k, T_k is its temperature, and D_k is its thickness; c_k is the heat capacity of layer k. For layer 0 (mesa plus gold plus bond wire) q_0 denotes the Joule power density q_m produced by the in-plane and out-of-plane currents in the mesa, plus the power density q_B produced by the bond wire. The latter contribution has turned out to be very useful in the simulations since, for high enough q_B, the hot spot forming in the mesa is located near the wire position. In the layers representing the base crystal and the glue there is no heat generation; i.e., $q_k = 0$ here. These layers have a length L_b which we have taken as $2L_s$. The mesa is centered above the base crystal.

The electric circuit is sketched in Fig. 1(c). We have grouped the N IJJs in the stack to M segments, each containing $G = N/M$ IJJs, assumed to have identical properties.

The mesa is biased by an external current density $j_{\mathrm{ext}}(x)$ which enters the mesa in the z direction with a density proportional to the local BSCCO conductance $\sigma_c(x) = \rho_c^{-1}(x)$; i.e., we assumed that the Au layer has a low enough resistance to freely distribute the current injected by the bond wire along x before it enters the IJJ stack. The interface of the stack to the base crystal is treated as a ground.

Figure 1(d) shows the lumped circuit approximation for a piece of the *single* IJJ n, located between x and $x + dx$. For the current flow along z, we consider a Josephson current with critical current $I_{c,n}$, a resistive component with $R_{c,n}$, and a capacitive component C_n. Nyquist noise is considered via a random current source $I^N_{z,n}$ with spectral power density $4k_BT_m/R_{c,n}$. The in-plane current flow in the nth BSCCO layer is described by a resistive component $R_{ab,n}$ and an inductive component $L_{ab,n}$ which is the kinetic inductance associated with in-plane supercurrents. We also consider an in-plane noise current $I^N_{x,n}$ with a spectral power distribution $4k_BT_m/R_{ab,n}$.

As described in the Appendix this leads to a sine-Gordon-like equation for the mth segment of the IJJ stack:

$$\begin{aligned} Gsd_s\left(\frac{\dot{\gamma}'_m}{\rho_{ab}}\right)' + d_s\left(j^N_{x,m+1} - j^N_{x,m}\right)' + G\lambda_k^2(n_s\gamma'_m)' \\ = 2j_{z,m} - j_{z,m+1} - j_{z,m-1}. \end{aligned} \tag{3}$$

The index m runs from 1 to M and enumerates the M segments. The characteristic length $\lambda_k = [\Phi_0 d_s/(2\pi\mu_0 j_{c0}\lambda_{ab0}^2)]^{1/2}$, with the 4.2 K value of the in-plane London penetration depth λ_{ab0} and the magnetic permeability μ_0. The in-plane resistivity is denoted ρ_{ab} and $n_s = \lambda_{ab0}^2/\lambda_{ab}^2$ denotes the Cooper pair

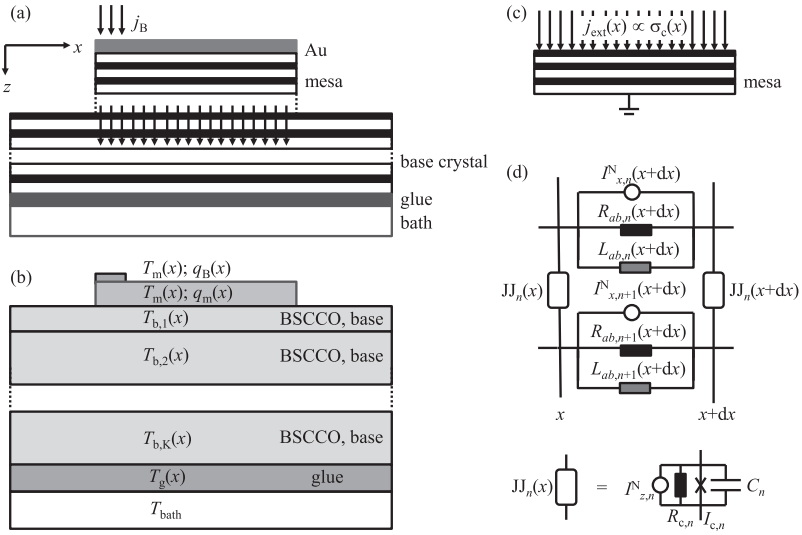

FIG. 1. General geometry and simplifications used for modeling. (a) Sketch of mesa geometry. (b) Sketch of geometry for thermal description. The Joule power density q_m is produced in the mesa and q_B is the Joule power density produced by the bias lead. The temperatures of the various layers are indicated. (c) Simplified geometry considered for the electrical description together with (d) the lumped circuit approximation. In (d) one element describing the mesa between positions x and $x + dx$ and the IJJ n embedded between the superconducting layers n and $n + 1$ is shown. The in-plane currents in the nth layer are approximated by an inductor $L_{ab,n}$ (supercurrent), a resistor $R_{ab,n}$ (quasiparticle current), and a noise source $I^N_{x,n}$. The interlayer current is described by the Josephson current with critical current $I_{c,n}$, a resistor $R_{c,n}$, a capacitor C_n, and a noise source $I^N_{z,n}$.

density. Time is normalized to $\Phi_0/2\pi j_{c0}\rho_{c0}s$, resistivities to ρ_{c0} (4.2 K value of c-axis resistivity), and current densities to j_{c0} (4.2 K value of Josephson current critical density). The primes denote the derivative with respect to x, and γ_m is the Josephson phase difference of each IJJ in segment m. We have further assumed that resistivities and critical current densities are the same for all layers, i.e., do not depend on m. For the in-plane noise current the normalized form of the spectral density is $4\Gamma_0(T_m/T_0)d_s s/(dx L_s \rho_{ab})$, with $T_0 = 4.2$ K, $\Gamma_0 = 2\pi k_B T_0/I_{c0}\Phi_0$, and $I_{c0} = j_{c0} W L_s$.

For the current densities $j_{z,m}$ one finds

$$j_{z,m} = \beta_{c0}\ddot{\gamma}_m + \frac{\dot{\gamma}_m}{\rho_{c,m}} + j_c \sin(\gamma_m) + j^N_{z,m}, \tag{4}$$

with $\beta_{c0} = 2\pi j_{c0}\rho^2_{c0}\epsilon\epsilon_0 s/\Phi_0$; ϵ_0 is the vacuum permittivity and ϵ is the BSCCO dielectric constant. The normalized spectral density of $j^N_{z,m}$ is $4\Gamma_0(T_m/T_0)L_s/(dx\rho_c)$.

The in-plane supercurrent densities in electrode m (the CuO_2 layer interfacing segments m and $m + 1$) are expressed as

$$j^s_{x,m} = \frac{\lambda^2_k}{d_s} n_s \phi'_m, \tag{5}$$

where ϕ_m is the phase of the superconducting wave function in electrode m. The resistive currents in electrode m are given by

$$j^r_{x,m} = \frac{s}{\rho_{ab}}\dot{\phi}'_m, \tag{6}$$

and the ϕ_m and γ_m are related via

$$\gamma_m = \frac{\phi'_{m+1} - \phi'_m}{G}, \tag{7}$$

allowing us to evaluate the in-plane currents once all γ_m and in addition ϕ'_m of one of the outermost electrodes are known.

The expression for the current density j_{ext} is

$$j_{ext} = \frac{\langle j_{ext}\rangle}{\langle\sigma_c\rangle\,\rho_c}, \tag{8}$$

where the brackets denote spatial averaging.

Note that Eqs. (3) and (4) together with Eq. (2) have the same form as the equations for a stack of M single junctions rather than M segments. On the thermal side the difference is that the M segments produce the same Joule heat as the full N junction stack (a stack of, say, 20 junctions would not heat up significantly). On the electromagnetic side the first difference is the rescaling of the length λ_k which is multiplied by $G^{0.5}$, as well as a rescaling of the in-plane resistance ρ_{ab} which is divided by G [see first and third terms on the left-hand side of Eq. (2)]. As we will see in Sec. III there are robust in-phase standing waves along the stack. The mode

velocity of these waves increases M and, in order to keep physics independent of the segmentation, we kept the product $\beta_{c0}G$ constant. This modification is discussed and justified in detail in the Appendix. With these scalings the electrothermal properties calculated are very similar for all values of G and follow simple scaling rules, as shown in Sec. III.

B. Choice of parameters

We perform our calculations for an $N = 700$ IJJ mesa with lateral dimension $L_s = 300\ \mu$m. The length of the base crystal is $L_b = 600\ \mu$m and its thickness is $D_b = 30\ \mu$m. The mesa is centered above the base crystal. The thickness of the glue layer is $D_g = 20\ \mu$m. The BSCCO critical temperature is $T_c = 85$ K.

For $\rho_c(T)$ we take a 4.2 K value of $10^3\ \Omega$cm and the temperature dependence used in Ref. [62]. Above the transition temperature T_c it is based on measured data. Below T_c, ρ_c is extrapolated to give good agreement to measured IVCs. Figure 2(a) shows this functional form. We have based the BSCCO in-plane resistivity ρ_{ab} on microwave surface impedance measurements [76]. In general, the real part of the in-plane conductivity σ_1 below T_c runs over a low-temperature maximum and in addition is likely to be strongly frequency dependent [77]. Being mostly interested in temperatures well above 20 K we linearized this quantity for temperatures between 20 K and T_c and took σ_1 as a constant below 20 K. For temperatures above T_c we assumed that ρ_{ab} increases linearly with temperature. This yields $\rho_{ab}(T)/\rho_{ab}(T_c) = T/T_c$ for temperatures above T_c, $\rho_{ab}(T)/\rho_{ab}(T_c) = [1 + a(T_c - T)]^{-1}$ for $20\ \text{K} < T < T_c$, and $\rho_{ab}(T)/\rho_{ab}(T_c) = [1 + a(T_c - 20\ \text{K})]^{-1}$ for $T < 20$ K. For a we used a value of 0.08 K^{-1}. The resulting curve is shown in Fig. 2(a). We further used $\rho_{ab}(T_c) = 20\ \mu\Omega$ cm. This value sounds somewhat low. However, we assume that only layers of thickness $d_s = 0.3$ nm are conducting while the interlayers of thickness $d_i = 1.2$ nm are insulating. This results in an averaged in-plane resistivity of 100 $\mu\Omega$ cm, which is realistic.

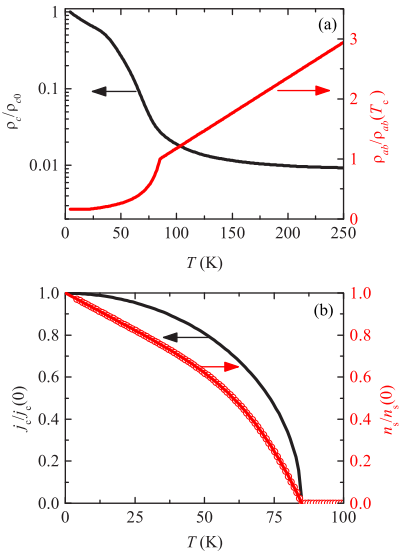

FIG. 2. (Color online) Temperature dependencies of various parameters used for calculations. (a) Out-of-plane (left scale) and in-plane (right scale) resistivities. (b) Josephson critical current density (left scale) and superfluid density (right scale).

For the Josephson critical current density at $T = 4.2$ K we use $j_{c0} = 200$ A/cm^2. For the temperature dependence of j_c, for $T < T_c = 85$ K we use [cf. Fig. 2(b)]

$$j_c(T) = j_c(0)[1 - (T/T_c)^2]^{1/2}. \tag{9}$$

For $T > T_c$, $I_c(T) = 0$. Equation (9) roughly approximates $I_c(T)$ data of small-sized BSCCO stacks [2].

The superfluid density $n_s(T) \propto \lambda_{ab}^2(T)/\lambda_{ab}^2(0)$ is taken from Ref. [78]. The temperature dependence of this curve can be fitted very well by

$$n_s(T) = n_s(0)[1 - (T/T_c)^6][1 - 0.6(T/T_c)]. \tag{10}$$

Figure 2(b) shows by points data from Ref. [78] and by a line the fit function, Eq. (10). For $\lambda_{ab}(0)$ we have used a value of 260 nm.

With the above choice of parameters, assuming a mesa width of $W = 50\ \mu$m, we obtain the following 4.2 K values for the electrical part of the model. Critical current $I_{c0} = 30$ mA, c-axis resistance per junction $R_{c0} = 1\ \Omega$, $I_{c0}R_{c0} = 30$ mV, characteristic frequency $f_{c0} = 14.5$ THz, and noise parameter $\Gamma_0 \approx 5 \times 10^{-6}$. The characteristic power density $p_{c0} = j_{c0}^2\rho_{c0}$ is 4×10^7 W/cm^3, yielding, for a stack volume of 1.5×10^{-8} cm^3, a characteristic power P_{c0} of 0.6 W. For λ_c one obtains 296 μm and $\lambda_k = 0.76\ \mu$m.

Further, assuming a (temperature independent) dielectric constant $\epsilon = 12$ (diffraction index 3.5) we obtain for the Josephson plasma frequency $f_{pl0} \approx 41$ GHz. The McCumber parameter (for $G = 1$) is $\beta_{c0} \approx 1.25 \times 10^5$. The 4.2 K value of the in-phase mode velocity c_1 [see Eq. (A9)] is 8.8×10^7 m/s. c_1 decreases $\propto n_s^{1/2}$ with temperature. In our simulations we keep the product $\beta_{c0}G$ constant in order to (approximately) fix the 4.2 K value of c_1. Still, c_1 slightly increases with increasing G. To compensate for this we have used $\beta_{c0}G = 1.4 \times 10^5$ for calculations with G between 14 and 70; cf. Appendix, Fig. 17.

For the BSCCO thermal conductivities we use 4.2 K values $\kappa_{ab} = 2.76$ W/mK and $\kappa_c = 0.32$ W/mK. For Au we use $\kappa_{Au} = 100$ W/mK and for the glue $\kappa_g = 0.5$ W/mK; the two latter values were taken as temperature independent for simplicity. The heat capacities, determining the time dependence of establishing temperature distributions in the various layers, we simply kept constant, keeping in mind that we are, for the moment, mainly interested in the Josephson dynamics which is much faster than the dynamics of the thermal part. That is, although solving dynamic equations, we are interested in situations where the temperature distributions are basically stationary. We thus used a heat capacity per volume of 2 J/m^3 K for all layers.

For the heat produced by the bond wire we used $\rho_B = 0.02\rho_{c0}$ and a diameter (along x) $L_B = 30\ \mu$m.

C. Numerical details and quantities calculated

Equations (2) and (3) were discretized along x using equally spaced grid points. A fifth-order Runge-Kutta scheme was used to evolve these equations in time. We reduced the number of grid points X along the stack as much as possible to speed up the calculations; $X = 50$ was used for the simulations shown and some of the results were confirmed using $X = 100$. For the base crystal and the glue layer $2X$ grid points were used. The base crystal was split into $K = 4$ segments. For a given set of input parameters, in a first initializing step we solved, for typically 10^9 time units, Eq. (2) for out-of-plane quasiparticle currents only to achieve stationary distributions for the temperature and j_{ext}. Then, in a second initializing step, Eq. (2) was solved simultaneously with Eq. (3) over typically $10^4/v$ time units. Here, v is the temperature-dependent normalized averaged dc voltage across a junction, $v = V/(NV_{c0})$ (we divided the integration time by v to keep the number of Josephson oscillations constant). After this second initializing step which is necessary to bring the electric circuit into a stationary state the $M \times X$ Josephson phases $\gamma_m(x)$ and also other quantities such as $\dot{\gamma}_m(x)$, in-plane and out-of-plane current densities, etc., were tracked as a function of time to produce time averages of these quantities or to make Fourier transforms. To obtain (hysteretic or even multibranched) current-voltage characteristics (IVCs) one often starts at, say, zero bias current and then varies this current using the values for the various variables from the previous current for initialization. We did not use this concept but instead initialized each current, as described above, to obtain reproducible states in different runs.

Apart from calculating IVCs and distributions of the thermal and electrical quantities in the mesa we were also interested in THz emission. In experiment one finds that a significant power is emitted in the z direction [69,79], which must be due to currents oscillating in the CuO_2 planes. In our simulations we do not calculate electric and magnetic fields outside the IJJ stack and thus do not have access to the Poynting vector to calculate emission properties [50]. Instead, we start from the power density $q_{x,av}$ produced by the resistive part of the in-plane currents $j^r_{x,m}$, averaged over the stack volume. It is given by

$$q_{x,\mathrm{av}} = \frac{d_s}{Ns}\frac{1}{L_s}\int_0^{L_s} dx \left(\rho_{ab}\sum_{m=1}^{M+1} j^{r2}_{x,m}\right). \qquad (11)$$

Because of our boundary conditions $j^{r2}_{x,m}$ and thus also $q_{x,av}$ have no dc component. Next, we take time traces of $q_{x,av}$, Fourier-transform them, and look at the peak in $q_{x,av}(f)$ which occurs at twice the Josephson frequency. We denote the peak value as q_{xp}. Our normalization power densities are in units of $j_{c0}^2\rho_{c0}$ which, integrated over the stack volume, yields a characteristic power of 0.6 W. Thus, q_{xp} can also be viewed as the in-plane power in the stack in units of 0.6 W. Of course, q_{xp} is the *dissipated* rather than the *emitted* power. However, it seems natural that both quantities track each other.

III. RESULTS

A. Current voltage characteristics and in-plane power

We first discuss dc characteristics of an $M = 20$ segment stack, with $G = N/M = 35$ and $\beta_{c0} = 4000$ ($G\beta_{c0} = 1.4 \times 10^5$). Data are for bath temperatures between 10 K and 70 K. The bias lead had a diameter along x of $L_B = 30\ \mu$m and its left edge was positioned 30 μm from the left edge of the mesa. Figure 3(a) shows by solid lines IVCs, as they have been calculated in the first initialization step. Here, current flow is assumed to be purely in the z direction and only resistive currents (with resistance ρ_c) are taken into account in the heat diffusion equations. The IVCs show the typical back-bending which is due to self-heating. By points we indicate calculated IVCs using the full model equations (heat diffusion plus coupled sine-Gordon equations). For each bias current the c-axis electric fields in each segment ($\propto \dot{\gamma}_m$) have been initialized so that all IJJs are in their resistive state. For not too low bias currents the points are basically

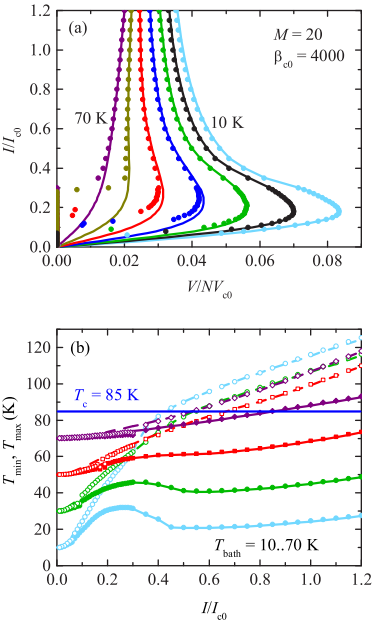

FIG. 3. (Color online) Simulation results for an $M = 20$ segment stack, with $G = N/M = 35$ and $\beta_{c0} = 4000$ for bath temperatures between 10 K and 70 K. (a) IVCs after first initialization step, with only resistive c-axis currents taken into account (lines). Full calculation including Josephson currents, displacement currents, and in-plane currents (dots). (b) Maximum and minimum temperatures in the stack vs normalized bias current. Lines (solid for T_{min}, dashed for T_{max}): after first initialization step; symbols (solid for T_{min}, open for T_{max}): full calculation.

on top of the lines showing that dissipation due to c-axis quasiparticle currents is the dominating effect for self-heating. At low-bias currents there is a switch-back to either some "inner" branch of the IVC (some junctions resistive, some others in zero-voltage state) or to the zero-voltage branch. We note that, for a given IVC, inner branches can be traced out in principle, although we have not done this in the IVCs shown. Figure 3(b) displays the maximum ($T_{\max}$) and minimum ($T_{\min}$) temperatures in the stack as a function of bias current. Data are for bath temperatures between 10 K and 70 K, in steps of 20 K. By lines we show $T_{\max}$ and $T_{\min}$ as calculated in the first initialization step. At low temperatures and currents both $T_{\max}$ and $T_{\min}$ increase with increasing current. With further current increase $T_{\min}$ runs over a maximum, while $T_{\max}$ exhibits a strong increase. This is a typical signature of hot spot formation starting at the maxima of $T_{\min}$. With increasing bath temperature these features are washed out. For $T_{\rm bath} > 50$ K they are not visible anymore indicating that here the concept of a hot spot becomes useless. Further note that for $T_{\rm bath} = 70$ K, the $T_{\min}$ curve intersects the $T_{\max}$ curve for $T_{\rm bath} = 50$ K, while the $T_{\max}$ curve for $T_{\rm bath} = 70$ K lies almost on top of the $T_{\max}$ curve for $T_{\rm bath} = 30$ K. This reflects the fact that temperature differences in the stack are much stronger in the presence of a hot spot than for the more homogeneous case of $T_{\rm bath} = 70$ K. The results for the full calculation are shown by symbols. As for the IVC the symbols are basically on top of the lines for not too low bias currents. For low bias, when the IVC of the stack has switched to an inner branch or to the zero-voltage state, $T_{\max}$ exhibits a jump towards lower temperatures and coincides with $T_{\min}$ at low bias.

In Fig. 4 we show for two selected bath temperatures (20 K and 50 K) IVCs, as calculated from the full model

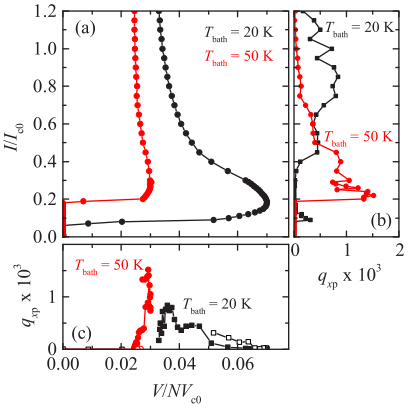

FIG. 4. (Color online) Full calculation results for two selected bath temperatures: (a) IVCs and (b), (c) in-plane power dissipation q_{xp} vs bias current (b) and vs voltage across stack (c). In (b) and (c) squares are for $T_{\rm bath} = 20$ K and circles for $T_{\rm bath} = 50$ K. In (c) the solid symbols are for the high-bias region and open symbols for the low-bias region.

together with the in-plane power q_{xp}. q_{xp} was calculated from Fourier transforms of time traces taken over $512/\nu$ time units (about 40 Josephson oscillations), with an elementary step of $0.5/\nu$ time units. The Fourier spectra were averaged 10 times and integrated from $0.9 f_e$ to $1.1 f_e$ where f_e is the peak frequency of $q_{x,\rm av}(f)$. With this "short" time Fourier transform the frequency resolution is low and the linewidth of $q_{x,\rm av}(f)$ is in fact much larger than its actual linewidth obtained for long-term integration (see below). This resembles the experimental situation where the Fourier spectrometers used for measuring THz emission have a linewidth of several GHz, whereas the real linewidth of the Josephson emission is in the sub-GHz range.

For $T_{\rm bath} = 20$ K q_{xp} is large mainly at high bias and is peaked at currents near $0.8 I_{c0}$; cf. Fig. 4(b). Note that q_{xp} is lower for the values of the normalized bias current of 1.05 and 0.95 than for their adjacent values. This is not due to thermal noise but results from two competing modes in the stack (standing-wave patterns) with different wavelengths. As a function of voltage the value of q_{xp} (at $T_{\rm bath} = 20$ K) is large near a normalized voltage of 0.04 per junction, corresponding to a Josephson frequency of about 580 GHz. At the maximum, $q_{xp} \approx 8 \times 10^{-4}$, corresponding to 0.48 mW.

For $T_{\rm bath} = 50$ K, q_{xp} rises with decreasing current and has a peak near $0.2 I_{c0}$ and for a normalized voltage near 0.03. The peak value is about 0.0015, i.e., by about a factor of 2 larger than the maximum value observed in the 20 K curve. The in-plane power q_{xp} shown in Figs. 4(b) and 4(c) exhibits some structure (as it may be similar to the one observed experimentally for the THz emission power [9]) but does not give a conclusive picture on how either the power or the structures evolve with bath temperature, dc voltage, and bias current. In fact, in experiment one often observes that there is emission both at low bias and at high bias, with the larger power observed in the low-bias regime. To obtain a more systematic picture for q_{xp}, we calculated, for bath temperatures between 4 K and 70 K, in steps of 2 K, a large number of IVCs together with q_{xp} for each point and plot them as the color scale in the IVC family; cf. Fig. 5. In the graph we have also indicated by black symbols the currents above (below) which the maximum temperature in the stack was above (below) $T_c = 85$ K (T_c line).

Figure 5 shows that the maximum of q_{xp} is in the low-bias regime for currents below $0.5 I_{c0}$ and voltages per junction below $0.05 V_{c0}$. The in-plane power in the high-bias regime is lower and confined in a voltage region between roughly $0.02 V_{c0}$ and $0.05 V_{c0}$ per junction. In the low-voltage region at high bias the temperature in the stack is above T_c at (almost) each value of x. There are almost no supercurrents left in the stack, and the remaining ac Josephson currents do not excite resonant modes. Thus, obviously, q_{xp} is low. However, at normalized voltages above 0.05 the value of q_{xp} is also low, although the temperature in the stack is well below T_c. This regime will be addressed in more detail in the next subsection.

For selected bias points we also performed long-term (over 5200 Josephson oscillations) Fourier transforms of $q_{x,\rm av}$. It turned out that the linewidth Δf of $q_{x,\rm av}(f)$ was close to the resolution limit (i.e., the peak in the Fourier transform consisted of only 3 points) both in the high- and the low-bias regimes. For example, at $I/I_{c0} = 0.6$ and $T_{\rm bath} = 20$ K, $\Delta f <$ 75 MHz, and at $I/I_{c0} = 0.3$ and $T_{\rm bath} = 50$ K, $\Delta f < 50$ MHz.

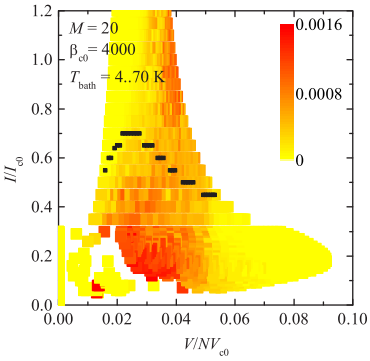

FIG. 5. (Color online) In-plane power q_{xp} (color scale) as a function of normalized bias current and normalized voltage across the stack. The bath temperature was varied between 4 K and 70 K in steps of 2 K. Black symbols indicate the currents above (below) which the maximum temperature in the stack was above (below) $T_c = 85$ K (T_c line).

For such small linewidths residual drifts in the temperature distribution in the stack are likely to affect the results and thus we did not go for even longer integration times. We thus cannot make a conclusive statement about Δf and its scaling with $T_{\rm bath}$ or M. However, it seems that the strong broadening of the emission spectra at low bias, which is observed experimentally [15], is not contained in the present model. In the simplified model of Ref. [73] Δf became large in the low-bias regime once a spread in the junction critical currents and resistivities was introduced. This is not implemented yet in the present model.

B. Local properties

We now look, for selected bias points, at local properties. Figure 6 shows time averages at $T_{\rm bath} = 20$ K and $I = 0.6I_{c0}$. The temperature distribution $T_m(x)$ shows a maximum temperature above T_c (a hot spot) located near $x = 70$ μm. This is slightly to the right of the input lead which extends from $x = 30$ μm to $x = 60$ μm. Note that a large fraction of the right-hand side of the stack and a small fraction on the left-hand side are at temperatures below T_c. The dissipated power density $\langle q_z(x)\rangle$ generated by out-of-plane currents, averaged over time and all segments at each position x, is also shown in Fig. 6. Here we added the heat production of the bias lead which appears as an additional rectangle on top of the Gaussian-shaped power density generated by the out-of-plane currents. While $\langle q_z(x)\rangle$ is smooth, except for the contribution created by the lead, its counterpart for the power density $\langle q_x(x)\rangle$ generated by in-plane currents exhibits pronounced oscillations, with a wavelength of about 75 μm. The oscillations appear for $x > 120$ μm, i.e., in the superconducting right-hand part of the stack.

To obtain more insight into the dynamics of the stack we monitored the time dependence of the in-plane and

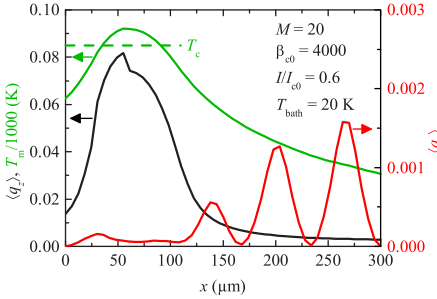

FIG. 6. (Color online) Time-averaged distribution of dissipated power density $q_z(x)$ generated by c-axis currents (black line, left scale), the temperature $T_m(x)$ in the mesa (green line, left scale), and time average of power density of dissipated power $q_x(x)$ generated by in-plane currents (red line, right scale). At given x position q_z and q_x have been averaged over all segments. The bath temperature is 20 K and the bias current is $0.6I_{c0}$. The noise parameter is $\Gamma_0 = 5 \times 10^{-5}$.

out-of-plane currents. In the presence of fluctuations these quantities look very noisy. We thus, for demonstration, initialized our simulation with a "noisy" set of variables and then turned off the fluctuations; i.e., we set $\Gamma_0 = 0$. Figure 7 shows two snapshots of the Josephson currents $j_c(T_m)\sin\gamma_m$. Curves for adjacent segments are vertically offset. Note that in regions with $T_m > T_c$ the supercurrents are zero. Looking at the curves at time t_1 one notes that at the left superconducting part of the stack the curves of segments 11–20 bend downwards while for segments 1–10 some of the curves are bent upwards and some downwards. On the right-hand part of the stack in segments 5–20 there are clear oscillations along x, with nodes

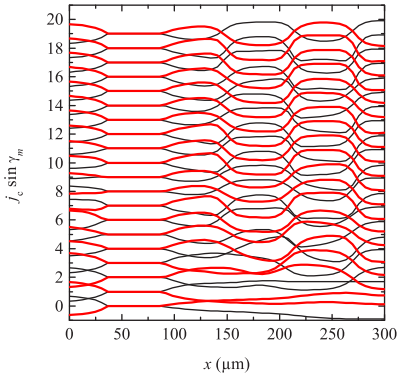

FIG. 7. (Color online) Two snapshots of Josephson currents $j_c(T_m)\sin\gamma_m$ at normalized times t_1 (black curves) and t_2 (red curves), differing by roughly half of an oscillation period. Snapshots are for $M = 20$, $I = 0.6I_{c0}$, and $T_{\rm bath} = 20$ K. Curves for adjacent segments are vertically offset.

near $x = 148$, 209, and 274 μm. In fact, the snapshot has been made at a time when the supercurrent to the left of the node at $x = 209$ μm was near its maximum. The curves at t_1 are for a time where the supercurrents at the same position were roughly at their minima. The three nodes of $j_c(T_m)\sin\gamma_m$ in the superconducting part of the mesa and the fact that, left (right) of a given zero, the supercurrents rise to their maximum (minimum), i.e., $\sin\gamma_m \to \pm 1$, indicate that lines of vortices and antivortices have formed. These are chains of π kinks [31,32,38,43,45–47,80] located at the three nodes. It has been conjectured before that such states appear in mesa structures subject to strong self-heating [18].

Figures 8(a) and 8(b) show snapshots of the in-plane supercurrent densities $j^s_{x,m}(x)$ at the same times t_1 and t_2, respectively. The curve for electrode 1 is indicated by a green line; the curve for electrode M is shown by a red line. In contrast to the Josephson current densities of Fig. 7 the $j^s_{x,m}(x)$ at given x do not reverse sign at t_1 compared to t_2; i.e., the $j^s_{x,m}(x)$ distribution is almost static, as expected for π-kink lines. In the inset of Fig. 8(b) the currents $j^s_{x,m}(x)$ are shown versus layer index m for $x = 150$ μm and times t_1 (solid symbols) and t_2 (open symbols). Besides the fact that open and solid symbols are located almost on top of each other one notes that $j^s_{x,m}(x)$ versus m oscillates between negative and positive values. For several values of m, $j^s_{x,m}(x)$ is near zero. In this case a vortex extends over the two segments adjacent to the center layer. In contrast to the supercurrents the quasiparticle currents $j^r_{x,m}(x)$ have basically the same polarity for all layer indices m at given x; cf. Fig. 8(c) for a snapshot at time t_1 and the inset of this figure for a plot of $j^r_{x,m}(x)$ versus m at $x = 270$ μm. The highest amplitudes of $j^r_{x,m}(x)$ are reached in the uppermost layers (with low values of m). For $m > 2$ this amplitude decreases with increasing m, i.e., towards the base crystal which we treat as a ground. Figure 8(d) shows a snapshot of $j^r_{x,m}(x)$ at time t_2. All curves $j^r_{x,m}(x)$ have reversed sign compared to Fig. 8(c). Note that the oscillations of $j^r_{x,m}(x)$ extend across the hot area; i.e., the in-plane resistive currents are coupled across the whole stack. The oscillation in the hot part of the stack is in fact also vaguely visible in $\langle q_x(x)\rangle \propto \langle j^{r2}_{x,m}(x)\rangle$; cf. Fig. 6.

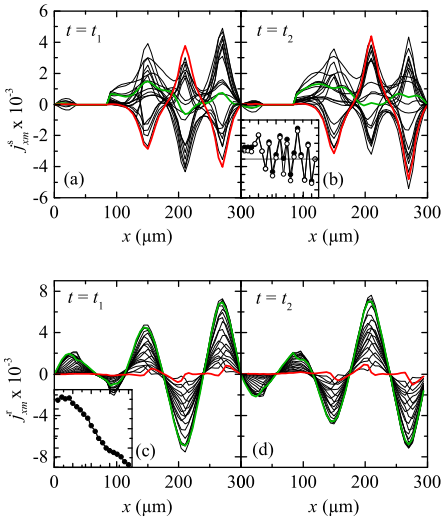

FIG. 8. (Color online) Snapshots of in-plane supercurrent densities $j^s_{x,m}(x)$ at (a) time t_1 and (b) time t_2. Snapshots of in-plane quasiparticle current densities $j^r_{x,m}(x)$ at (c) time t_1 and (d) time t_2. Inset in (b) shows values of $j^s_{x,m}(x)$ at $x = 150$ μm vs m at times t_1 (solid symbols) and t_1 (open symbols). Zero value of $j^r_{x,m}$ is indicated by a horizontal line. Inset in (c) shows $j^r_{x,m}(x)$ at $x = 270$ μm vs m at time t_1. In the graphs green (red) lines indicate the current densities in electrodes $m = 1$ ($m = M$). $I = 0.6I_{c0}$, $T_{bath} = 20$ K, and $M = 20$.

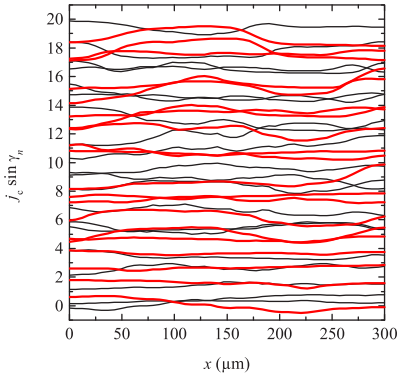

FIG. 9. (Color online) Two snapshots of Josephson currents $j_c(T_m)\sin\gamma_m$ at times t_1 (black curves) and t_2 (red curves), differing by roughly half of an oscillation period. Data are for $I = 0.3I_{c0}$, $T_{bath} = 20$ K, and $M = 20$. Curves for adjacent segments are vertically offset.

Figures 7 and 8 demonstrate that, at the bias current and temperature considered, the stack is in a resonant state involving π-kink states in its dynamics. $j^r_{x,m}(x)$ exhibits $k = 5$ half waves along the stack. The oscillation frequency, cf. Fig. 8(a), is $0.04 f_{c0} = 580$ GHz. This corresponds to a mode velocity $c_1 = 2L_s f/k = 7 \times 10^7$ m/s—roughly the value expected from Eq. (A9) if we use an average temperature of 50 K for the superconducting part of the stack.

We next investigate the bias point $I = 0.3I_{c0}$ at $T_{bath} = 20$ K. For this bias condition the normalized voltage per junction is $v = 0.06$ and the in-plane power q_{xp} is very small; cf. Fig. 4. Figure 9 shows snapshots for the Josephson currents at two different times. All curves are very smooth and do not show a sign of synchronization. At least for a homogeneous stack one would associate such a current distribution with a McCumber state. We thus see from Fig. 9 together with Fig. 5 that for too high dc voltages across the stack synchronization of the different segments has not been achieved. This basically happens, for the parameters used, for all voltages per junction (normalized frequencies) larger than about 0.05. We conclude that there is a maximum frequency for the resonant modes that

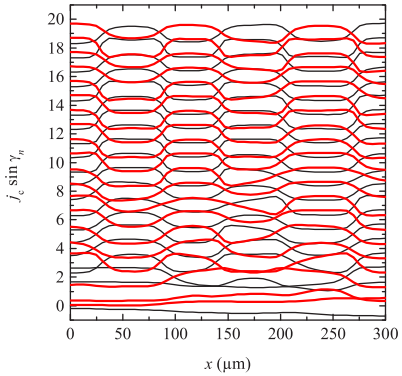

FIG. 10. (Color online) Two snapshots of Josephson currents $j_c(T_m)\sin\gamma_m$ at times t_1 and t_2, differing by roughly half of an oscillation period. Data are for $I = 0.3I_{c0}$, $T_{bath} = 50$ K, and $M = 20$. Curves for adjacent segments are vertically offset.

can be excited. This frequency in fact depends on the mode velocity. For example, for $G = 35$ and $\beta_{c0} = 4000$ standing waves appeared at least up to $v = 0.7$, as will be shown in Sec. III C.

Figure 10 shows two snapshots of Josephson currents $j_c(T_m)\sin\gamma_m$ at normalized times t_1 (black curves) and t_2 (red curves) for $I = 0.3I_{c0}$ and $T_{bath} = 50$ K. Figure 11 shows time averages of the power densities $q_z(x)$ and $q_x(x)$ plus the local temperature $T_l(x)$. No hot spot is present at this bias point. The formation of a standing wave is clearly visible in both graphs. In a plot of quasiparticle currents $j^r_{x,m}(x)$ versus x (not shown) one observes 5 half waves, i.e., essentially the same

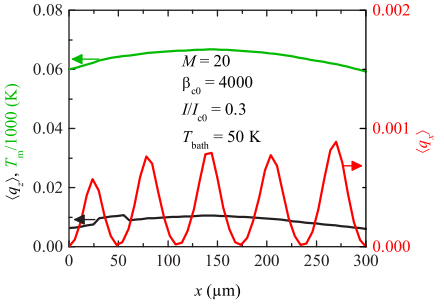

FIG. 11. (Color online) Time-averaged distribution of dissipated power density $q_z(x)$ generated by c-axis currents (black line, left scale), the temperature $T_m(x)$ in the mesa (green line, left scale), and the time average of power density $q_x(x)$ generated by in-plane currents (red line, right scale). At given x position $q_z(x)$ and $q_x(x)$ have been averaged over all M segments. $T_{bath} = 50$ K, $I = 0.3I_{c0}$, and $M = 20$. The noise parameter is $\Gamma_0 = 5 \times 10^{-5}$.

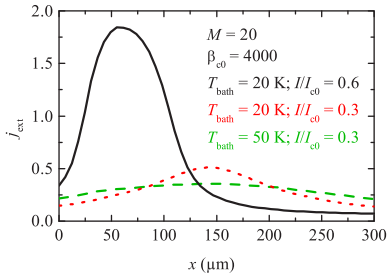

FIG. 12. (Color online) Bias current density $j_{ext}(x)$ for different values of T_{bath} and I/I_{c0}.

resonance as in Fig. 8. In fact, we have seen similar resonant patterns, with various wave indices k, for many bias currents and temperatures, whenever a substantial emission was found. The formation of standing waves associated with π-kink states thus seems to be a robust feature both in the high- and in the low-bias regimes.

We finally briefly look at the bias current density $j_{ext}(x)$. Figure 12 shows this quantity for the bias conditions discussed above, i.e., $T_{bath} = 20$ K; $I/I_{c0} = 0.6$, $T_{bath} = 20$ K; $I/I_{c0} = 0.3$ and $T_{bath} = 50$ K; $I/I_{c0} = 0.3$. For $T_{bath} = 20$ K and $I/I_{c0} = 0.6$, i.e., in the presence of a hot spot, most of the bias current flows through the hot region, leading to a very low current density in the "cold" parts of the stack. By contrast the current density profiles are much more smooth at the two other bias points and the current density is in fact higher than for the high-bias case. Thus, the bias condition in the cold region is comparable in all cases. For $T_{bath} = 20$ K and $I/I_{c0} = 0.6$ and $T_{bath} = 50$ K and $I/I_{c0} = 0.3$ also the dc voltage drop across the stack in the cold part is similar and one may not be very surprised that comparable wave patterns appear.

C. Scaling behavior

The results shown above were all for $M = 20$. We next investigate the scaling behavior with M. Figure 13 shows for M between 10 and 50 the in-plane dissipated power q_{xp} (color scale) at each point of an IV family taken at bath temperatures between 20 K and 70 K in steps of 2 K. One notes that plots (b) ($M = 20$; $G = 35$; data selected from Fig. 5), (c) ($M = 35$; $G = 20$), and (d) ($M = 50$; $G = 14$) look very similar in the sense that q_{xp} is large at about the same voltages and bias currents. For $M = 10$ one observes differences particularly in the high-bias regime where q_{xp} is suppressed at high voltages. Here it turned out that no standing-wave patterns as discussed in the previous section have formed. Instead, the current densities in the stack fluctuated strongly along x. The length scale of these fluctuations (we investigated this also with simulations using up to 200 grid points along x) was only a few λ_k. Similar solutions were in fact also found for the $M = 20$ case when the in-plane resistivity ρ_{ab0} was increased by a factor of 5 or more. Thus, for the parameters used in Fig. 13 there is a qualitative change between $M = 10$ and $M = 20$. Further, between $M = 10$ and $M = 50$ the maximum value

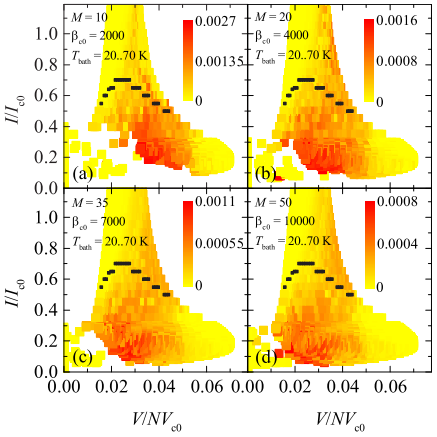

FIG. 13. (Color online) In-plane power q_{xp} (color scale) as a function of normalized bias current and normalized voltage across the stack for 4 values of M as a function of normalized bias current and normalized voltage across stack. T_{bath} was varied between 20 K and 70 K in steps of 2 K. The product $\beta_{c0}G = 1.4 \times 10^5$ is kept constant. Black symbols denote the T_c line.

of q_{xp} decreased by a factor of about 3.4. For M between 20 and 350 we also looked at q_{xp} for $I = 0.6I_{c0}$ at $T_{bath} = 20$ K and for $I = 0.3I_{c0}$ at $T_{bath} = 50$ K. Here, q_{xp} dropped from, respectively, 4.6×10^{-4} to 2.2×10^{-5} and from 7.5×10^{-4} to 2.5×10^{-5}, which is very roughly proportional to G^{-1}. For $M = 700$ ($G = 1$) one may thus expect maximum values of q_{xp} around 5×10^{-5}, corresponding to 30 μW. In all cases the in-plane power dissipation is small compared to the total dc power input, which amounts to, e.g., ∼15 mW at $I = 0.6I_{c0}$, $T_{bath} = 20$ K.

For comparison to the data of Fig. 13, in Fig. 14 we show q_{xp} as a function of bias current and voltage for $M = 10$ and

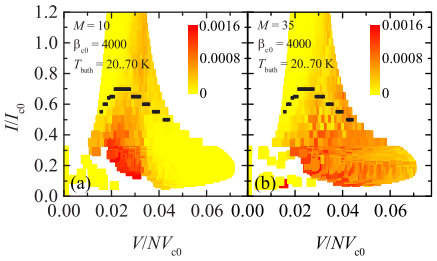

FIG. 14. (Color online) In-plane power q_{xp} (color scale) as a function of normalized bias current and normalized voltage across the stack for (a) $M = 10$ and (b) $M = 35$. $\beta_{c0} = 4000$. T_{bath} was varied between 20 K and 70 K in steps of 2 K. The product $\beta_{c0}G = 1.4 \times 10^5$ is kept constant. Black symbols denote the T_c line.

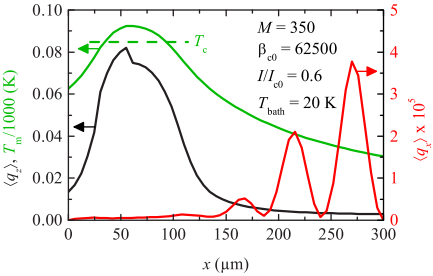

FIG. 15. (Color online) For the case of $M = 350$: Time-averaged distribution of dissipated power density $q_z(x)$ generated by c-axis currents (black line, left scale), the temperature $T_m(x)$ in the mesa (green line, left scale), and the time average of dissipated power density $q_x(x)$ generated by in-plane currents (red line, right scale). At given x position q_z and q_x have been averaged over all segments. $T_{bath} = 20$ K and the $I = 0.6I_{c0}$. The noise parameter is $\Gamma_0 = 5 \times 10^{-5}$.

$M = 35$ at a fixed value of $\beta_{c0} = 4000$. In this case the mode velocity c_1 is proportional to $M^{1/2}$. As a consequence, for $M = 10$, the region where q_{xp} is large has shifted to lower voltages compared to the case of $M = 20$, and for $M = 35$ it shifted to higher voltages, confirming the proportionality of the regions developing strong standing waves to c_1.

For $I/I_{c0} = 0.6$ and $T_{bath} = 20$ K, as well as for $I/I_{c0} = 0.3$ and $T_{bath} = 50$ K, we also calculated current and field distributions for large values of M up to 350 (it was not yet possible to stabilize calculations for $M = 700$). The time-averaged power densities and the temperature profile were very similar to the ones shown in Figs. 6 and 11. Figure 15 shows an example for $M = 350$ and $I/I_{c0} = 0.6$, $T_{bath} = 20$ K. The graph looks almost identical to Fig. 6, with the main difference that $\langle q_x \rangle$ has decreased by a factor of about 40.

D. Comparisons to experiment

We now compare our theoretical results to experimental findings, with respect to the role of the hot spot position and LTSLM imaging of standing-wave patterns. We will also comment on THz emission properties in relation to the dissipated in-plane power.

In our simulations we have modeled the heat produced by the bond wire by an additional heat source located near the left edge of the stack. In experiment the hot spot has been moved along x by using two current injection leads on the mesa and biasing them with different ratios of currents [7]. This method has also been used in simulations [62]. It further has been shown in experiment that the appearance of standing-wave patterns and the emission power depend on the position of the hot spot [7,26]. In the present model we performed some calculations at $M = 20$ and $I/I_{c0} = 0.6$, $T_{bath} = 20$ K where we varied the position of the hot spot simply by changing the location of the current lead. Standing waves appeared for basically all hot spot positions and the average voltage was almost independent of its position. However, q_{xp} was lower by

about a factor of 2 when the hot spot was located at the center of the stack. Further, for several positions of the bond wire we observed the competition of two different wave patterns, leading to fluctuations in q_{xp} as a function of the position of the bond wire.

In the simulations standing waves were a robust feature over a wide range of bias currents and bath temperatures. By contrast, in LTSLM imaging [3,7,9] standing-wave patterns are seen much less often, indicating that the simulations overestimate the stability of cavity resonances. We also attempted to model LTSLM images by introducing an additional heater representing the LTSLM laser beam and monitoring the beam-induced changes $\Delta V(x_b)$ of the dc voltage across the stack versus laser beam position x_b. We did obtain a response proportional to the beam-induced changes of the c-axis conductance as simulated previously [62]; however there were only very faint signatures of the wave patterns. This is likely to be caused by the fact that we inject the bias current j_{ext} purely along the c axis proportional to the local c-axis conductance. In more detail, one may obtain $\Delta V(x_b)$ from a power balance equating the change in input power $I\Delta V$ and the sum of the (time averaged) changes in the integrated in-plane and out-of-plane dissipation:

$$I\Delta V = \Delta\left\langle \int d(x,y,z)(q_z + q_x)\right\rangle = \int d(x,y,z)(\langle\Delta q_z\rangle + \langle\Delta q_x\rangle). \quad (12)$$

The brackets denote time averaging and the integration is over the stack volume. As discussed above, $\langle q_x(x)\rangle$ exhibits clear modulations but is small compared to $\langle q_z(x)\rangle$. Snapshots of $\langle q_z(x)\rangle$ indeed exhibit time-dependent wavy modulations (not shown). However, they occur on a large static background representing the dc power in the stack and are thus averaged out in $\langle q_z\rangle$. To obtain a significant wave signature in LTSLM either $\langle q_z\rangle$ should exhibit strong modulations or some in-plane voltage should be picked up in the measurements. The latter is the likely scenario and consistent with previous observations that the observed patterns are associated with magnetic fields rather than electric fields [7].

We finally comment on the relation of the THz emission power P_e observed in experiment and the absorbed in-plane power q_{xp} calculated numerically. In general, these quantities can be very different. For example, if an out-of-phase mode has formed across the stack, q_{xp} can be large while P_e will be very small [42]. On the other hand, for in-phase modes, as we see them in our simulations, a major part of the in-plane currents contributes constructively to the ac magnetic field produced at the boundaries of the stack. In fact, preliminary simulations performed with radiative boundary conditions indicate that the emitted power is on the order of 5%–10% of the absorbed ac power. In the absence of a standing wave, like for the McCumber-like state shown in Fig. 9, both the ac electric field and the ac magnetic field at the boundaries are small and we expect both q_{xp} and the emitted power to be small as well. With these caveats in mind, let us look at some experimental data for P_e. The experimental findings will be discussed in detail in a separate publication. The measurements have been performed on a $165 \times 60\ \mu m^2$ large Z-type IJJ stack [14] consisting of

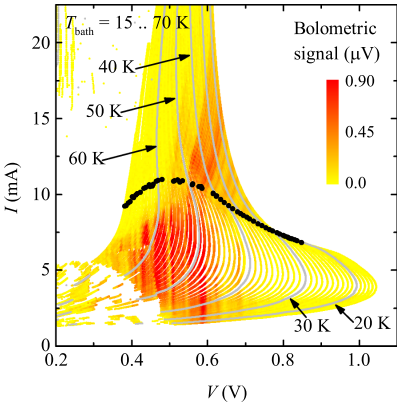

FIG. 16. (Color online) Experimental data for a $165 \times 60\ \mu m^2$ large Z-type IJJ stack consisting of $N = 480$ IJJs: Emitted power (color scale) as a function of bias current and voltage across the stack. The bath temperature was varied between 15 K and 70 K in steps of 0.5 K. Black symbols indicate the currents where a hot spot has formed. The contact resistance is subtracted from each IVC.

$N = 480$ IJJs. The electrothermal behavior of such Z-type stacks is in fact similar to mesa structures. Figure 16 shows P_e as the color scale for a large family of IVCs taken at bath temperatures between 15 K and 70 K. On a qualitative level this plot can be compared to Fig. 5 or to Fig. 13.

In dimensioned units the maximum voltage per junction in Fig. 13 at 20 K is about 2.1 mV and is in line with the corresponding 20 K value of 2.1 mV in Fig. 16. In the experimental data the highest emission signals are seen in the absence of a hot spot for voltages between 0.6 V and 0.4 V, corresponding to, respectively, 1.25 mV and 0.8 mV per IJJ. On a somewhat lower power level the emission continues into the hot spot region. For voltages larger than 0.7 V the emission is basically absent.

Comparing the color distributions in Fig. 13 and Fig. 16 the only qualitative, but striking, difference is the appearance of a stripelike modulation of P_e in Fig. 16. In the low-bias regime these stripes appear at about constant voltage while in the high-bias regime they are tilted to the right. A detailed discussion of the stripes—we find similar patterns also for other structures such as bare IJJ stacks embedded between Au layers—is out of the scope of this paper. We just briefly mention here that, by measuring the frequency of emission f_e using a superconducting integrated receiver [15], we found that also in the high-bias regime f_e is almost constant along a given stripe. The reason for the observed tilt of the stripes is that in the presence of a hot spot there is an additional dc voltage due to in-plane currents, which is picked up by the voltage leads.

Further, the stripe features are most likely not due to different resonant modes inside the IJJ stack but are probably

caused by extrinsic effects such as interferences within the substrate or other parts of the setup.

IV. SUMMARY

In summary, by using 1D coupled sine-Gordon equations combined with heat diffusion equations, we have numerically investigated the thermal and electromagnetic properties of a 300 μm long intrinsic Josephson junction stack consisting of $N = 700$ junctions. The junctions in the stack were combined to M segments. We assumed that inside each segment all junctions behave identically. Most simulations were performed for $M = 20$; i.e., each segment consisted of $N/M = 35$ junctions. The thermal properties were (by ansatz and the fact that $\langle q_x \rangle \ll \langle q_z \rangle$) basically independent of M and showed the appearance of a hot spot for high-bias currents. For M between 20 and 50 local current and electric field distributions were similar, provided that the mode velocity in the stack was chosen to be independent of M. In particular, robust standing-wave patterns appeared and were identified to be associated with π-kink states. For two bias points we confirmed that the same waves/π-kink states are also present for $M = 350$. For the case of $M = 10$ (and also lower values of M) solutions with strongly fluctuating current densities and electric fields appeared at high-bias currents, replacing the long-wavelength standing-wave patterns. This causes some problems with models treating intrinsic Josephson junction stacks as a single "giant" junction ($M = 1$), since the formation of π kinks requires at least 2 segments. For modest values of M (e.g., $M = 2$) there may be some effective values of the parameters to reproduce the physics of the large IJJ stacks. However, at least for the parameter values and boundary conditions used in this work, M should be 20 or larger.

Also, one should be cautious when extrapolating the results to $M = N$ and to a real 3D situation. There might be qualitative changes in electromagnetic behavior, as they have been seen in our simulations for high-bias currents and segment numbers between $M = 10$ and $M = 20$. With respect to 3D stacks it has been found in experiment that emission properties scale inversely proportional with the width of the stack, indicating that also a standing wave has formed along the stack width. This cannot be described within the 1D coupled sine-Gordon equations. An extension to the 2D version of these equations remains to be done.

ACKNOWLEDGMENTS

We gratefully acknowledge financial support by the National Natural Science Foundation of China (Grant No. 11234006), the Priority Academic Program Development of Jiangsu Higher Education Institutions, the Deutsche Forschungsgemeinschaft (Project No. KL930/12-1), Grants-in-Aid for Scientific Research from JSPS, RFBR Grants No. 13-02-00493-a and No. 14-02-91335, and the Ministry of Education and Science of the Russian Federation (No. 14.607.21.0100).

APPENDIX: BASIC EQUATIONS AND NUMERICAL DETAILS

The general geometry of the mesa structure under consideration has been introduced in Sec. II A; cf. Fig. 1.

1. Thermal description

As stated in Sec. II A we write for the heat diffusion in the kth layer

$$c_k \dot{T}_k = \frac{d}{dx}\left(\kappa_{\parallel,k}\frac{d}{dx}T_k\right) + \frac{2}{D_k}(j_{\mathrm{in},k} - j_{\mathrm{out},k}) + q_k. \quad \text{(A1)}$$

We assume that T_k is the temperature in the center of layer k along x. Introducing the auxiliary temperature $T_{\mathrm{h},k}$ as the temperature at the interface between layers k and $k-1$ one obtains for the heat current densities

$$j_{\mathrm{in},k} = \kappa_{\perp,k}(T_{\mathrm{h},k} - T_k)\frac{2}{D_k} \quad \text{(A2)}$$

and

$$j_{\mathrm{out},k} = \kappa_{\perp,k}(T_k - T_{\mathrm{h},k+1})\frac{2}{D_k}, \quad \text{(A3)}$$

where $\kappa_{\perp,k}$ is the out-of-plane thermal conductivity of layer k. We demand $j_{\mathrm{in},k} = j_{\mathrm{out},k-1}$, yielding $T_{\mathrm{h},k} = (a_k T_k + a_{k-1}T_{k-1})/(a_k + a_{k-1})$, with $a_k = \kappa_{\perp,k}/D_k$.

For the mesa including the Au layer ($k = 0$)$T_0 = T_{\mathrm{m}}$. There is no heat flow into this layer and thus $T_{\mathrm{h},0} = T_{\mathrm{m}}$ here. For the effective thermal conductivity of the mesa/gold layer, since for in-plane heat flow the BSCCO stack and the Au layer are in parallel, we take the weighted average

$$\kappa_{\parallel,0} = \frac{D_{\mathrm{m}}\kappa_{ab} + D_{\mathrm{Au}}\kappa_{\mathrm{Au}}}{D_{\mathrm{m}} + D_{\mathrm{Au}}} \quad \text{(A4)}$$

of the BSCCO in-plane thermal conductivity κ_{ab} and the gold thermal conductivity κ_{Au}. The perpendicular heat conductivity is limited by the BSCCO c-axis thermal conductivity κ_c and we thus use $\kappa_{\perp,0} = \kappa_c$ for this layer. During simulations it has turned out that the effect of self-heating is too strong compared to full 3D simulations as described in Ref. [62]. The reason is that in our 1D scenario there is no heat flow in a given layer along the y direction (we have confirmed this by 3D simulations of a very narrow structure). To compensate for this we decreased the effective mesa thickness by a factor 2 compared to its real thickness in Eq. (A1). An expression for the Joule heat power density q_{m} produced in the mesa will be given below; cf. Eq. (A10). For the total heat generation we add a contribution by the contacting bond wire, expressed as

$$q_{\mathrm{B}} = \langle j_{\mathrm{B}} \rangle^2 \rho_{\mathrm{B}} f(x), \quad \text{(A5)}$$

where ρ_{B} is some effective resistivity associated with the wire, having a diameter L_{B} along x. $\langle j_{\mathrm{B}} \rangle = I/L_{\mathrm{B}}$ is the spatially averaged applied current density. The function $f(x)$ equals 1 in the wire and is zero outside.

In the layers representing the base crystal and the glue there is no heat generation; i.e., $q_k = 0$ for all $k \neq 0$. These layers have a length L_{b} which we have taken as $2L_{\mathrm{s}}$. The mesa is centered above the base crystal. For the layer interfacing the mesa ($k = 1$) the heat flow current density $j_{\mathrm{in},1}$ is nonzero only above the mesa. For the bottom of the glue layer ($k = K + 1$)

we have the boundary condition $T_{h,K+2} = T_{bath}$ and, finally, for the in-plane heat flow, von Neumann boundary conditions are used; i.e., we assume that no heat is transported through the boundaries of the mesa and the base along x.

For further calculations we normalized time to $\Phi_0/2\pi j_{c0}\rho_{c0}s$. Power densities are normalized to $j_{c0}^2\rho_{c0}$, electric fields to $j_{c0}\rho_{c0}$, current densities to j_{c0}, and resistivities to ρ_{c0}. This leads to heat capacities normalized to $\Phi_0 j_{c0}/2\pi s$ (in units of K^{-1}) and heat conductivities normalized to $j_{c0}^2\rho_{c0}$ (in units of $\mu m^2/K$).

2. Electrical circuit

The electric circuit is sketched in Figs. 1(c) and 1(d). Let us consider a piece of the nth IJJ, located between x and $x + dx$. For the current flow along z, we use an RCSJ-type description; i.e., we consider a Josephson current with critical current $I_{c,n} = j_{c,n}dxW$, a resistive component with $R_{c,n} = \rho_{c,n}s/dxW$, and a capacitive component with $C_n = \epsilon_n\epsilon_0 dxW/s$. Nyquist noise is considered via a current source producing a random current $I^N_{z,n} = j^N_{z,n}dxW$ with spectral power density $4k_BT_m/R_{c,n}$. For simplicity, we will assume that $\rho_{c,n}$, $j_{c,n}$, and ϵ_n are the same for all junctions; i.e., we omit the index n. The in-plane current flow in the nth BSCCO layer is described by a resistive component $R_{ab,n} = \rho_{ab,n}dx/Wd_s$ and an inductive component $L_{ab,n} = \mu_0\lambda_{ab}^2 dx/Wd_s$. $L_{ab,n}$ is the kinetic inductance associated with in-plane supercurrents. Here, λ_{ab} is the in-plane magnetic penetration depth of BSCCO. We also consider an in-plane noise current $I^N_{x,n} = j^N_{x,n}d_sW$ with spectral power distribution $4k_BT_m/R_{ab,n}$. Note that we have neglected the geometric inductance $L_g \approx \mu_0 s dx/W$ in the superconducting in-plane current paths. There are several reasons for this. First, this inductance, for the parameters we are interested in, is much smaller than the kinetic inductance. Second, in the standard description of IJJ stacks it leads to an out-of-plane length scale $\lambda_c = [\Phi_0/(2\pi\mu_0 j_{c0}s)]^{1/2} \approx 300\,\mu m$ which is comparable to the length of the mesa studied here (300 μm). Thus, even if the kinetic contributions cancel, the finite value of λ_c would not lead to long-junction effects. It is thus safe to ignore the geometric inductance. Further, from a more practical point of view, if $L_{g,n}$ were included in the superconducting path it should also be considered for the resistive in-plane paths which would strongly complicate the resulting sine-Gordon-like equations.

Using Kirchhoff's laws, after some math one finds for the nth IJJ

$$sd_s\left(\frac{\dot\gamma_n'}{\rho_{ab}}\right)' + d_s\left(j^N_{x,n+1} - j^N_{x,n}\right)' + \lambda_k^2(n_s\gamma_n')' = 2j_{z,n} - j_{z,n+1} - j_{z,n-1}. \quad \text{(A6)}$$

Here, the index n runs from 1 to N. The various parameters and normalizations have been already introduced in Sec. II A.

For the current densities $j_{z,n}$ in the z direction one finds

$$j_{z,n} = \beta_{c0}\ddot\gamma_n + \frac{\dot\gamma_n}{\rho_{c,n}} + j_c\sin(\gamma_n) + j^N_{z,n}, \quad \text{(A7)}$$

with $\beta_{c0} = 2\pi j_{c0}\rho_{c0}^2\epsilon\epsilon_0 s/\Phi_0$.

In Eq. (A6) ρ_{ab} and n_s depend on temperature and thus, in general, on x. For spatially constant parameters one would obtain a term $\propto \dot\gamma_n''/\rho_{ab}$ (dissipation due to in-plane currents) and a term $\propto \gamma_n''$ which are familiar from the coupled sine-Gordon equations [81,82]. The term describing in-plane dissipation is often neglected. However, as has been pointed out in Ref. [59] it plays a crucial role for the synchronization of large IJJ stacks. Further note that, at T_c, n_s as well as j_c go to zero. Then, Eq. (A6) has no contributions arising from supercurrents anymore. In Refs. [65,66] the temperature dependence of n_s has been missed.

The calculations presented below are for a huge junction number $N = 700$. For such N it is basically hopeless to solve Eq. (A6) on a reasonable time scale. Let us thus, before proceeding with expressions for the in-plane currents and for the normalized noise currents, introduce the concept of segments consisting of G IJJs. We divide the N junction stack into M segments, each consisting of $G = N/M$ junctions (note that N must contain M as a factor to make G integer). Being interested in dynamic states where all junctions oscillate coherently we assume that, within a segment, the γ_n and their derivatives are the same. Summing up over all junctions Eq. (A6) turns into

$$Gsd_s\left(\frac{\dot\gamma_m'}{\rho_{ab}}\right)' + d_s\left(j^N_{x,m+1} - j^N_{x,m}\right)' + G\lambda_k^2(n_s\gamma_m')' = 2j_{z,m} - j_{z,m+1} - j_{z,m-1}. \quad \text{(A8)}$$

The index m runs from 1 to M. Equation (A8) has almost the same form as Eq. (A6), but with an effective length $\lambda_k \propto G^{1/2}$ and an effective $\rho_{ab} \propto G^{-1}$.

For Eq. (A7) no modification seems to be necessary, except for the fact that the index n should be replaced by m labeling the segments. There is, however, a subtle point. As shown in the main text, resonant modes appeared in the solutions of Eq. (A8). For a *homogeneous* M junction stack in the limit $\rho_{ab} \to \infty$ one can find a set of M collective resonances [83,84], associated with mode velocities c_m, with $m = 1 \ldots M$. The resonance where all junctions oscillate in-phase has $m = 1$ and, rewritten for the segmentation and the boundary conditions we use, has the form [12]

$$c_1 = 2\pi f_{pl}\lambda_J\sqrt{G}\frac{1}{\sqrt{1 - 2\tilde s\cos\frac{\pi}{2M+1}}}, \quad \text{(A9)}$$

where $\lambda_J \approx \lambda_k/\sqrt{2}$ for $\lambda_c \gg \lambda_k$ and $\tilde s = [2 + Gd_s s n_s/\lambda_{ab}^2]^{-1}$. The small term $Gd_s s n_s/\lambda_{ab}^2$ originates from the geometric inductance of the superconducting layers which we neglect in our simulations. We thus work in the limit $s = 0.5$. f_{pl} is the Josephson plasma frequency. In our notation frequencies are normalized to $f_{c0} = \Phi_0/(j_{c0}\rho_{c0}s)$. Then, with $(f_{c0}/f_{pl})^2 = \beta_c$, under the condition $N \gg M \gg 1$ we have (at $T = 4.2$ K) $c_1 \approx 4M\lambda_k\sqrt{G}\,f_{c0}/\sqrt{\beta_{c0}} = 4N\lambda_k f_{c0}/\sqrt{\beta_{c0}G}$. Thus, to keep physics independent of M, c_1 should be kept constant while changing M and thus (approximately) the product $\beta_{c0}G$ should be kept constant.

This procedure, however, leads to too strong ac electric fields and particularly the in-plane resistive currents get too strong. In Eq. (A8) we have assumed that $\dot\gamma_n'$ is the same for all G junctions inside a segment. The term $\propto \dot\gamma_n'$ originates from the difference of the resistive in-plane currents of layers n and $n + 1$ and thus the in-plane currents inside a segment should be extrapolated linearly between in-plane currents

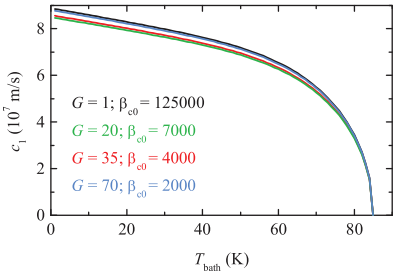

FIG. 17. (Color online) Calculated mode velocity c_1 vs bath temperature in the limit of vanishing dissipation for $G = 1$ ($M = N = 700$), $G = 20$ ($M = 50$), $G = 35$ ($M = 20$), and $G = 70$ ($M = 10$). For $G = 1$, $\beta_{c0} = 1.25 \times 10^5$; for the other curves $\beta_{c0}G = 1.4 \times 10^5$.

of the outermost layers in the segment. This results in an extremely high in-plane power dissipation. As a consequence, for example the temperature in the stack shows a strong spatial modulation, of order of some 10 K, imprinted by the standing wave. This is clearly not seen in experiment. Further, in simulations we found that the in-plane power density is strongly suppressed when increasing M (and thus β_{c0}). Thus, in order to return to physical properties which scale reasonably with M we reduced the in-plane power dissipation by considering only the contributions of the outermost layers in a segment. Example simulations for very large numbers of M up to 350 showed that the wave patterns and other properties scale reasonably with this procedure. Figure 17 shows c_1 versus $T_{\rm bath}$ for $G = 1$ ($M = N = 700$), $G = 20$ ($M = 50$), $G = 35$ ($M = 20$), and $G = 70$ ($M = 10$). For $G = 1$, $\beta_{c0} = 1.25 \times 10^5$; for the other curves we have used $\beta_{c0}G = 1.4 \times 10^5$.

Thus, for the power dissipation $q_{\rm m}$ we use (in dimensioned units) the expression

$$q_{\rm m} = \left(Gs \sum_{m=1}^{M} \frac{E_{z,m}^2}{\rho_c} + d_s \rho_{ab} \sum_{m=1}^{M+1} j_{x,m}^{r2} \right) \frac{1}{Ns}. \qquad \text{(A10)}$$

The first term on the right-hand side represents Joule heat generation in the BSCCO stack due to out-of-plane currents, with the electric field $E_{z,m}$ across one of the IJJs in segment m. In normalized units, $E_{z,m}$ is replaced by $\dot{\gamma}_m$. The second term represents the in-plane dissipation, with the resistive current densities $j_{x,m}^r$ flowing in the mth superconducting layer. The generated power density is averaged over the mesa thickness Ns.

We turn to explicit expressions for the in-plane currents. Using, for a piece of length dx of the mth superconducting layer, London's equation $E_{x,m} = \mu_0 \lambda_{ab}^2 \dot{j}_{x,n}^s$, where $E_{x,m}$ is the in-plane electric field and relating the in-plane voltage drop $E_{x,m}dx$ to the time derivative of the phase ϕ_m of the superconducting wave function in this electrode, $E_{x,m}dx = \Phi_0[\dot{\phi}_m(x + dx) - \dot{\phi}_m(x)]/2\pi$, we find in our normalized units

$$j_{x,m}^s = \frac{\lambda_k^2}{d_s} n_s \phi'_m \qquad \text{(A11)}$$

and for the resistive currents experiencing the same electric field one obtains

$$j_{x,m}^r = \frac{e_{x,m}}{\rho_{ab}} = \frac{s}{\rho_{ab}} \dot{\phi}'_m. \qquad \text{(A12)}$$

The index m runs from 1 to $M + 1$ and refers to the CuO_2 layers terminating a segment. $e_{x,m}$ is the normalized in-plane electric field. The ϕ_m and γ_m are related via

$$\gamma_m = \frac{\phi'_{m+1} - \phi'_m}{G}, \qquad \text{(A13)}$$

allowing us to evaluate the in-plane currents once all γ_m and in addition ϕ'_m of one of the outermost electrodes are known. Note the above relations hold both for the individual layers in the N junction stack (using n instead of m) as for the electrodes addressed in the segmented stack.

This brings us to the boundary conditions. We treat the base crystal as a ground; i.e., we demand that for segment M in Eq. (A8) $j_{z,m+1} = j_{z,m}$. Then, the in-plane currents in the superconducting layer $M + 1$ are zero, leading to $\phi'_{M+1} = 0$. The boundary condition for the c-axis currents in junction 1 interfacing the Au layer, i.e., the determination of the current density $j_{z,m-1}$ in Eq. (A8), is more problematic. In a first attempt we have explicitly also considered the Au layer as an additional resistive element in parallel to the in-plane resistor describing the quasiparticle currents in the topmost BSCCO CuO_2 layer. For realistic resistivities this led to heavy numerical instabilities. We next considered the Au layer to be an ideal conductor. The approach worked, however converged with reasonable computing times only if a resistive layer—i.e., a contact resistance—for the out-of-plane currents was introduced between the topmost BSCCO electrode and the Au layer. We thus decided on a simplified description where we assume that the bias current can freely disperse in the Au layer and perhaps some incoherent layer on top of the BSCCO mesa, and finally enters the topmost IJJ according to the local c-axis conductivity; i.e., we used

$$j_{\rm ext} = \frac{\langle j_{\rm ext} \rangle}{\langle \sigma_c \rangle \rho_c}, \qquad \text{(A14)}$$

where the brackets denote spatial averaging and $\sigma_c = \rho_c^{-1}$.

For the in-plane boundary conditions we used $\gamma'_m(0) = \gamma'_m(L_s) = 0$; i.e., there is no energy flow out of the stack along x.

[1] L. Ozyuzer, A. E. Koshelev, C. Kurter, N. Gopalsami, Q. Li, M. Tachiki, K. Kadowaki, T. Yamamoto, H. Minami, H. Yamaguchi *et al.*, Science **318**, 1291 (2007).

[2] R. Kleiner, F. Steinmeyer, G. Kunkel, and P. Müller, Phys. Rev. Lett. **68**, 2394 (1992).

[3] H. B. Wang, S. Guénon, J. Yuan, A. Iishi, S. Arisawa, T. Hatano, T. Yamashita, D. Koelle, and R. Kleiner, Phys. Rev. Lett. **102**, 017006 (2009).

[4] H. Minami, I. Kakeya, H. Yamaguchi, T. Yamamoto, and K. Kadowaki, Appl. Phys. Lett. **95**, 232511 (2009).

[5] C. Kurter, K. E. Gray, J. F. Zasadzinski, L. Ozyuzer, A. E. Koshelev, Q. Li, T. Yamamoto, K. Kadowaki, W.-K. Kwok, M. Tachiki *et al.*, IEEE Trans. Appl. Supercond. **19**, 428 (2009).

[6] K. E. Gray, L. Ozyuzer, A. E. Koshelev, C. Kurter, K. Kadowaki, T. Yamamoto, H. Minami, H. Yamaguchi, M. Tachiki, W.-K. Kwok, and U. Welp, IEEE Trans Appl. Supercond. **19**, 3755 (2009).

[7] S. Guénon, M. Grünzweig, B. Gross, J. Yuan, Z. Jiang, Y. Zhong, A. Iishi, P. Wu, T. Hatano, D. Koelle *et al.*, Phys. Rev. B **82**, 214506 (2010).

[8] C. Kurter, L. Ozyuzer, T. Proslier, J. F. Zasadzinski, D. G. Hinks, and K. E. Gray, Phys. Rev. B **81**, 224518 (2010).

[9] H. B. Wang, S. Guénon, B. Gross, J. Yuan, Z. G. Jiang, Y. Y. Zhong, M. Gruenzweig, A. Iishi, P. H. Wu, T. Hatano *et al.*, Phys. Rev. Lett. **105**, 057002 (2010).

[10] M. Tsujimoto, K. Yamaki, K. Deguchi, T. Yamamoto, T. Kashiwagi, H. Minami, M. Tachiki, K. Kadowaki, and R. A. Klemm, Phys. Rev. Lett. **105**, 037005 (2010).

[11] H. Koseoglu, F. Turkoglu, Y. Simsek, and L. Ozyuzer, J. Supercond. Nov. Magn. **24**, 1083 (2011).

[12] T. M. Benseman, A. E. Koshelev, K. E. Gray, W.-K. Kwok, U. Welp, K. Kadowaki, M. Tachiki, and T. Yamamoto, Phys. Rev. B **84**, 064523 (2011).

[13] K. Yamaki, M. Tsujimoto, T. Yamamoto, A. Furukawa, T. Kashiwagi, H. Minami, and K. Kadowaki, Opt. Express **19**, 3193 (2011).

[14] J. Yuan, M. Y. Li, J. Li, B. Gross, A. Ishii, K. Yamaura, T. Hatano, K. Hirata, E. Takayama-Muromachi, P. H. Wu *et al.*, Supercond. Sci. Technol. **25**, 075015 (2012).

[15] M. Y. Li, J. Yuan, N. Kinev, J. Li, B. Gross, S. Guénon, A. Ishii, K. Hirata, T. Hatano, D. Koelle *et al.*, Phys. Rev. B **86**, 060505(R) (2012).

[16] Z. Wang, B. Fan, P. Wang, L. Ji, X. J. Zhao, and S. L. Yan, J. Supercond. Nov. Mag. **25**, 2259 (2012).

[17] M. Tsujimoto, H. Minami, K. Delfanazari, M. Sawamura, R. Nakayama, T. Kitamura, T. Yamamoto, T. Kashiwagi, T. Hattori, and K. Kadowaki, J. Appl. Phys. **111**, 123111 (2012).

[18] I. Kakeya, Y. Omukai, T. Yamamoto, K. Kadowaki, and M. Suzuki, Appl. Phys. Lett. **100**, 242603 (2012).

[19] M. Tsujimoto, T. Yamamoto, K. Delfanazari, R. Nakayama, T. Kitamura, M. Sawamura, T. Kashiwagi, H. Minami, M. Tachiki, K. Kadowaki *et al.*, Phys. Rev. Lett. **108**, 107006 (2012).

[20] F. Turkoglu, H. Koseoglu, Y. Demirhan, L. Ozyuzer, S. Preu, S. Malzer, Y. Simsek, P. Müller, T. Yamamoto, and K. Kadowaki, Supercond. Sci. Technol. **25**, 125004 (2012).

[21] D. Oikawa, A. Irie, and K. Yamaki, IEEE Trans. Appl. Supercond. **23**, 1500604 (2013).

[22] D. Y. An, J. Yuan, N. Kinev, M. Y. Li, Y. Huang, M. Ji, H. Zhang, Z. L. Sun, L. Kang, B. B. Jin *et al.*, Appl. Phys. Lett. **102**, 092601 (2013).

[23] T. M. Benseman, A. E. Koshelev, W.-K. Kwok, U. Welp, V. K. Vlasko-Vlasov, K. Kadowaki, H. Minami, and C. Watanabe, J. Appl. Phys. **113**, 133902 (2013).

[24] T. M. Benseman, K. E. Gray, A. E. Koshelev, W.-K. Kwok, U. Welp, H. Minami, K. Kadowaki, and T. Yamamoto, Appl. Phys. Lett. **103**, 022602 (2013).

[25] T. M. Benseman, A. E. Koshelev, W.-K. Kwok, U. Welp, K. Kadowaki, J. R. Cooper, and G. Balakrishnan, Supercond. Sci. Technol. **26**, 085016 (2013).

[26] H. Minami, C. Watanabe, K. Sato, S. Sekimoto, T. Yamamoto, T. Kashiwagi, R. A. Klemm, and K. Kadowaki, Phys. Rev. B **89**, 054503 (2014).

[27] C. Watanabe, H. Minami, T. Yamamoto, T. Kashiwagi, R. A. Klemm, and K. Kadowaki, J. Phys.: Condens. Matter **26**, 172201 (2014).

[28] M. Ji, J. Yuan, B. Gross, F. Rudau, D. Y. An, M. Y. Li, X. J. Zhou, Y. Huang, H. C. Sun, Q. Zhu *et al.*, Appl. Phys. Lett. **105**, 122602 (2014).

[29] L. N. Bulaevskii and A. E. Koshelev, Phys. Rev. Lett. **99**, 057002 (2007).

[30] A. E. Koshelev and L. N. Bulaevskii, Phys. Rev. B **77**, 014530 (2008).

[31] L. Goren and E. Altman, Phys. Rev. B **79**, 174509 (2009).

[32] S. Lin and X. Hu, Phys. Rev. Lett. **100**, 247006 (2008).

[33] V. M. Krasnov, Phys. Rev. Lett. **103**, 227002 (2009).

[34] R. A. Klemm and K. Kadowaki, J. Phys.: Condens. Matter **22**, 375701 (2010).

[35] Y. Nonomura, Phys. Rev. B **80**, 140506 (2009).

[36] M. Tachiki, S. Fukuya, and T. Koyama, Phys. Rev. Lett. **102**, 127002 (2009).

[37] N. Pedersen and S. Madsen, IEEE Trans Appl. Supercond. **19**, 726 (2009).

[38] X. Hu and S. Z. Lin, Phys. Rev. B **80**, 064516 (2009).

[39] T. Koyama, H. Matsumoto, M. Machida, and K. Kadowaki, Phys. Rev. B **79**, 104522 (2009).

[40] A. Grib and P. Seidel, Phys. Status Solidi RRL **3**, 302 (2009).

[41] W. Zhou, C. Wang, and Q.-H. Chen, Phys. Rev. B **82**, 184514 (2010).

[42] V. M. Krasnov, Phys. Rev. B **82**, 134524 (2010).

[43] A. E. Koshelev, Phys. Rev. B **82**, 174512 (2010).

[44] S. Savel'ev, V. A. Yampol'skii, A. L. Rakhmanov, and F. Nori, Rep. Prog. Phys. **73**, 026501 (2010).

[45] S.-Z. Lin and X. Hu, J. Supercond. Nov. Magn. **23**, 1025 (2010).

[46] S.-Z. Lin and X. Hu, Phys. Rev. B **82**, 020504 (2010).

[47] S.-Z. Lin and X. Hu, Physica C **470**, S201 (2010).

[48] S. O. Katterwe, A. Rydh, H. Motzkau, A. B. Kulakov, and V. M. Krasnov, Phys. Rev. B **82**, 024517 (2010).

[49] A. A. Yurgens, Phys. Rev. B **83**, 184501 (2011).

[50] T. Koyama, H. Matsumoto, M. Machida, and Y. Ota, Supercond. Sci. Technol. **24**, 085007 (2011).

[51] T. Tachiki and T. Uchida, Physica C **471**, 1206 (2011).

[52] T. M. Slipchenko, D. V. Kadygrob, D. Bogdanis, V. A. Yampol'skii, and A. A. Krokhin, J. Phys.: Conf. Ser. **234**, 042035 (2010).

[53] V. M. Krasnov, Phys. Rev. B **83**, 174517 (2011).

[54] A. A. Yurgens and L. N. Bulaevskii, Supercond. Sci. Technol. **24**, 015003 (2011).

[55] S.-Z. Lin, X. Hu, and L. Bulaevskii, Phys. Rev. B **84**, 104501 (2011).

[56] H. Asai, M. Tachiki, and K. Kadowaki, Phys. Rev. B **85**, 064521 (2012).

[57] H. Asai, M. Tachiki, and K. Kadowaki, Appl. Phys. Lett. **101**, 112602 (2012).

[58] Y.-X. Zhang, Y.-C. Zhou, L. Dong, and S.-G. Liu, Appl. Phys. Lett. **101**, 123503 (2012).

[59] S.-Z. Lin and X. Hu, Phys. Rev. B **86**, 054506 (2012).

[60] Y. O. Averkov, V. M. Yakovenko, V. A. Yampolskii, and F. Nori, Phys. Rev. Lett. **109**, 027005 (2012).

[61] A. Grib and P. Seidel, Low Temp. Phys. **38**, 321 (2012).
[62] B. Gross, S. Guénon, J. Yuan, M. Y. Li, J. Li, A. Iishi, R. G. Mints, T. Hatano, P. H. Wu, D. Koelle *et al.*, Phys. Rev. B **86**, 094524 (2012).
[63] S. S. Apostolov, T. N. Rokhmanova, S. I. Khankina, V. M. Yakovenko, and V. A. Yampolskii, Low Temp. Phys. **38**, 880 (2012).
[64] F. Liu, S. Z. Lin, and X. Hu, Supercond. Sci. Technol. **26**, 025003 (2013).
[65] H. Asai and S. Kawabata, Physica C **494**, 121 (2013).
[66] H. Asai and S. Kawabata, Appl. Phys. Lett. **101**, 112601 (2014).
[67] A. Grib and P. Seidel, Phys. Status Solidi B **251**, 1040 (2014).
[68] S. Z. Lin, J. Appl. Phys. **115**, 173901 (2014).
[69] T. Kashiwagi, M. Tsujimoto, T. Yamamoto, H. Minami, K. Yamaki, K. Delfanzari, K. Deguchi, N. Orita, T. Koike, R. Nakayama *et al.*, Jpn. J. Appl. Phys. **51**, 010113 (2012).
[70] U. Welp, K. Kadowaki, and R. Kleiner, Nat. Photonics **7**, 702 (2013).
[71] I. Kawayama, C. Zhang, H. B. Wang, and M. Tonouchi, Supercond. Sci. Technol. **26**, 093002 (2013).
[72] S. Sekimoto, C. Watanabe, H. Minami, T. Yamamoto, T. Kashiwagi, R. A. Klemm, and K. Kadowaki, Appl. Phys. Lett. **103**, 182601 (2013).
[73] B. Gross, J. Yuan, D. Y. An, M. Y. Li, N. Kinev, X. J. Zhou, M. Ji, Y. Huang, T. Hatano, R. G. Mints *et al.*, Phys. Rev. B **88**, 014524 (2013).
[74] A. V. Gurevich and R. G. Mints, Rev. Mod. Phys. **59**, 941 (1987).
[75] E. Spenke, Wissenschaftliche Veroeffentlichungen aus den Siemens-Werken **15**, 92 (1936).
[76] S.-F. Lee, D. C. Morgan, R. J. Ormeno, D. M. Broun, R. A. Doyle, J. R. Waldram, and K. Kadowaki, Phys. Rev. Lett. **77**, 735 (1996).
[77] T. S. Nunner and P. J. Hirschfeld, Phys. Rev. B **72**, 014514 (2005).
[78] T. Jacobs, S. Sridhar, Q. Li, G. D. Gu, and N. Koshizuka, Phys. Rev. Lett. **75**, 4516 (1995).
[79] K. Kadowaki, M. Tsujimoto, K. Yamaki, T. Yamamoto, T. Kashiwagi, H. Minami, M. Tachiki, and R. A. Klemm, J. Phys. Soc. Jpn. **79**, 023703 (2010).
[80] X. Hu and S. Z. Lin, Phys. Rev. B **78**, 134510 (2008).
[81] S. Sakai, P. Bodin, and N. F. Pedersen, J. Appl. Phys. **73**, 2411 (1993).
[82] R. Kleiner, P. Müller, H. Kohlstedt, N. F. Pedersen, and S. Sakai, Phys. Rev. B **50**, 3942 (1994).
[83] R. Kleiner, Phys. Rev. B **50**, 6919 (1994).
[84] S. Sakai, A. V. Ustinov, H. Kohlstedt, A. Petraglia, and N. F. Pedersen, Phys. Rev. B **50**, 12905 (1994).

Publication 2

Three-Dimensional Simulations of the Electrothermal and Terahertz Emission Properties of $Bi_2Sr_2CaCu_2O_8$ Intrinsic Josephson Junction Stacks

F. Rudau,[1] R. Wieland,[1] J. Langer,[1] X. J. Zhou,[2,3] M. Ji,[2,3] N. Kinev,[4] L. Y. Hao,[2,3] Y. Huang,[2,3] J. Li,[3] P. H. Wu,[3] T. Hatano,[2] V. P. Koshelets,[4] H. B. Wang,[2,3] D. Koelle,[1] and R. Kleiner[1]

[1]*Physikalisches Institut and Center for Quantum Science (CQ) in LISA⁺, Universität Tübingen, D-72076 Tübingen, Germany*

[2]*National Institute for Materials Science, Tsukuba 3050047, Japan*

[3]*Research Institute of Superconductor Electronics, Nanjing University, Nanjing 210093, China*

[4]*Kotel'nikov Institute of Radio Engineering and Electronics, Moscow 125009, Russia*

(Received 19 October 2015; revised manuscript received 1 February 2016; published 27 April 2016)

We use 2D coupled sine-Gordon equations combined with 3D heat diffusion equations to numerically investigate the thermal and electromagnetic properties of a $250 \times 70\ \mu m^2$ intrinsic Josephson junction stack. The 700 junctions are grouped to 20 segments; we assume that in a segment all junctions behave identically. At large input power, a hot spot forms in the stack. Resonant electromagnetic modes oscillating either along the length [$(0, n)$ modes] or the width [$(m, 0)$ modes] of the stack or having a more complex structure can be excited both with and without a hot spot. At fixed bath temperature and bias current, several cavity modes can coexist in the absence of a magnetic field. The (1, 0) mode considered to be the most favorable mode for terahertz emission can be stabilized by applying a small magnetic field along the length of the stack. A strong field-induced enhancement of the emission power is also found in experiment for an applied field around 5.9 mT.

DOI: 10.1103/PhysRevApplied.5.044017

I. INTRODUCTION

Stacks of intrinsic Josephson junctions (IJJs) in the high-temperature superconductor $Bi_2Sr_2CaCu_2O_8$ (BSCCO) emit coherent radiation at terahertz frequencies [1]. The emitted frequency f_e follows the Josephson relation $f_e = V_J/\Phi_0$, where Φ_0 is the flux quantum ($\Phi_0^{-1} = 483.6$ GHz/mV), and V_J is the voltage across a single junction. In BSCCO, superconductivity is restricted to $d_s = 0.3$ nm thick CuO_2 sheets separated by barrier layers to form an $s = 1.5$ nm thick IJJ [2]. In Ref. [1], stacks of approximately 700 IJJs, with a length $L_s \sim 300\ \mu m$ and a width W_s of some 10 μm have been realized as mesas on top of BSCCO single crystals. These mesas emitted radiation between 0.35 and 0.85 THz, with an integrated output power of approximately 1 μW. The emission frequency scaled as W_s^{-1}, indicating that cavity modes oscillating along the width of the stack are responsible for synchronization. Terahertz radiation from IJJ stacks became a hot topic both in experiment [3–35] and theory [36–66]; for a recent review, see Ref. [67].

IJJ stacks containing 500–2000 junctions have been patterned as mesas but also as bare IJJ stacks contacted by Au layers (GBG structures) [16,17,20,24] and as all-superconducting structures [11]. Emission frequencies range from 0.3 to 2.4 THz. For the best stacks, an emission power P_e in the range of tens of microwatts has been achieved [17,19,20,32,33], and arrays of mesas showed emission with P_e up to 0.61 mW [19]. The physics of the huge IJJ stacks is affected by Joule heating [1,3,5,6,8,13,18,22,26,30,49,52,54,55,63]. For sufficiently low-bias currents, the temperature rises only slightly to values above the bath temperature T_{bath}, and the voltage V across the stack increases with increasing bias current I. With increasing I and input power, the current-voltage characteristics (IVCs) start to backbend, and, at some bias current in the backbending region, a hot spot forms in the stack [3,6,8,13,18,21–23,25,26,34,68], creating a region heated to temperatures above the critical temperature T_c. Similar effects also occur in other systems [69,70]. The terahertz emission properties of the IJJ stacks are affected by the hot spot. For example, it has been found that the linewidth of radiation is much narrower in the high-bias regime than at low bias [12,60]. Other properties such as the emission frequency seem to be basically independent of the hot-spot position, leading to some debate as to whether the hot spot is helpful for radiation or just coexists with the radiating regions [20,22,23]. In fact, recent results showed that there is a strong interaction [28]. Further, cooling has been improved by sandwiching the stacks between substrates with high thermal conductivity. In the first attempts, maximum emission frequencies near 1.05 THz were obtained [24,68]. This value was recently improved to 2.4 THz for disk-shaped stacks [33]. In terms of modeling, many calculations of electrodynamics have been based on a homogeneous temperature distribution, while calculations of the thermal properties were based on solving the heat diffusion equations in the absence of Josephson

currents [49,52,54]. Some attempts have been made to combine both electrodynamics and thermodynamics, either by using arrays of pointlike IJJs [59,60,64] or by incorporating temperature-induced effects into an effective model describing the whole stack as a single "giant" junction [55,62,63]. Reference [66] modeled the combined thermal and electromagnetic properties of BSCCO stacks via one-dimensional coupled sine-Gordon equations for an $N = 700$ junction stack where the IJJs were grouped into M segments [66].

II. MODEL

The model introduced here extends the 2D approach of Ref. [66] to 3D, enabling us to model IJJ stacks realistically. We first give a brief outline of the features which go beyond Ref. [66]. We consider a mesa consisting of $N = 700$ IJJs; cf. Fig. 1(a). The mesa has a length $L_s = 250$ μm along x and a width $W_s = 70$ μm along y. It is covered by a gold layer and centered on a 30-μm-thick base crystal of length $L_b = 2L_s$ and width $W_b = 2W_s$. The base crystal is mounted by a 20-μm-thick glue layer to a sample holder kept at $T_{\rm bath}$. A bias current I is injected via a bond wire into the Au layer and leaves the mesa into the base crystal. The model contains a variety of parameters (in-plane and out-of-plane resistivities, Josephson critical current density, Cooper pair density, thermal conductances, etc.) which depend on the temperature. We assume that these parameters are spatially constant for spatially *constant* T. For an inhomogeneous temperature distribution in the stack, they vary in space through their dependence on the local temperature $T(x, y, z)$, which is found by self-consistently solving the thermal equations (requiring Joule heat dissipation as an input from the electric circuit) and the electrical equations (requiring the temperature distribution in the mesa, as determined from the thermal circuit).

For the thermal description [cf. Fig. 1(b)], we assume that the mesa plus the contacting Au layer and the bond wire have a temperature $T_m(x, y)$ which is constant along z but can vary along x and y. The BSCCO base crystal is split into K segments, the kth segment being at a temperature $T_{b,k}(x, y)$. For this geometry, we solve the heat diffusion equation

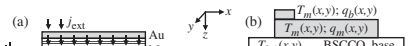

FIG. 1. Geometry used for modeling. Sketch of the mesa and electric current flow in the z direction (a). Geometry for thermal description (b), where q_m and q_b, respectively, denote the Joule power density produced in the mesa and by the bias lead. The temperatures of the various layers are indicated.

$$c\dot{T} = \nabla(\kappa\nabla T) + q_m + q_b, \tag{1}$$

with the specific heat capacity c, the (anisotropic) thermal conductivity κ, and the power densities q_m and q_b for heat generation in the mesa and the bond wire, respectively. For high enough q_b, the hot spot is controllably located near the wire position.

For the electric circuit, we group the N IJJs in the mesa to M segments, each containing $G = N/M$ IJJs, assumed to have identical properties. The bond wire injects an electric current density $j_{\rm ext}$ to the Au layer, which we assume to have a low enough resistance to freely distribute the current before it enters the IJJ stack in the z direction with a density $j_{z,\rm Au}$ proportional to the local BSCCO conductance $\sigma_c(x, y) = \rho_c^{-1}(x, y)$. The full expression is $j_{z,\rm Au} = \langle j_{\rm ext}\rangle\sigma_c(x, y)/\langle\sigma_c\rangle$, the brackets denoting spatial averaging. The interface stack-base crystal is treated as a ground. The z-axis currents consist of Josephson currents with critical current density $j_c(x, y)$, (Ohmic) quasiparticle currents with resistivity $\rho_c(x, y)$, and displacement currents with dielectric constant ϵ. To avoid weakly stable solutions, we also add Nyquist noise created by the quasiparticle currents. The in-plane currents consist of a superconducting part characterized by a Cooper pair density $n_s(x, y)$, a quasiparticle component with resistivity $\rho_{ab}(x, y)$, and a Nyquist noise component. For constant $T_m(x, y) = 4.2$ K, we index the above quantities by an additional "0" and assume that they are constant with respect to x and y. The temperature dependence of the various parameters is close to experimental curves and plotted in detail in Ref. [66]. We further use $T_c = 85$ K.

One obtains sine-Gordon-like equations for the Josephson phase differences $\gamma_m(x, y)$ in the mth segment of the IJJ stack:

$$Gsd_s\nabla\left(\frac{\nabla\dot{\gamma}_m}{\rho_{ab}}\right) + d_s\nabla(j^N_{x,m+1} - j^N_{x,m}) + G\lambda_k^2\nabla(n_s\nabla\gamma_m) = 2j_{z,m} - j_{z,m+1} - j_{z,m-1}. \tag{2}$$

Here, $m = 1, \ldots, M$, $\nabla = (\partial/\partial x, \partial/\partial y)$, and $\lambda_k = [\Phi_0 d_s/(2\pi\mu_0 j_{c0}\lambda_{ab0}^2)]^{1/2}$, with the in-plane London penetration depth λ_{ab0} and the magnetic permeability μ_0. Quantities $j^N_{x,m}$ are the in-plane noise current densities. Time is normalized to $\Phi_0/2\pi j_{c0}\rho_{c0}s$, resistivities to ρ_{c0}, and current densities to j_{c0}. Equation (2) neglects geometric inductances; i.e., it assumes that kinetic inductances dominate (valid if L_s, $W_s < \lambda_c$; $\lambda_c \sim 300$ μm is the out-of-plane penetration depth).

For the out-of-plane current densities $j_{z,m}$, one finds

$$j_{z,m} = \beta_{c0}\ddot{\gamma}_m + \frac{\dot{\gamma}_m}{\rho_{c,m}} + j_c\sin(\gamma_m) + j^N_{z,m}, \tag{3}$$

with $\beta_{c0} = 2\pi j_{c0}\rho_{c0}^2\varepsilon\varepsilon_0 s/\Phi_0$; ε_0 is the vacuum permittivity, and the $j^N_{z,m}$ are the out-of-plane noise current densities.

From the gauge-invariant Josephson phase differences γ_m, as calculated from Eqs. (2) and (3), we obtain the phase ϕ_m of the superconducting wave function in electrodes m (the CuO_2 layer interfacing segments m and $m+1$) via

$$\nabla\gamma_m = \frac{2\pi s}{\Phi_0}(B_{y,m}, -B_{x,m}) + \frac{\nabla(\phi_{m+1}-\phi_m)}{G}. \quad (4)$$

Here, $B_{x,m}$ and $B_{y,m}$ are, respectively, the x and y components of the magnetic field in the mth segment.

The in-plane supercurrent densities in units of j_{c0}, $\vec{j}^s_m = (j^s_{x,m}, j^s_{y,m})$, in electrode m are expressed as

$$\vec{j}^s_m = \frac{\lambda_k^2 n_s}{d_s}\left(\nabla\phi_m - \frac{2\pi}{\Phi_0}\vec{A}_m\right). \quad (5)$$

$\vec{A}_m = (A_{x,m}, A_{y,m})$ denotes the in-plane components of the vector potential in electrode m. The resistive currents $\vec{j}^r_m = (j^r_{x,m}, j^r_{y,m})$ in electrode m are given by

$$\vec{j}^r_m = \frac{s}{\rho_{ab}}\frac{d}{dt}\left(\nabla\phi_m - \frac{2\pi}{\Phi_0}\vec{A}_m\right). \quad (6)$$

In our calculations, we assume that the z components of $\mathrm{curl}\vec{j}^s_m$ and of $\mathrm{curl}\vec{j}^r_m$ vanish, and, thus, inside the superconducting layers, the total magnetic field in the z direction is zero.

For the thermal parameters, we use the same values as in Ref. [66]. The bond wire with resistivity $\rho_b = 0.02\rho_{c0}$ is assumed to be a 25-μm-wide square located at the left edge of the mesa. Further, $\rho_{c0} = 10^3\ \Omega\,\mathrm{cm}$, $\rho_{ab0} = 8\ \mu\Omega\,\mathrm{cm}$, $j_{c0} = 200\ \mathrm{A/cm^2}$, $\lambda_{ab0} = 260$ nm, and $\varepsilon = 12$. For our geometry, one obtains a critical current $I_{c0} = 35$ mA, a c-axis resistance per junction $R_{c0} = 0.86\ \Omega$, a characteristic voltage $V_{c0} = I_{c0}R_{c0} = 30$ mV, and a characteristic frequency $f_{c0} = I_{c0}R_{c0}/\Phi_0 = 14.5$ THz. The characteristic power density $p_{c0} = j_{c0}^2\rho_{c0}$ is $4\times10^7\ \mathrm{W/cm^3}$, yielding for a stack volume of $1.84\times10^{-8}\ \mathrm{cm^3}$ a power P_{c0} of 0.74 W. For λ_k, one obtains 0.76 μm. The 4.2 K value of the in-phase mode velocity $c_1 = 8.8\times10^7$ m/s [66]. We keep the product $\beta_{c0}G$ constant in order to (approximately) fix the 4.2 K value of c_1 and use $\beta_{c0} = 4000$ for $G = 35$ ($M = 20$). We further divide ac electric fields and in-plane current densities by G to make the results only weakly dependent on M. For selected bias conditions, the scaling is tested using $M = 50$.

The differential equations are discretized using 50 (9) grid points along x (y) for the mesa and 100 (18) grid points for the base crystal [71], which is split into $K = 4$ segments. A fifth-order Runge-Kutta scheme is used to evolve these equations in time. After some initialization steps [66], various quantities partially averaged over spatial coordinates are tracked as a function of time to produce time averages or to make Fourier transforms.

III. RESULTS

Figure 2 shows for $T_{\mathrm{bath}} = 20$ K the averaged distributions of the power density $\langle q_\parallel(x,y)\rangle$ dissipated by in-plane currents for five values of $I/I_{c0} = 0.65$ Fig. 2(a) to 0.1 Fig. 2(e). Averaging is over time and the z direction in the mesa. This type of plot, also used in Ref. [66], is useful to visualize resonance patterns, with nodes (antinodes) appearing at the minima (maxima) of $\langle q_\parallel(x,y)\rangle$ [72]. The left (right) graphs are at high (low) bias where a hot spot is present (absent). In Figs. 2(a) and 2(e), the modulations along x are due to a cavity mode oscillating along x [a $(0,n)$ mode], with $n = 2$ and 3, respectively. In Fig. 2(c), a cavity mode oscillating along y is excited [a (1,0) mode]. The spatial variations in Figs. 2(b) and 2(d) have a more complicated structure which is not easy to explain by a superposition of different cavity modes. The patterns also show that "linear thinking" in terms of separating ac Josephson currents and resonant modes can be dangerous. Near the antinodes of the standing waves, vortex-antivortex pairs oscillate back and forth, colliding at the center of the antinode [66]. The collision zones should form a continuous line leaving the stack either at its edges or into the hot-spot area. All patterns fulfill this requirement.

In general, not all segments in the stack are synchronized. We investigate this by monitoring the dc voltages ($\propto$ Josephson oscillation frequency f_J) v_m ($m = 1,\ldots,M$) across the individual segments. For example, for the modes of Figs. 2(a)–2(c), for the two to three uppermost segments, v_m is about 1% higher than for the other (locked) segments. For the mode of Fig. 2(d), only small groups of two to five adjacent segments are locked. For the mode of Fig. 2(e), two groups of segments (one to seven and 10–20) oscillated at slightly different frequencies.

Note that $\langle q_\parallel(x,y)\rangle$ can have similar values for the $(0,n)$ and (1,0) modes; compare, e.g., Figs. 2(a) and 2(c). We expect that both types of modes radiate. However, for comparable values of $\langle q_\parallel(x,y)\rangle$, the *emission* power of the $(0,n)$ modes, with $n > 1$, will be lower, because the contributions of the oscillating (in-plane) currents to the magnetic vector potential partially cancel each other.

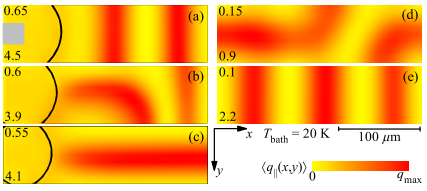

FIG. 2. Power density $\langle q_\parallel(x,y)\rangle$ in units of $10^{-5}\times j_{c0}^2\rho_{c0}$ (color scale) for five values of normalized bias current I/I_{c0} (upper left numbers); values for $q_{\max}$ at the bottom left. The gray square in (a) indicates the position of the bond wire. Regions enclosed by the black line are at $T_m \geq T_c$.

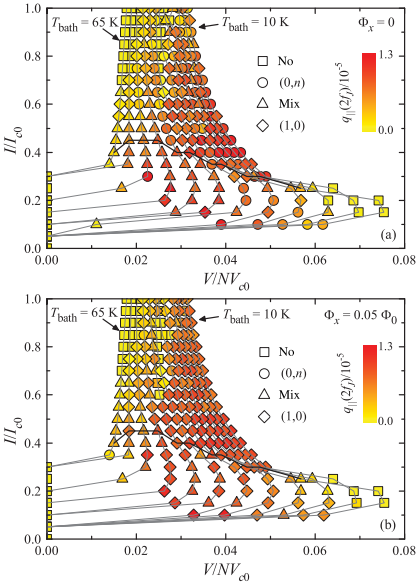

FIG. 3. Power density $q_\parallel(2f_J)$ in units of $10^{-5} \times j_{c0}^2\rho_{c0}$ (color scale) vs normalized bias current and voltage across the stack for an applied magnetic field along x of (a) 0 and (b) 1 mT (0.05 Φ_0 per junction), applied along x. T_{bath} is varied from 10 to 65 K in steps of 5 K. $(0, n)$ modes, (1,0) modes, mixed resonances, and nonresonant states are marked by, respectively, circles, diamonds, triangles, and squares. The gray lines indicate IVCs at fixed T_{bath}. For data points at or above the black line (T_c line) a hot spot forms in the stack.

For the (1,0) mode, the in-plane currents at a given time have the same sign everywhere in the stack.

Figure 3(a) shows, for zero applied magnetic field, how different modes in the stack evolve as a function of I and T_{bath}. We record 12 IVCs for T_{bath} between 10 and 65 K. For each value of I and T_{bath}, we evaluate the type of mode by inspecting the plots as in Fig. 2 and encode it as the shape of the symbol in Fig. 3(a). To have a measure of the strength of a given mode, we record time traces $q_\parallel(t)$ of the power generated by in-plane currents, averaged over the stack volume. After Fourier transform, we extract from $q_\parallel(f)$ the power density $q_\parallel(2f_J)$ arising from the Josephson oscillations appearing as a peak at twice the Josephson frequency f_J. This quantity is plotted as the color scale for each data point. In Fig. 3(a), there are three regions where $q_\parallel(2f_J)$ is low: (i) for $I/I_{c0} > 0.5$ and $T_{bath} > 55$ K, (ii) for T_{bath} around 35 K and $I/I_{c0} > 0.65$, and (iii) for $V/NV_{c0} > 0.06$. In region (i), no or only a small fraction of the stack is superconducting; Josephson oscillations are absent or restricted to a small area. In region (ii) the in-plane and out-of-plane currents exhibit short-wavelength oscillations along x and y, indicative of a mode with spatial variations shorter than our grid spacing. The spectrum of $q_\parallel(f)$ is broad, with no significant peaks. In region (iii), where V and f_J are highest, all currents and fields vary smoothly, but no resonance is excited. In the presence of a hot spot [data points at or above the black line in Fig. 3(a)], $q_\parallel(2f_J)$ is large in a ribbon between $V/NV_{c0} \sim 0.025$ and 0.05. This regime extends down to approximately 0.02 in the low-bias regime. The relative broadness of this regime may look surprising, since resonant modes are excited; however, it can be understood from the facts that the mode velocities depend on the temperature [66] and vary significantly over the data points in Fig. 3(a). Also, the quality factor of the cavity modes is low (of order 10) at elevated temperatures. Most important, one notes that $(0, n)$, (1,0), and mixed modes vary almost randomly. Further simulations reveal that even for the same value of I and T_{bath}, different resonant modes can be excited. However, it should be possible to support the (1,0) mode favored for radiation by applying a small static magnetic field along x, imprinting a linear phase gradient and, consequently, a small gradient on the Josephson current along y. Figure 3(b) organized like Fig. 3(a) shows the resulting data for a small field B_x of 1 mT corresponding to a flux of $0.05\Phi_0$ per junction. The amplitudes of $q_\parallel(2f_J)$ are similar as in the zero-field case; however, the (1,0) mode has stabilized over a wide range of bias current and bath temperature.

IV. COMPARISON TO EXPERIMENT

We also test experimentally the potential benefit of a small magnetic field oriented along x, using a 75×330 μm^2 large GBG structure with $N \approx 760$, mounted on a sapphire lens. Figure 4 shows for (a) $B_x = 0$ and (b) $B_x = 5.9$ mT ($0.32\Phi_0$ per junction) families of IVCs measured for 10 K $\leq T_{bath} \leq$ 45 K. IVCs at 0 and 5.9 mT are measured alternately at given T_{bath}. The accuracy in aligning the field with respect to out-of-plane tilts is better than 0.5°, and with respect to in-plane tilts, it is about 2°. The simultaneously detected terahertz emission power P_e measured via a Ge bolometer is plotted as a color scale. In the high-bias regime, the maximum emission power $P_{e,\max}$ is 27.5 μW, while at low bias, it is 0.21 μW. We, thus, use different values for $P_{e,\max}$ for $I > 8$ mA and for $I < 8$ mA; for fixed I, $P_{e,\max}$ is the same in Figs. 4(a) and 4(b). For $B_x = 0$, the emission is strong for I between 10 and 20 mA and T_{bath} between 10 and 40 K. One notes short-period oscillations in P_e which presumably are extrinsic in origin. These oscillations have been observed before [28,35,66]. Apart from that, the plots clearly show that for $B_x = 5.9$ mT, over a wide range of currents and bath temperatures, P_e increases significantly in some of the stripelike regions up to a factor of 2.7. In the low-bias

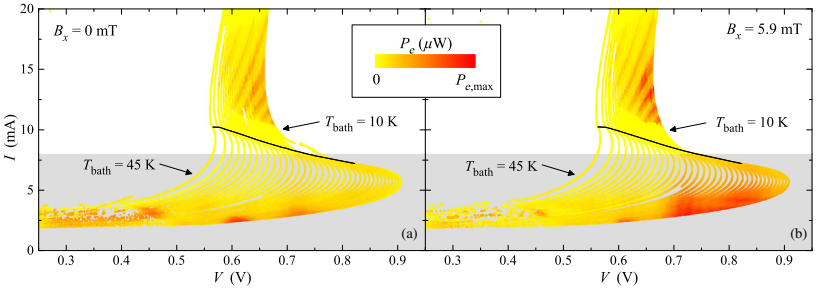

FIG. 4. Experimental data for a GBG structure: terahertz emission power P_e (color scale) for a large number of IVCs, measured at bath temperatures between 10 and 45 K for (a) $B_x = 0$ and (b) $B_x = 5.9$ mT. In both (a) and (b) $P_{e,\max} = 27.5$ μW for $I > 8$ mA and $P_{e,\max} = 0.21$ μW for $I < 8$ mA. Black lines in (a) and (b) indicate the T_c line.

regime, the effect is seen even more drastically, although on a much lower level of $P_{e,\max}$. The idea of applying a small field parallel to the long side of the stack, as suggested by the simulations, thus, seems to work. For other field orientations, the effect is not observed. Even a small field component perpendicular to the layers strongly suppresses P_e [73]. For the measurements shown above for out-of-plane tilts larger than about 1° (the precise value depends on bias current and bath temperature), the enhancement in emission power is lost in the high-bias regime. At the low-bias regime, the critical tilts are on the order of 3°–5°. Further, our simulations suggest that a field applied parallel to the short side is not helpful because a $(0, n)$ mode with $n > 1$ is not promoted by an applied flux well below $\Phi_0/2$ per junction. In Ref. [73], a 20% increase of P_e is observed for fields oriented in the a-b plane. Unfortunately, the field direction relative to the mesa edges is not reported.

V. SUMMARY

In summary, we present 3D simulations of the thermal and electromagnetic properties of a mesa consisting of 700 intrinsic junctions. Resonant modes can be excited in the stack both in the presence and in the absence of a hot spot, exhibiting standing waves either along the length [$(0, n)$ modes] or the width [(1,0) mode] of the stack. Also, more complex mixed modes are found. At fixed bath temperature and bias current, different modes can coexist. By applying a small magnetic field along the length of the stack, it is possible to stabilize the (1,0) mode considered to be the best mode for terahertz emission. In experiment, we find a strong field-induced enhancement of the emission power for a stand-alone stack for fields of around 5.9 mT, small enough to be created by a simple electromagnet.

ACKNOWLEDGMENTS

We gratefully acknowledge financial support by the National Natural Science Foundation of China (Grants No. 11234006 and No. 61501220), the Priority Academic Program Development of Jiangsu Higher Education Institutions, Jiangsu Provincial Natural Science Fund (Grant No. BK20150561), the Deutsche Forschungsgemeinschaft (Project No. KL930/13-1), JSPS KAKENHI Grant No. 25289108, Ministry of Education and Science of the Russian Federation (Grant No. 14.613.21.0046; ID RFMEFI61315X0046), and the EU-FP6-COST Action MP1201.

[1] L. Ozyuzer, A. E. Koshelev, C. Kurter, N. Gopalsami, Q. Li, M. Tachiki, K. Kadowaki, T. Yamamoto, H. Minami, H. Yamaguchi, T. Tachiki, K. E. Gray, W.-K. Kwok, and U. Welp, Emission of coherent THz radiation from superconductors, Science **318**, 1291 (2007).

[2] R. Kleiner, F. Steinmeyer, G. Kunkel, and P. Müller, Intrinsic Josephson Effects in $Bi_2Sr_2CaCu_2O_8$ Single Crystals, Phys. Rev. Lett. **68**, 2394 (1992).

[3] H. B. Wang, S. Guénon, J. Yuan, A. Iishi, S. Arisawa, T. Hatano, T. Yamashita, D. Koelle, and R. Kleiner, Hot Spots and Waves in $Bi_2Sr_2CaCu_2O_8$ Intrinsic Josephson Junction Stacks: A Study by Low Temperature Scanning Laser Microscopy, Phys. Rev. Lett. **102**, 017006 (2009).

[4] H. Minami, I. Kakeya, H. Yamaguchi, T. Yamamoto, and K. Kadowaki, Characteristics of terahertz radiation emitted from the intrinsic Josephson junctions in high-T_c superconductor $Bi_2Sr_2CaCu_2O_{8+\delta}$, Appl. Phys. Lett. **95**, 232511 (2009).

[5] C. Kurter, K. E. Gray, J. F. Zasadzinski, L. Ozyuzer, A. E. Koshelev, Q. Li, T. Yamamoto, K. Kadowaki, W. K. Kwok, M. Tachiki, and U. Welp, Thermal management in large Bi2212 mesas used for terahertz sources, IEEE Trans. Appl. Supercond. **19**, 428 (2009).

[6] S. Guénon, M. Grünzweig, B. Gross, J. Yuan, Z. G. Jiang, Y. Y. Zhong, M. Y. Li, A. Iishi, P. H. Wu, T. Hatano, R. G. Mints, E. Goldobin, D. Koelle, H. B. Wang, and R. Kleiner, Interaction of hot spots and THz waves in $Bi_2Sr_2CaCu_2O_8$

intrinsic Josephson junction stacks of various geometry, Phys. Rev. B **82**, 214506 (2010).

[7] C. Kurter, L. Ozyuzer, T. Proslier, J. F. Zasadzinski, D. G. Hinks, and K. E. Gray, Counterintuitive consequence of heating in strongly-driven intrinsic junctions of $Bi_2Sr_2CaCu_2O_{8+\delta}$ mesas, Phys. Rev. B **81**, 224518 (2010).

[8] H. B. Wang, S. Guénon, B. Gross, J. Yuan, Z. G. Jiang, Y. Y. Zhong, M. Grünzweig, A. Iishi, P. H. Wu, T. Hatano, D. Koelle, and R. Kleiner, Coherent Terahertz Emission of Intrinsic Josephson Junction Stacks in the Hot Spot Regime, Phys. Rev. Lett. **105**, 057002 (2010).

[9] M. Tsujimoto, K. Yamaki, K. Deguchi, T. Yamamoto, T. Kashiwagi, H. Minami, M. Tachiki, K. Kadowaki, and R. A. Klemm, Geometrical Resonance Conditions for THz Radiation from the Intrinsic Josephson Junctions in $Bi_2Sr_2CaCu_2O_{8+\delta}$, Phys. Rev. Lett. **105**, 037005 (2010).

[10] T. M. Benseman, A. E. Koshelev, K. E. Gray, W.-K. Kwok, U. Welp, K. Kadowaki, M. Tachiki, and T. Yamamoto, Tunable terahertz emission from $Bi_2Sr_2CaCu_2O_{8+\delta}$ mesa devices, Phys. Rev. B **84**, 064523 (2011).

[11] J. Yuan, M. Y. Li, J. Li, B. Gross, A. Ishii, K. Yamaura, T. Hatano, K. Hirata, E. Takayama Muromachi, P. H. Wu, D. Koelle, R. Kleiner, and H. B. Wang, Terahertz emission from $Bi_2Sr_2CaCu_2O_{8+\delta}$ intrinsic Josephson junction stacks with all-superconducting electrodes, Supercond. Sci. Technol. **25**, 075015 (2012).

[12] M. Y. Li, J. Yuan, N. Kinev, J. Li, B. Gross, S. Guénon, A. Ishii, K. Hirata, T. Hatano, D. Koelle, R. Kleiner, V. P. Koshelets, H. B. Wang, and P. H. Wu, Linewidth dependence of coherent terahertz emission from $Bi_2Sr_2CaCu_2O_8$ intrinsic Josephson junction stacks in the hot-spot regime, Phys. Rev. B **86**, 060505 (2012).

[13] I. Kakeya, Y. Omukai, T. Yamamoto, K. Kadowaki, and M. Suzuki, Effect of thermal inhomogeneity for terahertz radiation from intrinsic Josephson junction stacks of $Bi_2Sr_2CaCu_2O_{8+\delta}$, Appl. Phys. Lett. **100**, 242603 (2012).

[14] M. Tsujimoto, H. Minami, K. Delfanazari, M. Sawamura, R. Nakayama, T. Kitamura, T. Yamamoto, T. Kashiwagi, T. Hattori, and K. Kadowaki, Terahertz imaging system using high-T_c superconducting oscillation devices, J. Appl. Phys. **111**, 123111 (2012).

[15] M. Tsujimoto, T. Yamamoto, K. Delfanazari, R. Nakayama, T. Kitamura, M. Sawamura, T. Kashiwagi, H. Minami, M. Tachiki, K. Kadowaki, and R. A. Klemm, Broadly Tunable Subterahertz Emission from Internal Branches of the Current-Voltage Characteristics of Superconducting $Bi_2Sr_2CaCu_2O_{8+\delta}$ Single Crystals, Phys. Rev. Lett. **108**, 107006 (2012).

[16] T. Kashiwagi, M. Tsujimoto, T. Yamamoto, H. Minami, K. Yamaki, K. Delfanzari, K. Deguchi, N. Orita, T. Koike, R. Nakayama, T. Kitamura, M. Sawamura, S. Hagino, K. Ishida, K. Ivancovic, H. Asai, M. Tachiki, R. A. Klemm, and K. Kadowaki, High temperature superconductor terahertz emitters: Fundamental physics and its applications, Jpn. J. Appl. Phys. **51**, 010113 (2012).

[17] D. Y. An *et al.*, Terahertz emission and detection both based on high-T_c superconductors: Towards an integrated receiver, Appl. Phys. Lett. **102**, 092601 (2013).

[18] T. M. Benseman, A. E. Koshelev, W.-K. Kwok, U. Welp, V. K. Vlasko Vlasov, K. Kadowaki, H. Minami, and C. Watanabe, Direct imaging of hot spots in $Bi_2Sr_2CaCu_2O_{8+\delta}$ mesa terahertz sources, J. Appl. Phys. **113**, 133902 (2013).

[19] T. M. Benseman, K. E. Gray, A. E. Koshelev, W.-K. Kwok, U. Welp, H. Minami, K. Kadowaki, and T. Yamamoto, Powerful terahertz emission from $Bi_2Sr_2CaCu_2O_{8+\delta}$ mesa arrays, Appl. Phys. Lett. **103**, 022602 (2013).

[20] S. Sekimoto, C. Watanabe, H. Minami, T. Yamamoto, T. Kashiwagi, R. A. Klemm, and K. Kadowaki, Continuous 30 μW terahertz source by a high-T_c superconductor mesa structure, Appl. Phys. Lett. **103**, 182601 (2013).

[21] F. Turkoglu, L. Ozyuzer, H. Koseoglu, Y. Demirhan, S. Preu, S. Malzer, Y. Simsek, H. B. Wang, and P. Müller, Emission of the THz waves from large area mesas of superconducting $Bi_2Sr_2CaCu_2O_8$ by the injection of spin polarized current, Physica (Amsterdam) **491C**, 7 (2013).

[22] H. Minami, C. Watanabe, K. Sato, S. Sekimoto, T. Yamamoto, T. Kashiwagi, R. A. Klemm, and K. Kadowaki, Local SiC photoluminescence evidence of hot spot formation and sub-THz coherent emission from a rectangular $Bi_2Sr_2CaCu_2O_{8+\delta}$ mesa, Phys. Rev. B **89**, 054503 (2014).

[23] C. Watanabe, H. Minami, T. Yamamoto, T. Kashiwagi, R. A. Klemm, and K. Kadowaki, Spectral investigation of hot spot and cavity resonance effects on the terahertz radiation from high-T_c superconducting $Bi_2Sr_2CaCu_2O_{8+\delta}$ mesas, J. Phys. Condens. Matter **26**, 172201 (2014).

[24] M. Ji, J. Yuan, B. Gross, F. Rudau, D. Y. An, M. Y. Li, X. J. Zhou, Y. Huang, H. C. Sun, Q. Zhu, J. Li, N. Kinev, T. Hatano, V. P. Koshelets, D. Koelle, R. Kleiner, W. W. Xu, B. B. Jin, H. B. Wang, and P. H. Wu, $Bi_2Sr_2CaCu_2O_8$ intrinsic Josephson junction stacks with improved cooling: Coherent emission above 1 THz, Appl. Phys. Lett. **105**, 122602 (2014).

[25] M. Tsujimoto, H. Kambara, Y. Maeda, Y. Yoshioka, Y. Nakagawa, and I. Kakeya, Dynamic Control of Temperature Distributions in Stacks of Intrinsic Josephson Junctions in $Bi_2Sr_2CaCu_2O_{8+\delta}$ for Intense Terahertz Radiation, Phys. Rev. Applied **2**, 044016 (2014).

[26] C. Watanabe, H. Minami, T. Kitamura, K. Asanuma, K. Nakade, T. Yasui, Y. Saiwai, Y. Shibano, T. Yamamoto, T. Kashiwagi, R. A. Klemm, and K. Kadowaki, Influence of the local heating position on the terahertz emission power from high-T_c superconducting $Bi_2Sr_2CaCu_2O_{8+\delta}$ mesas, Appl. Phys. Lett. **106**, 042603 (2015).

[27] X. J. Zhou, J. Yuan, H. Wu, Z. S. Gao, M. Ji, D. Y. An, Y. Huang, F. Rudau, R. Wieland, B. Gross, N. Kinev, J. Li, A. Ishii, T. Hatano, V. P. Koshelets, D. Koelle, R. Kleiner, H. B. Wang, and P. H. Wu, Tuning the Terahertz Emission Power of an Intrinsic Josephson-Junction Stack with a Focused Laser Beam, Phys. Rev. Applied **3**, 044012 (2015).

[28] X. J. Zhou, Q. Zhu, M. Ji, D. Y. An, L. Y. Hao, H. Sun, S. Ishida, F. Rudau, R. Wieland, J. Li, D. Koelle, H. Eisaki, Y. Yoshida, T. Hatano, R. Kleiner, H. B. Wang, and P. H. Wu, Three-terminal stand-alone superconducting terahertz emitter, Appl. Phys. Lett. **107**, 122602 (2015).

[29] L. Y. Hao *et al.*, Compact Superconducting Terahertz Source Operating in Liquid Nitrogen, Phys. Rev. Applied **3**, 024006 (2015).

[30] B. Gross, F. Rudau, N. Kinev, M. Tsujimoto, J. Yuan, Y. Huang, M. Ji, X. J. Zhou, D. Y. An, A. Ishii, P. H. Wu, T. Hatano, D. Koelle, H. B. Wang, V. P. Koshelets, and R.

Kleiner, Electrothermal behavior and terahertz emission properties of a planar array of two $Bi_2Sr_2CaCu_2O_{8+\delta}$ intrinsic Josephson junction stacks, Supercond. Sci. Technol. **28**, 055004 (2015).

[31] I. Kakeya, N Hirayama, Y. Omukai, and M. Suzuki, Temperature dependence of terahertz emission by an asymmetric intrinsic Josephson junction device, J. Appl. Phys. **117**, 043914 (2015).

[32] T. Kashiwagi, T. Yamamoto, T. Kitamura, K. Asanuma, C. Watanabe, K. Nakade, T. Yasui, Y. Saiwai, Y. Shibano, H. Kubo, K. Sakamoto, T. Katsuragawa, M. Tsujimoto, K. Delfanazari, R. Yoshizaki, H. Minami, R. A. Klemm, and K. Kadowaki, Generation of electromagnetic waves from 0.3 to 1.6 terahertz with a high-T_c superconducting $Bi_2Sr_2CaCu_2O_{8+\delta}$ intrinsic Josephson junction emitter, Appl. Phys. Lett. **106**, 092601 (2015).

[33] T. Kashiwagi, K. Sakamoto, H. Kubo, Y. Shibano, T. Enomoto, T. Kitamura, K. Asanuma, T. Yasui, C. Watanabe, K. Nakade, Y. Saiwai, T. Katsuragawa, M. Tsujimoto, R. Yoshizaki, T. Yamamoto, H. Minami, R. A. Klemm, and K. Kadowaki, A high-T_c intrinsic Josephson junction emitter tunable from 0.5 to 2.4 terahertz, Appl. Phys. Lett. **107**, 082601 (2015).

[34] T. M. Benseman, A. E. Koshelev, V. Vlasko-Vlasov, Y. Hao, W.-K. Kwok, U. Welp, C. Keiser, B. Gross, M. Lange, D. Kölle, R. Kleiner, H. Minami, C. Watanabe, and K. Kadowaki, Current Filamentation in Large $Bi_2Sr_2CaCu_2O_{8+\delta}$ Mesa Devices Observed via Luminescent and Scanning Laser Thermal Microscopy, Phys. Rev. Applied **3**, 044017 (2015).

[35] M. Tsujimoto, I. Kakeya, T. Kashiwagi, H. Minami, and K. Kadowaki, Cavity mode identification for coherent terahertz emission from high-T_c superconductors, Opt. Express **24**, 4591 (2016).

[36] L. N. Bulaevskii and A. E. Koshelev, Radiation Due to Josephson Oscillations in Layered Superconductors, Phys. Rev. Lett. **99**, 057002 (2007).

[37] A. E Koshelev and L. N. Bulaevskii, Resonant electromagnetic emission from intrinsic Josephson-junction stacks with laterally modulated Josephson critical current, Phys. Rev. B **77**, 014530 (2008).

[38] S. Z. Lin and X. Hu, Possible Dynamic States in Inductively Coupled Intrinsic Josephson Junctions of Layered High-T_c Superconductors, Phys. Rev. Lett. **100**, 247006 (2008).

[39] V. M. Krasnov, Nonlinear Nonequilibrium Quasiparticle Relaxation in Josephson Junctions, Phys. Rev. Lett. **103**, 227002 (2009).

[40] R. A. Klemm and K. Kadowaki, Output from a Josephson stimulated terahertz amplified radiation emitter, J. Phys. Condens. Matter **22**, 375701 (2010).

[41] M. Tachiki, S. Fukuya, and T. Koyama, Mechanism of Terahertz Electromagnetic Wave Emission from Intrinsic Josephson Junctions, Phys. Rev. Lett. **102**, 127002 (2009).

[42] N. F. Pedersen and S. Madsen, THz generation using fluxon dynamics in high temperature superconductors, IEEE Trans. Appl. Supercond. **19**, 726 (2009).

[43] X. Hu and S. Z. Lin, Cavity phenomena in mesas of cuprate high-T_c superconductors under voltage bias, Phys. Rev. B **80**, 064516 (2009).

[44] T. Koyama, H. Matsumoto, M. Machida, and K. Kadowaki, In-phase electrodynamics and terahertz wave emission in extended intrinsic Josephson junctions, Phys. Rev. B **79**, 104522 (2009).

[45] V. M. Krasnov, Coherent flux-flow emission from stacked Josephson junctions: Nonlocal radiative boundary conditions and the role of geometrical resonances, Phys. Rev. B **82**, 134524 (2010).

[46] A. E. Koshelev, Stability of dynamic coherent states in intrinsic Josephson-junction stacks near internal cavity resonance, Phys. Rev. B **82**, 174512 (2010).

[47] S. Z. Lin and X. Hu, Response and amplification of terahertz electromagnetic waves in intrinsic Josephson junctions of layered high-T_c superconductor, Phys. Rev. B **82**, 020504 (2010).

[48] S. O. Katterwe, A. Rydh, H. Motzkau, A. B. Kulakov, and V. M. Krasnov, Superluminal geometrical resonances observed in $Bi_2Sr_2CaCu_2O_{8+x}$ intrinsic Josephson junctions, Phys. Rev. B **82**, 024517 (2010).

[49] A. A. Yurgens, Temperature distribution in a large $Bi_2Sr_2CaCu_2O_{8+\delta}$ mesa, Phys. Rev. B **83**, 184501 (2011).

[50] T. Koyama, H. Matsumoto, M. Machida, and Y. Ota, Multiscale simulation for terahertz wave emission from the intrinsic Josephson junctions, Supercond. Sci. Technol. **24**, 085007 (2011).

[51] V. M. Krasnov, Terahertz electromagnetic radiation from intrinsic Josephson junctions at zero magnetic field via breather-type self-oscillations, Phys. Rev. B **83**, 174517 (2011).

[52] A. Yurgens and L. N. Bulaevskii, Temperature distribution in a stack of intrinsic Josephson junctions with their CuO-plane electrodes oriented perpendicular to supporting substrate, Supercond. Sci. Technol. **24**, 015003 (2011).

[53] S. Z. Lin, X. Hu, and L. N. Bulaevskii, Synchronization in a one-dimensional array of point Josephson junctions coupled to a common load, Phys. Rev. B **84**, 104501 (2011).

[54] B. Gross, S. Guénon, J. Yuan, M. Y. Li, J. Li, A. Ishii, R. G. Mints, T. Hatano, P. H. Wu, D. Koelle, H. B. Wang, and R. Kleiner, Hot-spot formation in stacks of intrinsic Josephson junctions in $Bi_2Sr_2CaCu_2O_8$, Phys. Rev. B **86**, 094524 (2012).

[55] H. Asai, M. Tachiki, and K. Kadowaki, Three-dimensional numerical analysis of terahertz radiation emitted from intrinsic Josephson junctions with hot spots, Phys. Rev. B **85**, 064521 (2012).

[56] H. Asai, M. Tachiki, and K. Kadowaki, Proposal of terahertz patch antenna fed by intrinsic Josephson junctions, Appl. Phys. Lett. **101**, 112602 (2012).

[57] Y. X. Zhang, Y. C. Zhou, L. Dong, and S. G. Liu, Coherent terahertz radiation from high-harmonic component of modulated free-electron beam in a tapered two-asymmetric grating structure, Appl. Phys. Lett. **101**, 123503 (2012).

[58] S. Z. Lin and X. Hu, In-plane dissipation as a possible synchronization mechanism for terahertz radiation from intrinsic Josephson junctions of layered superconductors, Phys. Rev. B **86**, 054506 (2012).

[59] A. Grib and P. Seidel, The influence of standing waves on synchronization and self-heating of Josephson junctions in resonant systems, Low Temp. Phys. **38**, 321 (2012).

[60] B. Gross, J. Yuan, D. Y. An, M. Y. Li, N. Kinev, X. J. Zhou, M. Ji, Y. Huang, T. Hatano, R. G. Mints, V. P. Koshelets, P. H. Wu, H. B. Wang, D. Koelle, and R. Kleiner, Modeling the linewidth dependence of coherent terahertz emission from intrinsic Josephson junction stacks in the hot-spot regime, Phys. Rev. B **88**, 014524 (2013).

[61] F. Liu, S. Z. Lin, and X. Hu, Cavity phenomenon and terahertz radiation of a tall stack of intrinsic Josephson junctions wrapped by a dielectric material, Supercond. Sci. Technol. **26**, 025003 (2013).

[62] H. Asai and S. Kawabata, An effect of temperature distribution on terahertz phase dynamics in intrinsic Josephson junctions, Physica (Amsterdam) **494C**, 121 (2013).

[63] H. Asai and S. Kawabata, Intense terahertz emission from intrinsic Josephson junctions by external heat control, Appl. Phys. Lett. **104**, 112601 (2014).

[64] A. Grib and P. Seidel, The influence of external separate heating on the synchronization of Josephson junctions, Phys. Status Solidi (b) **251**, 1040 (2014).

[65] S. Z. Lin, Mutual synchronization of two stacks of intrinsic Josephson junctions in cuprate superconductors, J. Appl. Phys. **115**, 173901 (2014).

[66] F. Rudau, M. Tsujimoto, B. Gross, T. E. Judd, R. Wieland, E. Goldobin, N. Kinev, J. Yuan, Y. Huang, M. Ji, X. J. Zhou, D. Y. An, A. Ishii, R. G. Mints, P. H. Wu, T. Hatano, H. B. Wang, V. P. Koshelets, D. Koelle, and R. Kleiner, Thermal and electromagnetic properties of $Bi_2Sr_2CaCu_2O_8$ intrinsic Josephson junction stacks studied via one-dimensional coupled sine-Gordon equations, Phys. Rev. B **91**, 104513 (2015).

[67] U. Welp, K. Kadowaki, and R. Kleiner, Superconducting emitters of THz radiation, Nat. Photonics **7**, 702 (2013).

[68] T. Kitamura, T. Kashiwagi, T. Yamamoto, M. Tsujimoto, C. Watanabe, K. Ishida, S. Sekimoto, K. Asanuma, T. Yasui, K. Nakade, Y. Shibano, Y. Saiwai, H. Minami, R. A. Klemm, and K. Kadowaki, Broadly tunable, high-power terahertz radiation up to 73 K from a stand-alone $Bi_2Sr_2CaCu_2O_{8+\delta}$ mesa, Appl. Phys. Lett. **105**, 202603 (2014).

[69] A. Vl. Gurevich and R. G. Mints, Self-heating in normal metals and superconductors, Rev. Mod. Phys. **59**, 941 (1987).

[70] E. Spenke, Zur technischen Beherrschung des Wärmedurchschlages von Heissleitern, Wiss. Veröffentl. Siemens-Werken **15**, 92 (1936).

[71] Note that for $M = 20$ and the relatively low number of grid points along x and y, we cannot resolve modes that fluctuate strongly in space, like antiphase oscillations of different junctions or static triangular fluxon lattices appearing in magnetic fields on the order of a flux quantum per junction. However, we are mainly interested in dynamic in-phase solutions which can be captured well with the discretization used.

[72] A perhaps more natural choice is to look at the time average $\langle E_z^2(x,y)\rangle$ of the square of the z-axis electric fields. However, $E_z(x,y,z,t)$ has a large dc component, and features of oscillating standing waves are only weakly visible.

[73] K. Yamaki, M. Tsujimoto, T. Yamamoto, H. Minami, and K. Kadowaki, Magnetic field effects on THz radiation from rectangular shape Bi2212 IJJs, Physica (Amsterdam) **470C**, S804 (2010).

Publication 3

IOP Publishing Superconductor Science and Technology
Supercond. Sci. Technol. **28** (2015) 055004 (10pp) doi:10.1088/0953-2048/28/5/055004

Electrothermal behavior and terahertz emission properties of a planar array of two $Bi_2Sr_2CaCu_2O_{8+\delta}$ intrinsic Josephson junction stacks

B Gross[1], F Rudau[1], N Kinev[2], M Tsujimoto[1,3], J Yuan[4], Y Huang[4,5], M Ji[4,5], X J Zhou[4,5], D Y An[5], A Ishii[4], P H Wu[5], T Hatano[4], D Koelle[1], H B Wang[4,5], V P Koshelets[2] and R Kleiner[1]

[1] Physikalisches Institut—Experimentalphysik II and Center for Collective Quantum Phenomena in LISA$^+$, Universität Tübingen, Auf der Morgenstelle 14, D-72076 Tübingen, Germany
[2] Kotel'nikov Institute of Radio Engineering and Electronics, Moscow, Russia
[3] Kyoto University, Kyoto, Japan
[4] National Institute for Materials Science, Tsukuba 3050047, Japan
[5] Research Institute of Superconductor Electronics, Nanjing University, Nanjing 210093, People's Republic of China

E-mail: borisgross@arcor.de

Received 30 November 2014, revised 11 February 2015
Accepted for publication 22 February 2015
Published 19 March 2015

Abstract

We report on the investigation of the electrothermal behavior and the terahertz (THz) emission properties of two nearby $Bi_2Sr_2CaCu_2O_{8+\delta}$ (BSCCO) intrinsic Josephson junction stacks, using a combination of electric transport and THz emission measurements plus low temperature scanning laser microscopy. We start with a compact BSCCO stack (placed in a z-shaped structure between two BSCCO electrodes) with lateral dimensions of $330 \times 60\ \mu m^2$ and $0.7\ \mu m$ height, consisting of about 480 junctions. After characterization, a 200 nm wide slit was introduced by focused ion beam milling, splitting the stack into two halves connected by continuous superconducting electrodes. In a third step, the upper electrode was also split, leading to a structure where the two stacks can be biased separately. In all configurations hot-spot formation was observed. Despite the separation into two stacks only a single hot spot formed, which, depending on the bias condition, could either be located in one of the stacks or extend into both stacks with its center in the slit. In none of the structures it was possible to achieve mutual synchronization of the two stacks, indicating that additional synchronizing elements or the presence of a base crystal as for mesa structures may be necessary for the operation of parallel array structures.

Keywords: intrinsic Josephson junction, terahertz, high temperature superconductor

(Some figures may appear in colour only in the online journal)

1. Introduction

Josephson junctions are attractive sources of radiation because of the fact that the emitted frequency f_e is tunable by an applied dc voltage V, following the relation $f_e = V/\Phi_0$, where $\Phi_0 = 2.07 \times 10^{-15}$ Wb is the flux quantum. One obtains an emission frequency of 483.6 GHz per mV of applied voltage. There are, however, several drawbacks. A single junction delivers only very little power, usually well below 1 nW. Also, a typical junction has a low impedance and is not well matched to the environment. Using conventional superconductors such as Nb these problems have been

overcome by using 1D or 2D arrays of Josephson junctions oscillating coherently, see e.g. [1–3]. Ideally the emission power increases quadratically with the junction number.

In 2007 it has been shown that intrinsic Josephson junctions (IJJs) [4] in the high temperature superconductor $Bi_2Sr_2CaCu_2O_{8+\delta}$ (BSCCO) can emit coherent radiation at THz frequencies [5]. Here, stacks of hundreds of IJJs have been patterned as a mesa structure on the surface of a BSCCO single crystal. A typical mesa has a length of ∼300 μm, a width around 30–80 μm and a thickness of about 1 μm, corresponding to a serial array of about 670 IJJs. Although the power emitted into free space was below 1 μW in these initial experiments, it triggered numerous experimental [6–27] and theoretical [28–49] investigations; for recent reviews, see [17, 50, 51]. IJJ stacks have been realized as mesa structures, a pedestal standing on top of a base crystal, but also as more sophisticated structures like bare IJJ stacks contacted by Au layers [17, 19, 23] and as all-superconducting z-shaped structures [12]. For the best stacks, emission powers in the range of tens of μW have been achieved [19, 20, 23].

Due to their poor thermal conductivity IJJ stacks are subject to enormous self-heating [5–7, 10, 16, 20, 22, 25, 39, 44–46], causing the formation of hot spots, i.e. regions heated to temperatures above the superconducting transition temperature T_c. Hot-spot formation in IJJ stacks has been imaged by low temperature scanning laser microscopy (LTSLM) [6, 8, 10], by thermoluminescence [20, 22, 25] and has been analyzed theoretically using heat-diffusion equations [39, 40, 44, 45]. There is still some debate to what extent the presence of a hot-spot is helpful or not for THz emission [25, 27]. For example, in its presence the linewidth of radiation is much lower than in its absence [13, 24]. On the other hand Joule heating limits the maximum voltage V per junction that can be achieved. At low bias currents (low-bias regime) the voltage across the IJJ stack increases with increasing current. For large enough currents the self-heating leads to a decrease in the c-axis resistance and finally a back-bending of the current–voltage characteristic (IVC). In this regime of negative differential resistance (high-bias regime) hot-spot formation occurs in a similar way as it also has been observed in other conductors having a negative temperature coefficient of their resistance [52]. For a stack consisting of $N \sim 1000$ IJJs one typically obtains a maximum voltage per junction V_{max} of about 1.5–2 mV, limiting the emission frequency to values below 1 THz. If one would increase N to much larger numbers, V_{max} would decrease further, making IJJ stacks inattractive for THz emission.

Although proposals [40] and experimental attempts [53] have been made to provide better cooling, the best way to increase the emission power while keeping V_{max} reasonably large is to use planar arrays of IJJ stacks [21, 27, 47, 54]. Recently, arrays of 8 parallel mesas have been realized [21]. It was possible to synchronize up to three stacks of the array and achieve an output power of 0.61 mW at an emission frequency of 0.51 THz. Evidence for synchronized emission in this work and in [54] was provided by the scaling of the emission power with the square of the junction number. On the other hand, the strong heating evident in these samples may have affected the radiation impedance of each stack, making statements about a scaling with the junction number difficult. In addition it is important to find out more details about the mechanism of synchronization, e.g., whether it is purely electromagnetic in origin, or caused (or assisted) by thermal currents.

To address such issues we have investigated the electrothermal behavior and the emission properties of the simplest possible array—two stacks in parallel. We have chosen all-superconducting z-structures which, on the one hand are easy to manipulate and, on the other hand have the potential for integrating a large number of stacks [55].

For our investigation we started with a IJJ stack in a z-shaped BSCCO structure. After characterization, using focused ion beam (FIB) milling we cut a slit into the stack splitting it into two halves, which were still connected in parallel by continuous electrodes. Having characterized this geometry we cut the upper electrode via FIB.

The reminder of this paper is organized as follows. In section 2 we describe the fabrication process and the measurement techniques. Section 3.1 presents and analyses data for the sample before FIB milling, and in sections 3.2 and 3.3 results are presented for the sample after the first and the second milling process, respectively. We discuss the results in section 4 and conclude with section 5.

2. Samples and measurement techniques

The IJJ stack we study has been fabricated using a double-sided technique as described in [12]. In brief, a 30 nm thick gold layer was deposited on a freshly cleaved, slightly underdoped BSCCO single crystal, which has been glued to a substrate with epoxy prior to this. The superconducting transition temperature of the crystal is $T_c = 87$ K. A pre-structure was patterned into the surface with optical lithography and argon ion milling. Subsequently, the structure was turned upside down and glued to a second substrate. The first substrate was removed and the BSCCO surface was cleaved until the desired thickness of the remaining crystal was reached. Now the final structure of the IJJ stack was patterned into the crystal and covered by a protecting gold layer of 30 nm.

In contrast to mesas standing on top of a base crystal, the electrodes connecting the stack are superconducting, allowing real four-terminal measurements. The electrodes typically have a thickness of less than 1 μm. The stack we investigate is designed in an overlap geometry as sketched in figures 1(a) and (b). The stack has dimensions of $330 \times 60 \times 0.7$ μm^3 and consists of about 480 IJJs. After performing electric transport, LTSLM and THz detection measurements (for details, see below), the sample was modified in an additional patterning step. Using FIB milling the IJJ stack was cut into two halves of almost equal size, separated by a slit of around 200 nm in width, cf figure 1. The two stacks still share the same superconducting electrodes and are connected in parallel. Thus, this sample can be understood as a very simple array structure, appropriate for studying generic features of arrays.

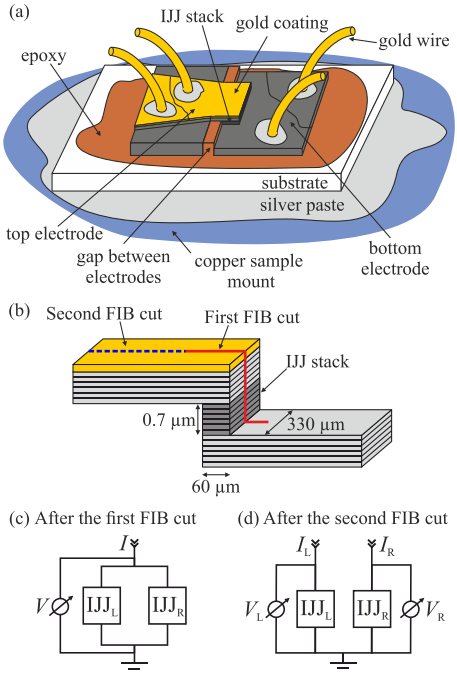

Figure 1. (a) Sketch of a BSCCO IJJ overlap structure fabricated with the double-sided technique. (b) The red and the dashed blue line indicate the two FIB cuts in an enlarged view of the overlap structure. The block diagrams show the electric biasing scheme of the IJJ stacks after (c) the first and (d) the second FIB milling step.

After investigating this configuration by electric transport, LTSLM and THz detection, the top electrode of the two stacks was separated in a second FIB milling step, making the bias currents of the stacks independent of each other.

The setup for LTSLM is described in [56]. In brief, the beam of a laser diode is focused and scanned across the sample surface. The induced local heating at position (x_0, y_0) of about $\Delta T \approx$ 2–3 K in an area A_L of a few μm^2 and a depth of about 0.5 μm leads to a voltage change $\Delta V(x_0, y_0)$ across the IJJ stack, which serves as contrast for the LTSLM image. In particular, the temperature distribution in the stack can be reconstructed from this signal, based on the impact of the local heating on the *c*-axis quasi-particle transport, see [44]. The signal is given by

$$\Delta V(x_0, y_0) \approx \frac{-IR_{\mathrm{eff}}^2 \Delta T A_L}{h} \frac{\mathrm{d}\sigma_c}{\mathrm{d}T}\Big(T(x_0, y_0)\Big). \qquad (1)$$

$R_{\mathrm{eff}} = V/I$ is the (ohmic) sample resistance at a given current I. $\mathrm{d}\sigma_c/\mathrm{d}T$ denotes the temperature derivative of the *c*-axis electrical conductivity and h is the sample thickness. For better comparability of LTSLM signals at different bias points we introduce a normalized voltage signal

$$\Delta V_{\mathrm{norm}} = \Delta V / \left(IR_{\mathrm{eff}}^2\right). \qquad (2)$$

The THz detection setup, allowing for bolometric detection and for Fourier spectrometry, is described in detail in the supplement of [8]. The crystal is mounted in a continuous flow cryostat with a polyethylene window. The emitted radiation, chopped with a frequency of 80 Hz, is collected by a 90° of *f*-axis parabolic mirror (2″ diameter, focal length 10 cm) and deflected towards two lamellar split mirrors, which divide the incoming radiation into two beams with almost equal intensity. A phase difference is introduced by moving one of these mirrors with a translation stage. Via a second parabolic mirror the radiation is deflected to the bolometer. A 3 THz cut-off type filter is used in front of the bolometer. The frequency resolution, depending on the maximum mirror displacement, is 10–15 GHz. During the measurements of the data for the present paper we have improved the positioning unit for the IJJ stack. Therefore, the bolometric signal detected from the pristine stack is significantly smaller than for later measurements.

We also performed some measurements of THz radiation using a superconducting Nb/AlN/NbN integrated receiver (SIR) for detection, which is able to resolve the linewidth of the THz radiation [13]. The SIR comprises, on a single chip, a planar antenna combined with a superconductor-insulator-superconductor (SIS) mixer, a superconducting flux-flow oscillator (FFO) acting as local oscillator, and a SIS harmonic mixer for the FFO phase locking. The frequency of the local oscillator is continuously tunable from 350 to 750 GHz, while the SIS mixer is effectively matched to the planar antenna between 450 and 700 GHz, limiting the SIR operation range. A frequency resolution of the SIR well below 100 kHz has been confirmed [57].

3. Results

3.1. Pristine stack

We first discuss data, as taken from the pristine, i.e. uncut, stack.

3.1.1. Electric properties and THz emission. The black (red) graph in figure 2(a) shows the measured IVC for the pristine sample at a bath temperature of T_b = 42 K in the high (low) bias regime. Apart from the absence of a contact resistance the IVC is similar to the IVCs of comparably sized mesa structures, showing the typical back bending at high input power. The maximum voltage per junction V_{max} is about 1.4 mV and thus roughly the same as for mesa structures. In fact, because of the significantly thinner bottom electrode of this structure compared to a base crystal one might expect a better thermal coupling to the bath and a larger V_{max}. This is

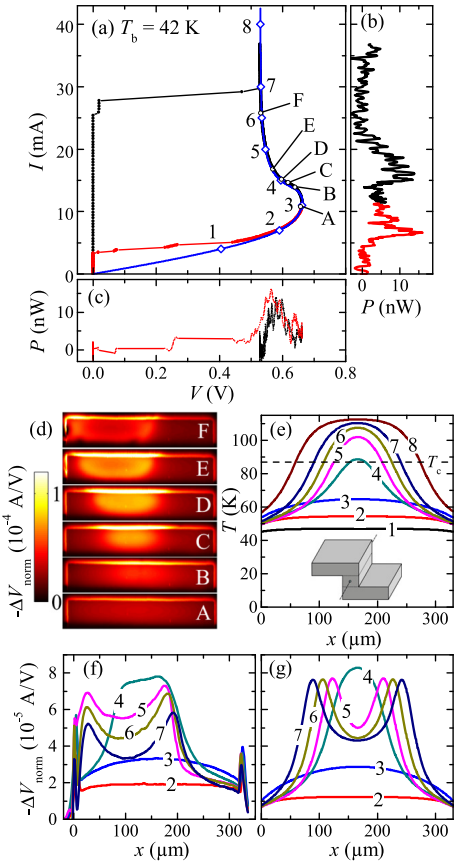

Figure 2. Data of the pristine overlap structure at T_b = 42 K. (a) Measured (black—high bias, red—low bias) and simulated (blue) IVCs. Detected radiation signal versus (b) current and (c) voltage, color code as in (a). (d) LTSLM images recorded for the bias points A–F marked in (a). (e) Simulated $T(x)$-profiles along the line indicated in the inset for the bias points 1–8 marked in (a). Measured (f) and simulated (g) LTSLM voltage responses for the same linescan and bias points as the $T(x)$-profiles in (e).

not observed, indicating that the glue layer is the bottleneck for the thermal coupling to the bath.

Figures 2(b) and (c) display the bolometric radiation signal depending on (b) the current through and (c) the voltage across the stack. Since the sample was somewhat out of focus the overall signal is comparatively small. Still, one clearly observes that there are relatively broad emission peaks both in the high- and low-bias region. Plotted as a function of voltage these peaks nearly coincide, cf figure 2(c). For the low-bias emission power peak at around V = 565 mV our THz spectrometer showed an emission frequency f_e = 562 GHz. In the high-bias regime, the emission power peaks around 580 mV with f_e = 577 GHz. For both peaks the Josephson relation gives a junction number $N \approx 487$, indicating that basically all junctions in the stack participate in radiation.

3.1.2. Electrothermal properties. Figure 2(d) shows a series of LTSLM images taken at bias points A–F in figure 2(a). At bias point A only a smooth voltage response is seen which becomes peaked in images B and C, indicating that a hot spot has formed near the center of the stack. With increasing bias current the hot spot moves towards the left and grows in size, cf images D, E and F. This behavior is somewhat different from hot-spot formation in mesa structures. Mesas are typically electrically contacted with a wire attached to the the mesa surface by silver paste. The hot spot forms near the contact point, although it prefers, in principle, the point of worst cooling [44]. For the double-sided structure there is no contacting wire and thus, not surprizingly, the hot spot initially forms near the center of the stack.

To model the IVC and the temperature distribution in the stack we solved the nonlinear heat diffusion equation with finite element analysis as in [44], accounting as good as possible for the real geometry and the electrical and thermal parameters of the materials involved. The thickness of the electrodes was taken to be 0.8 μm, the gap between top and bottom electrode was 20 μm, the thickness of the glue layer 20 μm and the gold layer 30 nm, respectively. The current was injected through the large surface of the upper electrode by defining a corresponding boundary condition. Equally, the ground is defined on the bottom electrode. The calculated IVC is shown by the blue curve in figure 2(a). For this curve the subgap c-axis resistivity $\rho_c(T)$ of BSCCO below T_c, which eludes experimental access in our case, has been adjusted until measured and simulated IVC showed a good agreement. For all other simulated curves shown below this $\rho_c(T)$ has been used without further modification. Figure 2(e) shows the simulated $T(x)$-profiles along the line indicated in the inset for the bias points labelled 1–8 in figure 2(a). While for bias points 1–3 only a smooth temperature distribution is seen, at point 4 a hot spot has formed, which grows in size and increases in temperature with increasing bias current, reaching peak temperatures well above T_c.

To compare experiment and simulation we first show experimental linescans of the LTSLM response in figure 2(f), for the bias points 2–7 in figure 2(a). The linescans are taken along the center of the stack, see the line in the inset of figure 2(e). While the linescans 2 and 3 are relatively smooth, for the bias points 4–7 they show the characteristic double-peak structure which is observed in the presence of hot spots. The LTSLM response is given by equation (1), i.e. it only indirectly yields the temperature distribution in the stack. To compare this with theory, rather than inverting the experimental curves to obtain $T(x)$ we have used the calculated temperature profiles of figure 2(e) to calculate the normalized LTSLM response from equation (2). The result is shown in figure 2(g). The measured response is reproduced well, except

for the drift of the hot spot to the left. This drift is presumably due to local inhomogeneities arising e.g. from a varying thickness of the glue layer, which is not incorporated in the simulations. We also observe that the LTSLM response is stronger at the sample edges. This originates in the absence of the protecting gold layer, a side effect of the fabrication process, leading to increased heating by the laser. The characteristic double-hump feature of the hot spot stems from the presence of a maximum in $d\sigma_c/dT\,(T)$ close to $T = T_c$, reducing the response signal for temperatures above T_c. Also note, that the normalization by IR_{eff}^2 seems not to fully compensate a signal reduction for increasing input power, compare linescans 5–7 with the simulated equivalents.

3.2. Two parallel stacks

We now study the overlap structure after adding the slit, as shown in figures 1(b) and (c).

3.2.1. Electric properties and THz emission. Figure 3(a) shows by black (low-bias regime), red (region of negative differential resistance) and blue (region of positive differential resistance at high bias) curves the IVC of the double stack for T_b = 42 K and voltages between 0.45 and 0.7 V, in comparison with the IVC of the pristine overlap structure (dark green and orange symbols, denoting low- and high-bias region, respectively). The inset of figure 3(a) shows the IVCs of the pristine and cut sample on a wider voltage scale. One notes that in comparison to the pristine stack, the backbending between 10 and 25 mA of the resistive branch became stronger. Further, the IVC now has positive differential resistance above 25 mA in contrast to negative differential resistance before. Quite surprisingly, as a new feature a hysteresis appears for currents between 38 and 45 mA. The detected radiation signal for the cut sample is shown in figure 3(c) versus current and (e) versus voltage, in comparison with the radiation signal detected for the pristine sample, cf figures 3(b) and (d). As before milling, the sample shows emission both for low bias currents and in the hot spot nucleation regime, with emission frequencies between 596 and 506 GHz, i.e. at comparable frequencies as in the pristine case. In addition, for high bias currents (between 30 and 40 mA) emission peaks appear which did not exist before with frequencies of about 550 GHz. Likely, the origin of these new emission peaks is the positive differential resistance occuring in this regime, which directs the IVC to the voltage range that allowed for strong THz emission at lower currents. As we will see below, in this part of the IVC one of the stacks is at a temperature above T_c, while the other stack is still superconducting, although at a (inhomogeneous) temperature which is significantly above T_b. All of the determined frequencies, indicated by numbers in GHz in figures 3(b) and (c), obey the Josephson relation $f_e = V/(N\Phi_0)$, with $N \approx 481$ within measurement accuracy.

In the interferometer measurements the linewidth is resolution limited to around 15 GHz and always one single emission line is detected. It is not resolved, if both stacks emit coherently at the same frequency, if they emit slightly detuned

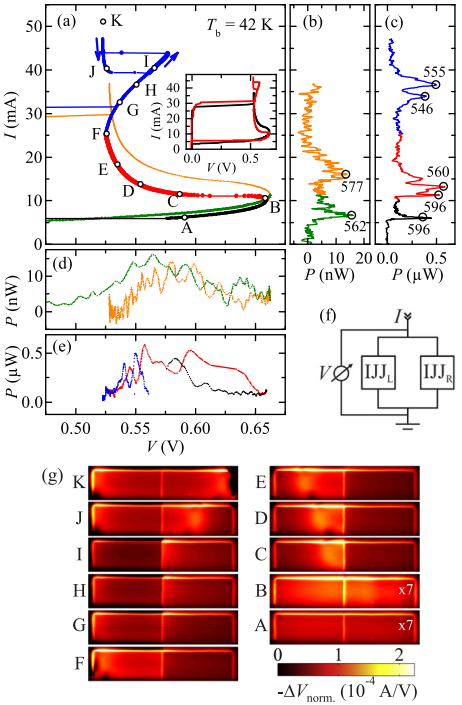

Figure 3. Comparison of data before and after FIB milling for T_b = 42 K: (a) IVCs on different voltage scales. Detected radiation signal versus (b), (c) current and (d), (e) voltage. In (a) the low- and the high-bias regimes of the pristine stack are indicated by dark green and orange colors, respectively. For the IVC of the stack after FIB milling the low-bias regime is indicated by black symbols. Red symbols indicate the region of negative differential resistance and blue symbols the region of positive differential resistance at high bias. Graphs (b) and (d) are for the pristine stack, (c) and (e) for the stack after FIB milling, using the same color code as in (a). Numbers in (b) and (c) are measured radiation frequencies in GHz. In (f) the equivalent electric circuit is depicted schematically. (g) LTSLM images for the stack after FIB milling, taken at bias points A–K indicated in (a). For a better comparison, the signals in the images A and B were multiplied by a factor of 7.

within the resolution, or if only one stack emits. To resolve this, we also performed some linewidth measurements at T_b = 42 K with the SIR. Similar measurements on mesa structures are described in [13]. For all SIR measurements on the overlap structure with two stacks in parallel two frequency lines were observed in the low-bias regime as well as in the back-bending regime. The observed separation between the two emission lines ranged from some ten MHz to several GHz. The linewidth of radiation varied in the low-bias regime between 162 and 568 MHz and in the back-bending regime between 43 and 271 MHz. The smaller values of Δf in the presence of a hot spot are compatible with the measurements

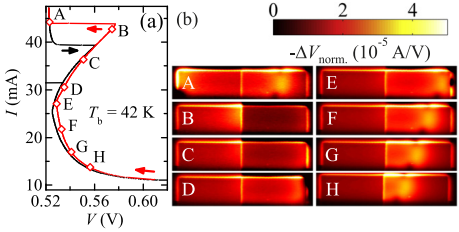

Figure 4. Data after FIB milling at T_b = 42 K (a) IVC for normal (black) and reverse (red) hot-spot formation. (b) LTSLM images for the bias points indicated in (a).

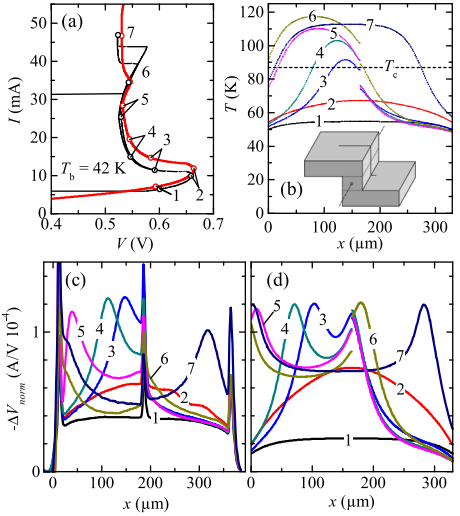

Figure 5. (a) Measured (black) and simulated (red) IVCs of the two parallel IJJ stacks at T_b = 42 K and (b) simulated $T(x)$-profiles taken along the line indicated in the inset, for the bias points labelled in (a). Experimental (c) and simulated (d) LTSLM voltage responses taken along the line indicated in (b).

in [13] for a standard mesa. Thus, the two stacks did not emit coherently and even worse, the frequency of oscillation was slightly different in the two stacks despite the fact that they were connected by continuous superconducting electrodes.

3.2.2. Electrothermal properties. To analyze the electro-thermal behavior we show in figure 3(g) LTSLM images for the bias points labelled A–K in figure 3(a). While in images A and B the LTSLM signal is almost homogeneous, in images C to F it is seen that hot-spot formation takes place in the left stack, rather than in the center, as for the pristine stack. The hot spot nucleates directly at the slit milled by FIB technique. With increasing current its center moves towards the center of the left stack and simultaneously grows in size until it eventually covers the complete left stack. In the regime of positive differential resistance in the IVC the hot spot starts to extend to the stack right of the slit (cf images G–I), however, only after a jump in the IVC it really covers a significant part of the right stack, as seen in image J. At bias point K both stacks seem to be completely occupied by the hot spot. In this state, i.e. for bias currents between images J and K no THz emission was observed.

We also note that, since the two stacks are almost equally sized, one might expect that the initial hot-spot formation can also occur in the right stack. Indeed we were able to realize this by keeping the bias current at around 11 mA, where dI/dV approaches almost zero and the system is quite unstable. By chance, one or the other configuration is realized, when the current is increased. The IVC follows a slightly different path in the reverse hot spot configuration. See figure 4(a) for the corresponding IVCs and (b) for the LTSLM images showing the reverse hot spot formation.

For a first understanding of the electro-thermal properties of the sample after FIB milling we note that with the slit the in-plane heat flow through the stack is interrupted. The situation resembles the discrete resistor model [44, 58, 59] where it has been found that, compared to a symmetric temperature distribution, one of the resistors can get hot while the other becomes colder. In our geometry the two stacks are spatially distributed, but the same mechanism should lead to a symmetry broken state. For a more quantitative analysis we solved the heat diffusion equation for the slit geometry, using the electrical and thermal parameters of the pristine stack. The slit in the simulations was 200 nm wide, not only separating the two stacks and the gold layer on top of them, but also fully extending into the bottom electrode. This accounts for the fact, that the FIB milling was carried out much longer than necessary, ensuring a complete division of the two stacks. The measured (black) and calculated (red) IVCs are shown in figure 5(a). Those are in qualitative agreement. However, it seems that the effect of heating is somewhat weaker in the simulated stack. Also, instead of the hysteretic region at high bias, the simulations yielded a kink slightly below 40 mA, rather than the hysteresis observed in the real sample. We note here that, for higher T_b, the hysteresis disappears in experiment and a kink similar as in the simulation is observed. Figure 5(b) shows the calculated temperature distribution for the points 1–7 on the simulated IVC. For point 1, taken in the low-bias region, there is only a weak temperature modulation and the overall temperature is only slightly above T_b. The situation is similar at bias point 2, where V is maximum, with a more elevated overall temperature. At higher currents the hot spot starts to form. Throughout the region of negative differential resistance the peak temperature of the hot spot increases, passing T_c near point 3 and reaching a value around 110 K at bias point 5. Note that the hot spot is basically confined to the left stack throughout this regime. In the regime of positive differential resistance, between points 5 and 6, the right hand tail of the hot spot notably starts to extend to the right stack and the

maximum temperature rises to more than 120 K (point 6). Above a current of 40 mA, where the voltage has decreased and the differential resistance is negative again, the hot spot has moved significantly to the right, now also occupying a big part of the right stack. We emphasize that the maximum hot-spot temperature has decreased by about 10 K, compare $T(x)$-profiles 6 and 7. Figures 5(c) and (d) compare experimental and calculated linescans of the LTSLM response for the points indicated in figure 5(a). For the comparison we have chosen the points such that the different regimes in the IVC, where the thermal behavior qualitatively changes, are covered. Note that for all points in the experimental curves there are strong edge signals that appear both near the slit and the sample edges. We will ignore them in the following discussion. Points 1 and 2 are taken in the low-bias regime and at the voltage maximum, respectively. Here, the LTSLM response is relatively smooth both in the theoretical and in the experimental curve. However, in the experimental curve at point 2 there are shallow wiggles in the right hand stack for $x > 200\,\mu$m. The wiggles arise from standing electromagnetic waves, as it has been addressed in previous publications [6, 8, 10]. The formation of the hot spot (bias point 3) and its growth (bias points 4 and 5), best seen by following the hump in the the left stack in the experimental data, is nicely reproduced by the simulation. Note, however, that in the theoretical curve both two humps are visible. In the experimental curve the right hand side hump is either obscured by the edge signal at the slit or the temperature jumps at the slit from a value well above T_c to a value well below T_c. At point 6 ΔV_{norm} in the left stack is relatively smooth due to the fact that here the temperature is basically above T_c everywhere. In the right stack there is an upturn of $-\Delta V_{\mathrm{norm}}$ near the slit indicating that also in this stack the temperature has reached T_c near its left edge. At point 7 this upturn has turned into a hump located close to the right side, i.e. also the temperature in the right stack is close to or above T_c.

3.3. Two independently biased stacks

In a second FIB milling step, the top electrode of the two stacks has been separated.

3.3.1. Electric properties and THz emission. The simplified equivalent circuit diagram is depicted in figure 1(d). The currents injected into the left stack, I_{L}, and into the right stack, I_{R}, can now be chosen independently, implying that the voltages across the two stacks can be adjusted arbitrarily. Due to the proximity of the stacks they will still interact thermally, and possibly there is also an interaction and synchronization of the Josephson currents due to electromagnetic coupling.

Figure 6(a) shows IVCs of the right stack for different currents through the left stack, which is always operated in its resistive state, except for $I_{\mathrm{L}} = 0$. The outermost branch (blue curve) in the graph corresponds to $I_{\mathrm{L}} = 0$. With increasing I_{L} the voltage across the right stack (V_{R}) decreases at given I_{R}, due to the fact that the Joule heating of the left stack also leads to a temperature rise in the right stack. Note that this

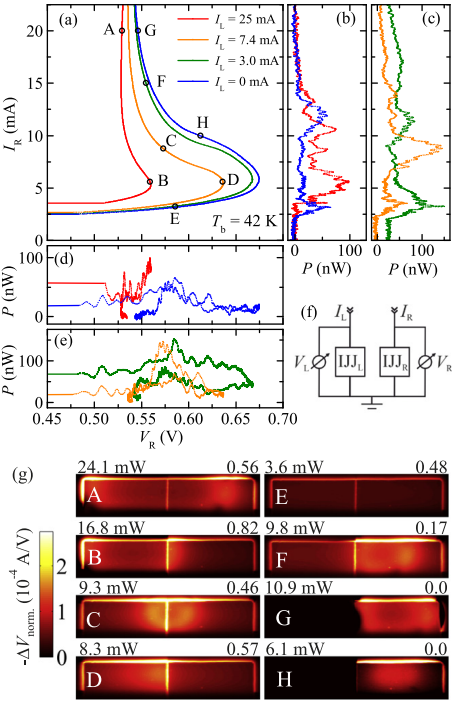

Figure 6. (a) IVC of the right stack for different currents through the left stack as indicated in the graph, while the left stack is in its resistive state (except for $I_{\mathrm{L}} = 0$). The corresponding emission signal versus current is shown in (b) and (c) and versus voltage in (d) and (e). (f) shows the equivalent electric circuit schematically. In (g) LTSLM images for the bias points indicated in (a) are shown. Values at top left of the images denote the total input power P_{DC} and at top right the current ratio $I_{\mathrm{L}}/(I_{\mathrm{L}} + I_{\mathrm{R}})$.

happens vice versa, and therefore the voltage across the left stack (V_{L}) is shifted when I_{R} is swept. The detected THz signal is shown versus I_{R} in figures 6(b) and (c) and versus V_{R} in figures 6(d) and (e). For the orange and green branch I_{L} has been chosen such that the maximum achievable emission for, respectively, high and low bias currents at this bath temperature was realized. The emission characteristics for $I_{\mathrm{L}} = 0$ resembles the behavior of the pristine stack, as two dominating emission peaks with similar voltage occur, one at low and one at high bias currents. Solely biasing the left stack leads to a similar picture. When increasing I_{L} both stacks may contribute to the emitted radiation, cf figures 6(c) and (e) for the emission power for $I_{\mathrm{L}} = 3$ mA (green) and 7.4 mA (orange).

For $I_{\mathrm{L}} = 3$ mA, the emission characteristics plotted versus I_{R} or V_{R} still look very similar as for the single stacks. However, the left stack contributes to the detected emission

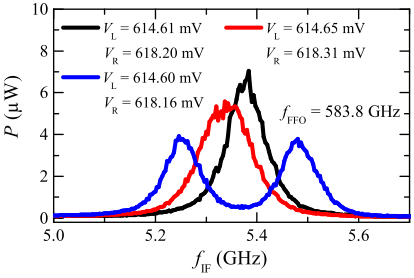

Figure 7. SIR spectra for different voltages of the two stacks. f_{FFO} is the frequency of the local oscillator.

signal, which is about 25 nW for $I_R = 0$ mA. Interestingly, this value is similar for high values of I_R, as e.g. 25 mA, where the right stack is essentially above T_c and does not contribute to the emission. However, for intermediate currents I_R and especially in the low-bias regime, both stacks contribute to the emission, leading to a quite broad low-bias emission peak with a maximum value of about 150 nW. This is roughly twice the value of the low-bias emission peak obtained for $I_L = 0$. This does not imply however, that the two stacks are synchronized (more arguments on this will be given below). Within the 15 GHz resolution of our Fourier spectrometer the emission frequency in the low-bias peak is 562 GHz and about the same as for the low-bias peaks of the left (right) stack for $I_R = 0$ ($I_L = 0$). Also, this is the same emission frequency for which the pristine stack had the maximum emission amplitude in the low-bias regime.

For $I_L = 7.4$ mA, i.e. in the high-bias regime of the left stack, where a hot spot is present, there is again one low-bias peak in $P(I_R)$ at a current and voltage position which is comparable to the case of $I_L = 0$. At $I_R = 8.8$ mA and V_R near 0.57 V a strong peak appears, which, in terms of I_R, seems to be unrelated to the peaks observed at lower values of I_L. Note, however, that the voltage position of the peak is comparable to the high-bias peak for $I_L = 0$. As we will see below, in the vicinity of this bias condition there is a hot spot which extends into both stacks and is centered in the slit between them. This may be a favorable condition for radiation.

Finally, for $I_L = 25$ mA, cf figures 6(b) and (d), the emission curves strongly differ from the $I_L = 0$ case, showing, as a function of I_R, a series of emission peaks between 5 mA and 15 mA. Here, the accessible voltage range and the sample temperatures differ significantly from the other branches, at least partly explaining this behavior.

To get more insight into the linewidth of radiation we also studied the sample after the second FIB cut using the SIR. It turned out, that the linewidth of the radiation has its minimum (approxmately 25 MHz) for T_b around 40 K, when biasing the sample in the negative differential regime, as has been observed for mesas [13]. Here, synchonization of the two stacks seems to be most promising. We tried to adjust the voltages of the stacks in this regime, while monitoring the spectra, to achieve a synchronized state. figure 7 shows typical spectra obtained for this procedure. The blue spectrum features two peaks, each coming from a different stack. A peak immediately moves in the spectrum, when the voltage of the corresponding stack is changed. For the red spectrum the two peaks already overlap strongly and seem to merge into one single peak for the black spectrum. The linewidth remains almost constant (80 MHz), when comparing the blue peaks with the black one. The sum of the amplitudes of the blue peaks, however, is more than 10% larger than the amplitude of the black peak. It seems that, at least in the present configuration, two separate stacks do not synchronize by itself without an additional mechanism. Unfortunately, the sample was destroyed before reaching the regime of the 25 MHz linewidth. However, we can state that for the configuration we studied here synchronization is at least very difficult, if not impossible.

3.3.2. Electrothermal properties. We continue with the electro-thermal behavior of the independently biased stacks. Figure 6(g) shows LTSLM images, taken at the bias points indicated by A–H in figure 6(a). The images reveal, that only *one* hot spot forms inside the two stacks, rather than two. This is a consequence of the strong thermal coupling between the two stacks due to their proximity. In other configurations, where the stacks are further apart, a hot spot forms in each stack [27]. This is an important aspect that has to be considered when designing array structures. From figure 6(g) one can also see that the hot-spot size and its position can be manipulated by adjusting the currents I_L and I_R. Roughly, one can state that a larger total input power P_{DC} increases the hot-spot size and its temperature, while the current ratio $I_L/(I_L + I_R)$ sets the position of the hot spot, similarly as in [10]. Figure 6(g) exemplarily shows some possible configurations. For $I_L = 0$ the hot spot is fully situated in the right stack, cf LTSLM images G and H. The left stack cannot provide a signal in this case. By increasing the current ratio the hot spot moves towards the left stack as shown by image F ($I_L = 3$ mA). For almost equal currents, cf image C, the hot spot is located at the center of the two stacks. By further increasing the current ratio the hot spot moves to the left stack, cf images D and B. For small P_{DC} no hot spot occurs (image E). It appears for increasing P_{DC}, cf images H and D, and occupies larger and larger areas of one (image B) or both stacks (image A). This shows, that the hot spot can be manipulated quite freely in such a structure.

Again, finite element simulations have been carried out, keeping all parameters as in the former calculations, only changing the geometry to account for the second FIB milling step. The overall electro-thermal behavior of the two independent stacks is confirmed. Figure 8(a) shows the simulated IVCs in comparison with the measured curves. Curve 1 (measured) and 2 (simulated), both for constant $I_L = 25$ mA, agree in shape, however, the simulated curve shows less pronounced heating and reaches higher voltages. The same is true for the curves with $I_L = 7.4$ and 3 mA. Although the match between simulated and measured IVCs is

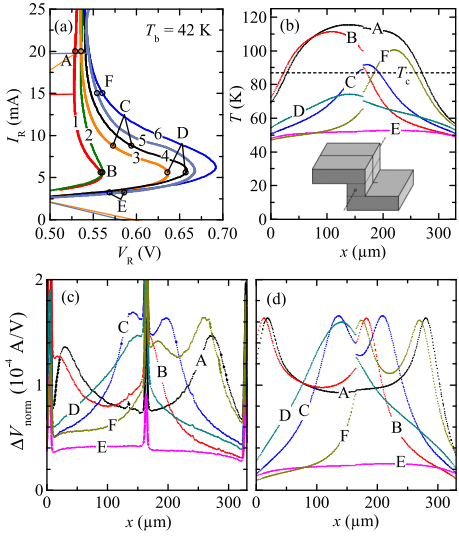

Figure 8. (a) Simulated IVCs of the right stack for I_L = 25 mA (labeled # 2), 7.4 mA (# 4) and 3 mA (# 6). The corresponding measured IVCs are, respectively, labeled by numbers 1, 3 and 5. (b) $T(x)$-profiles for the bias points indicated by letters in (a) taken along the line indicated in the inset in (b). Experimental (c) and simulated (d) LTSLM voltage responses taken along the line indicated in the inset in (b).

not perfect, the simulation adequately reproduces the shift of the IVC to lower voltages for increasing I_L. Selected $T(x)$-profiles are shown in figure 8(b), which again confirm the experimentally observed positioning and formation of the hot spot, as described by means of the LTSLM images. For completeness, also measured and simulated LTSLM linescans are shown in figures 8(c) and (d), respectively. The agreement between the measured and calculated linescans is of similar quality as before, capturing all qualitative features.

4. Discussion

In the previous section we have seen that the electro-thermal properties of the two IJJ stacks, as well as the bias points exhibiting strong THz emission, depend strongly on the electrical integration, the thermal anchoring and the biasing scheme. For example, after the first FIB cut a new hysteretic branch appeared on the IVC which was absent in the pristine structure, cf figure 3(a). Extrapolating such findings to many parallel stacks one can easily imagine that multi-stack arrangements will show a very complex behavior which will be hard to control.

In none of the arrangements of the two stacks we observed synchronized radiation, despite of the presence of interaction by the mutually impinging THz fields, by electrical currents in the superconducting electrodes or by a shared hot spot serving as a common, distributed load.At least some theoretical calculations indicated that two stacks connected in parallel, like our arrangement after the first FIB cut, should be synchronized [47, 49]. Obviously, an additional synchronization mechanism, as the cavity resonance within a single stack, seems to be necessary. In [21] and [54] synchronization was achieved for mesa structures patterned on the same base crystal, which is a lot thicker than the bottom electrode in our z-structure, suggesting that interaction via the base crystal is important. This is in line with the suggestion made in [21] and [48], that THz plasma waves in the base crystal promote synchronization. In this case, the distance between the stacks and (or) the thickness of the base crystal should be crucial parameters.

The two different stack configurations which we discussed here share the appearance of a single hot spot, a consequence of the strong thermal coupling between the stacks, which is primarily provided by the bottom electrode. A set of simulations, where we moved the stacks further apart from each other (while keeping their size constant), suggests a smooth progression from the appearance of one hot spot to the appearance of two hot spots. For a distance of 50 μm two hot spots are clearly distinguishable, almost centred in their respective stack. Reducing the distance between the stacks moves the hot spots away from their center position increasing their proximity. For 15 to 5 μm distance it gets difficult to distinguish the two hot spots and below 5 μm only one hot spot appears. It may well be advantageous for planar arrays of IJJ stacks to reduce the number of hot spots by smartly arranging the stacks: in [21] the synchronization of more than three stacks was prevented by excessive heating, which would be greatly reduced, if two to four stacks 'shared' one hot spot. At the same time it may support the synchronization amongst the IJJs within each stack [13].

5. Summary

In summary, we have investigated the electrothermal behavior and the THz emission properties of two nearby BSCCO IJJ stacks using a combination of transport and THz emission measurements plus LTSLM. The study was motivated by the fact that parallel arrays of stacks are a promising option to realize a high power superconducting THz emitter. We observed the formation of one single hot spot, which may be found in various configurations, depending on bias condition and structure of the two stacks. The impact of the respective thermal configuration on the shape of the current–voltage characteristics and the occurrence of THz emission was discussed. Further we analysed under which conditions two hot spots are to be expected. In none of the designs it was possible to achieve mutual synchronization of the two stacks, indicating that additional synchronizing elements may be necessary for the operation of parallel array structures.

Acknowledgments

We gratefully acknowledge financial support by the National Natural Science Foundation of China (Grant No. 11234006), the Priority Academic Program Development of Jiangsu Higher Education Institutions, the Deutsche Forschungsgemeinschaft (Project KL930/12-1), the Grants-in-Aid for scientific research from JSPS, RFBR grants 13-02-00493-a, 14-02-91335 and 14-02-31374, and grant No. 14.607.21.0100 by the Ministry of Education and Science of the Russian Federation.

References

[1] Darula M, Doderer T and Beuven S 1999 *Supercond. Sci. Technol.* **12** R1
[2] Barbara P, Cawthorne A B, Shitov S V and Lobb C J 1999 *Phys. Rev. Lett.* **82** 1963
[3] Song F, Müller F, Behr R and Klushin M 2009 *Appl. Phys. Lett.* **95** 172501
[4] Kleiner R, Steinmeyer F, Kunkel G and Müller P 1992 *Phys. Rev. Lett.* **68** 2394
[5] Ozyuzer L *et al* 2007 *Science* **318** 1291
[6] Wang H B, Guénon S, Yuan J, Iishi A, Arisawa S, Hatano T, Yamashita T, Koelle D and Kleiner R 2009 *Phys. Rev. Lett.* **102** 017006
[7] Kurter C, Ozyuzer L, Proslier T, Zasadzinski J F, Hinks D G and Gray K E 2010 *Phys. Rev.* B **81** 224518
[8] Wang H B *et al* 2010 *Phys. Rev. Lett.* **105** 057002
[9] Tsujimoto M, Yamaki K, Deguchi K, Yamamoto T, Kashiwagi T, Minami H, Tachiki M, Kadowaki K and Klemm R A 2010 *Phys. Rev. Lett.* **105** 037005
[10] Guenon S *et al* 2010 *Phys. Rev.* B **82** 214506
[11] Benseman T M, Koshelev A E, Gray K E, Kwok W-K, Welp U, Kadowaki K, Tachiki M and Yamamoto T 2011 *Phys. Rev.* B **84** 064523
[12] Yuan J *et al* 2012 *Supercond. Sci. Technol.* **25** 075015
[13] Li M *et al* 2012 *Phys. Rev.* B **86** 060505
[14] Tsujimoto M *et al* 2012 *Phys. Rev. Lett.* **108** 107006
[15] Tsujimoto M, Minami H, Delfanazari K, Sawamura M, Nakayama R, Kitamura T, Yamamoto T, Kashiwagi T, Hattori T and Kadowaki K 2012 *J. Appl. Phys.* **111** 123111
[16] Kakeya I, Omukai Y, Yamamoto T, Kadowaki K and Suzuki M 2012 *Appl. Phys. Lett.* **100** 242603
[17] Kashiwagi T *et al* 2012 *Japan J. Appl. Phys.* **51** 010113
[18] Turkoglu F, Koseoglu H, Demirhan Y, Ozyuzer L, Preu S, Malzer S, Simsek Y, Müller P, Yamamoto T and Kadowaki K 2012 *Supercond. Sci. Technol.* **25** 125004
[19] An D Y *et al* 2013 *Appl. Phys. Lett.* **102** 092601
[20] Benseman T M, Koshelev A E, Kwok W-K, Welp U, Vlasko-Vlasov V K, Kadowaki K, Minami H and Watanabe C 2013 *J. Appl. Phys.* **113** 133902
[21] Benseman T M, Gray K E, Koshelev A E, Kwok W-K, Welp U, Minami H, Kadowaki K and Yamamoto T 2013 *Appl. Phys. Lett.* **103** 022602
[22] Benseman T M, Koshelev A E, Kwok W-K, Welp U, Kadowaki K, Cooper J R and Balakrishnan G 2013 *Supercond. Sci. Technol.* **26** 085016
[23] Sekimoto S, Watanabe C, Minami H, Yamamoto T, Kashiwagi T, Klemm R A and Kadowaki K 2013 *Appl. Phys. Lett.* **103** 182601
[24] Gross B *et al* 2013 *Phys. Rev.* B **88** 014524
[25] Minami H, Watanabe C, Sato K, Sekimoto S, Yamamoto T, Kashiwagi T, Klemm R A and Kadowaki K 2014 *Phys. Rev.* B **89** 054503
[26] Kashiwagi T *et al* 2014 *Appl. Phys. Lett.* **104** 082603
[27] Watanabe C, Minami H, Yamamoto T, Kashiwagi T, Klemm R A and Kadowaki K 2014 *J. Phys.: Condens. Matter* **26** 172201
[28] Koshelev A E and Bulaevskii L N 2008 *Phys. Rev.* B **77** 014530
[29] Koshelev A E 2008 *Phys. Rev.* B **78** 174509
[30] Lin S and Hu X 2008 *Phys. Rev. Lett.* **100** 247006
[31] Krasnov V M 2009 *Phys. Rev. Lett.* **103** 227002
[32] Tachiki M, Fukuya S and Koyama T 2009 *Phys. Rev. Lett.* **102** 127002
[33] Pedersen N and Madsen S 2009 *IEEE Trans. Appl. Supercond.* **19** 726
[34] Lin S-Z and Hu X 2010 *Phys. Rev.* B **82** 020504
[35] Krasnov V M 2010 *Phys. Rev.* B **82** 134524
[36] Koshelev A E 2010 *Phys. Rev.* B **82** 174512
[37] Koyama T, Matsumoto H, Machida M and Ota Y 2011 *Supercond. Sci. Technol.* **24** 085007
[38] Krasnov V M 2011 *Phys. Rev.* B **83** 174517
[39] Yurgens A 2011 *Phys. Rev.* B **83** 184501
[40] Yurgens A and Bulaevskii L N 2011 *Supercond. Sci. Technol.* **24** 015003
[41] Asai H, Tachiki M and Kadowaki K 2012 *Phys. Rev.* B **85** 064521
[42] Lin S-Z and Hu X 2012 *Phys. Rev.* B **86** 054506
[43] Averkov Y O, Yakovenko V M, Yampolskii V A and Nori F 2012 *Phys. Rev. Lett.* **109** 027005
[44] Gross B *et al* 2012 *Phys. Rev.* B **86** 094524
[45] Asai H and Kawabata S 2014 *Appl. Phys. Lett.* **104** 112601
[46] Grib A and Seidel P 2014 *Phys. Stat. Solidi* B **251** 1040
[47] Lin S Z 2014 *J. Appl. Phys.* **115** 173901
[48] Lin S-Z and Koshelev A E 2013 *Physica C* **491** 24
[49] Shukrinov Y M, Rahmonov I R, Plecenik A, Seidel P, Il'ichev E and Nawrocki W 2014 *Supercond. Sci. Technol.* **27** 124007
[50] Welp U, Kadowaki K and Kleiner R 2013 *Nat. Photonics* **7** 702
[51] Kawayama I, Zhang C, Wang H B and Tonouchi M 2013 *Supercond. Sci. Technol.* **26** 093002
[52] Gurevich A V and Mints R G 1987 *Rev. Mod. Phys.* **59** 941
[53] Ji M *et al* 2014 *Appl. Phys. Lett.* **105** 122602
[54] Orita N, Minami H, Koike T, Yamamoto T and Kadowaki K 2010 *Physica* C **470** S786
[55] Wang H B, Wu P H, Chen J, Maeda K and Yamashita T 2002 *Appl. Phys. Lett.* **80** 1604
[56] Wang H B *et al* 2009 *Phys. Rev.* B **80** 224507
[57] Koshelets V P, Ermakov A B, Filippenko L V, Kinev N V, Kiselev O S, Torgashin M Y, de Lange A, de Lange G, Pripolzin S I and Vaks V L 2010 *Proc. SPIE* **7854** 78540J
[58] Spenke E 1935 *Electr. Eng. (Arch. fuer Elektrotech.)* **30** 728
[59] Spenke E 1936 *Wiss. Verff. a. d. Siemens-Werken* **15** 92

Publication 4

Self-Mixing Spectra of Terahertz Emitters Based on $Bi_2Sr_2CaCu_2O_{8+\delta}$ Intrinsic Josephson-Junction Stacks

Ya Huang,[1,2] Hancong Sun,[1,2] Deyue An,[1,2] Xianjing Zhou,[1,2] Min Ji,[1,2] Fabian Rudau,[3] Raphael Wieland,[3] Johannes S. Hampp,[3] Olcay Kizilaslan,[3,4] Jie Yuan,[5] Nickolay Kinev,[6] Oleg Kiselev,[6] Valery P. Koshelets,[6] Jun Li,[1] Dieter Koelle,[3] Reinhold Kleiner,[3,†] Biaobing Jin,[1] Jian Chen,[1] Lin Kang,[1] Weiwei Xu,[1] Huabing Wang,[1,*] and Peiheng Wu[1]

[1]*Research Institute of Superconductor Electronics, Nanjing University, Nanjing 210023, China*
[2]*National Institute for Materials Science, Tsukuba 305-0047, Japan*
[3]*Physikalisches Institut and Center for Quantum Science in LISA⁺, Universität Tübingen, D-72076 Tübingen, Germany*
[4]*Department of Biomedical Engineering, Faculty of Engineering, Inonu University, 44280 Malatya, Turkey*
[5]*Condensed Matter Physics, Institute of Physics, Chinese Acadamy of Sciences, Beijing 100190, China*
[6]*Kotel'nikov Institute of Radio Engineering and Electronics, Moscow 125009, Russia*

(Received 25 July 2017; revised manuscript received 19 September 2017; published 10 November 2017)

Josephson junctions can serve as mixers for electromagnetic radiation, producing difference frequencies $|mf_s - nf_{LO}|$ of the signal frequency f_s and the local oscillator frequency f_{LO}, where the latter can be provided by ac Josephson currents, and m and n are natural numbers. In order to obtain a better understanding of the purity of the terahertz radiation generated by stacks of intrinsic Josephson junctions (IJJs), we study self-mixing—i.e., f_s is also produced by Josephson currents *inside* the stacks—in the difference-frequency range between 0.1 and 3.0 GHz. Simultaneously, we perform off-chip terahertz emission detection and transport measurements. We find that at high-bias currents, when a hot spot has formed in the stack, the power level of self-mixing can be low and sometimes is even absent at the terahertz emission peak, pointing to a good phase locking among all IJJs. By contrast, at low-bias currents where no hot spot exists, the self-mixing products are pronounced even if the terahertz emission peaks are strong. The mixing products at high operation temperature, at which the temperature variation within the stack is moderate, are minor, indicating that the low junction resistance, perhaps in combination with the lowered Josephson critical current density, may play a similar role for synchronization as the hot spot does at low temperature. While these observations are helpful for the task to synchronize thousands of IJJs, the observation of self-mixing in general may offer a simple method in evaluating the coherence of terahertz radiation produced by the IJJ stacks.

DOI: 10.1103/PhysRevApplied.8.054023

I. INTRODUCTION

The possibility to generate coherent terahertz emission using stacks of intrinsic Josephson junctions (IJJs) in the high-transition-temperature (high-T_c) superconductor $Bi_2Sr_2CaCu_2O_{8+\delta}$ (BSCCO) has led to intensive research, both in terms of experiment [1–37] and theory [38–62]; for recent reviews, see Refs. [63–65]. A unit cell of BSCCO consists of superconducting CuO_2 layers and insulating BiO and SrO layers, resulting in natural (intrinsic) Josephson junctions along the c axis [66]. A single crystal of 1.5-μm thickness forms a stack of $N \sim 1000$ IJJs. If the voltage across all IJJs is equal, the junctions oscillate at a frequency $f_J = V/N\Phi_0$, where Φ_0 is the flux quantum and V is the voltage across the whole stack of IJJs. This makes BSCCO stacks interesting candidates for tunable (by voltage) terahertz oscillators, provided that the IJJs can be made to oscillate in phase over a certain range of voltages. Coherent off-chip terahertz emission was first demonstrated for 1-μm-thick BSCCO stacks, with an extrapolated output power of up to 0.5 μW for frequencies between 0.5 and 0.85 THz [1]. The emission frequency f_e turned out to be inversely proportional to the width of the stack. Because of that, it has been proposed that resonant modes utilizing the stack as a cavity and oscillating along the width of the stack play an important role for synchronization. A variety of cavity resonances have indeed been found in subsequent experiments [1–4,6,7,9,10]. The nonuniform part of the ac Josephson currents synchronizes with the cavity modes enhancing emission [6,61,62]. Also, efforts to improve the terahertz emission properties have increased the emitted power to up to tens of microwatts [19,21,22,28] and the emission frequency range from 0.3 to 2.4 THz [25,27,28]. Li *et al.* [14] utilized a Nb/AlN/NbN integrated receiver for

*hbwang@nju.edu.cn
†kleiner@uni-tuebingen.de

measuring the linewidth Δf_e of terahertz radiation from IJJ stacks, and found $\Delta f_e \sim 500$ MHz and 23 MHz at low-bias and high-bias regimes, respectively. For a theoretical discussion, see Ref. [54]. At high-bias currents, Joule heating of the IJJ stacks becomes severe. The BSCCO c-axis resistance decreases with increasing temperature. As a consequence, current voltage characteristics (IVCs) exhibit a positive differential resistance at low currents, but start to backbend at larger currents, exhibiting a negative differential resistance. Above some current in the backbending regime the current and temperature distribution in the stack becomes strongly nonuniform—a hot spot, i.e., a region with a temperature above T_c, forms [3,7,15,20,48,53]. The hot spot grows in size with increasing current. At not-too-large currents the hot spot coexists with regions that are still superconducting and produce terahertz radiation. The hot spot affects the properties of the terahertz radiation, as evidenced by the strongly different values for Δf_e under, respectively, high-bias and low-bias conditions. In particular, ac currents generated by the Josephson effect may lead to additional ac currents flowing through the hot area. These currents, in turn, may lead to an improved synchronization [54], in addition to synchronization effects mediated by cavity resonances.

The exact role of the hot spot for terahertz generation and phase synchronization is discussed controversially [14,23,24,54]. To better understand the underlying mechanisms, it is interesting to study the gradual evolution of the terahertz emission properties with changing bias current and relate them to transport properties. To attain this goal, we develop a technique to study the purity of the emitted terahertz radiation via self-mixing and combine this with simultaneous off-chip terahertz emission detection and transport measurements. The idea of self-mixing is that, due to the nonlinearity of the Josephson elements, two or more nearby terahertz emission peaks produce mixing signals at the difference frequencies (and multiples thereof) which can be detected at MHz and GHz frequencies. By contrast, if all IJJs oscillate at the same frequency, there will be no output signal due to self-mixing.

II. SAMPLES AND MEASUREMENT TECHNIQUES

We perform measurements on stand-alone BSCCO stacks embedded between gold electrodes, a gold-BSCCO-gold (GBG) structure, which is shown schematically together with the experimental setup in Fig. 1. Data for two different samples are presented [67]. Sample 1 is fabricated from a BSCCO single crystal with $T_c = 89$ K. Both the top and the bottom gold layers are 100 nm thick. The square stand-alone stack is 240 μm long, 240 μm wide, and about 1.8 μm thick. The rectangular sample 2, fabricated from a single crystal with $T_c = 84$ K, is 320 μm long, 60 μm wide, and about 1.2 μm thick. The stacks are glued onto sapphire (sample 1) and MgO (sample 2) substrates and are mounted onto a hemispherical silicon

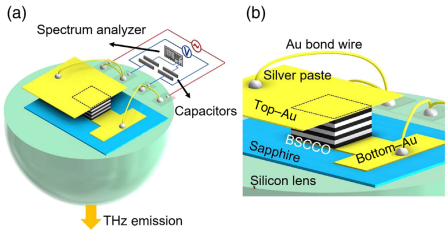

FIG. 1. (a) Schematic view of the experimental setup (not to scale), and (b) its closeup showing the BSCCO intrinsic Josephson-junction stack in GBG geometry.

lens (6 mm in diameter). Sample 1 is set in a helium flow cryostat and sample 2 is placed into a Gifford-McMahon cryocooler. IVCs and the terahertz emission power P_e are measured simultaneously, utilizing either a Golay cell (sample 1) or a $YBa_2Cu_3O_7$ grain-boundary junction [19] (sample 2) as a detector. In the latter case we quote the height $h_{\rm step}$ of the radiation-induced Shapiro step as a measure for the emitted terahertz power ($h_{\rm step}$ follows the Bessel function J_1 as a function of radiation amplitude; here, we work in the linear regime, where approximately $h_{\rm step} \propto P_e^{1/2}$). For some bias points, terahertz emission spectra are taken using a homemade Fourier spectrometer. For the (simultaneous) detection of self-mixing the voltage leads are connected to semirigid cables through two 470-pF capacitors as shown in Fig. 1(a). The mixing signal is amplified by a low noise amplifier with a gain of 35 dB (sample 1) or 50 dB (sample 2), in the frequency range from 100 MHz to 3 GHz, and then subsequently monitored by a spectrum analyzer.

III. RESULTS

For sample 1, Figs. 2(a) to 2(c) show (a) the IVC and (b),(c) P_e vs, respectively, I and V at a bath temperature $T_b = 40$ K. When the current I through the IJJ stack is increased from zero, the stack is in its zero-voltage state up to about 20 mA. When increasing I further, first some junctions and, at $I = 60$ mA, basically all IJJs have switched to their resistive state. Lowering the current in the resistive state, the IVC exhibits a negative differential resistance down to about 28.5 mA. For lower currents the IVC exhibits a positive differential resistance and, for currents below 10 mA, groups of IJJs switch back to the zero-voltage state. Terahertz emission, cf. Figs. 2(b) and 2(c), is on a high power level in the current range from 20 to 7 mA, which is in a regime where there is no hot spot in the sample. The maximum emission power is found at $I = 10.49$ mA, where the voltage across the stack is 1.26 V. The emission power P_e is 2.98 μW at this bias. Emission can be also found in the high-bias regime—i.e., in

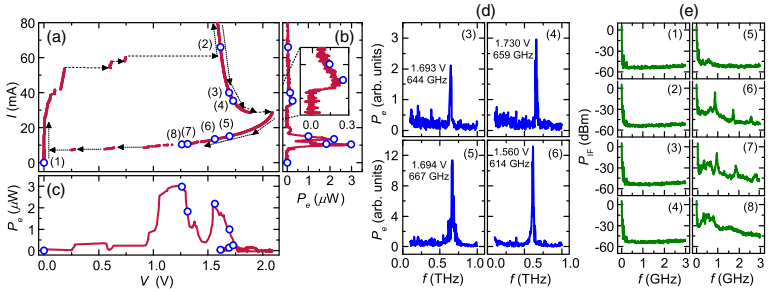

FIG. 2. For sample 1: IVC (a) and terahertz emission power vs (b) bias current and (c) voltage at $T_b = 40$ K. Graphs (d) show Fourier spectra of emitted radiation taken at bias points (3) to (6) indicated in (a). Graphs (e) show IF spectra measured at bias points (1) to (8) indicated in (a). The inset in (b) is an enlargement of the emitting region at high bias, between 25 and 45 mA.

the presence of a hot spot—in a narrow current interval. Overall, the emission power of this sample at high bias is considerably lower than that which is detected at low bias.

Figure 2(d) shows spectra of the emitted terahertz radiation measured at the bias points (3) to (6) indicated in Fig. 2(a). These bias points are located on the outermost branch of the IVC where all IJJs in the stack are resistive [at bias points (7) and (8) some of the IJJs may have switched back to the zero-voltage state]. There is only one emission peak in each spectrum, occurring at the frequencies and voltages indicated in the graphs. From the emission frequencies f_e and the corresponding voltages across the IJJs stack, using $V = Nf_e\Phi_0$, we can estimate the number of IJJs involved in radiation as $N = 1250 \pm 20$, which is consistent with the thickness of the IJJ stack (1.8 μm). At the points of strongest emission, it is likely that cavity resonances are excited. The case of a square IJJ stack is discussed in Refs. [62,65]. The resonances occur at frequencies $f_r = (c_1/2L)\sqrt{k^2 + l^2}$, where k and l are integers and c_1 is the mode velocity of the in-phase resonance depending on T_b and the thickness of the stack [3]. $L = 240$ μm is the length of the square. At temperatures well below T_c and a stack thickness well above the in-plane London penetration depth $c_1 \approx (6\text{–}7) \times 10^7$ m/s, making the (4,2) and (2,4) modes occurring in an estimated frequency range between 580 and 670 GHz the most suitable candidates for the low-bias emission peak in P_e vs V, cf. Fig. 2(b). If points (5) and (6) represent different resonances, the (3,3) mode is an alternative candidate for point (5). For the high-bias emission peak containing points (3) and (4), c_1 is likely to be lowered further. In addition, only part of the stack is superconducting, making it hard to estimate mode indices.

Figure 2(e) shows intermediate frequency (IF) spectra, as measured at the bias points (1) to (8) indicated in Fig. 2(a). The IF spectrum in the zero-voltage state at point (1) shows the noise background of the system. The IF spectrum in the resistive state at point (2), where the whole sample is hot and without terahertz emission, looks similar to the noise background. For points (3) and (4), a hot spot is present in the stack and a weak terahertz emission signal appears. At these bias points the IF signal resembles the background spectrum of point (1). By contrast, at point (5), taken in the low-bias regime, the IF signal is stronger than the background noise. For slightly lower bias currents the terahertz emission gets gradually stronger, cf. Fig. 2(b), and the IF spectra exhibit different profiles; an example is shown for point (6) where one can identify three peaks at, respectively, 0.86, 1.72, and 2.58 GHz. When the stack is biased at point (7), the IF spectrum shows several peaks, the three main ones occurring at 0.93, 1.86, and 2.79 GHz. At point (8), which is at the highest terahertz emission peak in the low-bias regime, there is again a substantial increase in IF noise power, however, with no prominent peaks.

For sample 1 the terahertz emission power in the high-bias regime is poor, and potential additional signals in the IF spectra at points (3) and (4) may be hidden in the background. Thus, for comparison, Fig. 3 shows data for sample 2, taken at $T_b = 18$ K. Figure 3(a) displays the outermost resistive branch of the IVC and 3(b) and 3(c) show h_{step} vs I and V, respectively. In the high-bias regime terahertz emission is on a high power level in the current range from 18.6 to 12 mA. The maximum emission power is found at $I = 17.3$ mA, corresponding to a voltage across the stack of 0.76 V. At this bias the emission power is 25 μW and f_e, determined from the voltage position of the Shapiro step induced in the detector junction, is 0.496 THz. In the whole emitting region f_e varied between 0.48 and 0.58 THz. From f_e and the corresponding voltage across the IJJs stack we estimate the number of IJJs involved in radiation as $N \sim 740$, which is somewhat less than expected from the thickness of the IJJs stack of 1.2 μm ($N \sim 800$). At low bias, a small emission peak is detected near the return current to the superconducting state. Here, f_e is about

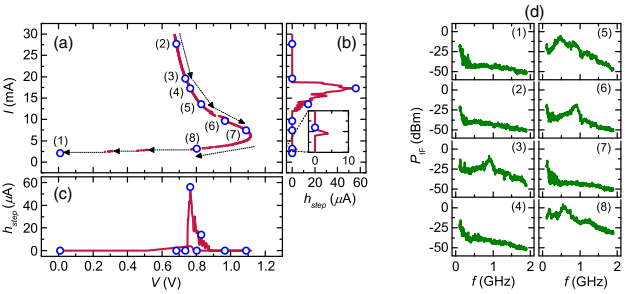

FIG. 3. For sample 2: IVC (a) and height h_{step} of the Shapiro step induced in the detector junction vs (b) bias current and (c) voltage at $T_b = 18$ K. Graphs (d) show eight IF spectra, measured at bias points (1) to (8) marked in (a). The inset in (b) is an enlargement of the emitting region at low bias, between 2.5 and 3.5 mA.

0.57 THz, and we estimate $N \sim 650$, i.e., some junctions seem to have switched back to the zero-voltage state. When attributing the high-bias emission peak in h_{step} vs V to a single resonance mode one finds that, for a mode velocity $c_1 = 6 \times 10^7$ m/s, a (1,0) mode having one half wave along the short side of the stack is compatible with the observed value of f_e. There also could be $(0, l)$ modes, with l counting half waves along the long side. The maximum emission power is in fact very high, favoring the (1,0) mode. For the low-bias emission near point (8) both the (1,0) and the (0,5) mode are candidates.

IF spectra are shown in Fig. 3(d) for the bias points indicated in (a). Spectrum (1) is taken at zero bias, yielding the noise background. Spectrum (2), taken at very high bias, resembles the noise background while at point (3), taken close to the onset of terahertz emission, the IF power has increased. At bias point (4) where terahertz emission is strongest, the IF spectrum is again close to the noise background while at point (5), where the terahertz emission power is still significant, a peak is visible in the IF spectrum. At bias point (6) the terahertz emission power is low but detectable. The corresponding IF spectrum is clearly above the background, in contrast to point (7) where neither at terahertz nor at the IF frequencies an emission power above background is detectable. Finally, the low-bias IF spectrum (8) is again above background and resembles the one of bias point (5). Note that at low bias the IF spectra could have contributions at higher frequencies than seen by our setup. High-resolution measurements of terahertz emission using the superconducting receiver [14] revealed low-bias linewidths that can exceed 5 GHz, implying that P_{IF} could have contributions up to such frequencies.

To understand the overall behavior of the IF spectra of Figs. 2 and 3, we suggest that the enhanced IF power (relative to the background) be due to self-mixing, occurring when the terahertz emission spectra consist of two or more nearby lines, with mixing signals and their harmonics appearing in the frequency window of the IF spectrum. By contrast, if the terahertz spectrum is pure or if no terahertz emission is present, we expect no additional IF signal. This would imply that in the low-bias regime phase lock is incomplete, in agreement with the observations of Ref. [14] and also in agreement with self-mixing data obtained for other IJJ stacks not included here. In the high-bias regime there seems to be good phase lock near the point of strongest emission, however, particularly at the end points (in bias current) of the emitting region phase lock is again incomplete. For bias point (5) in Fig. 3(d), although inside the emitting region, the IF spectrum is well above background; thus also here groups of IJJs seem to radiate at different frequencies. All emitting regions are at least compatible with the previous findings that cavity modes have been excited. However, the observed self-mixing signals indicate that for some bias conditions there is either a strong mode competition or additional synchronization via the hot spot is truly necessary to achieve complete phase lock. The latter conclusion is particularly supported by the differences observed between the high-bias and low-bias regimes.

Sample 1 also emitted at very high temperatures, and Fig. 4 shows data taken at $T_b = 80$ K. Figure 4(a) displays the IVC, and Figs. 4(b) and 4(c) show P_e vs I and V, respectively. Graphs (d) present Fourier spectra of emitted radiation at bias points (3) and (4) indicated in (a), and graphs (e) show IF spectra, as recorded at bias points (1) to (4). The IVC exhibits a positive differential resistance in the resistive state, for currents above 24 mA. At such elevated values of T_b the temperature in the stack, at least according to simulations, varies only modestly (a few K); a hot spot providing large temperature gradients is absent. Terahertz emission, cf. Figs. 4(b) and 4(c), is on a high power level in the current range from 33.9 to 24.6 mA. The maximum emission power of 1.69 μW is found at $I = 28.7$ mA, where the voltage across the stack is 0.528 V. The corresponding terahertz emission spectrum is shown in Fig. 4(d), bias point (3), with an emission frequency of 210 GHz, which is an unusual small value for IJJ stacks and presumably related to the fact that the Josephson plasma frequency $f_{pl}(T) \propto \sqrt{j_c(T)}$ depends on temperature, saturating at low temperatures and approaching zero

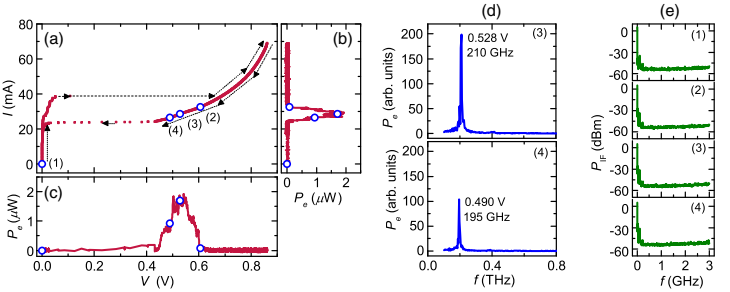

FIG. 4. For sample 1: IVC (a) and terahertz emission power vs (b) bias current and (c) voltage at $T_b = 80$ K. Fourier spectra of emitted radiation taken at point (3) and point (4) are shown in (d) and four IF spectra, measured at bias points (1) to (4), are shown in (e).

for $T \to T_c$ [68]. Using $V = Nf_e\Phi_0$, we can estimate the number of IJJs involved in radiation at this bias point as $N \approx 1215$, which is again consistent with the thickness of the IJJ stack (1.8 μm). Given that close to T_c the mode velocity c_1 very strongly depends on the sample temperature, we do not attempt to assign cavity-mode indices to possible resonances excited by ac Josephson currents.

The IF spectrum at point (1) gives the noise background of the system in the zero-voltage state. At bias point (2), which is at a current slightly above the onset of terahertz emission, the IF spectrum is at the background level. In fact, because of the high bath temperature, we cannot rule out that the temperature in the whole stack is above T_c at this bias. More importantly, the IF spectra are at the background level also at points (3) and (4), although strong terahertz emission occurs here. This indicates that good phase lock is achieved throughout the emitting region at this high bath temperature. This sounds counterintuitive but is in accordance with previous observations that the linewidth of radiation decreases with increasing bath temperature [14,54], suggesting that conditions for phase locking are fulfilled better at high bath temperatures, despite an increased thermal noise.

It is well known that the ability of serial arrays of Josephson junctions to phase lock strongly depends on the electrical parameters of the system [72]; in particular, the Stewart-McCumber parameter $\beta_c = 2\pi I_c R^2 C/\Phi_0$, where I_c, R, and C are, respectively, the junction critical current, resistance, and capacitance, should be not much larger than unity. Indeed, β_c decreases with increasing bath temperatures, which may explain our observations.

IV. CONCLUSIONS

In summary, in order to obtain a better understanding of the purity of the terahertz emission signal generated by BSCCO intrinsic junction stacks, we developed a technique to study the emitted terahertz radiation via self-mixing and combined this technique with simultaneous off-chip terahertz emission detection and transport measurements. We find that, at low bath temperatures, in the low-bias regime the terahertz emission (although showing only a single peak) is accompanied with noisy IF spectra, sometimes exhibiting several peaks. This indicates that groups of junctions oscillate at different frequencies. By contrast, in the high-bias regime the IF spectra can be near the background level. This points to a better ability to phase lock all IJJs in the presence of a hot spot, in agreement with the previous observation that in the high-bias regime the linewidth Δf_e of terahertz radiation is much lower than at low bias [14]. Our data also indicate good phase lock at $T_b = 80$ K, which is important for potential applications using cryocoolers or liquid nitrogen as coolant.

ACKNOWLEDGMENTS

We gratefully acknowledge financial support by the National Natural Science Foundation of China (No. 11234006, No. 61611130069, No. 11227904, No. 61371036, No. 61521001, and No. 61501220), the Fundamental Research Funds for the Central Universities and Jiangsu Key Laboratory of Advanced Techniques for Manipulating Electromagnetic Waves, the Priority Academic Program Development of Jiangsu Higher Education Institutions (PAPD), Jiangsu Provincial Natural Science Fund (No. BK20150561), the RFBR Grant No. 17-52-12051, and the Deutsche Forschungsgemeinschaft via project KL930-13/2.

Y. H. and H. C. S. contributed equally to this work.

[1] L. Ozyuzer, A. E. Koshelev, C. Kurter, N. Gopalsami, Q. Li, M. Tachiki, K. Kadowaki, T. Yamamoto, H. Minami, H. Yamaguchi, T. Tachiki, K. E. Gray, W.-K. Kwok, and U. Welp, Emission of coherent THz radiation from superconductors, Science **318**, 1291 (2007).

[2] K. Kadowaki, H. Yamaguchi, K. Kawamata, T. Yamamoto, H. Minami, I. Kakeya, U. Welp, L. Ozyuzer, A. Koshelev, C. Kurter, K. E. Gray, and W.-K. Kwok, Direct observation of tetrahertz electromagnetic waves emitted from intrinsic Josephson junctions in single crystalline $Bi_2Sr_2CaCu_2O_{8+\delta}$, Physica (Amsterdam) **468C**, 634 (2008).

[3] H. B. Wang, S. Guénon, J. Yuan, A. Iishi, S. Arisawa, T. Hatano, T. Yamashita, D. Koelle, and R. Kleiner, Hot Spots and Waves in $Bi_2Sr_2CaCu_2O_8$ Intrinsic Josephson Junction Stacks: A Study by Low Temperature Scanning Laser Microscopy, Phys. Rev. Lett. **102**, 017006 (2009).

[4] H. Minami, I. Kakeya, H. Yamaguchi, T. Yamamoto, and K. Kadowaki, Characteristics of terahertz radiation emitted from the intrinsic Josephson junctions in high-T_c superconductor $Bi_2Sr_2CaCu_2O_{8+\delta}$, Appl. Phys. Lett. **95**, 232511 (2009).

[5] K. E. Gray, L. Ozyuzer, A. E. Koshelev, C. Kurter, K. Kadowaki, T. Yamamoto, H. Minami, H. Yamaguchi, M. Tachiki, W.-K. Kwok, and U. Welp, Emission of terahertz waves from stacks of intrinsic Josephson junctions, IEEE Trans Appl. Supercond. **19**, 886 (2009).

[6] K. Kadowaki, M. Tsujimoto, K. Yamaki, T. Yamamoto, T. Kashiwagi, H. Minami, M. Tachiki, and R. A. Klemm, Evidence for a dual-source mechanism of THz radiation from rectangular mesas of single crystalline $Bi_2Sr_2CaCu_2O_{8+\delta}$ intrinsic Josephson junctions, J. Phys. Soc. Jpn. **79**, 023703 (2010).

[7] S. Guénon, M. Grünzweig, B. Gross, J. Yuan, Z. G. Jiang, Y. Y. Zhong, M. Y. Li, A. Iishi, P. H. Wu, T. Hatano, R. G. Mints, E. Goldobin, D. Koelle, H. B. Wang, and R. Kleiner, Interaction of hot spots and THz waves in $Bi_2Sr_2CaCu_2O_{8+\delta}$ intrinsic Josephson junction stacks of various geometry, Phys. Rev. B **82**, 214506 (2010).

[8] C. Kurter, L. Ozyuzer, T. Proslier, J. F. Zasadzinski, D. G. Hinks, and K. E. Gray, Counterintuitive consequence of heating in strongly-driven intrinsic junctions of $Bi_2Sr_2CaCu_2O_{8+\delta}$ mesas, Phys. Rev. B **81**, 224518 (2010).

[9] H. B. Wang, S. Guénon, B. Gross, J. Yuan, Z. G. Jiang, Y. Y. Zhong, M. Grünzweig, A. Iishi, P. H. Wu, T. Hatano, D. Koelle, and R. Kleiner, Coherent Terahertz Emission of Intrinsic Josephson Junction Stacks in the Hot Spot Regime, Phys. Rev. Lett. **105**, 057002 (2010).

[10] M. Tsujimoto, K. Yamaki, K. Deguchi, T. Yamamoto, T. Kashiwagi, H. Minami, M. Tachiki, K. Kadowaki, and R. A. Klemm, Geometrical Resonance Conditions for THz Radiation from the Intrinsic Josephson Junctions in $Bi_2Sr_2CaCu_2O_{8+\delta}$, Phys. Rev. Lett. **105**, 037005 (2010).

[11] H. Koseoglu, F. Turkoglu, Y. Simsek, and L. Ozyuzer, The fabrication of THz emitting mesas by reactive ion-beam etching of superconducting Bi2212 with multilayer masks, J. Supercond. Novel Magn. **24**, 1083 (2011).

[12] T. M. Benseman, A. E. Koshelev, K. E. Gray, W.-K. Kwok, U. Welp, K. Kadowaki, M. Tachiki, and T. Yamamoto, Tunable terahertz emission from $Bi_2Sr_2CaCu_2O_{8+\delta}$ mesa devices, Phys. Rev. B **84**, 064523 (2011).

[13] J. Yuan, M. Y. Li, J. Li, B. Gross, A. Ishii, K. Yamaura, T. Hatano, K. Hirata, E. Takayama-Muromachi, P. H. Wu, D. Koelle, R. Kleiner, and H. B. Wang, Terahertz emission from $Bi_2Sr_2CaCu_2O_{8+\delta}$ intrinsic Josephson junction stacks with all-superconducting electrodes, Supercond. Sci. Technol. **25**, 075015 (2012).

[14] M. Y. Li, J. Yuan, N. Kinev, J. Li, B. Gross, S. Guénon, A. Ishii, K. Hirata, T. Hatano, D. Koelle, R. Kleiner, V. P. Koshelets, H. B. Wang, and P. H. Wu, Linewidth dependence of coherent terahertz emission from $Bi_2Sr_2CaCu_2O_{8+\delta}$ intrinsic Josephson junction stacks in the hot-spot regime, Phys. Rev. B **86**, 060505(R) (2012).

[15] I. Kakeya, Y. Omukai, T. Yamamoto, K. Kadowaki, and M. Suzuki, Effect of thermal inhomogeneity for terahertz radiation from intrinsic Josephson junction stacks of $Bi_2Sr_2CaCu_2O_{8+\delta}$, Appl. Phys. Lett. **100**, 242603 (2012).

[16] T. Kashiwagi, M. Tsujimoto, T. Yamamoto, H. Minami, K. Yamaki, K. Delfanzari, K. Deguchi, N. Orita, T. Koike, R. Nakayama, T. Kitamura, M. Sawamura, S. Hagino, K. Ishida, K. Ivanovic, H. Asai, M. Tachiki, R. A. Klemm, and K. Kadowaki, High temperature superconductor terahertz emitters: Fundamental physics and its applications, Jpn. J. Appl. Phys. **51**, 010113 (2012).

[17] M. Tsujimoto, T. Yamamoto, K. Delfanazari, R. Nakayama, T. Kitamura, M. Sawamura, T. Kashiwagi, H. Minami, M. Tachiki, K. Kadowaki, and R. A. Klemm, Broadly Tunable Subterahertz Emission from Internal Branches of the Current-Voltage Characteristics of Superconducting $Bi_2Sr_2CaCu_2O_{8+\delta}$ Single Crystals, Phys. Rev. Lett. **108**, 107006 (2012).

[18] F. Turkoglu, H. Koseoglu, Y. Demirhan, L. Ozyuzer, S. Preu, S. Malzer, Y. Simsek, P. Müller, T. Yamamoto, and K. Kadowaki, Interferometer measurements of terahertz waves from $Bi_2Sr_2CaCu_2O_{8+\delta}$ mesas, Supercond. Sci. Technol. **25**, 125004 (2012).

[19] D. Y. An, J. Yuan, N. Kinev, M. Y. Li, Y. Huang, M. Ji, H. Zhang, Z. L. Sun, L. Kang, B. B. Jin, J. Chen, J. Li, B. Gross, A. Ishii, K. Hirata, T. Hatano, V. P. Koshelets, D. Koelle, R. Kleiner, H. B. Wang, W. W. Xu, and P. H. Wu, Terahertz emission and detection both based on high-T_c superconductors: Towards an integrated receiver, Appl. Phys. Lett. **102**, 092601 (2013).

[20] T. M. Benseman, A. E. Koshelev, W.-K. Kwok, U. Welp, V. K. Vlasko-Vlasov, K. Kadowaki, H. Minami, and C. Watanabe, Direct imaging of hot spots in $Bi_2Sr_2CaCu_2O_{8+\delta}$ mesa terahertz sources, J. Appl. Phys. **113**, 133902 (2013).

[21] T. M. Benseman, K. E. Gray, A. E. Koshelev, W.-K. Kwok, U. Welp, H. Minami, K. Kadowaki, and T. Yamamoto, Powerful terahertz emission from $Bi_2Sr_2CaCu_2O_{8+\delta}$ mesa arrays, Appl. Phys. Lett. **103**, 022602 (2013).

[22] S. Sekimoto, C. Watanabe, H. Minami, T. Yamamoto, T. Kashiwagi, R. A. Klemm, and K. Kadowaki, Continuous 30 μW terahertz source by a high-T_c superconductor mesa structure, Appl. Phys. Lett. **103**, 182601 (2013).

[23] H. Minami, C. Watanabe, K. Sato, S. Sekimoto, T. Yamamoto, T. Kashiwagi, R. A. Klemm, and K. Kadowaki, Local SiC photoluminescence evidence of hot spot formation and sub-THz coherent emission from a rectangular $Bi_2Sr_2CaCu_2O_{8+\delta}$ mesa, Phys. Rev. B **89**, 054503 (2014).

[24] C. Watanabe, H. Minami, T. Yamamoto, T. Kashiwagi, R. A. Klemm, and K. Kadowaki, Spectral investigation of hot spot and cavity resonance effects on the terahertz radiation from high-T_c superconducting $Bi_2Sr_2CaCu_2O_{8+\delta}$, J. Phys. Condens. Matter **26**, 172201 (2014).

[25] M. Ji, J. Yuan, B. Gross, F. Rudau, D. Y. An, M. Y. Li, X. J. Zhou, Y. Huang, H. C. Sun, Q. Zhu, J. Li, N. Kinev, T. Hatano, V. P. Koshelets, D. Koelle, R. Kleiner, W. W. Xu, B. B. Jin, H. B. Wang, and P. H. Wu, $Bi_2Sr_2CaCu_2O_{8+\delta}$ intrinsic Josephson junction stacks with improved cooling:

Coherent emission above 1 THz, Appl. Phys. Lett. **105**, 122602 (2014).

[26] M. Tsujimoto, H. Kambara, Y. Maeda, Y. Yoshioka, Y. Nakagawa, and I. Kakeya, Dynamic Control of Temperature Distributions in Stacks of Intrinsic Josephson Junctions in $Bi_2Sr_2CaCu_2O_{8+\delta}$ for Intense Terahertz Radiation, Phys. Rev. Applied **2**, 044016 (2014).

[27] T. Kashiwagi, T. Yamamoto, T. Kitamura, K. Asanuma, C. Watanabe, K. Nakade, T. Yasui, Y. Saiwai, Y. Shibano, H. Kubo, K. Sakamoto, T. Katsuragawa, M. Tsujimoto, K. Delfanazari, R. Yoshizaki, H. Minami, R. A. Klemm, and K. Kadowaki, Generation of electromagnetic waves from 0.3 to 1.6 terahertz with a high-T_c superconducting $Bi_2Sr_2CaCu_2O_{8+\delta}$ intrinsic Josephson junction emitter, Appl. Phys. Lett. **106**, 092601 (2015).

[28] T. Kashiwagi, K. Sakamoto, H. Kubo, Y. Shibano, T. Enomoto, T. Kitamura, K. Asanuma, T. Yasui, C. Watanabe, K. Nakade, Y. Saiwai, T. Katsuragawa, M. Tsujimoto, R. Yoshizaki, T. Yamamoto, H. Minami, R. A. Klemm, and K. Kadowaki, A high-T_c intrinsic Josephson junction emitter tunable from 0.5 to 2.4 terahertz, Appl. Phys. Lett. **107**, 082601 (2015).

[29] C. Watanabe, H. Minami, T. Kitamura, K. Asanuma, K. Nakade, T. Yasui, Y. Saiwai, Y. Shibano, T. Yamamoto, T. Kashiwagi, R. A. Klemm, and K. Kadowaki, Influence of the local heating position on the terahertz emission power from high-T_c superconducting $Bi_2Sr_2CaCu_2O_{8+\delta}$ mesas, Appl. Phys. Lett. **106**, 042603 (2015).

[30] X. J. Zhou, J. Yuan, H. Wu, Z. S. Gao, M. Ji, D. Y. An, Y. Huang, F. Rudau, R. Wieland, B. Gross, N. Kinev, J. Li, A. Ishii, T. Hatano, V. P. Koshelets, D. Koelle, R. Kleiner, H. B. Wang, and P. H. Wu, Tuning the Terahertz Emission Power of an Intrinsic Josephson-Junction Stack with a Focused Laser Beam, Phys. Rev. Applied **3**, 044012 (2015).

[31] X. J. Zhou, Q. Zhu, M. Ji, D. Y. An, L. Y. Hao, H. C. Sun, S. Ishida, F. Rudau, R. Wieland, J. Li, D. Koelle, H. Eisaki, Y. Yoshida, T. Hatano, R. Kleiner, H. B. Wang, and P. H. Wu, Three-terminal stand-alone superconducting terahertz emitter, Appl. Phys. Lett. **107**, 122602 (2015).

[32] L. Y. Hao, M. Ji, J. Yuan, D. Y. An, M. Y. Li, X. J. Zhou, Y. Huang, H. C. Sun, Q. Zhu, F. Rudau, R. Wieland, N. Kinev, J. Li, W. W. Xu, B. B. Jin, J. Chen, T. Hatano, V. P. Koshelets, D. Koelle, R. Kleiner, H. B. Wang, and P. H. Wu, Compact Superconducting Terahertz Source Operating in Liquid Nitrogen, Phys. Rev. Applied **3**, 024006 (2015).

[33] T. Kashiwagi, T. Yamamoto, H. Minami, M. Tsujimoto, R. Yoshizaki, K. Delfanazari, T. Kitamura, C. Watanabe, K. Nakade, T. Yasui, K. Asanuma, Y. Saiwai, Y. Shibano, T. Enomoto, H. Kubo, K. Sakamoto, T. Katsuragawa, B. Marković, J. Mirković, R. A. Klemm, and K. Kadowaki, Efficient Fabrication of Intrinsic-Josephson-Junction Terahertz Oscillators with Greatly Reduced Self-Heating Effects, Phys. Rev. Applied **4**, 054018 (2015).

[34] T. M. Benseman, A. E. Koshelev, V. Vlasko-Vlasov, Y. Hao, W.-K. Kwok, U. Welp, C. Keiser, B. Gross, M. Lange, D. Kölle, R. Kleiner, H. Minami, C. Watanabe, and K. Kadowaki, Current Filamentation in Large $Bi_2Sr_2CaCu_2o_{8+\delta}$ Mesa Devices Observed via Luminescent and Scanning Laser Thermal Microscopy, Phys. Rev. Applied **3**, 044017 (2015).

[35] K. Nakade, T. Kashiwagi, Y. Saiwai, H. Minami, T. Yamamoto, R. A. Klemm, and K. Kadowaki, Applications using high-T_c superconducting terahertz emitters, Sci. Rep. **6**, 23178 (2016).

[36] M. Tsujimoto, K. Itsuhiro, K. Takanari, H. Minami, and K. Kadowaki, Cavity mode identification for coherent terahertz emission from high-T_c superconductors, Opt. Express **24**, 4591 (2016).

[37] O. Kizilaslan, F. Rudau, R. Wieland, J. S. Hampp, X. J. Zhou, M. Ji, O. Kiselev, N. Kinev, Y. Huang, L. Y. Hao, A. Ishii, M. A. Aksan, T. Hatano, V. P. Koshelets, P. H. Wu, H. B. Wang, D. Koelle, and R. Kleiner, Tuning THz emission properties of $Bi_2Sr_2CaCu_2O_{8+\delta}$ intrinsic Josephson junction stacks by charge carrier injection, Supercond. Sci. Technol. **30**, 034006 (2017).

[38] L. N. Bulaevskii and A. E. Koshelev, Radiation due to Josephson Oscillations in Layered Superconductors, Phys. Rev. Lett. **99**, 057002 (2007).

[39] A. E. Koshelev, Alternating dynamic state self-generated by internal resonance in stacks of intrinsic Josephson junctions, Phys. Rev. B **78**, 174509 (2008).

[40] S. Z. Lin and X. Hu, Possible Dynamic States in Inductively Coupled Intrinsic Josephson Junctions of Layered High-T_c Superconductors, Phys. Rev. Lett. **100**, 247006 (2008).

[41] R. A. Klemm and K. Kadowaki, Output from a Josephson stimulated terahertz amplified radiation emitter, J. Phys. Condens. Matter **22**, 375701 (2010).

[42] M. Tachiki, S. Fukuya, and T. Koyama, Mechanism of Terahertz Electromagnetic Wave Emission from Intrinsic Josephson Junctions, Phys. Rev. Lett. **102**, 127002 (2009).

[43] N. F. Pedersen and S. Madsen, THz generation using fluxon dynamics in high temperature superconductors, IEEE Trans. Appl. Supercond. **19**, 726 (2009).

[44] X. Hu and S. Z. Lin, Cavity phenomena in mesas of cuprate high-T_c superconductors under voltage bias, Phys. Rev. B **80**, 064516 (2009).

[45] T. Koyama, H. Matsumoto, M. Machida, and K. Kadowaki, In-phase electrodynamics and terahertz wave emission in extended intrinsic Josephson junctions, Phys. Rev. B **79**, 104522 (2009).

[46] V. M. Krasnov, Coherent flux-flow emission from stacked Josephson junctions: Nonlocal radiative boundary conditions and the role of geometrical resonances, Phys. Rev. B **82**, 134524 (2010).

[47] A. E. Koshelev, Stability of dynamic coherent states in intrinsic Josephson-junction stacks near internal cavity resonance, Phys. Rev. B **82**, 174512 (2010).

[48] A. A. Yurgens, Temperature distribution in a large $Bi_2Sr_2CaCu_2O_{8+\delta}$ mesa, Phys. Rev. B **83**, 184501 (2011).

[49] V. M. Krasnov, Terahertz electromagnetic radiation from intrinsic Josephson junctions at zero magnetic field via breather-type self-oscillations, Phys. Rev. B **83**, 174517 (2011).

[50] M. Tachiki, K. Ivanovic, K. Kadowaki, and T. Koyama, Emission of terahertz electromagnetic waves from intrinsic Josephson junction arrays embedded in resonance LCR circuits, Phys. Rev. B **83**, 014508 (2011).

[51] S. Z. Lin and X. Hu, In-plane dissipation as a possible synchronization mechanism for terahertz radiation from

intrinsic Josephson junctions of layered superconductors, Phys. Rev. B **86**, 054506 (2012).

[52] Yu. O. Averkov, V. M. Yakovenko, V. A. Yampolskii, and F. Nori, Conversion of Terahertz Wave Polarization at the Boundary of a Layered Superconductor due to the Resonance Excitation of Oblique Surface Waves, Phys. Rev. Lett. **109**, 027005 (2012).

[53] B. Gross, S. Guénon, J. Yuan, M. Y. Li, J. Li, A. Ishii, R. G. Mints, T. Hatano, P. H. Wu, D. Koelle, H. B. Wang, and R. Kleiner, Hot-spot formation in stacks of intrinsic Josephson junctions in $Bi_2Sr_2CaCu_2O_{8+\delta}$, Phys. Rev. B **86**, 094524 (2012).

[54] B. Gross, J. Yuan, D. Y. An, M. Y. Li, N. Kinev, X. J. Zhou, M. Ji, Y. Huang, T. Hatano, R. G. Mints, V. P. Koshelets, P. H. Wu, H. B. Wang, D. Koelle, and R. Kleiner, Modeling the linewidth dependence of coherent terahertz emission from intrinsic Josephson junction stacks in the hot-spot regime, Phys. Rev. B **88**, 014524 (2013).

[55] F. Liu, S. Z. Lin, and X. Hu, Cavity phenomenon and terahertz radiation of a tall stack of intrinsic Josephson junctions wrapped by a dielectric material, Supercond. Sci. Technol. **26**, 025003 (2013).

[56] H. Asai and S. Kawabata, Intense terahertz emission from intrinsic Josephson junctions by external heat control, Appl. Phys. Lett. **104**, 112601 (2014).

[57] A. Grib and P. Seidel, The influence of external separate heating on the synchronization of Josephson junctions, Phys. Status Solidi B **251**, 1040 (2014).

[58] F. Rudau, M. Tsujimoto, B. Gross, T. E. Judd, R. Wieland, E. Goldobin, N. Kinev, J. Yuan, Y. Huang, M. Ji, X. J. Zhou, D. Y. An, A. Ishii, R. G. Mints, P. H. Wu, T. Hatano, H. B. Wang, V. P. Koshelets, D. Koelle, and R. Kleiner, Thermal and electromagnetic properties of $Bi_2Sr_2CaCu_2O_8$ intrinsic Josephson junction stacks studied via one-dimensional coupled sine-Gordon equations, Phys. Rev. B **91**, 104513 (2015).

[59] F. Rudau, R. Wieland, J. Langer, X. J. Zhou, M. Ji, N. Kinev, L. Y. Hao, Y. Huang, J. Li, P. H. Wu, T. Hatano, V. P. Koshelets, H. B. Wang, D. Koelle, and R. Kleiner, Three-Dimensional Simulations of the Electrothermal and Terahertz Emission Properties of $Bi_2Sr_2CaCu_2O_8$ Intrinsic Josephson Junction Stacks, Phys. Rev. Applied **5**, 044017 (2016).

[60] H. Asai and S. Kawabata, Control of circularly polarized THz wave from intrinsic Josephson junctions by local heating, Appl. Phys. Lett. **110**, 132601 (2017).

[61] D. P. Cerkoney, C. Reid, C. M. Doty, A. Gramajo, T. D. Campbell, M. A. Morales, K. Delfanazari, M. Tsujimoto, T. Kashiwagi, T. Yamamoto, C. Watanabe, H. Minami, K. Kadowaki, and R. A Klemm, Cavity mode enhancement of terahertz emission from equilateral triangular microstrip antennas of the high-T_c superconductor $Bi_2Sr_2CaCu_2O_{8+\delta}$, J. Phys. Condens. Matter **29**, 015601 (2017).

[62] R. A. Klemm, A. E. Davis, and Q. X. Wang, Terahertz emission from thermally managed square intrinsic Josephson junction microstrip antennas, IEEE J. Sel. Top. Quantum Electron. **23**, 8501208 (2017).

[63] U. Welp, K. Kadowaki, and R. Kleiner, Superconducting emitters of THz radiation, Nat. Photonics **7**, 702 (2013).

[64] I. Kakeya and H. B. Wang, Terahertz-wave emission from Bi2212 intrinsic Josephson junctions: A review on recent progress, Supercond. Sci. Technol. **29**, 073001 (2016).

[65] T. Kashiwagi, H. Kubo, K. Sakamoto, T. Yuasa, Y. Tanabe, C. Watanabe, T. Tanaka, Y. Komori, R. Ota, G. Kuwano, K. Nakamura, T. Katsuragawa, M. Tsujimoto, T. Yamamoto, R. Yoshizaki, H. Minami, K. Kadowaki, and R. A. Klemm, The present status of high-T_c superconducting terahertz emitters, Supercond. Sci. Technol. **30**, 074008 (2017).

[66] R. Kleiner, F. Steinmeyer, G. Kunkel, and P. Müller, Intrinsic Josephson Effects in $Bi_2Sr_2CaCu_2O_{8+\delta}$ Single Crystals, Phys. Rev. Lett. **68**, 2394 (1992).

[67] Sample 1 emitted up to unusually high bath temperatures, this is why we include this stack as our main sample. However, at low bath temperature, emission at high bias is poor, and thus we include a second sample for reference, exhibiting strong terahertz emission under these conditions. Also for other stacks we find that IF spectra are much more structured at low bias than in the high-bias regime.

[68] In fact, for the BSCCO stacks the resistive state and the corresponding terahertz emission appear to be cut off at about 4 times the Josephson plasma frequency. One may speculate that the cutoff is reached when the Josephson oscillations excite plasma waves associated with the lowest mode velocity [69,70] $c_N \approx \bar{c}\sqrt{2}$ and having wavelengths around the Josephson length λ_J. Here, $\bar{c}$ is the Swihart velocity, $\bar{c} = 2\pi f_{\rm pl}\lambda_J/\sqrt{2}$, yielding a cutoff frequency of about 4–5 $f_{\rm pl}$. For BSCCO $f_{\rm pl}(0)$ depends on the doping state of the crystal and, for the samples discussed here, is on the order of 100 GHz [71].

[69] S. Sakai, A. V. Ustinov, H. Kohlstedt, A. Petraglia, and N. F. Pedersen, Theory and experiment on electromagnetic-wave-propagation velocities in stacked superconducting tunnel structures, Phys. Rev. B **50**, 12905 (1994).

[70] R. Kleiner, T. Gaber, and G. Hechtfischer, Stacked long Josephson junctions in zero magnetic field: A numerical study of coupled one-dimensional sine-Gordon equations, Phys. Rev. B **62**, 4086 (2000).

[71] I. Kakeya, T. Wada, R. Nakamura, and K. Kadowaki, Two-phase collective modes in a Josephson vortex lattice in the intrinsic Josephson junction $Bi_2Sr_2CaCu_2O_{8+\delta}$, Phys. Rev. B **72**, 014540 (2005).

[72] P. Hadley, M. R. Beasley, and K. Wiesenfeld, Phase locking of Josephson junction arrays, Appl. Phys. Lett. **52**, 1619 (1988).

Publication 5

Tuning the Terahertz Emission Power of an Intrinsic Josephson-Junction Stack with a Focused Laser Beam

X. J. Zhou,[1,2,3] J. Yuan,[4] H. Wu,[2,5] Z. S. Gao,[2] M. Ji,[1,2] D. Y. An,[1] Y. Huang,[1] F. Rudau,[6] R. Wieland,[6] B. Gross,[6] N. Kinev,[7] J. Li,[1] A. Ishii,[2] T. Hatano,[2] V. P. Koshelets,[7] D. Koelle,[6] R. Kleiner,[6] H. B. Wang,[1,2,3,*] and P. H. Wu[1]

[1]*Research Institute of Superconductor Electronics, Nanjing University, Nanjing 210093, China*
[2]*National Institute for Materials Science, Tsukuba 3050047, Japan*
[3]*Cooperative Innovation Centre of Terahertz Science, Chengdu 610054, China*
[4]*National Lab for Superconductivity, Institute of Physics, Chinese Academy of Sciences, Beijing 100190, China*
[5]*Key Laboratory of Artificial Micro- and Nano-Structures of Ministry of Education, School of Physics and Technology, Wuhan University, Wuhan 430072, China*
[6]*Physikalisches Institut and Center for Collective Quantum Phenomena in LISA$^+$, Universität Tübingen, D-72076 Tübingen, Germany*
[7]*Kotel'nikov Institute of Radio Engineering and Electronics, Moscow 125009, Russia*

(Received 5 February 2015; revised manuscript received 1 April 2015; published 21 April 2015)

We report on tuning the THz emission of a $Bi_2Sr_2CaCu_2O_8$ (BSCCO) intrinsic Josephson-junction stack by a focused laser beam which is scanned across the stack. The emission power P_e increases by up to 75% upon laser irradiation for a bath temperature near 22 K. The laser-induced changes in the voltage V_{dc} across the stack and in the emission power are measured simultaneously. The maximum of the laser-induced changes in emission power ΔP_e is achieved by irradiating the stack on the location where the local temperature is about the critical temperature T_c. However, ΔP_e is found to be proportional to the laser-induced global voltage change ΔV_{dc}, irrespective of the laser position. This unexpected *global* response is likely to be related to a change in the *average* stack temperature and is consistent with the change in P_e when increasing the bath temperature by about 0.2 K. This tuning method can be employed in the application of BSCCO THz sources.

DOI: 10.1103/PhysRevApplied.3.044012

I. INTRODUCTION

Developing compact, tunable sources for THz generation is a highly active field of research [1,2]. Recently, it was found that intrinsic Josephson-junction (IJJ) stacks, naturally formed in the cuprate superconductor $Bi_2Sr_2CaCu_2O_8$ (BSCCO), can emit coherent radiation at submillimeter wavelengths [3]. In Ref. [3], stacks consisting of about 700 IJJs with a typical length of 300 μm are realized as mesa structures on top of BSCCO single crystals. An emission power P_e of up to 0.5 μW is detected for emission frequencies f_e between 0.5 and 0.8 THz. A lot of work has been performed following this discovery [4–48]; for a recent review, see Ref. [49]. P_e is raised to 82 μW with stand-alone structures, which are no longer patterned on a BSCCO base crystal [27,33]. By synchronizing three mesas patterned on the same base crystal, P_e is increased to 610 μW [30]. The linewidth of radiation can be as low as 6 MHz [44] and the maximum emission frequency reaches 1.6 THz [48]. In the IJJ stacks, THz emission is generated by the ac Josephson effect, yielding an emission frequency $f_e = 2eV_{dc}/Nh$, where N is the number of junctions and V_{dc} is the total dc voltage across the stack. This relation assumes that the voltage drop V_{dc}/N is the same for all junctions. Furthermore, the Josephson relation suggests that f_e is freely tunable by the applied voltage (0.4836 THz per mV across each IJJ), perhaps up to the superconducting energy gap, which would yield a maximum emission frequency of some 10 THz. However, in real systems, there is strong Joule heating, leading, e.g., to the formation of hot spots (regions heated to temperatures above the critical temperature T_c) in the stack [7,13,14,29,31,36,43] and also limiting the maximum voltage per junction to values less than 3 mV. Furthermore, collective cavity modes utilizing the whole stack as a resonator seem to play an important role for synchronizing the IJJs [3,13,14].

Understanding—and ideally also controlling—the relations between THz emission, the inhomogeneous temperature distribution in the stack, and the mechanism of synchronization is a key issue in optimizing the device, not only with respect to P_e, f_e, and the linewidth of emission but also with respect to the tunability of both P_e and f_e. A series of papers addresses the issue of thermal management [6,17,24,40,41,45–48]. In particular, it is proposed that P_e can be enhanced by using a focused laser to locally increase the temperature variation in the stack, thereby strongly exciting plasma waves in the stack [41]. This method is used in the present work, although

*hbwang1000@gmail.com

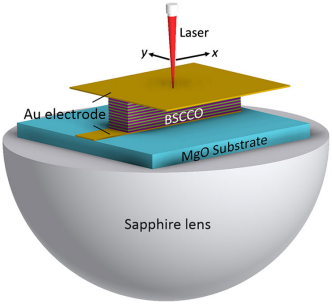

FIG. 1. Sketch of the GBG structure sample mounted on a hemispheric sapphire lens. A focused laser can scan across the sample surface while emission is detected through the lens by a Si bolometer (not shown in the sketch).

with the difference that, in Ref. [41], an initially homogeneous temperature distribution is assumed while, in our experiment, the sample investigated emits THz radiation in the presence of a hot spot. Measurements are done on an IJJ stack embedded between two gold layers, the gold-BSCCO-gold (GBG) structure [40]. By scanning the laser at half width along the length of the stack in the hot-spot regime, we succeed in changing P_e continuously at a constant bias current I. The variations in P_e are strongest when the laser is focused on a location where the local temperature in the stack roughly equals T_c.

Very recently, a similar experiment was performed using mesa structures. Also here, an increase of P_e is observed and appears when the hot-spot position is moved to a mesa end by locally heating the mesa surface with an 80 mW laser beam.

II. EXPERIMENTAL METHOD

A schematic diagram of the GBG structure is shown in Fig. 1. The lateral dimension of the sample studied in this work is about $290 \times 50\ \mu\text{m}^2$. The sample is mounted on a hemispheric sapphire lens. A laser with wavelength $\lambda = 1310$ nm and a spot diameter of about 1 μm is focused onto the surface of the stack. The laser can scan across the surface of the stack with submicrometer precision. Using a Si bolometer, we measure the emission power of the sample from the other side of the hemispheric lens while keeping the laser on at the same time. The power detection and frequency measurement are similar to our previous work [14]. By modulating the laser power with a 10 kHz square signal and detecting the global differential voltage response ΔV of the stack with a lock-in technique while the sample is biased at a constant current, the setup can also be used as a low-temperature scanning laser microscope (LTSLM) [7,13,14,24]. In the present study, we use a comparatively strong beam power; thus, the LTSLM is operated in a manipulation mode rather than an imaging mode. In fact, we estimate that the maximum power of the laser beam arriving at the sample is in the range 2–5 mW. However, most of this intensity is reflected from the Au layer covering the mesa. From the change in the dc voltage across the stack upon laser irradiation, we estimate that a power of 100 μW or less (depending on the laser position and bias current) is absorbed by the mesa.

III. RESULTS AND DISCUSSIONS

In Fig. 2(a), the outermost branch of the current-voltage characteristic, at a bath temperature $T_b = 22$ K, is shown by a solid red line, and the emitted power, for the laser beam turned off, is presented in Fig. 2(b) as a function of bias current. Terahertz emission is only detected at the high-bias regime, from $(I, V_{\text{dc}}) \sim (50\ \text{mA}, 0.93\ \text{V})$ to $\sim(20\ \text{mA}, 0.88\ \text{V})$. For the peak in P_e at $(I, V_{\text{dc}}) = (28\ \text{mA}, 0.883\ \text{V})$, the emission frequency is found to be about 690 GHz, corresponding to $N \approx 620$ IJJs in the resistive state. By its color scale, Fig. 2(a) also shows the LTSLM signals $-\Delta V$ for a family of LTSLM linescans recorded for a large number of bias currents. The linescans are taken along the length of the stack at half of its width. In the graph, the two vertical dashed lines indicate the left and right boundaries of the stack. For currents below 20 mA, there is a strong signal near the left edge of the stack. This edge is not covered by the top Au layer and is much more sensitive to laser irradiation than other areas. One further observes that, near $I \approx 7$ mA, the strong LTSLM response extends significantly from the left edge of the stack toward the center of the stack. In this bias regime, where V_{dc} starts to bend back, a hot spot nucleates and is, presumably, to some extent, moved toward the interior of the stack by the laser beam during scanning. A similar effect (i.e., a laser-induced shift of the hot-spot position) is seen in Ref. [47]. For larger currents, $-\Delta V$ is more restricted to the left part of the stack and develops a local maximum inside the stack, which shifts to the right with increasing current (cf. the tilted, dashed line). This kind of maximum is typical for the edge of a hot spot [24]; i.e., we observe that, for currents above 12 mA, a stable hot spot forms in the left part of the stack and the hot spot increases in size with increasing current. In this regime, the reaction of the hot spot on the laser beam is close to the standard imaging mode; i.e., it slightly increases in size but its position remains fixed [24]. This seems natural because, with increasing dc input power, the relative contribution of the laser beam to local heat production becomes smaller.

Next, we investigate how P_e varies when the laser is positioned at different locations x_L along the stack. For the measurement, we place the laser at a given value x_L for 150 ms, measure P_e, and then vary x_L in steps of 1 μm. Figure 3(a) shows the resulting P_e vs x_L for $T_b = 22$ K and $I = 28$ mA. The lower horizontal dashed line in the graph

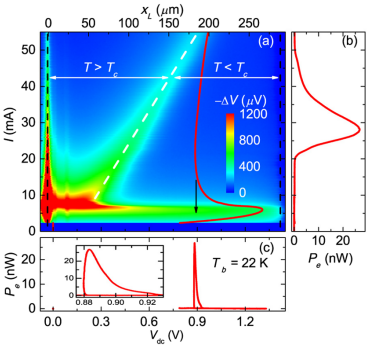

FIG. 2. For a bath temperature $T_b = 22$ K. (a) I-V characteristic (red line, bottom scale) and LTSLM signal $-\Delta V$ for a family of linescans along the length of the stack at half width, taken at different values of I (color scale). Graphs (b) and (c) show the emitted power P_e vs, respectively, I and $V_{\rm dc}$ when the laser is turned off. The inset in (c) shows P_e vs $V_{\rm dc}$ on an expanded voltage scale. The tilted dashed line in (a) separates regions where the stack temperature T is above (below) T_c. Vertical dashed lines indicate the edges of the stack.

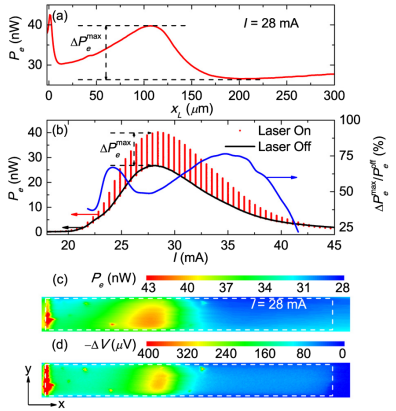

FIG. 3. (a) Emission power with laser positioned at coordinate x_L for a bias current of 28 mA. (b) P_e vs bias current while sweeping the laser, for discrete values of I, from $x_L = 10$ μm to $x_L = 300$ μm (left scale). The black line indicates $P_e^{\rm off}$ vs I, as measured for the laser turned off; thus, the vertical red lines indicate, for each current, the maximum laser-induced change $\Delta P_e^{\rm max}$. Right-hand scale, blue curve: ratio $\Delta P_e^{\rm max}/P_e^{\rm off}$ vs I. For $I = 28$ mA, (c) shows a 2D plot of P_e vs laser position (x_L, y_L) and (d) shows a 2D LTSLM image $-\Delta V$ vs (x_L, y_L). In (c) and (d), the boundaries of the stack are indicated by the dashed boxes. The bath temperature is 22 K.

indicates the emission power $P_e^{\rm off}$ when the laser is turned off. P_e varies from 26 nW to 42 nW when the laser is focused on the different locations of the sample. The largest emission power in the *interior* of the stack $P_e^{\rm max}$, indicated by the upper horizontal line in the graph, occurs for $x_L = 106$ μm, which in fact is close to the location where $-\Delta V$ has its local maximum [cf. Figs. 3(d) and 4(b)]. Figure 3(b) summarizes how P_e varies with I: for each current (step width $\Delta I = 0.5$ mA), the laser is scanned from $x_L = 10$ μm to $x_L = 300$ μm; i.e., we exclude the strong signal from the left edge for this measurement. In the graph, we also plot by a black line $P_e^{\rm off}$ vs I, as measured when the laser is turned off; thus, the vertical red lines indicate for each current the maximum laser-induced change $\Delta P_e^{\rm max}$. The normalized ratio $\Delta P_e^{\rm max}/P_e^{\rm off}$ is shown by the blue curve in Fig. 3(b), referring to the right axis of this graph. As can be seen, the emission power is enhanced for almost every bias current and $\Delta P_e^{\rm max}/P_e^{\rm off}$ reaches values between 50% and 80% for currents between 23 mA and 39 mA. For $I = 28$ mA and $T_b = 22$ K, Fig. 3(c) shows how P_e varies when the laser is scanned both along the x and y directions. There is a hot zone at the left edge of the stack and another hot zone near $x_L = 100$ μm. For comparison, Fig. 3(d) shows the 2D LTSLM image $-\Delta V$ vs laser position (x_L, y_L). One notes that the two images are very similar, leading to the suspicion that the laser-induced change ΔP_e in emission power is (almost) proportional to the laser-induced voltage change ΔV, independent of the laser position.

To study this further, we compare, in Fig. 4, for $T_b = 22$ K and four selected bias currents, (a) the laser-induced change in dc voltage $-\Delta V_{\rm dc}$, (b) the LTSLM signal $-\Delta V$, and (c) the laser-induced change ΔP_e in emission power. Note that $\Delta V_{\rm dc}$ and ΔV would be the same if the laser is modulated arbitrarily slowly, rather than with 10 kHz. For measuring $\Delta V_{\rm dc}$ (and ΔP_e), the laser, while still modulated, is kept at a fixed position x_L for 150 ms. Thus, $\Delta V_{\rm dc}$ measures laser-induced temperature changes which occur within 150 ms of (modulated) laser irradiation while ΔV gives the short time response. Not very surprisingly, the overall amplitude of $\Delta V_{\rm dc}$ is larger than the amplitude of ΔV and the positions of the minima (the hot-spot edges) are slightly shifted to the left for $\Delta V_{\rm dc}$ compared to ΔV. More importantly, the shape of $-\Delta V$ vs x_L is basically the same as the shape of ΔP_e vs x_L. In Fig. 4(d), we plot ΔP_e vs $-\Delta V_{\rm dc}$ for the four bias currents and all values of x_L; i.e., x_L runs as a parameter in this graph. In the plot, we exclude the data from the edge peak, because here the time delay of the Si bolometer relative to the voltmeter causes a significant phase shift between ΔP_e and $\Delta V_{\rm dc}$. For the rest of the x_L values, one obtains straight lines for all currents, confirming the proportionality of ΔP_e and $\Delta V_{\rm dc}$. Note that the slopes $\Delta P_e/\Delta V_{\rm dc}$ amount to about -3 nW/mV for

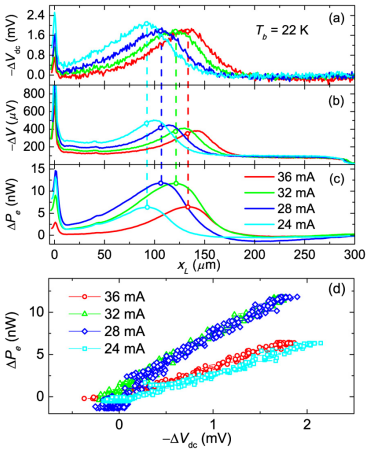

FIG. 4. Four linescans of the laser along the width of the stack. (a) Global laser-induced change in the dc voltage $-\Delta V_{\rm dc}$ across the stack, (b) LTSLM signal $-\Delta V$, and (c) change in emission power ΔP_e vs coordinate x_L on the scanning line. (d) Plot of ΔP_e vs $-\Delta V_{\rm dc}$ for laser positioned from $x_L = 10$ μm to 300 μm.

bias currents of, respectively, 24 mA and 36 mA and to about -6 nW/mV for bias currents 28 mA and 32 mA. The large values of $|\Delta P_e/\Delta V_{\rm dc}|$ are in fact obtained near the center of the emission peak in P_e vs, respectively, I and $V_{\rm dc}$; cf. Figs. 2(b), 2(c), and 3(b).

The proportionality $\Delta P_e \propto \Delta V_{\rm dc}$ is unexpected. In view of the proposal of Ref. [41], one might assume that there is a big difference if the laser is positioned inside the hot-spot region compared to a position where the stack temperature is below T_c. Furthermore, when the laser is positioned near the edges of the stack, the local electric and magnetic field distribution, and thus the radiation impedance [15], might change, giving rise to a change in $P_e(x_L, y_L)$. In particular, one would expect signals in Fig. 3(c) or in Fig. 4(c) on the cold edge of the stack. This is not observed. For the experiments described in Ref. [47], performed on mesa structures, it is concluded that the laser-induced enhancement of the emission power is realized by an adjustment of the hot-spot position. Also for this case, we do not see a reason why $P_e(x_L, y_L)$ and $\Delta V(x_L, y_L)$ should be strictly proportional to each other.

Accepting the proportionality of ΔP_e to the global response $\Delta V_{\rm dc}$, one might assume that by changing $V_{\rm dc}$ with the amount $\Delta V_{\rm dc}$, one simply moves toward a lower voltage in the P_e vs $V_{\rm dc}$ curve of Fig. 2(c). However, the bias currents in Fig. 4 are chosen so that in P_e vs $V_{\rm dc}$ points on both sides of the emission peak are covered; thus, one should get different signs of the response, e.g., for $I = 24$ mA and 36 mA. With the laser turned on, there is also a slight increase in the average stack temperature which to some extent is equivalent to an increase of the bath temperature. For the sample, we find that, for the bias currents of interest, $V_{\rm dc}$ changes by about 3–4 mV/K. Thus, the laser-induced relative change in voltage corresponds to a change in T_b of about 0.2 K. By changing T_b for fixed values of the bias current, we find that P_e in fact oscillates as a function $\Delta V_{\rm dc}$ and, near the bath temperature of 22 K, increases by more than a factor of 5 when increasing T_b by only 2 K. A 0.2 K laser-induced temperature change is thus compatible with the increase in P_e that we observe.

IV. SUMMARY

In summary, we investigate the response of a BSCCO intrinsic Josephson-junction stack, embedded between two gold electrodes, to a focused laser beam which is scanned across the stack. The laser-induced changes in the voltage $V_{\rm dc}$ across the stack and in the THz emission power P_e are measured simultaneously. The study is motivated by the recent theoretical study [41] proposing that a laser beam locally heating the stack, thereby causing a critical current inhomogeneity, can give rise to a strong enhancement of P_e in comparison with the homogeneous state. In our experiment, the sample does not emit in the low-bias regime, neither in the absence nor in the presence of the laser beam. However, the laser-induced changes of the emission power are found at the high-bias regime in the presence of a hot spot. For a bath temperature near 22 K, the laser-induced changes $\Delta P_e(x_L, y_L)$ are proportional to the voltage change $\Delta V_{\rm dc}(x_L, y_L)$ for all values of the position (x_L, y_L) of the laser beam. $\Delta V_{\rm dc}(x_L, y_L)$ itself, and consequently also $\Delta P_e(x_L, y_L)$, strongly depends on the (x_L, y_L) position, being, e.g., large near the edge of the hot spot. The laser-induced change of the voltage across the stack is essentially determined by the temperature dependence of the BSCCO c-axis conductance, as is analyzed in Ref. [24]. In fact, we would have expected that different mechanisms lead to laser-induced changes of the emission power, in which case $\Delta P_e(x_L, y_L)$ and $\Delta V_{\rm dc}(x_L, y_L)$ should have different dependences on the local beam position. The unexpected *global* response is likely to be related to a change in the *average* stack temperature and is consistent with the change in P_e when increasing the bath temperature by about 0.2 K.

ACKNOWLEDGMENTS

We gratefully acknowledge financial support by the National Natural Science Foundation of China (Grant No. 11234006), the Priority Academic Program Development of Jiangsu Higher Education Institutions, the Deutsche Forschungsgemeinschaft (Project No. KL930/12-1), the Grants-in-Aid for Scientific

Research from JSPS (No. 25289108), and RFBR Grants No. 13-02-00493-a and No. 14-02-91335, and Ministry of Education and Science of the Russian Federation Grant No. 14.607.21.0100.

[1] B. Ferguson and X. C. Zhang, Materials for terahertz science and technology, Nat. Mater. **1**, 26 (2002).
[2] M. Tonouchi, Cutting-edge terahertz technology, Nat. Photonics **1**, 97 (2007).
[3] L. Ozyuzer, A. E. Koshelev, C. Kurter, N. Gopalsami, Q. Li, M. Tachiki, K. Kadowaki, T. Yamamoto, H. Minami, H. Yamaguchi, T. Tachiki, K. E. Gray, W.-K. Kwok, and U. Welp, Emission of coherent THz radiation from superconductors, Science **318**, 1291 (2007).
[4] S. Z. Lin and X. Hu, Possible Dynamic States in Inductively Coupled Intrinsic Josephson Junctions of Layered High-T_c Superconductors, Phys. Rev. Lett. **100**, 247006 (2008).
[5] A. E. Koshelev, Alternating dynamic state self-generated by internal resonance in stacks of intrinsic Josephson junctions, Phys. Rev. B **78**, 174509 (2008).
[6] C. Kurter, K. E. Gray, J. F. Zasadzinski, L. Ozyuzer, A. E. Koshelev, Q. Li, T. Yamamoto, K. Kadowaki, W.-K. Kwok, M. Tachiki, and U. Welp, Thermal management in large Bi2212 mesas used for terahertz sources, IEEE Trans. Appl. Supercond. **19**, 428 (2009).
[7] H. B. Wang, S. Guénon, J. Yuan, A. Iishi, S. Arisawa, T. Hatano, T. Yamashita, D. Koelle, and R. Kleiner, Hot Spots and Waves in $Bi_2Sr_2CaCu_2O_8$ Intrinsic Josephson Junction Stacks: A Study by Low Temperature Scanning Laser Microscopy, Phys. Rev. Lett. **102**, 017006 (2009).
[8] M. Tachiki, S. Fukuya, and T. Koyama, Mechanism of Terahertz Electromagnetic Wave Emission from Intrinsic Josephson Junctions, Phys. Rev. Lett. **102**, 127002 (2009).
[9] N. F. Pedersen and S. Madsen, THz generation using fluxon dynamics in high temperature superconductors, IEEE Trans Appl. Supercond. **19**, 726 (2009).
[10] A. E. Koshelev, Stability of dynamic coherent states in intrinsic Josephson-junction stacks near internal cavity resonance, Phys. Rev. B **82**, 174512 (2010).
[11] S. Z. Lin and X. Hu, Response and amplification of terahertz electromagnetic waves in intrinsic Josephson junctions of layered high-T_c superconductor, Phys. Rev. B **82**, 020504 (2010).
[12] M. Tsujimoto, K. Yamaki, K. Deguchi, T. Yamamoto, T. Kashiwagi, H. Minami, M. Tachiki, K. Kadowaki, and R. A. Klemm, Geometrical Resonance Conditions for THz Radiation from the Intrinsic Josephson Junctions in $Bi_2Sr_2CaCu_2O_{8+\delta}$, Phys. Rev. Lett. **105**, 037005 (2010).
[13] H. B. Wang, S. Guénon, B. Gross, J. Yuan, Z. G. Jiang, Y. Y. Zhong, M. Grünzweig, A. Iishi, P. H. Wu, T. Hatano, D. Koelle, and R. Kleiner, Coherent Terahertz Emission of Intrinsic Josephson Junction Stacks in the Hot Spot Regime, Phys. Rev. Lett. **105**, 057002 (2010).
[14] S. Guénon, M. Grünzweig, B. Gross, J. Yuan, Z. G. Jiang, Y. Y. Zhong, M. Y. Li, A. Iishi, P. H. Wu, T. Hatano, R. G. Mints, E. Goldobin, D. Koelle, H. B. Wang, and R. Kleiner, Interaction of hot spots and terahertz waves in $Bi_2Sr_2CaCu_2O_8$ intrinsic Josephson junction stacks of various geometry, Phys. Rev. B **82**, 214506 (2010).
[15] V. M. Krasnov, Coherent flux-flow emission from stacked Josephson junctions: Nonlocal radiative boundary conditions and the role of geometrical resonances, Phys. Rev. B **82**, 134524 (2010).
[16] V. M. Krasnov, Terahertz electromagnetic radiation from intrinsic Josephson junctions at zero magnetic field via breather-type self-oscillations, Phys. Rev. B **83**, 174517 (2011).
[17] A. Yurgens, Temperature distribution in a large $Bi_2Sr_2CaCu_2O_{8+\delta}$ mesa, Phys. Rev. B **83**, 184501 (2011).
[18] T. M. Benseman, A. E. Koshelev, K. E. Gray, W.-K. Kwok, U. Welp, K. Kadowaki, M. Tachiki, and T. Yamamoto, Tunable terahertz emission from $Bi_2Sr_2CaCu_2O_{8+\delta}$ mesa devices, Phys. Rev. B **84**, 064523 (2011).
[19] T. Koyama, H. Matsumoto, M. Machida, and Y. Ota, Multiscale simulation for terahertz wave emission from the intrinsic Josephson junctions, Supercond. Sci. Technol. **24**, 085007 (2011).
[20] M. Tsujimoto, H. Minami, K. Delfanazari, M. Sawamura, R. Nakayama, T. Kitamura, T. Yamamoto, T. Kashiwagi, T. Hattori, and K. Kadowaki, Terahertz imaging system using high-T_c superconducting oscillation devices, J. Appl. Phys. **111**, 123111 (2012).
[21] S. Z. Lin and X. Hu, In-plane dissipation as a possible synchronization mechanism for terahertz radiation from intrinsic Josephson junctions of layered superconductors, Phys. Rev. B **86**, 054506 (2012).
[22] M. Y. Li, J. Yuan, N. V. Kinev, J. Li, B. Gross, S. Guénon, A. Ishii, K. Hirata, T. Hatano, D. Koelle, R. Kleiner, V. P. Koshelets, H. B. Wang, and P. H. Wu, Linewidth dependence of coherent terahertz emission from $Bi_2Sr_2CaCu_2O_8$ intrinsic Josephson junction stacks in the hot-spot regime, Phys. Rev. B **86**, 060505(R) (2012).
[23] I. Kakeya, Y. Omukai, T. Yamamoto, K. Kadowaki, and M. Suzuki, Effect of thermal inhomogeneity for terahertz radiation from intrinsic Josephson junction stacks of $Bi_2Sr_2CaCu_2O_{8+\delta}$, Appl. Phys. Lett. **100**, 242603 (2012).
[24] B. Gross, S. Guénon, J. Yuan, M. Y. Li, J. Li, A. Ishii, R. G. Mints, T. Hatano, P. H. Wu, D. Koelle, H. B. Wang, and R. Kleiner, Hot-spot formation in stacks of intrinsic Josephson junctions in $Bi_2Sr_2CaCu_2O_8$, Phys. Rev. B **86**, 094524 (2012).
[25] J. Yuan, M. Y. Li, J. Li, B. Gross, A. Ishii, K. Yamaura, T. Hatano, K. Hirata, E. Takayama-Muromachi, P. H. Wu, D. Koelle, R. Kleiner, and H. B. Wang, Terahertz emission from $Bi_2Sr_2CaCu_2O_8$ intrinsic Josephson junction stacks with all-superconducting electrodes, Supercond. Sci. Technol. **25**, 075015 (2012).
[26] T. Kashiwagi, M. Tsujimoto, T. Yamamoto, H. Minami, K. Yamaki, K. Delfanazari, K. Deguchi, N. Orita, T. Koike, R. Nakayama, T. Kitamura, M. Sawamura, S. Hagino, K. Ishida, K. Ivanovic, H. Asai, M. Tachiki, R. A. Klemm, and K. Kadowaki, High temperature superconductor terahertz emitters: Fundamental physics and its applications, J. Appl. Phys. **51**, 010113 (2012).
[27] S. Sekimoto, C. Watanabe, H. Minami, T. Yamamoto, T. Kashiwagi, R. A. Klemm, and K. Kadowaki, Continuous

30 μW terahertz source by a high-T_c superconductor mesa structure, Appl. Phys. Lett. **103**, 182601 (2013).

[28] I. Kawayama, C. H. Zhang, H. B. Wang, and M. Tonouchi, Study on terahertz emission and optical/terahertz pulse responses with superconductors, Supercond. Sci. Technol. **26**, 093002 (2013).

[29] T. M. Benseman, A. E. Koshelev, W.-K. Kwok, U. Welp, K. Kadowaki, J. R. Cooper, and G. Balakrishnan, The ac Josephson relation and inhomogeneous temperature distributions in large $Bi_2Sr_2CaCu_2O_{8+\delta}$ mesas for THz emission, Supercond. Sci. Technol. **26**, 085016 (2013).

[30] T. M. Benseman, K. E. Gray, A. E. Koshelev, W.-K. Kwok, U. Welp, H. Minami, K. Kadowaki, and T. Yamamoto, Powerful terahertz emission from $Bi_2Sr_2CaCu_2O_{8+\delta}$ mesa arrays, Appl. Phys. Lett. **103**, 022602 (2013).

[31] T. M. Benseman, A. E. Koshelev, W.-K. Kwok, U. Welp, V. K. Vlasko-Vlasov, K. Kadowaki, H. Minami, and C. Watanabe, Direct imaging of hot spots in $Bi_2Sr_2CaCu_2O_{8+\delta}$ mesa terahertz sources, J. Appl. Phys. **113**, 133902 (2013).

[32] B. Gross, J. Yuan, D. Y. An, M. Y. Li, N. V. Kinev, X. J. Zhou, M. Ji, Y. Huang, T. Hatano, R. G. Mints, V. P. Koshelets, P. H. Wu, H. B. Wang, D. Koelle, and R. Kleiner, Modeling the linewidth dependence of coherent terahertz emission from intrinsic Josephson junction stacks in the hot-spot regime, Phys. Rev. B **88**, 014524 (2013).

[33] D. Y. An, J. Yuan, N. V. Kinev, M. Y. Li, Y. Huang, M. Ji, H. Zhang, Z. L. Sun, L. Kang, B. B. Jin, J. Chen, J. Li, B. Gross, A. Ishii, K. Hirata, T. Hatano, V. P. Koshelets, D. Koelle, R. Kleiner, H. B. Wang, W. W. Xu, and P. H. Wu, Terahertz emission and detection both based on high-T_c superconductors: Towards an integrated receiver, Appl. Phys. Lett. **102**, 092601 (2013).

[34] F. Turkoglu, L. Ozyuzer, H. Koseoglu, Y. Demirhan, S. Preu, S. Malzer, Y. Simsek, H. B. Wang, and P. Müller, Emission of the THz waves from large area mesas of superconducting $Bi_2Sr_2CaCu_2O_8$ by the injection of spin polarized current, Physica (Amsterdam) C **491**, 7 (2013).

[35] K. Kadowaki, M. Tsujimoto, K. Delfanazari, T. Kitamura, M. Sawamura, H. Asai, T. Yamamoto, K. Ishida, C. Watanabe, and S. Sekimoto, Quantum terahertz electronics (QTE) using coherent radiation from high temperature superconducting $Bi_2Sr_2CaCu_2O_8$ intrinsic Josephson junctions, Physica (Amsterdam) C **491**, 2 (2013).

[36] H. Minami, C. Watanabe, K. Sato, S. Sekimoto, T. Yamamoto, T. Kashiwagi, R. A. Klemm, and K. Kadowaki, Local SiC photoluminescence evidence of hot spot formation and sub-THz coherent emission from a rectangular $Bi_2Sr_2CaCu_2O_{8+\delta}$ mesa, Phys. Rev. B **89**, 054503 (2014).

[37] T. Kashiwagi, K. Nakade, B. Markovic, Y. Saiwai, H. Minami, T. Kitamura, C. Watanabe, K. Ishida, S. Sekimoto, K. Asanuma, T. Yasui, Y. Shibano, M. Tsujimoto, T. Yamamoto, J. Mirkovic, and K. Kadowaki, Reflection type of terahertz imaging system using a high-T_c superconducting oscillator, Appl. Phys. Lett. **104**, 022601 (2014).

[38] T. Kashiwagi, K. Nakade, Y. Saiwai, H. Minami, T. Kitamura, C. Watanabe, K. Ishida, S. Sekimoto, K. Asanuma, T. Yasui, Y. Shibano, M. Tsujimoto, T. Yamamoto, B. Markovic, J. Mirkovic, R. A. Klemm, and K. Kadowaki, Computed tomography image using sub-terahertz waves generated from a high-T_c superconducting intrinsic Josephson junction oscillator, Appl. Phys. Lett. **104**, 082603 (2014).

[39] A. Grib and P. Seidel, The influence of external separate heating on the synchronization of Josephson junctions, Phys. Status Solidi B **251**, 1040 (2014).

[40] M. Ji, J. Yuan, B. Gross, F. Rudau, D. Y. An, M. Y. Li, X. J. Zhou, Y. Huang, H. C. Sun, Q. Zhu, J. Li, N. Kinev, T. Hatano, V. P. Koshelets, D. Koelle, R. Kleiner, W. W. Xu, B. B. Jin, H. B. Wang, and P. H. Wu, $Bi_2Sr_2CaCu_2O_8$ intrinsic Josephson junction stacks with improved cooling: Coherent emission above 1 THz, Appl. Phys. Lett. **105**, 122602 (2014).

[41] H. Asai and S. Kawabata, Intense terahertz emission from intrinsic Josephson junctions by external heat control, Appl. Phys. Lett. **104**, 112601 (2014).

[42] T. Kitamura, T. Kashiwagi, T. Yamamoto, M. Tsujimoto, C. Watanabe, K. Ishida, S. Sekimoto, K. Asanuma, T. Yasui, K. Nakade, Y. Shibano, Y. Saiwai, H. Minami, R. A. Klemm, and K. Kadowaki, Broadly tunable, high-power terahertz radiation up to 73 K from a stand-alone $Bi_2Sr_2CaCu_2O_{8+\delta}$ mesa, Appl. Phys. Lett. **105**, 202603 (2014).

[43] M. Tsujimoto, H. Kambara, Y. Maeda, Y. Yoshioka, Y. Nakagawa, and I. Kakeya, Dynamic control of temperature distributions in stacks of intrinsic Josephson junctions in $Bi_2Sr_2CaCu_2O_{8+\delta}$ for intense terahertz radiation, Phys. Rev. Appl. **2**, 044016 (2014).

[44] H. B. Wang, M. Y. Li, J. Yuan, N. Kinev, J. Li, B. Gross, S. Guénon, A. Ishii, T. Hatano, D. Koelle, R. Kleiner, V. P. Koshelets, and P. H. Wu, in *IEEE Proceedings of the 37th International Conference on Infrared, Millimeter, and Terahertz Waves* (IEEE, New York, 2012).

[45] A. Yurgens and L. N. Bulaevskii, Temperature distribution in a stack of intrinsic Josephson junctions with their CuO-plane electrodes oriented perpendicular to supporting substrate, Supercond. Sci. Technol. **24**, 015003 (2011).

[46] H. Asai, M. Tachiki, and K. Kadowaki, Three-dimensional numerical analysis of terahertz radiation emitted from intrinsic Josephson junctions with hot spots, Phys. Rev. B **85**, 064521 (2012).

[47] C. Watanabe, H. Minami, T. Kitamura, K. Asanuma, K. Nakade, T. Yasui, Y. Saiwai, Y. Shibano, T. Yamamoto, T. Kashiwagi, R. A. Klemm, and K. Kadowaki, Influence of the local heating position on the terahertz emission power from high-T_c superconducting $Bi_2Sr_2CaCu_2O_{8+\delta}$ mesas, Appl. Phys. Lett. **106**, 042603 (2015).

[48] T. Kashiwagi, T. Yamamoto, T. Kitamura, K. Asanuma, C. Watanabe, K. Nakade, T. Yasui, Y. Saiwai, Y. Shibano, H. Kubo, K. Sakamoto, T. Katsuragawa, M. Tsujimoto, K. Delfanazari, R. Yoshizaki, H. Minami, R. A. Klemm, and K. Kadowaki, Generation of electromagnetic waves from 0.3 to 1.6 terahertz with a high-T_c superconducting $Bi_2Sr_2CaCu_2O_{8+\delta}$ intrinsic Josephson junction emitter, Appl. Phys. Lett. **106**, 092601 (2015).

[49] U. Welp, K. Kadowaki, and R. Kleiner, Superconducting emitters of THz radiation, Nat. Photonics **7**, 702 (2013).

Publication 6

Three-terminal stand-alone superconducting terahertz emitter

Xianjing Zhou,[1,2] Qiang Zhu,[1] Min Ji,[1,2] Deyue An,[1,2] Luyao Hao,[1,2] Hancong Sun,[1] Shigeyuki Ishida,[3] Fabian Rudau,[4] Raphael Wieland,[4] Jun Li,[1] Dieter Koelle,[4] Hiroshi Eisaki,[3] Yoshiyuki Yoshida,[3] Takeshi Hatano,[2] Reinhold Kleiner,[4] Huabing Wang,[1,2,a)] and Peiheng Wu[1]

[1]*Research Institute of Superconductor Electronics, Nanjing University, Nanjing 210093, China*
[2]*National Institute for Materials Science, Tsukuba 3050047, Japan*
[3]*Electronics and Photonics Research Institute, Advanced Industrial Science and Technology, Tsukuba 3058568, Japan*
[4]*Physikalisches Institut and Center for Collective Quantum Phenomena in LISA$^+$, Universität Tübingen, Tübingen D-72076, Germany*

(Received 19 July 2015; accepted 10 September 2015; published online 22 September 2015)

We report on the electrothermal behavior and the terahertz emission properties of a stand-alone $Bi_2Sr_2CaCu_2O_8$ intrinsic Josephson junction stack contacted in a three-terminal configuration. One terminal is used as a collective ground while the other two, contacting the stack from its right and left side, allow to vary the current injection profile. At high bias, a hot spot forms in the stack. Its appearance and position can be controlled by varying the ratios of the injected currents. Depending on this ratio, the emitted power can vary by an order of magnitude. Further, for a given total injection current, the device allows to vary the emission frequency on a 10% level by altering the injection profile. The overall tunability of the emission frequency, varying also the total bias current, is on the order of 20%. © *2015 AIP Publishing LLC*. [http://dx.doi.org/10.1063/1.4931623]

The study of emitters of coherent terahertz (THz) radiation made of $Bi_2Sr_2CaCu_2O_8$ (BSCCO) became a hot topic in recent years,[1–49] for a recent review, see Ref. 50. BSCCO naturally forms 1.5 nm thick intrinsic Josephson junctions (IJJs).[51] To create a THz emitter, one patterns a stack of hundreds of such IJJs from a single crystal. Typically, the stack is $\sim$300 μm long and $\sim$50 μm wide. It is often patterned as a mesa on top of a BSCCO base crystal. The stack is usually current biased and operated in the resistive state of all IJJs. If the voltages across each junction are identical, the stack radiates at the Josephson frequency $f_e = V/N\Phi_0$, where V is the total voltage, N is the number of IJJs, and Φ_0 is the flux quantum. For $V/N = 1$ mV, $f_e = 483.6$ GHz. The IJJs in the stack presumably become phase synchronized via the excitation of resonant modes utilizing the whole mesa as a cavity.[1] The maximum voltage V_{max} across the stack is limited by Joule heating. The BSCCO out-of-plane resistivity strongly decreases with increasing temperature. Consequently, when increasing the bias current I from zero at a given bath temperature T_b, V initially increases but starts to decrease when Joule heating becomes dominant.[1] For typical mesas, V_{max}/N is 1–2 mV, limiting emission frequencies to the sub-THz regime. At high bias the current and temperature distributions in the stack become strongly nonuniform and high-temperature regions (hot spots) coexist with moderately hot regions which are still superconducting.[5,11,12,15,21,22,27,34,41,43,47]

Besides mesas, a variety of different structures have been realized, including all-superconducting z-type stacks[23] and stand-alone stacks embedded between Au layers.[24,25,31,38,46] The emission power P_e obtained from the stand-alone stacks is often much higher than the one from mesas, reaching values up to 82 μW.[25,28,31,46] For arrays of mesas $P_e \sim 0.6$ mW has been achieved.[28] Cooling has been improved by sandwiching the stacks between substrates with high thermal conductivity. In first attempts, maximum emission frequencies near 1.05 THz were obtained.[38,40] This value was improved to more than 1.6 THz recently.[46]

The connection between hot spots, THz emission and the cavity modes has been discussed controversially. In the presence of the hot spot, the linewidth of radiation is much lower than in its absence,[20] indicating that it contributes to phase locking. Low temperature scanning laser microscopy (LTSLM) revealed that the presence of standing wave patterns depends on the hot spot position.[12] Other publications emphasized that f_e does not change much if a sudden change in the hot spot position occurs, indicating that both phenomena are in essence independent.[34,41]

For mesas the hot spot position and P_e can be manipulated, either by using two different current injection points on top of the mesa[12,42] or by using a laser to locally heat the stack.[43] For a stand-alone stack, it has been shown that in the hot-spot regime local heating by a laser beam can lead to enhanced THz emission.[44]

In view of these observations, we fabricate a stand-alone stack in a three-terminal configuration. The current is sent into the stack via two injectors, and the total current is collected at the ground. The idea is to form a tunable THz emitter allowing to control the position of the hot spot and, as a result, tune P_e and f_e. The device also allows to study the relation between THz emission and the hot spot in more detail.

Figure 1 shows a sketch of the device. To fabricate it, we first anneal a BSCCO single crystal at 650 °C, 18 Pa Ar, and 2 Pa O_2 for 48 h. After annealing, the critical temperature T_c is $\sim$83 K. Then the crystal is cut into small pieces and one flat piece is glued with epoxy onto a Si substrate. By

a)Electronic mail: hbwang1000@gmail.com

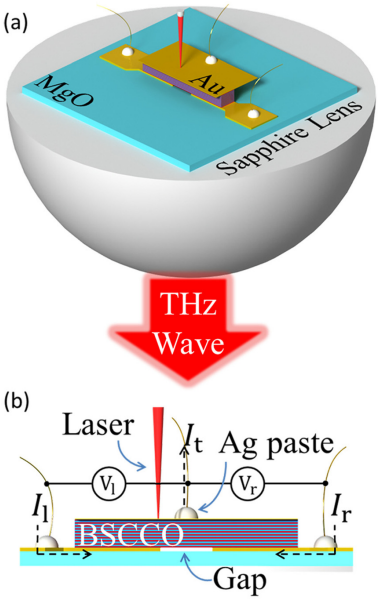

FIG. 1. (a) Sketch of the three-terminal stand-alone IJJ stack mounted on a sapphire lens and (b) side view of the stack. A gap is formed on the bottom Au layer, thus the injected current can be divided into a left bias current I_l and a right bias current I_r. The total bias current $I_t = I_r + I_l$ is collected at the top Au electrode. For LTSLM, a laser beam is focused onto the top Au electrode.

mechanical exfoliation, a fresh surface is created and a 120 nm Au layer as electrode is evaporated on this surface immediately after exfoliation. A $50 \times 330\ \mu m^2$ rectangular pattern with two injecting ports is transferred to the photoresist on the crystal surface by photolithography. After a $\sim 1\ \mu$m thick mesa is formed by ion milling, we partially remove the Au layer in the middle of the rectangle with a KI solution to separate the two injectors. Then a MgO substrate is glued to the mesa top with epoxy. The two substrates are separated, making the stack stand alone on the MgO substrate. After a second exfoliation, a 30 nm thick Au layer is deposited on this stack as a ground terminal. A second photolithography and ion milling step is performed to remove the residual BSCCO on the two injectors. The dimension of the stack after removing the residual BSCCO on the electrodes is $50 \times 300\ \mu m^2$. Its thickness is $\sim 0.6\ \mu$m. The gap on the bottom Au layer between two injectors is $\sim 75\ \mu$m wide.

The sample is mounted onto a hemispheric sapphire lens used to collect the emission. The THz wave radiates through a home-made Fourier transform infrared spectrometer, used to measure radiation spectra, and finally reaches a Si bolometer. To perform LTSLM, a focused laser with a spot diameter of $\sim 1\ \mu$m, locally heating the sample, can scan across the sample. The laser-induced local temperature rise causes changes $\Delta V\ (x_L, y_L)$ of the total voltage across the stack which depend on the laser position (x_L, y_L) and serve as the contrast for an LTSLM image. Electric transport, LTSLM, and emission measurements can be performed simultaneously.

For $T_b = 20$ K, Fig. 2 shows the current voltage characteristics (IVCs) I_t vs. V_l for six different ratios of the current I_r through the right lead over the total current $I_t = I_r + I_l$, where I_l is the current through the left lead. The voltage V_l was measured between the left lead and ground. In the figure, the dashed arrows indicate the current sweep sequence, starting at $I_t = 0$. At low currents, all IJJs are in the zero voltage state. With increasing current, first some and finally all IJJs jump to the resistive state. When lowering the currents, all IJJs remain resistive down to about 1.5 mA. There are nonlinear and temperature dependent contact resistances between all Au leads and the BSCCO stack. For $I_r/I_t = 1$, only the resistance $R_{c,gr}$ between the stack and the ground electrode adds to V_l while for the other ratios there is a substantial contribution from the contact resistance $R_{c,l}$ at the left electrode, increasing with a decreasing ratio I_r/I_t. Since the temperature distribution in the stack and thus also $R_{c,l}$ depends on I_r/I_t, it is basically impossible to correct V_l for the contact resistances,[52] in order to, e.g., relate V_l and f_e. Still one clearly observes back-bending for all IVCs for $I_t > 6.5$ mA, which is characteristic for overheating. All data discussed below were taken on the outermost branch of the IVC where all IJJs are resistive.

For $T_b = 20$ K, Fig. 3 shows a series of LTSLM images at $I_t = 16$ mA. I_t was chosen so that a hot spot has formed in the stack. In LTSLM, the signal $\Delta V\ (x_L, y_L)$ induced by a hot spot is largest near the hot-spot edges.[22] A big enough hot spot thus appears as a ring-shaped feature with a moderate signal $\Delta V\ (x_L, y_L)$ in its interior and almost no signal in the cold part of the stack. In Figs. 3(a) and 3(b) ($I_r/I_t = 0$ and 0.2), the hot spot is located in the left part of the stack. For $I_r/I_t = 0.4$ it has moved to the right, and for $I_r/I_t \geq 0.6$, it is basically situated in the right half of the stack, cf. Figs. 3(d)–3(f). No standing wave features, as they have been seen regularly in mesas,[5,11,12] are visible in the cold part of the stack. This seems to be a general feature of stand-alone stacks when operated at high bias in the presence of a hot spot. In fact, LTSLM has difficulties to visualize a potential half wave across the width of the stack, without further

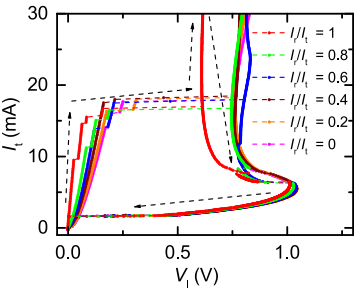

FIG. 2. Current voltage characteristics at $T_b = 20$ K, for six ratios I_r/I_t. The voltage V_l has been measured between the left electrode and ground. Dashed arrows indicate the direction of the current sweeps, starting at $I_t = V_l = 0$.

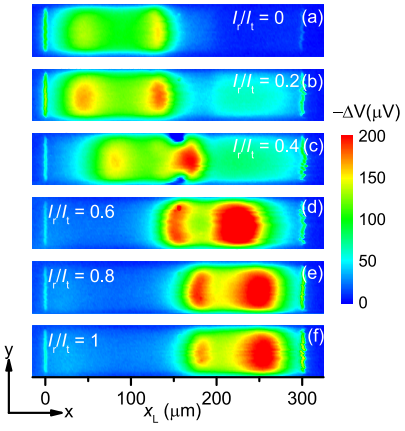

FIG. 3. LTSLM images for six ratios of I_r/I_t between 0 and 1. $T_b = 20$ K and $I_t = 16$ mA.

modulations along the length. We thus cannot rule out the presence of such a standing wave.

In Figs. 4(a)–4(f), we show, for $T_b = 20$ K, how the hot spot evolves when varying I_t for different ratios of I_r/I_t. I_t is increased in steps of 0.5 mA. For each value of I_t, line scans ΔV (x_L), taken along the center of the stack at half width, are color coded. One first notes that the pairs (a)–(f), (b)–(e), and

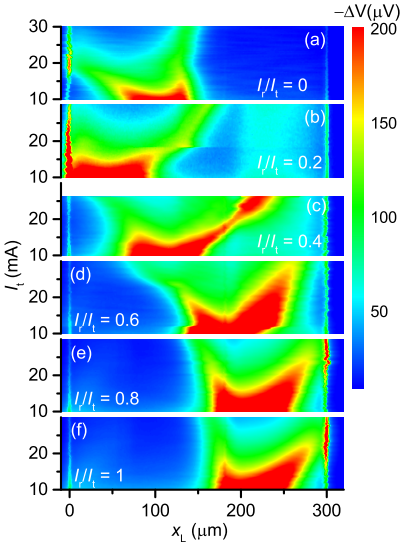

FIG. 4. For $T_b = 20$ K and six values of I_r/I_t: LTSLM line scans, taken along the center of stack, for I_t from 10 mA to 30 mA, with a step size of 0.5 mA. In (c), data have been taken up to $I_t = 26$ mA only.

(c)–(d) are not exactly mirror symmetric. This is presumably caused by the somewhat different contact resistances $R_{c,l}$ and $R_{c,r}$ of the left and right current injector providing different Joule heating for comparable values of I_t. For $I_r/I_t = 0$, the hot-spot center is near $x_L = 100\ \mu$m for $I_t = 10$ mA. With increasing I_t the hot area increases in size and, for $I_t > 12$ mA, exhibits the characteristic double peak structure with the strongest response obtained from its edges. For $I_t > 20$ mA, the complete left part of the stack is hot. With increasing I_t, the hot-spot center moves to the left while its right edge initially moves to the left and, for $I_t > 20$ mA extends towards the right side of the stack. This behavior is different from the previous experiments on mesas.[12,22] Although Figs. 3(a) and 3(b) indicated that the hot-spot position is very similar for $I_r/I_t = 0$ and 0.2, Fig. 4(b) reveals clear differences. For $I_r/I_t = 0.2$, the hot-spot center moves to the right over the whole range of currents I_t and also the right edge of the hot spot grows monotonously towards the right edge of the stack. For $I_r/I_t = 0.4$, cf. Fig. 4(c), the hot spot nucleates in the left part of the stack; with increasing current, its right edge moves rapidly towards the right. For $I_r/I_t \geq 0.6$, it is mainly situated in the right side of the stack, extending significantly to the left part only for $I_r/I_t = 0.6$ and $I_t > 20$ mA.

Figure 5(a) displays, for $T_b = 20$ K, P_e vs. I_t. In the low-bias regime, marked by a yellow ribbon in the main graph and expanded in the inset, P_e vs. I_t is peaked at currents of about 2 mA and 2.5 mA. It depends only weakly on the ratio I_r/I_t, which is not very surprising, since no hot spot has formed for these bias conditions. For the two main peaks, f_e differs by about 140 GHz. Two different cavity modes may be excited there, differing by one half wave along the long side of the stack.[53] For currents between 2.6 and 7 mA, the stack does not emit significantly. Here, the IVCs exhibit their voltage maximum V_{max} and f_e would exceed 1 THz. In principle, there are cavity modes at these frequencies but they seem to be not excited. It is worth to mention that also in numerical simulations no resonances were excited near V_{max}, due to strong in-plane damping.[48] In the high-bias regime, the overall variations of P_e with respect to both I_t and I_r/I_t are drastic. For fixed I_r/I_t, P_e exhibits short-period oscillations on top of an envelope which depends on I_r/I_t. The short-period oscillations have been observed before.[48] Presently, it is unclear whether they are intrinsic in origin or arise from interferences caused by the environment (substrate, sample holder, lens, etc.). The frequency difference between adjacent maxima in these oscillations is about 15 GHz, which is far too small to be explainable by a change of an internal cavity mode. Apart from these oscillations, one observes that, for $I_r/I_t = 1$, P_e exhibits a peak for I_t values between 15 and 21 mA, with a maximum value exceeding the low-bias emission by more than a factor of 3. When decreasing I_r/I_t to 0.8 and further to 0.6, the emission peak broadens while the maximum intensities decrease to roughly half of the maximum emission power obtained for $I_r/I_t = 1$. Interestingly, in Figs. 4(e) and 4(f), the hot spot size and location are similar for given I_t, while the differences are bigger for Fig. 4(d). This is not fully reflected in Fig. 5. For $I_r/I_t \leq 0.4$, P_e is lower than the emission power obtained at low bias. For $I_r/I_t = 0.4$—where the hot spot size and position

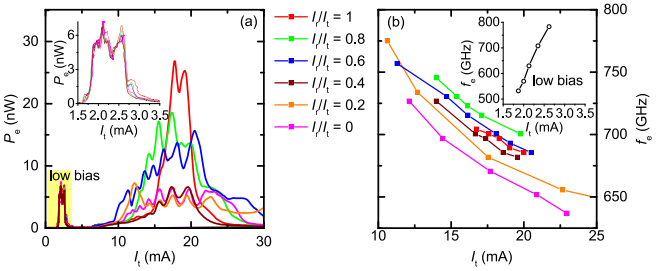

FIG. 5. For $T_b = 20$ K and six values of I_r/I_t: (a) P_e vs. I_t and (b) f_e vs. I_t. In (a), the expanded low-bias regime is shown as an inset. The low-bias regime of f_e vs. I_t is shown as an inset in (b).

depend strongly on I_t, cf. Fig. 4(c)—significant emission is obtained only for I_t between 15 and 22 mA, while for $I_r/I_t = 0.2$ and 0 the range of emission is much broader. Further, P_e is comparatively high (low) when the hot spot is located in the right (left) part of the stack. It is presently unclear whether this is due to inhomogeneities in the stack or due to some asymmetries in the way the hemispheric lens collects the radiation. In any case, it seems that fine details of the current distribution in the stack matter, which are not purely reflected in the temperature distribution or the hot spot position. This strong sensitivity on bias conditions and geometry may also explain why published data on emission intensities scatter strongly.

Finally, Fig. 5(b) displays, for $T_b = 20$ K, f_e vs. I_t for six ratios of I_r/I_t. For fixed I_r/I_t, f_e can be varied by 10%–20% by changing I_t. For fixed I_t, f_e can be varied by about 8% by changing I_r/I_t. Note that for a given I_t, f_e varies nonmonotonously with I_r/I_t, yielding smallest values for $I_r/I_t = 0$ and 0.2, and largest $I_r/I_t = 0.8$ and 0.6.

In summary, we reported on the electrothermal behavior and the THz emission properties of a stand-alone BSCCO intrinsic Josephson junction stack contacted such that the injected total bias current I_t can be split in two parts, I_r and I_l. In the high-bias regime, we observed a hot spot, the appearance and position of which can be tuned by altering the ratio I_r/I_t. In the presence of hot spots, the emitted power P_e depends strongly and nonmonotonously on I_t and I_r/I_t. Depending on these quantities, P_e may or may not exceed the power emitted at low bias. For given I_t the emission frequency f_e can be varied on a 10% level by altering I_r/I_t, and the overall tunability of f_e is on the order of 20%. In LTSLM no standing electromagnetic wave patterns were visible. It is thus unclear whether the exact hotspot position just favors or disfavors resonant modes of the stack, or affects the emission by, e.g., altering the boundary conditions for radiation.

We gratefully acknowledge the financial support by the National Natural Science Foundation of China (Grant Nos. 11234006 and 61501220), the Priority Academic Program Development of Jiangsu Higher Education Institutions, Jiangsu Provincial Natural Science Fund, Fundamental Research Funds for the Central Universities, the Deutsche Forschungsgemeinschaft (Project No. Kl930/13-1), JSPS KAKENHI Grant No. 25289108, and by the EU-FP6-COST Action MP1201.

[1]L. Ozyuzer, A. E. Koshelev, C. Kurter, N. Gopalsami, Q. Li, M. Tachiki, K. Kadowaki, T. Yamamoto, H. Minami, H. Yamaguchi, T. Tachiki, K. Gray, W. K. Kwok, and U. Welp, Science **318**, 1291 (2007).
[2]S. Z. Lin and X. Hu, Phys. Rev. Lett. **100**, 247006 (2008).
[3]A. E. Koshelev, Phys. Rev. B **78**, 174509 (2008).
[4]C. Kurter, K. E. Gray, J. Zasadzinski, L. Ozyuzer, A. E. Koshelev, Q. Li, T. Yamamoto, K. Kadowaki, W. K. Kwok, M. Tachiki, and U. Welp, IEEE Trans. Appl. Supercond. **19**, 428 (2009).
[5]H. B. Wang, S. Guénon, J. Yuan, A. Iishi, S. Arisawa, T. Hatano, T. Yamashita, D. Koelle, and R. Kleiner, Phys. Rev. Lett. **102**, 017006 (2009).
[6]M. Tachiki, S. Fukuya, and T. Koyama, Phys. Rev. Lett. **102**, 127002 (2009).
[7]N. F. Pedersen and S. Madsen, IEEE Trans Appl. Supercond. **19**, 726 (2009).
[8]A. E. Koshelev, Phys. Rev. B **82**, 174512 (2010).
[9]S. Z. Lin and X. Hu, Phys. Rev. B **82**, 020504 (2010).
[10]M. Tsujimoto, K. Yamaki, K. Deguchi, T. Yamamoto, T. Kashiwagi, H. Minami, M. Tachiki, and K. Kadowaki, Phys. Rev. Lett. **105**, 037005 (2010).
[11]H. B. Wang, S. Guénon, B. Gross, J. Yuan, Z. G. Jiang, Y. Y. Zhong, M. Grünzweig, A. Iishi, P. H. Wu, T. Hatano, D. Koelle, and R. Kleiner, Phys. Rev. Lett. **105**, 057002 (2010).
[12]S. Guénon, M. Grünzweig, B. Gross, J. Yuan, Z. G. Jiang, Y. Y. Zhong, A. Iishi, P. H. Wu, T. Hatano, D. Koelle, H. B. Wang, and R. Kleiner, Phys. Rev. B **82**, 214506 (2010).
[13]V. M. Krasnov, Phys. Rev. B **82**, 134524 (2010).
[14]V. M. Krasnov, Phys. Rev. B **83**, 174517 (2011).
[15]A. Yurgens, Phys. Rev. B **83**, 184501 (2011).
[16]T. M. Benseman, A. E. Koshelev, K.-E. Gray, W. K. Kwok, U. Welp, K. Kadowaki, M. Tachiki, and T. Yamamoto, Phys. Rev. B **84**, 064523 (2011).
[17]T. Koyama, H. Matsumoto, M. Machida, and Y. Ota, Supercond. Sci. Technol. **24**, 085007 (2011).
[18]M. Tsujimoto, H. Minami, K. Delfanazari, M. Sawamura, R. Nakayama, T. Kitamura, T. Yamamoto, T. Kashiwagi, T. Hattori, and K. Kadowaki, J. Appl. Phys. **111**, 123111 (2012).
[19]S. Z. Lin and X. Hu, Phys. Rev. B **86**, 054506 (2012).
[20]M. Y. Li, J. Yuan, N. V. Kinev, J. Li, B. Gross, S. Guénon, A. Ishii, K. Hirata, T. Hatano, D. Koelle, R. Kleiner, V. P. Koshelets, H. B. Wang, and P. H. Wu, Phys. Rev. B **86**, 060505(R) (2012).
[21]I. Kakeya, Y. Omukai, T. Yamamoto, K. Kadowaki, and M. Suzuki, Appl. Phys. Lett. **100**, 242603 (2012).
[22]B. Gross, S. Guénon, J. Yuan, M. Y. Li, J. Li, A. Iishi, R. G. Mints, T. Hatano, P. H. Wu, D. Koelle, H. B. Wang, and R. Kleiner, Phys. Rev. B **86**, 094524 (2012).
[23]J. Yuan, M. Y. Li, J. Li, B. Gross, A. Ishii, K. Yamaura, T. Hatano, K. Hirata, E. Takayama-Muromachi, P. H. Wu, D. Koelle, R. Kleiner, and H. B. Wang, Supercond. Sci. Technol. **25**, 075015 (2012).
[24]T. Kashiwagi, M. Tsujimoto, T. Yamamoto, H. Minami, K. Yamaki, K. Delfanzari, K. Deguchi, N. Orita, T. Koike, R. Nakayama, T. Kitamura, M. Sawamura, S. Hagino, K. Ishida, K. Ivancovic, H. Asai, M. Tachiki, R. A. Klemm, and K. Kadowaki, Jpn. J. Appl. Phys., Part 1 **51**, 010113 (2012).
[25]S. Sekimoto, C. Watanabe, H. Minami, T. Yamamoto, T. Kashiwagi, R. A. Klemm, and K. Kadowaki, Appl. Phys. Lett. **103**, 182601 (2013).
[26]I. Kawayama, C. Zhang, H. B. Wang, and M. Tonouchi, Supercond. Sci. Technol. **26**, 093002 (2013).

[27]T. M. Benseman, A. Koshelev, W. K. Kwok, U. Welp, K. Kadowaki, J. Cooper, and G. Balakrishnan, Supercond. Sci. Technol. **26**, 085016 (2013).
[28]T. M. Benseman, K. E. Gray, A. E. Koshelev, W.-K. Kwok, U. Welp, H. Minami, K. Kadowaki, and T. Yamamoto, Appl. Phys. Lett. **103**, 022602 (2013).
[29]T. M. Benseman, A. E. Koshelev, W.-K. Kwok, U. Welp, V. K. Vlasko-Vlasov, K. Kadowaki, H. Minami, and C. Watanabe, J. Appl. Phys. **113**, 133902 (2013).
[30]B. Gross, J. Yuan, D. Y. An, M. Y. Li, N. V. Kinev, X. J. Zhou, M. Ji, Y. Huang, T. Hatano, R. G. Mints, V. P. Koshelets, P. H. Wu, H. Wang, D. Koelle, and R. Kleiner, Phys. Rev. B **88**, 014524 (2013).
[31]D. Y. An, J. Yuan, N. V. Kinev, M. Y. Li, Y. Huang, M. Ji, H. Zhang, Z. L. Sun, L. Kang, B. B. Jin, J. Chen, J. Li, B. Gross, A. Ishii, K. Hirata, T. Hatano, V. P. Koshelets, D. Koelle, R. Kleiner, H. B. Wang, W. W. Xu, and P. H. Wu, Appl. Phys. Lett. **102**, 092601 (2013).
[32]F. Turkoglu, L. Ozyuzer, H. Koseoglu, Y. Demirhan, S. Preu, S. Malzer, Y. Simsek, H. B. Wang, and P. Müller, Physica C **491**, 7 (2013).
[33]K. Kadowaki, M. Tsujimoto, K. Delfanazari, T. Kitamura, M. Sawamura, H. Asai, T. Yamamoto, K. Ishida, C. Watanabe, and S. Sekimoto, Physica C **491**, 2 (2013).
[34]H. Minami, C. Watanabe, K. Sato, S. Sekimoto, T. Yamamoto, T. Kashiwagi, R. A. Klemm, and K. Kadowaki, Phys. Rev. B **89**, 054503 (2014).
[35]T. Kashiwagi, K. Nakade, B. Marković, Y. Saiwai, H. Minami, T. Kitamura, C. Watanabe, K. Ishida, S. Sekimoto, K. Asanuma, T. Yasui, Y. Shibano, M. Tsujimoto, T. Yamamoto, J. Mirković, and K. Kadowaki, Appl. Phys. Lett. **104**, 022601 (2014).
[36]T. Kashiwagi, K. Nakade, Y. Saiwai, H. Minami, T. Kitamura, C. Watanabe, K. Ishida, S. Sekimoto, K. Asanuma, T. Yasui, Y. Shibano, M. Tsujimoto, T. Yamamoto, B. Marković, J. Mirković, R. A. Klemm, and K. Kadowaki, Appl. Phys. Lett. **104**, 082603 (2014).
[37]A. Grib and P. Seidel, Phys. Status Solidi B **251**, 1040 (2014).
[38]M. Ji, J. Yuan, B. Gross, F. Rudau, D. Y. An, M. Y. Li, X. J. Zhou, Y. Huang, H. C. Sun, Q. Zhu, J. Li, N. Kinev, T. Hatano, V. P. Koshelets, D. Koelle, R. Kleiner, W. W. Xu, B. B. Jin, H. B. Wang, and P. H. Wu, Appl. Phys. Lett. **105**, 122602 (2014).
[39]H. Asai and S. Kawabata, Appl. Phys. Lett. **104**, 112601 (2014).
[40]T. Kitamura, T. Kashiwagi, T. Yamamoto, M. Tsujimoto, C. Watanabe, K. Ishida, S. Sekimoto, K. Asanuma, T. Yasui, K. Nakade, Y. Shibano, Y. Saiwai, H. Minami, R. A. Klemm, and K. Kadowaki, Appl. Phys. Lett. **105**, 202603 (2014).
[41]C. Watanabe, H. Minami, T. Yamamoto, T. Kashiwagi, R. A. Klemm, and K. Kadowaki, J. Phys.: Condens. Matter **26**, 172201 (2014).
[42]M. Tsujimoto, H. Kambara, Y. Maeda, Y. Yoshioka, Y. Nakagawa, and I. Kakeya, Phys. Rev. Appl. **2**, 044016 (2014).
[43]C. Watanabe, H. Minami, T. Kitamura, K. Asanuma, K. Nakade, T. Yasui, Y. Saiwai, Y. Shibano, T. Yamamoto, T. Kashiwagi, R. A. Klemm, and K. Kadowaki, Appl. Phys. Lett. **106**, 042603 (2015).
[44]X. J. Zhou, J. Yuan, H. Wu, Z. S. Gao, M. Ji, D. Y. An, Y. Huang, F. Rudau, R. Wieland, B. Gross, N. Kinev, J. Li, A. Ishii, T. Hatano, V. P. Koshelets, D. Koelle, R. Kleiner, H. B. Wang, and P. H. Wu, Phys. Rev. Appl. **3**, 044012 (2015).
[45]L. Hao, M. Ji, J. Yuan, D. An, M. Li, X. Zhou, Y. Huang, H. Sun, Q. Zhu, F. Rudau, R. Wieland, N. Kinev, J. Li, W. Xu, B. Jin, J. Chen, T. Hatano, V. Koshelets, D. Koelle, R. Kleiner, H. Wang, and P. Wu, Phys. Rev. Appl. **3**, 024006 (2015).
[46]T. Kashiwagi, T. Yamamoto, T. Kitamura, K. Asanuma, C. Watanabe, K. Nakade, T. Yasui, Y. Saiwai, Y. Shibano, H. Kubo, K. Sakamoto, T. Katsuragawa, M. Tsujimoto, K. Delfanazari, R. Yoshizaki, H. Minami, R. A. Klemm, and K. Kadowaki, Appl. Phys. Lett. **106**, 092601 (2015).
[47]T. M. Benseman, A. E. Koshelev, V. Vlasko-Vlasov, Y. Hao, W.-K. Kwok, U. Welp, C. Keiser, B. Gross, M. Lange, D. Kölle, R. Kleiner, H. Minami, C. Watanabe, and K. Kadowaki, Phys. Rev. Appl. **3**, 044017 (2015).
[48]F. Rudau, M. Tsujimoto, B. Gross, T. Judd, R. Wieland, E. Goldobin, N. Kinev, J. Yuan, Y. Huang, M. Ji, X. Zhou, D. An, A. Ishii, R. Mints, P. Wu, T. Hatano, H. Wang, V. Koshelets, D. Koelle, and R. Kleiner, Phys. Rev. B **91**, 104513 (2015).
[49]I. Kakeya, N. Hirayama, Y. Omukai, and M. Suzuki, J. Appl. Phys. **117**, 043914 (2015).
[50]U. Welp, K. Kadowaki, and R. Kleiner, Nat. Photonics **7**, 702 (2013).
[51]R. Kleiner, F. Steinmeyer, G. Kunkel, and P. Müller, Phys. Rev. Lett. **68**, 2394 (1992).
[52]The contact resistances depend nontrivially both on I_t and I_r/I_t. From a simultaneous measurement of V_t and V_r, for $I_r/I_t = 1$ ($I_r/I_t = 0$), $R_{c,t}$ ($R_{c,r}$) can be determined. However, the contact resistances $R_{c,t}$ (I_t, $I_r/I_t = 1$) and $R_{c,t}$ (I_t, $I_r/I_t = 0$) differ from the general functions $R_{c,t}$ (I_t, I_r/I_t) and $R_{c,r}$ (I_t, I_r/I_t).
[53]Using $\Delta f_e \approx c_1/(2L)$, with the mode velocity $c_1 \approx 7 \times 10^7$ m/s and the stack length $L = 300$ μm one finds $\Delta f_e \approx 120$ GHz.

Publication 7

IOP Publishing Superconductor Science and Technology
Supercond. Sci. Technol. 30 (2017) 034006 (7pp) https://doi.org/10.1088/1361-6668/aa55ae

Tuning THz emission properties of $Bi_2Sr_2CaCu_2O_{8+\delta}$ intrinsic Josephson junction stacks by charge carrier injection

O Kizilaslan[1,2], F Rudau[1], R Wieland[1], J S Hampp[1], X J Zhou[3,4], M Ji[3,4], O Kiselev[5], N Kinev[5], Y Huang[3,4], L Y Hao[4], A Ishii[3], M A Aksan[6], T Hatano[3], V P Koshelets[5], P H Wu[4], H B Wang[3,4], D Koelle[1] and R Kleiner[1]

[1] Physikalisches Institut and Center for Quantum Science (CQ) in LISA$^+$, Universität Tübingen, D-72076 Tübingen, Germany
[2] Inonu University, Department of Biomedical Engineering, Faculty of Engineering 44280, Malatya, Turkey
[3] National Institute for Materials Science, Tsukuba 3050047, Japan
[4] Research Institute of Superconductor Electronics, Nanjing University, Nanjing 210093, People's Republic of China
[5] Kotel'nikov Institute of Radio Engineering and Electronics, Russia
[6] Inonu University, Faculty of Arts and Sciences, Department of Physics, 44280 Malatya, Turkey

E-mail: olcay.kizilaslan@inonu.edu.tr

Received 9 November 2016, revised 14 December 2016
Accepted for publication 23 December 2016
Published 1 February 2017

Abstract

We report on doping and undoping experiments of terahertz (THz) emitting intrinsic Josephson junction stacks, where the change in charge carrier concentration is achieved by heavy current injection. The experiments were performed on stand-alone structures fabricated from a $Bi_2Sr_2CaCu_2O_{8+\delta}$ single crystal near optimal doping. The stacks contained about 930 intrinsic Josephson junctions. On purpose, the doping and undoping experiments were performed over only a modest range of charge carrier concentrations, changing the critical temperature of the stack by less than 1 K. We show that both undoping and doping is feasible also for the large intrinsic Josephson junction stacks used for THz generation. Even moderate changes in doping introduce large changes in the THz emission properties of the stacks. The highest emission power was achieved after *doping* a pristine sample.

Keywords: charge carrier injection, superconductors, Josephson junctions, THz emission

(Some figures may appear in colour only in the online journal)

1. Introduction

In the high-temperature superconductor $Bi_2Sr_2CaCu_2O_{8+\delta}$ (BSCCO) superconductivity is restricted to the 0.3 nm thick CuO_2 sheets which are separated by SrO and BiO barrier layers to intrinsically form a 1.5 nm thick Josephson junction [1]. Thus, a single crystal of 1 μm thickness forms a stack of ~670 intrinsic Josephson junctions (IJJs). Suitably patterned stacks emit coherent radiation at terahertz (THz) frequencies [2–4]. The emitted frequency f_e follows the Josephson relation $f_e = V_J/\Phi_0$, where Φ_0 is the flux quantum and $\Phi_0^{-1} \approx 483.6$ GHz mV^{-1}. V_J is the voltage across a single junction. THz radiation from IJJ stacks became a hot topic in recent years both in terms of experiment [5–36] and theory [37–61]; for recent reviews, see [3, 4]. IJJ stacks used for THz emission are often rectangular in shape, with lateral dimensions around 300 × 50 μm^2, and contain typically 500–2000 junctions. The stacks have been patterned as mesas on top of BSCCO base crystals and also as bare IJJ stacks contacted by Au layers (GBG structures) [16, 17, 20, 22] and as all-superconducting *Z*-shaped structures [11]. Emission frequencies range from 0.4–2.4 THz [30]. For the best stacks, an

emission power P_e in the range of tens of μW has been achieved [17, 19, 20, 30], and arrays of mesas showed emission with P_e up to 0.61 mW [19].

The IJJ stacks are affected by Joule heating [2, 5–8, 13, 18, 21, 24, 28, 49, 52–54, 59]. For sufficiently low bias currents, the temperature rises only slightly to values above the bath temperature T_b and the voltage V across the stack increases with increasing bias current I. With increasing I and input power the current–voltage characteristics (IVCs) start to back-bend and, at some bias current in the back-bending region, a hot spot forms in the stack [5, 6, 8, 13, 18, 21, 23, 24, 32], creating a region which is heated to temperatures above the critical temperature T_c. In the IJJ stacks one can thus distinguish a low-bias regime where the temperature in the stack varies only weakly and a high-bias regime where the hot spot has formed. THz emission can be observed in both regimes.

Almost all THz emitting IJJ stacks were based on slightly underdoped BSCCO, with the exception of [33], where Bi was partially substituted by Pb. Also here the crystal was in the underdoped regime. To our knowledge, for samples in the overdoped regime no THz emission has been observed so far. One thus wonders whether or not there is an optimal charge carrier concentration for THz emission, and how both the electromagnetic and thermal properties of the IJJ stacks change with doping. Unfortunately, even for a given charge carrier concentration there is a large sample-to-sample variation of the THz emission properties, making systematic investigations difficult.

For small stacks, with lateral dimensions of a few μm consisting of some 10 IJJs, it was shown that the charge carrier concentration can be changed reversibly *in situ* by heavy current injection [62–65]. The effect is different from electromigration and oxygen diffusion and presumably related to the (un)filling of charge traps in the insulating layers [62, 63]. Using current injection both doping (increase of charge carrier concentration) and undoping (decrease of charge carrier concentration) is possible. To change the doping state of a sample the voltage V across the stack needs to exceed some threshold value V_t, which—for small stacks—is of the order of 1.3 V for doping and 1.7 V for undoping [62]. V_t is only weakly dependent on the number of junctions in the stack. Above V_t, for a fixed current the carrier concentration changes gradually, which is reflected in a change in V as a function of time. The c-axis resistivity of BSCCO increases with decreasing charge carrier concentration. Thus, doping is observed as a decrease in V while undoping appears as an increase of V. The exact bias conditions for doping/undoping can in fact be complicated [63] and may depend on the stack type. For voltages below threshold the change in carrier concentration is persistent at low temperatures. Even at room temperature it changes only slowly, on the time scale of days.

The motivation of the present work was to study if charge carrier injection can also be employed for the large stacks used for THz generation and to what extent THz emission properties are affected by carrier injection. For these stacks currents of order 100 mA or larger need to be applied to reach V_t, leading to a Joule heat load of 150 mW or even more. This is two orders of magnitude larger than the heat load produced for 'small' mesas. In [62] it was mentioned that for large mesas containing 1000 IJJs undoping started at voltages of about 2.5 V but no details were given. As we will show both doping and undoping is possible for the large stacks under study, although the margins against destroying the sample are tight. We will also see that even moderate (un)doping strongly affects the THz emission properties. On purpose, the overall change in carrier concentration has been kept low, in order to systematically follow its impact on THz emission. Surprisingly, the highest emission power was found after *doping*, i.e. for the largest charge carrier concentration studied.

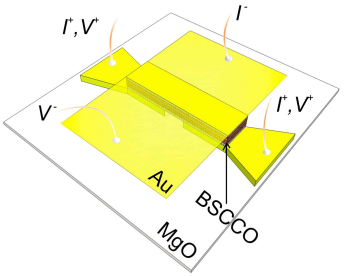

Figure 1. Sketch of the three-terminal stand-alone intrinsic Josephson junction stack used for the charge carrier injection experiments.

2. Samples and measurements

Doping and undoping experiments were performed on two mesas (lateral size: $70 \times 330\ \mu m^2$, critical temperature $T_c \approx 87$ K, junction number $N \approx 700$), and on two GBG structures contacted in a three-terminal configuration (lateral size: $50 \times 300\ \mu m^2$, $T_c \approx 88$ K, junction number $N \approx 930$). Undoping worked for all stacks, while doping was achieved for one mesa and one GBG structure. The overall (un)doping induced changes in T_c were below 1 K. For the mesas the overall THz emission power was very weak, although doping dependent. The THz emission power of the GBG structures was stronger. In the following we thus discuss data from these GBG structures, denoted stack 1 and 2.

The GBG structures are patterned in one step from the same single crystal which is near optimal doping. The stack geometry is sketched in figure 1. The sample preparation is similar to the one described in [26]. First, the crystal is glued with epoxy onto a Si substrate. Using a mechanical exfoliation method a fresh surface is created and a 120 nm Au layer as electrode is evaporated on this surface immediately after exfoliation. For each stack a $50 \times 330\ \mu m^2$ rectangular pattern with two injecting ports is transfered to the photoresist on the surface of the crystal by photolithography. After a mesa is formed by ion milling, the Au layer is removed partially in the middle of the rectangle with a KI solution to separate the two injectors. Then an MgO substrate is glued to the top of the

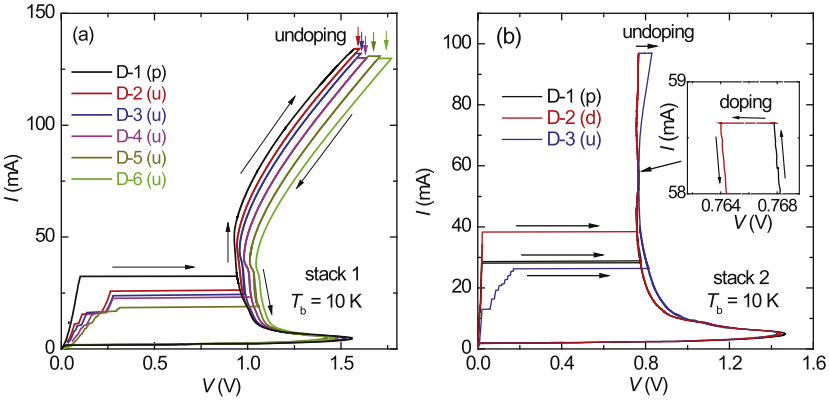

Figure 2. IVCs of (a) stack 1 and (b) stack 2 demonstrating the procedure of charge carrier injection. Curves labeled D-1, D-2 etc correspond to different doping states, starting with the pristine sample. Labels (p), (u) and (d) repectively indicate the pristine sample, undoping and doping. Bias conditions where (un)doping occurs are indicated. Measurements were performed at $T_b = 10$ K.

mesa with epoxy. The two substrates are separated, making the stacks stand alone on the MgO substrate. After a second exfoliation step another 30 nm thick Au layer is deposited on this stack as a ground terminal. A second photolithography and ion milling step is performed to remove the residual BSCCO on the injectors. The gap on the bottom Au layer between two injectors is about 75 μm wide. The thickness of both stacks is 1.4 μm, corresponding to $N \approx 930$ IJJs.

For the transport and emission measurements the samples were mounted inside an optical cryostat. The THz radiation was collected by parabolic mirrors and detected by a Ge bolometer. The c-axis resistance R was recorded as a function of bath temperature T_b, followed by a simultaneous measurement of the IVC and the emitted power at $T_b = 10$ K. Subsequently the current through the stack was strongly increased until either doping or undoping set in. After some hold time the current was reduced to zero. Measurements of R versus T_b and subsequently IVC and THz emission measurements were performed for the new doping level. This cycle was repeated several times until finally the sample got destroyed. For undoping a typical hold time was 0.5–1 h, precise numbers depending on the bias current and voltage V. For doping an initial decrease of V was seen at hold times of around 5 min, with a subsequent saturation of V for larger hold times.

For the measurements on stack 1 the two electrodes contacting the bottom of the stack were biased symmetrically; for the measurements on stack 2 only one of the split electrodes was used for current injection. The other was used as a voltage contact.

3. Results

To explain the procedure of charge carrier injection, figure 2(a) shows IVCs for stack 1. The stack was measured in a symmetrically biased two-terminal configuration, thus the contact resistances of the bottom and top electrodes to the BSCCO stack appear in the IVCs. Different colors distinguish IVCs for different doping states. The curve labeled D-1 is for the pristine sample. When increasing the current from zero one obtains near $I = 35$ mA an (instantaneous) switch from the zero voltage state of all IJJs to the fully resistive state, where all IJJs are in their resistive state. From the value of the switching current one infers a critical supercurrent density j_c of about 230 A cm^{-2}, which is in fact a factor of 4–5 lower than the critical supercurrent densities found for small-sized stacks [65]. For the large stacks used for THz generation it is likely that self-field effects limit j_c. When sweeping the current back and forth the fully resistive branch is reproducible, as long as the current is kept well below 130 mA. Undoping was performed at $I \approx 135$ mA, where $V \approx 1.56$ V. Here, V slowly drifts to larger voltages. When I is decreased after some hold time (45 min in this case) one obtains a new resistive branch (denoted D-2) representing a new doping state, with a decreased charge carrier density. In figure 2(a) the undoping process is perfomed 5 times, yielding IVCs labeled D-2 to D-6. Note that there are multiple switching steps on IVCs D-2 to D-6, indicating that upon undoping the stack becomes increasingly inhomogeneous.

Figure 2(b) shows IVCs for stack 2 for two charge carrier injection runs. Only one of the split electrodes was used for current bias, while the other was used for measuring V, i.e. a three terminal configuration was employed eliminating the contact resistance between the bottom current injection electrode and the stack. Curve D-1 shows the IVC for the pristine sample. The switch from the superconducting state to the fully resistive state occurs at $I = 28$ mA. Doping was achieved at $I \approx 59$ mA and $V \approx 0.77$ V. The corresponding IVC is labeled D-2. In fact, the change in V during the 30 min hold time was very modest at this bias, probably preventing to find the bias condition for doping for some of the other stacks.

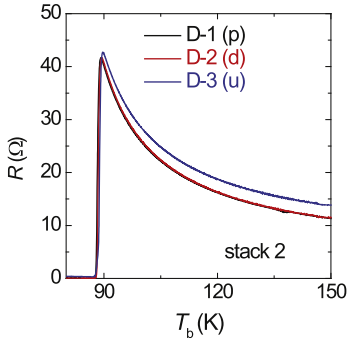

Figure 3. Temperature dependence of *c*-axis resistance for stack 2 for the pristine sample (D-1), after a doping step (D-2) and after subsequent undoping (D-3).

Further, note that the switching current from the superconducting state to the resistive state is now at 38 mA, i.e. by a factor of 1.4 higher than for IVC D-1. Like for the pristine state only a single switching step was observed, indicating that the doping procedure did not increase the sample inhomogeneity. Finally, at $I = 97$ mA undoping started and during undoping, with a hold time of 40 min, the voltage increased from 0.77 V to 0.83 V. The IVC for this new doping level is labeled D-3. On this curve, like for states D-2 to D-6 of stack 1, one observes multiple switching steps.

For bias currents below 40 mA the resistive branches of the three IVCs do not differ strongly from each other, indicating that the (low temperature) interlayer resistance has not changed very much during doping and undoping. This is also reflected in figure 3 showing R versus T_b curves for the three doping levels of stack 2. Curves for doping states D-1 and D-2 basically coincide, while for D-3 R is slightly higher, the difference to the D-1 and D-2 curves growing with increasing temperature. The critical temperatures for curves D-1 to D-3 differ by less than 0.5 K, which is within the error bars of the thermometer and consistent with the fact that the pristine sample was near optimal doping. Further, by comparing R versus T_b with V/I taken from the IVCs during undoping, we estimate that the stack temperature during undoping was around 200–250 K. Also for stack 1 the change in T_c was below 1 K. Thus, for both stacks and all (un)doping procedures the hole concentration was in the range 0.16 ± 0.01 holes per Cu atom.

Also note that in figure 2 the back-bending of the IVCs starting near $I = 5$ mA occurs at voltages V_{max} which are comparable (stack 1) or significantly larger (stack 2) than the high-current threshold voltages V_t for doping and undoping. We never found (un)doping effects in the low-bias region near V_{max}, where the hot spot has not yet formed and, according to simulations [60, 61], the temperature in the stack exceeds T_b by less than 40 K. Thus, either V_t strongly decreases with increasing temperature or a large current is needed in addition to start the (un)doping processes.

Let us now turn to the THz emission properties. For both samples emission occurred at currents below 10 mA, and this regime is shown in figure 4 for stack 1 and in figure 5 for stack 2. Figure 4(a) displays IVCs for doping state D-1 (pristine sample) and undoped states D-2, D-3, D-5 and D-6. In the back-bending region of the IVCs, i.e., for currents between 6 and 10 mA, the emission power P_e is very low for the pristine stack, rises for doping states D-2 and D-3 and is again almost absent for doping states D-4 and D-5, see figure 4(b). In this regime, there are peaks in P_e versus I which occur at very different currents for the different doping states. For currents between 4 and 6 mA, i.e. near V_{max}, only the pristine stack showed noticeable radiation, see figure 4(b). For currents between 2 and 4 mA the highest emission power was much stronger than for larger bias currents. In the low-bias regime, the emission data for the different doping states are best resolved in the P_e versus V plot, see figure 4(c). The highest values of P_e are observed for voltages below $V = 1$ V. Here, jumps in the IVCs indicate that some of the junctions have switched back to their superconducting state. Thus, the number of junctions in the resistive state varies, making it difficult to compare P_e for the different doping states. On the other hand, for voltages above 1.1 V for doping states D-1 to D-3, and above 0.98 V for doping states D-5 and D-6, no switch-back was detectable and presumably all IJJs were in their resistive state. For the pristine stack there is a peak in P_e near $V = 1.19$ V. For the marginally different doping states D-2 and D-3 one observes an emission peak near 1.15 V. At this voltage the IVC exhibits a bump indicating that an electromagnetic cavity mode has been excited. Such bumps in the IVCs of IJJ stacks have been observed before, see e.g. [2]. In figure 4 we have drawn a vertical line between graphs (a) and (c) to show that the bumps on the IVCs and the emission peaks for doping states D-2 and D-3 occur at the same voltage. A peak in P_e versus V and a corresponding bump in the IVC is also observed for doping state D-6, see left vertical line between figures 4(a) and (c). The emission peak in fact is asymmetric and may consist of a double-peak structure with peak voltages near 1.12 V and 1.06 V, respectively. For doping state D-5 an emission peak and a corresponding bump in the IVC occurs near $V = 1.02$ V. A possible explanation for the peaks and bumps and their variation for different doping states is that in the series D-1 to D-6 two different resonances have been excited. The voltage position of the peak seems to shift to lower values for the series D-1 to D-5. In a first approach one may associate the observed shift with a change in contact resistance during the various undoping steps. Indeed, as can be seen from figure 4(a) the contact resistance increases during undoping, from about 4.6 Ω for the pristine stack to about 15 Ω for doping state D-6. However, if one corrected the IVCs for the contact resistances the voltage shift in the bumps and peaks would *increase* rather than decrease. The shift thus needs further discussion.

For stacks 1 and 2 we do not have frequency resolved emission spectra but for other samples we found that in the fully resistive state and in particular also near bumps in the IVC almost all IJJs participate in radiation. We have also seen before that the bumps in the IVCs shift towards lower

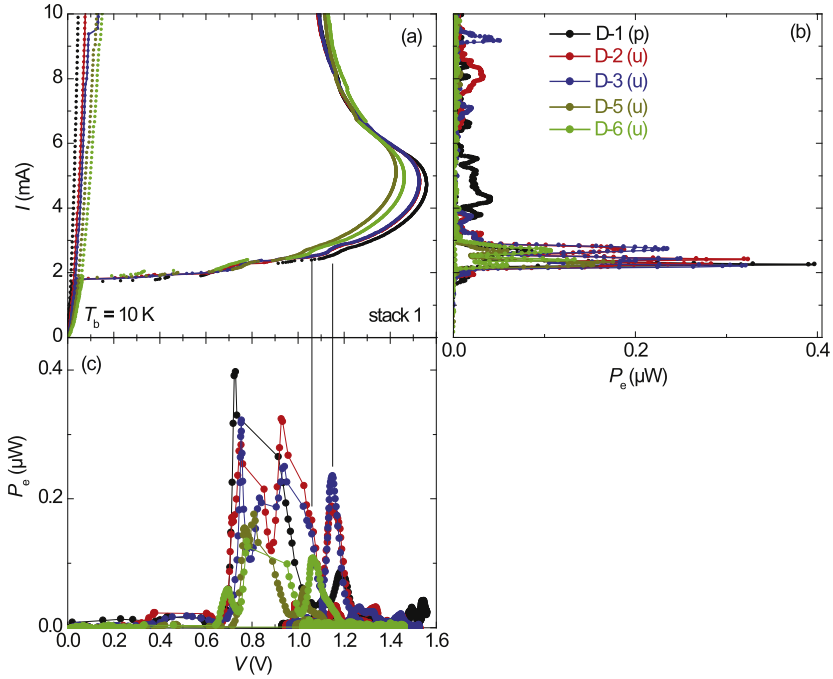

Figure 4. THz emission properties of stack 1, measured at $T_b = 10$ K for the 5 doping states indicated: (a) IVCs, (b) emitted power P_e versus I and (c) emitted power P_e versus V. Vertical lines between (a) and (c) are a guide to the eye indicating peaks in P_e versus V and corresponding bumps in the IVCs. Labels (p) and (u) indicate the pristine sample (p) and different runs of undoping (u).

voltages when increasing the bath temperature. A similar effect may work for stack 1. In the series D-1 to D-6 the hole carrier concentration decreases and the *c*-axis resistivity at given temperature increases. The *c*-axis resistivity at given hole carrier concentration strongly increases with decreasing temperature for underdoped samples and also near optimal doping. For a given current I and bath temperature this implies that the increase in resistance with decreasing charge carrier concentration can be over-compensated by the decrease of R due to the local temperature increase arising from Joule heating. The (in-phase) cavity resonance frequency is proportional to the mode velocity c_1 which decreases with increasing temperature, see e.g. [60]. We thus expect a decrease in the cavity mode resonance frequencies with increasing stack temperature. To explain the shift in the bumps in the IVCs and of the peaks in P_e versus V one may also consider a doping dependence of the dielectric constant ε and consequently of the diffraction index. Such a dependence was derived from measurements of the Josephson plasma frequency [66]. Near optimal doping ε decreases weakly with decreasing hole concentration. One would thus expect an *increase* of the cavity resonance frequency for the series D-1 to D-6.

Apart from such details the basic message of the overall figure 4 is that THz emission properties enormously depend on the doping state of the sample even for the modest changes we have introduced within our undoping sequence. This conclusion can also be given for the case of stack 2, for which THz emission data are shown in figure 5. For this stack THz emission occurred for currents below 8.5 mA. The highest emission power was detected for doping state D-2, which is remarkable since, typically, IJJ stacks fabricated from slightly underdoped crystals emit best. A possible reason could be an improvement of the local sample homogeneity during doping. As can be seen from a comparison of figures 5(a) and (c), both for the pristine stack and for doping state D-2 the highest emission occurred at voltages where some of the junctions have returned to their superconducting state. For currents between 5 and 8.5 mA, i.e. in the back-bending region of the IVCs peaks exhibiting some fine structures can be observed in P_e versus I. For all doping states there is a broad emission peak between 5.3 and 7 mA which has about the same amplitude for doping states D-1 and D-2 and a much smaller one for doping state D-3. Another peak is visible for all three doping states for currents in the low-bias regime near 3 mA and voltages near 1.05 V, see figure 5(c). Like for stack 1

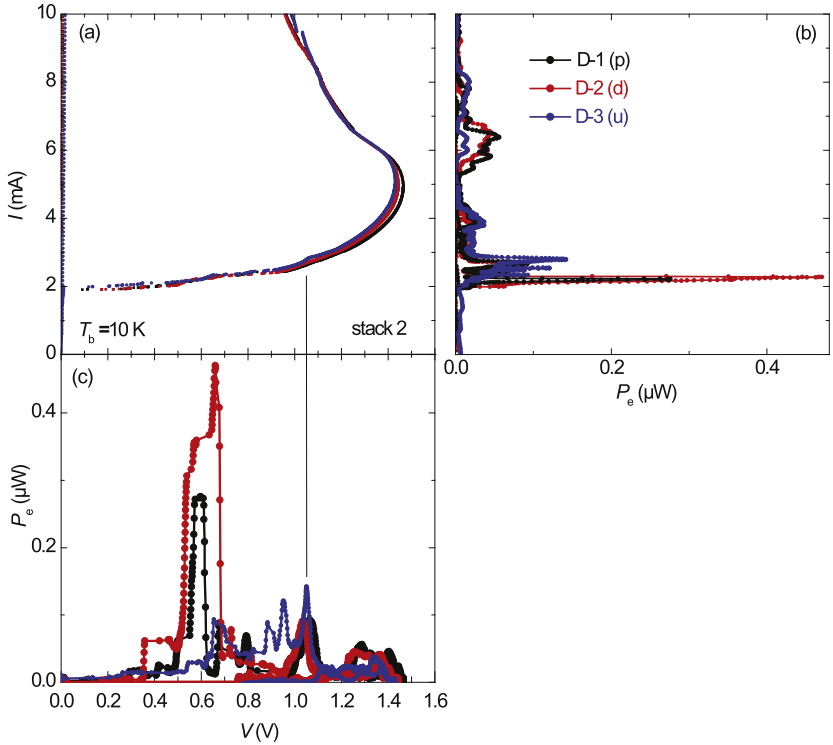

Figure 5. THz emission properties of stack 2, measured at $T_b = 10$ K for doping states D-1 to D-3. (a) IVCs, (b) emitted power P_e versus I and (c) emitted power P_e versus V. Vertical line between (a) and (c) is a guide to the eye indicating peaks in P_e versus V and corresponding bumps in the IVCs. Labels (p), (d) and (u) indicate the pristine (p), doped (d) and undoped (u) sample.

there is also an associated bump in the IVC, as indicated by the vertical line between figures 5(a) and (c). Both the peaks and the bumps are located at sligthly different voltage positions for the three doping states, the shift explainable as an effect of the change in local temperature. For doping state D-3 there are also emission peaks at 0.89 V and at 0.95 V. These peaks, observed in the fully resistive state of the sample, are absent for doping states D-1 and D-2.

4. Conclusions

In summary we have shown that doping by carrier injection is feasible also for the large IJJ stacks used for THz generation. Both doping and undoping has been demonstrated. Even moderate changes in the charge carrier concentration introduce large changes in the THz emission properties. This is our main message, giving a proof-of-principle that doping by carrier injection can be used to systematically modify and study the THz emission properties of such stacks. For example, we found the emission to be largest after *doping* the pristine sample. This was unexpected since, typically, best emission properties are found for slightly underdoped IJJ stacks. The observed improvement in emission power may be related to an improvement of sample inhomogeneities during the doping step.

In the present work we have intentionally altered the doping states of our samples only in a small range near optimal doping. However, extending doping and undoping studies of large THz emitting stacks over a wide range of charge carrier concentrations is possible in principle and may show the limits and optima of the THz emission properties of IJJ stacks with respect to charge carrier concentration.

Acknowledgments

We gratefully acknowledge financial support by the National Natural Science Foundation of China (Grant Nos. 11234006,

61501220), the Priority Academic Program Development of Jiangsu Higher Education Institutions, Jiangsu Provincial Natural Science Fund (BK20150561), the Deutsche Forschungsgemeinschaft (Project KL930/13-2), JSPS KAKENHI Grant Number 25289108, RFBR grant 14-02-91335, EU-FP6-COST Action MP1201 and by the Scientific and Technological Research Council of Turkey under contract no. TUBITAK (2219)-1059B191501336.

References

[1] Kleiner R, Steinmeyer F, Kunkel G and Müller P 1992 *Phys. Rev. Lett.* **68** 2394
[2] Ozyuzer L *et al* 2007 *Science* **318** 1291
[3] Welp U, Kadowaki K and Kleiner R 2013 *Nat. Photon.* **7** 702
[4] Kakeya I and Wang H 2016 *Supercond. Sci. Technol.* **29** 073001
[5] Wang H B, Guénon S, Yuan J, Iishi A, Arisawa S, Hatano T, Yamashita T, Koelle D and Kleiner R 2009 *Phys. Rev. Lett.* **102** 017006
[6] Guénon S *et al* 2010 *Phys. Rev.* B **82** 214506
[7] Kurter C, Ozyuzer L, Proslier T, Zasadzinski J F, Hinks D G and Gray K E 2010 *Phys. Rev.* B **81** 224518
[8] Wang H B *et al* 2010 *Phys. Rev. Lett.* **105** 057002
[9] Tsujimoto M, Yamaki K, Deguchi K, Yamamoto T, Kashiwagi T, Minami H, Tachiki M, Kadowaki K and Klemm R A 2010 *Phys. Rev. Lett.* **105** 037005
[10] Benseman T M, Koshelev A E, Gray K E, Kwok W-K, Welp U, Kadowaki K, Tachiki M and Yamamoto T 2011 *Phys. Rev.* B **84** 064523
[11] Yuan J *et al* 2012 *Supercond. Sci. Technol.* **25** 075015
[12] Li M Y *et al* 2012 *Phys. Rev.* B **86** 060505(R)
[13] Kakeya I, Omukai Y, Yamamoto T, Kadowaki K and Suzuki M 2012 *Appl. Phys. Lett.* **100** 242603
[14] Tsujimoto M, Minami H, Delfanazari K, Sawamura M, Nakayama R, Kitamura T, Yamamoto T, Kashiwagi T, Hattori T and Kadowaki K 2012 *J. Appl. Phys.* **111** 123111
[15] Tsujimoto M *et al* 2012 *Phys. Rev. Lett.* **108** 107006
[16] Kashiwagi T *et al* 2012 *Japan. J. Appl. Phys.* **51** 010113
[17] An D Y *et al* 2013 *Appl. Phys. Lett.* **102** 092601
[18] Benseman T M, Koshelev A E, Kwok W-K, Welp U, Vlasko-Vlasov V K, Kadowaki K, Minami H and Watanabe C 2013 *J. Appl. Phys.* **113** 133902
[19] Benseman T M, Gray K E, Koshelev A E, Kwok W-K, Welp U, Minami H, Kadowaki K and Yamamoto T 2013 *Appl. Phys. Lett.* **103** 022602
[20] Sekimoto S, Watanabe C, Minami H, Yamamoto T, Kashiwagi T, Klemm R A and Kadowaki K 2013 *Appl. Phys. Lett.* **103** 182601
[21] Minami H, Watanabe C, Sato K, Sekimoto S, Yamamoto T, Kashiwagi T, Klemm R A and Kadowaki K 2014 *Phys. Rev.* B **89** 054503
[22] Ji M *et al* 2014 *Appl. Phys. Lett.* **105** 122602
[23] Tsujimoto M, Kambara H, Maeda Y, Yoshioka Y, Nakagawa Y and Kakeya I 2014 *Phys. Rev. Appl.* **2** 044016
[24] Watanabe C *et al* 2015 *Appl. Phys. Lett.* **106** 042603
[25] Zhou X J *et al* 2015 *Phys. Rev. Appl.* **3** 044012
[26] Zhou X J *et al* 2015 *Appl.Phys. Lett.* **107** 122602
[27] Hao L *et al* 2015 *Phys. Rev. Appl.* **3** 024006
[28] Gross B *et al* 2015 *Supercond. Sci. Technol.* **28** 055004
[29] Kakeya I, Hirayama N, Omukai Y and Suzuki M 2015 *J. Appl. Phys.* **117** 043914
[30] Kashiwagi T *et al* 2015 *Appl. Phys. Lett.* **107** 082601
[31] Kashiwagi T *et al* 2015 *Phys. Rev. Appl.* **4** 054018
[32] Benseman T M *et al* 2015 *Phys. Rev. Appl.* **3** 044017
[33] Tsujimoto M, Maeda Y, Kambara H, Elarabi A, Yoshioka Y, Nakagawa Y, Wen Y, Doi T, Saito H and Kakeya I 2015 *Supercond. Sci. Technol.* **28** 105015
[34] Watanabe C, Minami H, Kitamura T, Saiwai Y, Shibano Y, Katsuragawa T, Kubo H, Kashiwagi T, Klemm R A and Kadowaki K 2016 *Supercond. Sci. Technol.* **29** 065022
[35] Nakade K, Kashiwagi T, Saiwai Y, Minami H, Yamamoto T, Klemm R A and Kadowaki K 2016 *Sci. Rep.* **6** 23178
[36] Tsujimoto M, Maeda Y, Elarabi A, Yoshioka Y, Nakagawa Y, Wen Y, Doi T, Saito H and Kakeya I 2016 *Opt. Express* **24** 4591
[37] Bulaevskii L N and Koshelev A E 2007 *Phys. Rev. Lett.* **99** 057002
[38] Lin S and Hu X 2008 *Phys. Rev. Lett.* **100** 247006
[39] Krasnov V M 2009 *Phys. Rev. Lett.* **103** 227002
[40] Tachiki M, Fukuya S and Koyama T 2009 *Phys. Rev. Lett.* **102** 127002
[41] Pedersen N and Madsen S 2009 *IEEE Trans Appl. Supercond.* **19** 726
[42] Hu X and Lin S Z 2009 *Phys. Rev.* B **80** 064516
[43] Koyama T, Matsumoto H, Machida M and Kadowaki K 2009 *Phys. Rev.* B **79** 104522
[44] Klemm R A and Kadowaki K 2010 *J. Phys.: Condens. Matter* **22** 375701
[45] Klemm R A and Kadowaki K 2010 *J. Supercond. Nov. Magn.* **23** 613
[46] Krasnov V M 2010 *Phys. Rev.* B **82** 134524
[47] Koshelev A E 2010 *Phys. Rev.* B **82** 174512
[48] Katterwe S O, Rydh A, Motzkau H, Kulakov A B and Krasnov V M 2010 *Phys. Rev.* B **82** 024517
[49] Yurgens A A 2011 *Phys. Rev.* B **83** 184501
[50] Koyama T, Matsumoto H, Machida M and Ota Y 2011 *Supercond. Sci. Technol.* **24** 085007
[51] Krasnov V M 2011 *Phys. Rev.* B **83** 174517
[52] Yurgens A A and Bulaevskii L N 2011 *Supercond. Sci. Technol.* **24** 015003
[53] Gross B *et al* 2012 *Phys. Rev.* B **86** 094524
[54] Asai H, Tachiki M and Kadowaki K 2012 *Phys. Rev.* B **85** 064521
[55] Lin S and Hu X 2012 *Phys. Rev.* B **86** 054506
[56] Grib A and Seidel P 2012 *Low Temp. Phys.* **38** 321
[57] Gross B *et al* 2013 *Phys. Rev.* B **88** 014524
[58] Liu F, Lin S Z and Hu X 2013 *Supercond. Sci. Technol.* **26** 025003
[59] Asai H and Kawabata S 2014 *Appl. Phys. Lett.* **101** 112601
[60] Rudau F *et al* 2015 *Phys. Rev.* B **91** 104513
[61] Rudau F *et al* 2016 *Phys. Rev. Appl.* **5** 044017
[62] Koval Y, Jin X, Bergmann C, Simsek Y, Ozyuzer L, Müller P, Wang H B, Behr G and Büchner B 2010 *Appl. Phys. Lett.* **96** 082507
[63] Motzkau H, Jacobs T, Katterwe S-O, Rydh A and Krasnov V M 2012 *Phys. Rev.* B **85** 144519
[64] Kizilaslan O, Simsek Y, Aksan M A, Koval Y and Müller P 2015 *Supercond. Sci. Technol.* **28** 085017
[65] Jacobs T, Simsek Y, Koval Y, Müller P and Krasnov V M 2016 *Phys. Rev. Lett.* **116** 067001
[66] Müller P 2016 in preparation

Publication 8

Compact Superconducting Terahertz Source Operating in Liquid Nitrogen

L. Y. Hao,[1] M. Ji,[1,2] J. Yuan,[2] D. Y. An,[1,2] M. Y. Li,[1,2] X. J. Zhou,[1,2] Y. Huang,[1,2] H. C. Sun,[1] Q. Zhu,[1] F. Rudau,[3] R. Wieland,[3] N. Kinev,[4] J. Li,[1,*] W. W. Xu,[1,5] B. B. Jin,[1,5] J. Chen,[1,5] T. Hatano,[2] V. P. Koshelets,[4] D. Koelle,[3] R. Kleiner,[3,†] H. B. Wang,[1,2,5,‡] and P. H. Wu[1]

[1]*Research Institute of Superconductor Electronics, Nanjing University, Nanjing 210093, People's Republic of China*

[2]*National Institute for Materials Science, Tsukuba 3050047, Japan*

[3]*Physikalisches Institut and Center for Collective Quantum Phenomena in LISA$^+$, Universität Tübingen, D-72076 Tübingen, Germany*

[4]*Kotel'nikov Institute of Radio Engineering and Electronics, 125009 Moscow, Russia*

[5]*Cooperative Innovation Centre of Terahertz Science, Chengdu 610054, People's Republic of China*

(Received 3 November 2014; revised manuscript received 24 December 2014; published 19 February 2015)

We report on a liquid-nitrogen-cooled compact source for continuous terahertz (THz) emission. The emitter is a $Bi_2Sr_2CaCu_2O_{8+\delta}$ intrinsic Josephson-junction stack embedded between two gold layers and sandwiched between two MgO substrates. The radiation is emitted to free space through a hollow metallic tube acting as a waveguide. The maximum emission power is 1.17 μW. The tunable emission frequency bandwidth is up to 100 GHz with a maximum emission power at 0.311 THz. Since the operation voltage is about 1 V and the current is less than 30 mA, we are able to drive this terahertz source at 77 K with only one commercial 1.5-V battery, just like a torch. This convenient and economical setup may find applications in fields like tracer-gas detection or nondestructive evaluation.

DOI: 10.1103/PhysRevApplied.3.024006

I. INTRODUCTION

Terahertz (THz) radiation covers the region from 0.3 THz (submillimeter) to 3 THz (far infrared) and is attracting increasing attention due to the variety of potential applications, including information and communication technology, biology and medical sciences, nondestructive evaluation, astronomical observation, and security [1–3]. The critical technical requirements are to develop powerful terahertz sources with certain features for different applications. One of the tasks is to develop compact and economical terahertz sources operated in a continuous-wave (cw) mode. Terahertz radiation for frequencies above 2 THz can be well generated using quantum cascade lasers. For frequencies below 1 THz, stacks of intrinsic Josephson junctions (IJJs) [4] in the high-transition-temperature (T_c) superconductor $Bi_2Sr_2CaCu_2O_{8+\delta}$ (BSCCO) have been shown to emit continuous and coherent radiation [5], with the possibility to tune the emitted frequency f_e by an applied dc voltage V, following the relation $f_e = V/N\Phi_0$. Here, Φ_0 is the flux quantum, with $\Phi_0^{-1} \approx 483.6$ GHz/mV. N is the number of IJJs in the stack, and V/N is the voltage per junction. In Ref. [5], stacks of about 1 μm in thickness (corresponding to 666 IJJs), a length L_s of about 300 μm, and a width W of some 10 μm have been realized as mesa structures on top of BSCCO single crystals contacted by Au layers. These mesas emitted radiation at frequencies between 0.5 and 0.8 THz, with an integrated output power on the order of 1 μW. The operation temperature was up to 50 K.

Terahertz radiation emitted from such IJJ stacks has become a hot topic in recent years [6–45]. The possibility to perform terahertz imaging has been demonstrated [22,40,41]. IJJ stacks containing typically 500–2000 junctions have been realized as mesa structures but also as bare IJJ stacks contacted by Au layers [gold-BSCCO-gold (GBG) structures] [28,30,36,38,43] and as all-superconducting Z-shaped structures [27]. Emission frequencies are in the range of 0.4–1 THz. For the best stacks—particularly, the GBG structures—emission powers in the range of tens of microwatts have been achieved [30,33,36], and arrays of stacks showed emission with a power up to 0.61 mW [33]. Both above-mentioned terahertz sources require cooling by liquid helium or by using cooling systems such as a Gifford-McMahon cryocooler or a Stirling cryocooler. In view of the applications, these cryogenic systems are inconvenient because of large equipment volume, electromagnetic noise, and mechanical vibrations [46,47].

Quite recently, attempts were reported to enhance the emission frequency to 1.05 THz and the tunable frequency range to more than 0.71 THz [43,45]. Particularly, in Ref. [43], the terahertz emission was observed at temperatures above 78 K, which allows the investigation and application of terahertz technology using liquid-nitrogen cooling.

*junli@nju.edu.cn
†kleiner@uni-tuebingen.de
‡hbwang1000@gmail.com

In the present work, we report on a portable and tunable terahertz source operated in liquid nitrogen, which can provide cw terahertz emission. The GBG structure sandwiched between two MgO substrates is utilized as the terahertz emitter. The terahertz emission can be transmitted to free space through a metal tube acting as a waveguide. For a proof of principle, we also operate our source like a torch, with only one commercial 1.5-V battery.

II. EXPERIMENTAL SETUP

The fabrication of the sandwiched GBG structure shown in Fig. 1(b) is described in Ref. [43]. The $230 \times 50\ \mu m^2$ BSCCO IJJ stack is 1.5 μm thick and consists of approximately 1000 junctions. The single crystals used are optimally doped with $T_c \sim 88$ K, which is the key factor for operating the device at liquid-nitrogen temperatures. In this GBG structure, the top gold layer can reflect the radiation of the IJJ stack to the MgO-1 substrate and then to a sapphire lens, enhancing the detectable emission power. We put another MgO substrate (MgO-2) on the top of the GBG structure to form a sandwich structure, using polyimide (polyimide-1) as glue and a thermal anchor. At a given bias current I and a given bath temperature T, the total voltage V across the stack as well as the terahertz emission frequencies are significantly increased compared to the GBG structure mounted to a single substrate [43].

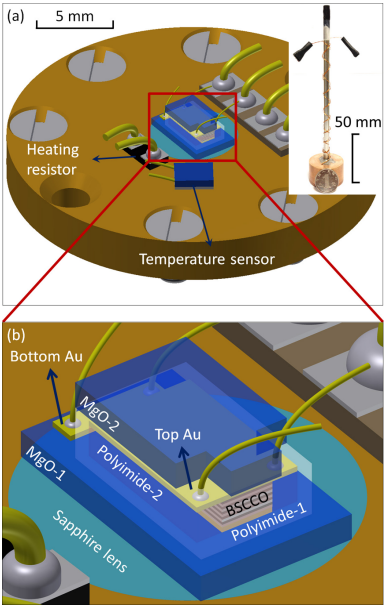

FIG. 1. Structure of the terahertz source. The inset in (a) is a photograph of the probe consisting of a stainless-steel tube acting as a waveguide and a hollow copper container hosting the emitter. The inner top part of the container is sketched upside down in (a). A close-up of the sandwiched GBG structure is shown in (b).

A photograph of the terahertz source is shown in the inset of Fig. 1(a). It consists of a copper container for holding the BSCCO emitter and a stainless-steel tube acting as a waveguide. Some pieces of black polyethylene films are employed on the outport of the waveguide to filter out some of the infrared background. An inside view of the copper container is presented in Fig. 1(a). The BSCCO emitter is fixed on a hemispherical sapphire lens with a 6 mm diameter. The terahertz waves are focused by the lens and then transmitted outward through the inner polished tube being a hollow circular waveguide with length of 180 mm and inner radius $r = 1.75$ mm. We also place an $R_{\rm heat} = 1$ kΩ heating resistor (heater) next to the lens to adjust the ambient temperature and, consequently, to expand the tunable frequency bandwidth.

III. RESULTS AND DISCUSSION

For a hollow metallic circular waveguide, the cutoff frequencies f_c of transverse magnetic (TM) and transverse electric (TE) waves are, respectively,

$$(f_c)_{np}^{\rm TM} = \frac{c x_{np}}{2\pi r}, \tag{1}$$

$$(f_c)_{np}^{\rm TE} = \frac{c x'_{np}}{2\pi r}, \tag{2}$$

where x_{np} and x'_{np} represent the pth roots of the nth-order Bessel functions and its derivatives, respectively; c is the speed of light. Then, f_c of the main mode TE_{11} is 50 GHz and, thus, far below the operating frequency. Therefore, for the tunable frequency range from 0.266 to 0.364 THz, there are multiple transmission modes, among which the one having the highest cutoff frequency is TE_{24} with $f_c = 0.359$ THz. The hollow circular waveguide transmits waves by bouncing them with the inner metallic surface; however, more reflections induce larger insertion losses [48,49]. By polishing the inner surface, the losses are reduced. Via simulation, the insertion loss L_I of the waveguide is estimated as about 10 dB according to the relation $L_I = -20\log_{10}|S_{12}|$(dB), where S_{12} is the transmission coefficient of the scattering matrix.

The power and the frequency (wavelength) of the terahertz emission are measured with a homemade Michelson interferometer armed with a Si bolometer. The power measurement is calibrated by a blackbody radiation source. The ratio between the power and the bolometer readout is 2.1×10^{-3} W/V. For the fast Fourier transform, the frequency resolution of the Michelson

interferometer is given by $\Delta f = c/(2d_{\max})\cos(\theta)$, where $d_{\max}$ is the maximum differential displacement of the lamellar mirrors and θ the angle of incidence [50]. In our setup, $d_{\max} = 20$ mm and $\theta \sim 0^{\circ}$; therefore, Δf can be estimated as 7.5 GHz. When the interferometer is inserted, the detected power is a factor of 4.3 lower than for direct bolometric detection.

Figure 2(a) shows a series of current-voltage characteristics (IVCs) for different temperatures ranging from the liquid-nitrogen boiling temperature (77 K) to the T_c (88 K) of the BSCCO emitter. The temperature of the emitter is varied using the heating resistor mounted on the copper container. The contact resistance R_{cont} from 2.1 to 4.6 Ω is subtracted from the IVC for each temperature. As shown in Fig. 2(a) by the horizontal dashed arrows, at 77 K all junctions have switched from the zero-voltage states to the resistive states when the bias current $I > 20$ mA. By further increasing I to 24 mA and then sweeping it down, the IVC is continuous until some of the IJJs in the stack retrap to their zero-voltage states at the retrapping current I_r (11 mA at 77 K). The highest voltage across the mesa is observed as 1 V at 77 K. Different from the typical heat-induced S-shaped curves at relatively low temperatures, the IVCs are always monotonic above the liquid-nitrogen temperature. With increasing temperature (heater power P_{heat}), the retrapping voltage is gradually decreasing, and the entire emission regime shifts to lower voltages, i.e., lower emission frequencies. When P_{heat} reaches 0.73 W, no emission can be detected anymore. When P_{heat} is increased to 1.0 W, the BSCCO stack goes normal; i.e., it reaches $T_c = 88$ K.

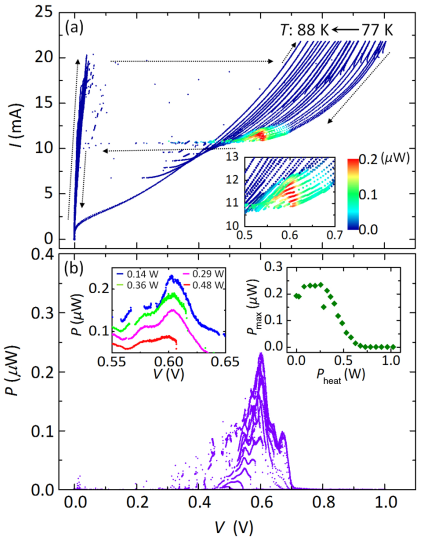

FIG. 2. IVCs and emission power (with interferometer inserted) obtained from the terahertz source for different temperatures T. The color contours represent different terahertz emission powers. (a) A series of IVCs. Dashed arrows denote the current sweep direction. The inset is a close-up of the emission region. (b) Emission power P as a function of the voltage V across the mesa. The right inset shows the maximum emission power $P_{\max}$ vs the heater power P_{heat}. The left inset shows P vs V on a magnified voltage scale for four different values of P_{heat}.

The emission region covers a current range from about 11 to 12.5 mA and, correspondingly, a voltage range from 0.5 to 0.7 V, as shown in the inset of Fig. 2(a). The maximum emission power is observed around 0.6 V, corresponding to 0.311 THz at most temperatures; cf. Fig. 2(b). As shown in more detail in the right inset of this graph, the power peak is about 0.23 μW at $P_{\text{heat}} = 0.26$ W and 0.19 μW at $P_{\text{heat}} = 0$. The highest value is 0.27 μW at $P_{\text{heat}} = 0.20$ W. These numbers are recorded via the Michelson interferometer and for $P_{\text{heat}} = 0.20$ W ($P_{\text{heat}} = 0$) correspond to 1.17 μW (1.08 μW) with direct bolometric detection.

In addition to the output power, the linewidth and the frequency tunability are important parameters for terahertz sources. Figure 3 shows at $P_{\text{heat}} = 0.20$ W emission spectra taken at the four bias points marked on the IVC in the inset. The full width at half maximum of the emission peak at 0.311 THz is 7.5 GHz, which is the resolution limit of the interferometer. We do not perform high-resolution measurements of the emission peak using a superconducting receiver [24], but note that, at least for the IJJ emitters investigated previously, the linewidth of radiation can be as narrow as 23 MHz [24,35].

Figure 4(a) shows the tunability of the emission frequency with the bias current indicated by vertical error bars at a given bath temperature. For instance, at $P_{\text{heat}} = 0.20$ W, it

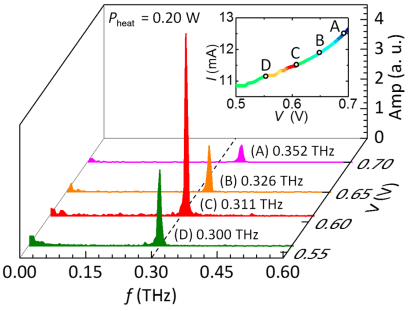

FIG. 3. Emission spectra at $P_{\text{heat}} = 0.20$ W of the four bias points marked on the IVC shown in the inset. The colors in the main panel are used to distinguish different spectra, whereas the color mapping in the inset corresponds to that in Fig. 2(a).

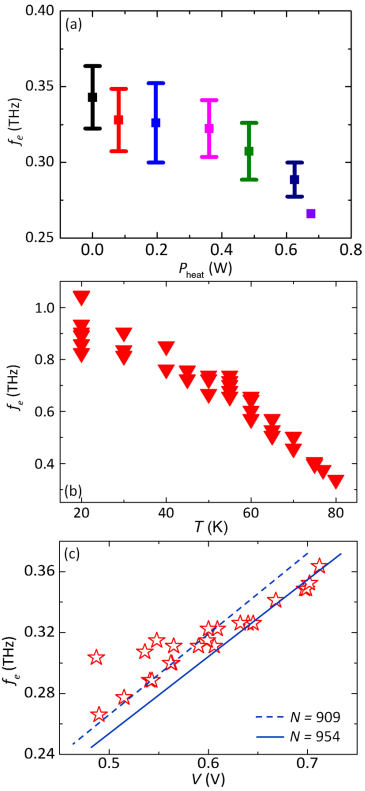

FIG. 4. (a) Frequency intervals of detectable emission vs the heater power P_{heat}. (b) Emission frequency f_e vs temperature T over a large temperature range up to 80 K, as measured with another setup [43]. (c) Emission frequency f_e vs voltage V across the mesa. The dashed and solid lines correspond to $V = Nf_e\Phi_0$ with $N = 909$ and 954, respectively.

amounts to 52.5 GHz with the maximum emission power at 0.311 THz. The emission frequency can also be tuned with the temperature, which in our setup, we vary using a resistor placed next to the sample. Figure 4(a) shows the resulting temperature and frequency changes for seven values of the heater power P_{heat}. The total tunable frequency range is as broad as 100 GHz, which makes it possible to have certain applications like spectrum analysis of materials.

Note that the fact that f_e decreases strongly with the temperature is consistent with the assumption that in-plane supercurrents via cavity resonances are important for synchronization [3]. These currents lead to a large kinetic inductance which diverges at T_c, and, consequently, the (in-phase) cavity mode velocity becomes small [9]. By contrast, a temperature independence of f_e would have suggested that in-plane currents dominantly flow in the gold layers, which does not seem to be the case at least for the GBG structure we use here.

In Fig. 4(c), for the measurements performed in liquid nitrogen, we plot f_e vs the voltage across the stack V. From the trend of the linear voltage dependence, we plot two fit lines, $N = 909$ and 954, which determine a range for the number of the active junctions that have contributed to the emission. There are some deviating data points. The reason is that some of the junctions in the stack have already switched back to the superconducting state. Thus, the voltage state turns to the inner branches of the IVC. The change in the number N of radiating junctions leads to a change in slope of the f_e vs V relation. For a given voltage, one observes a higher value of f_e, as described by Tsujimoto *et al.* [29].

To obtain a more portable and economical system, for a proof of principle, we also operate our terahertz source like a terahertz torch driven by a commercial battery. This operation is possible, since the maximum voltage is about 1 V and the current less than 30 mA. A 1.5-V battery is used as a voltage source, and two potentiometers with different resistors are utilized to adjust the output bias voltage. One of the potentiometers is 10 kΩ for coarse adjustment and the other is 100 Ω for fine adjustment. The current is obtained via a 10-Ω sampling resistor. Figure 5 shows an IVC and the emitted power for this operation mode.

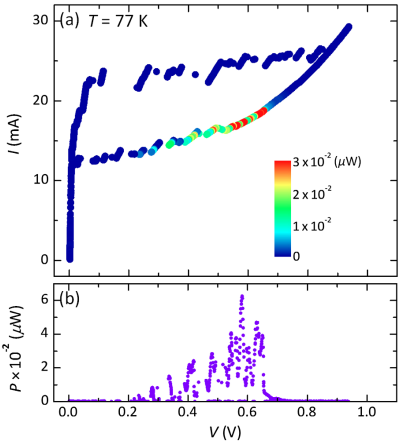

FIG. 5. Characteristics of the terahertz emitter ($T = 77$ K) when operated with a 1.5-V battery. (a) IVC and (b) emitted power P vs voltage V.

The maximum emission power measured with the interferometer is only about 0.063 μW, yielding 0.27 μW for direct detection. However, we note that the device is not optimized for this kind of operation; thus, an increase of the emitted power P will certainly be feasible.

Finally, let us say a few words why our terahertz source can work at such a high temperature. At least two important factors may contribute to the high-temperature operation. One is to diffuse the Joule heating efficiently. In conventional mesa structures, an IJJ stack is located on a thick BSCCO base crystal, through which the heat diffuses from the mesa to the substrate. In a GBG structure, the thick BSCCO base crystal is replaced by a gold layer glued on a substrate by polyimide inducing a better heating transfer. The sandwich structure further improves the cooling because the IJJ stack is wrapped with polyimide (having a reasonably high thermal conductivity) on the periphery resulting in more contact areas with the copper holder [36,43]. The other important factor to achieve maximum operation temperature is that the crystal is close to optimal doping. Note that, in general, the precise temperature dependence of the c-axis resistivity, which, in turn, depends strongly on doping [51], strongly affects the thermal and electrodynamic properties of an IJJ stack [19,26,35]. Most previous results on terahertz generation by intrinsic junctions have been obtained with slightly underdoped crystals. The results presented in our paper show that terahertz generation is also feasible using optimally doped stacks, allowing us to operate IJJ stacks as terahertz sources in liquid nitrogen.

IV. CONCLUSION

In summary, we design and investigate a portable and tunable terahertz radiation system for continuous-wave terahertz emission. The coolant is liquid nitrogen. The terahertz waves are transmitted to free space through a metal tube acting as a waveguide. We demonstrate that the power source can be a commercial 1.5-V battery, allowing the operation as a "terahertz torch." Along with satisfactory spectrum characteristics, the emission frequency is detected in the range of 0.266 to 0.364 THz. In virtue of its portability and frequency tunability, the system can be employed in practical applications. For example, for spectroscopy purposes, one can connect another tube containing some gas to the end of the waveguide. A terahertz detector can be attached easily to the end of this setup.

ACKNOWLEDGMENTS

This research is partly supported by the National Basic Research Program of China (973 Program) (Grants No. 2014CB339800 and No. 2011CBA00100), the National Natural Science Foundation of China (Grants No. 11234006, No. 51102188, No. 6127008, No. 2011CBA 00107, and No. 11227904), the Fundamental Research Funds for the Central Universities and Jiangsu Key Laboratory of Advanced Techniques for Manipulating Electromagnetic Waves, the China Academy of Engineering Physics (CAEP) THz Science and Technology Foundation (Grant No. CAEPTHZ201202), the Russian Foundation for Basic Research (RFBR) (Grants No. 13-02-00493-a and 14-02-91335) and the Ministry of Education and Science of the Russian Federation (Grant No. 14.607.21.0100), the Japan Science and Technology/Deutsche Forschungsgemeinschaft (JST/DFG) strategic Japanese-German International Cooperative Program, Project No. KL930/12-1 of the Deutsche Forschungsgemeinschaft, the Grants-in-Aid for scientific research from Japan Society for the Promotion of Science (JSPS) (Grant No. 25289108), and the Priority Academic Program Development of Jiangsu Higher Education Institutions (PAPD).

[1] M. Tonouchi, Cutting-edge terahertz technology, Nat. Photonics **1**, 97 (2007).
[2] B. Ferguson and X. C. Zhang, Materials for terahertz science and technology, Nat. Mater. **1**, 26 (2002).
[3] U. Welp, K. Kadowaki, and R. Kleiner, Superconducting emitters of THz radiation, Nat. Photonics **7**, 702 (2013).
[4] R. Kleiner, F. Steinmeyer, G. Kunkel, and P. Müller, Intrinsic Josephson Effects in $Bi_2Sr_2CaCu_2O_8$ Single Crystals, Phys. Rev. Lett. **68**, 2394 (1992).
[5] L. Ozyuzer, A. E. Koshelev, C. Kurter, N. Gopalsami, Q. Li, M. Tachiki, K. Kadowaki, T. Yamamoto, H. Minami, H. Yamaguchi, T. Tachiki, K. E. Gray, W.-K. Kwok, and U. Welp, Emission of coherent THz radiation from superconductors, Science **318**, 1291 (2007).
[6] S. Z. Lin and X. Hu, Possible Dynamic States in Inductively Coupled Intrinsic Josephson Junctions of Layered High-T_c Superconductors, Phys. Rev. Lett. **100**, 247006 (2008).
[7] A. E. Koshelev, Alternating dynamic state self-generated by internal resonance in stacks of intrinsic Josephson junctions, Phys. Rev. B **78**, 174509 (2008).
[8] C. Kurter, K. E. Gray, J. F. Zasadzinski, L. Ozyuzer, A. E. Koshelev, Q. Li, T. Yamamoto, K. Kadowaki, W.-K. Kwok, M. Tachiki, and U. Welp, Thermal management in large Bi2212 mesas used for terahertz sources, IEEE Trans. Appl. Supercond. **19**, 428 (2009).
[9] H. B. Wang, S. Guénon, J. Yuan, A. Iishi, S. Arisawa, T. Hatano, T. Yamashita, D. Koelle, and R. Kleiner, Hot Spots and Waves in $Bi_2Sr_2CaCu_2O_8$ Intrinsic Josephson Junction Stacks: A Study by Low Temperature Scanning Laser Microscopy, Phys. Rev. Lett. **102**, 017006 (2009).
[10] M. Tachiki, S. Fukuya, and T. Koyama, Mechanism of Terahertz Electromagnetic Wave Emission from Intrinsic Josephson Junctions, Phys. Rev. Lett. **102**, 127002 (2009).
[11] N. F. Pedersen and S. Madsen, THz generation using fluxon dynamics in high temperature superconductors, IEEE Trans. Appl. Supercond. **19**, 726 (2009).
[12] A. E. Koshelev, Stability of dynamic coherent states in intrinsic Josephson-junction stacks near internal cavity resonance, Phys. Rev. B **82**, 174512 (2010).

[13] S. Z. Lin and X. Hu, Response and amplification of terahertz electromagnetic waves in intrinsic Josephson junctions of layered high-T_c superconductor, Phys. Rev. B **82**, 020504 (2010).

[14] M. Tsujimoto, K. Yamaki, K. Deguchi, T. Yamamoto, T. Kashiwagi, H. Minami, M. Tachiki, K. Kadowaki, and R. A. Klemm, Geometrical Resonance Conditions for THz Radiation from the Intrinsic Josephson Junctions in $Bi_2Sr_2CaCu_2O_{8+\delta}$, Phys. Rev. Lett. **105**, 037005 (2010).

[15] H. B. Wang, S. Guénon, B. Gross, J. Yuan, Z. G. Jiang, Y. Y. Zhong, M. Grünzweig, A. Iishi, P. H. Wu, T. Hatano, D. Koelle, and R. Kleiner, Coherent Terahertz Emission of Intrinsic Josephson Junction Stacks in the Hot Spot Regime, Phys. Rev. Lett. **105**, 057002 (2010).

[16] S. Guénon, M. Grünzweig, B. Gross, J. Yuan, Z. G. Jiang, Y. Y. Zhong, M. Y. Li, A. Iishi, P. H. Wu, T. Hatano, R. G. Mints, E. Goldobin, D. Koelle, H. B. Wang, and R. Kleiner, Interaction of hot spots and terahertz waves in $Bi_2Sr_2CaCu_2O_8$ intrinsic Josephson junction stacks of various geometry, Phys. Rev. B **82**, 214506 (2010).

[17] V. M. Krasnov, Coherent flux-flow emission from stacked Josephson junctions: Nonlocal radiative boundary conditions and the role of geometrical resonances, Phys. Rev. B **82**, 134524 (2010).

[18] V. M. Krasnov, Terahertz electromagnetic radiation from intrinsic Josephson junctions at zero magnetic field via breather-type self-oscillations, Phys. Rev. B **83**, 174517 (2011).

[19] A. Yurgens, Temperature distribution in a large $Bi_2Sr_2CaCu_2O_{8+\delta}$ mesa, Phys. Rev. B **83**, 184501 (2011).

[20] T. M. Benseman, A. E. Koshelev, K. E. Gray, W.-K. Kwok, U. Welp, K. Kadowaki, M. Tachiki, and T. Yamamoto, Tunable terahertz emission from $Bi_2Sr_2CaCu_2O_{8+\delta}$ mesa devices, Phys. Rev. B **84**, 064523 (2011).

[21] T. Koyama, H. Matsumoto, M. Machida, and Y. Ota, Multiscale simulation for terahertz wave emission from the intrinsic Josephson junctions, Supercond. Sci. Technol. **24**, 085007 (2011).

[22] M. Tsujimoto, H. Minami, K. Delfanazari, M. Sawamura, R. Nakayama, T. Kitamura, T. Yamamoto, T. Kashiwagi, T. Hattori, and K. Kadowaki, Terahertz imaging system using high-T_c superconducting oscillation devices, J. Appl. Phys. **111**, 123111 (2012).

[23] S. Z. Lin and X. Hu, In-plane dissipation as a possible synchronization mechanism for terahertz radiation from intrinsic Josephson junctions of layered superconductors, Phys. Rev. B **86**, 054506 (2012).

[24] M. Y. Li, J. Yuan, N. V. Kinev, J. Li, B. Gross, S. Guénon, A. Ishii, K. Hirata, T. Hatano, D. Koelle, R. Kleiner, V. P. Koshelets, H. B. Wang, and P. H. Wu, Linewidth dependence of coherent terahertz emission from $Bi_2Sr_2CaCu_2O_8$ intrinsic Josephson junction stacks in the hot-spot regime, Phys. Rev. B **86**, 060505(R) (2012).

[25] I. Kakeya, Y. Omukai, T. Yamamoto, K. Kadowaki, and M. Suzuki, Effect of thermal inhomogeneity for terahertz radiation from intrinsic Josephson junction stacks of $Bi_2Sr_2CaCu_2O_{8+\delta}$, Appl. Phys. Lett. **100**, 242603 (2012).

[26] B. Gross, S. Guénon, J. Yuan, M. Y. Li, J. Li, A. Ishii, R. G. Mints, T. Hatano, P. H. Wu, D. Koelle, H. B. Wang, and R. Kleiner, Hot-spot formation in stacks of intrinsic Josephson junctions in $Bi_2Sr_2CaCu_2O_8$, Phys. Rev. B **86**, 094524 (2012).

[27] J. Yuan, M. Y. Li, J. Li, B. Gross, A. Ishii, K. Yamaura, T. Hatano, K. Hirata, E. Takayama-Muromachi, P. H. Wu, D. Koelle, R. Kleiner, and H. B. Wang, Terahertz emission from $Bi_2Sr_2CaCu_2O_{8+\delta}$ intrinsic Josephson junction stacks with all-superconducting electrodes, Supercond. Sci. Technol. **25**, 075015 (2012).

[28] T. Kashiwagi, M. Tsujimoto, T. Yamamoto, H. Minami, K. Yamaki, K. Delfanzari, K. Deguchi, N. Orita, T. Koike, R. Nakayama, T. Kitamura, M. Sawamura, S. Hagino, K. Ishida, K. Ivancovic, H. Asai, M. Tachiki, R. A. Klemm, and K. Kadowaki, High temperature superconductor terahertz emitters: Fundamental physics and its applications, Jpn. J. Appl. Phys. **51**, 010113 (2012).

[29] M. Tsujimoto, T. Yamamoto, K. Delfanazari, R. Nakayama, T. Kitamura, M. Sawamura, T. Kashiwagi, H. Minami, M. Tachiki, K. Kadowaki, and R. A. Klemm, Broadly Tunable Subterahertz Emission from Internal Branches of the Current-Voltage Characteristics of Superconducting $Bi_2Sr_2CaCu_2O_{8+\delta}$ Single Crystals, Phys. Rev. Lett. **108**, 107006 (2012).

[30] S. Sekimoto, C. Watanabe, H. Minami, T. Yamamoto, T. Kashiwagi, R. A. Klemm, and K. Kadowaki, Continuous 30 μW terahertz source by a high-T_c superconductor mesa structure, Appl. Phys. Lett. **103**, 182601 (2013).

[31] I. Kawayama, C. Zhang, H. B. Wang, and M. Tonouchi, Study on terahertz emission and optical/terahertz pulse responses with superconductors, Supercond. Sci. Technol. **26**, 093002 (2013).

[32] T. M. Benseman, A. E. Koshelev, W.-K. Kwok, U. Welp, K. Kadowaki, J. R. Cooper, and G. Balakrishnan, The ac Josephson relation and inhomogeneous temperature distributions in large $Bi_2Sr_2CaCu_2O_{8+\delta}$ mesas for THz emission, Supercond. Sci. Technol. **26**, 085016 (2013).

[33] T. M. Benseman, K. Gray, A. Koshelev, W.-K. Kwok, U. Welp, H. Minami, K. Kadowaki, and T. Yamamoto, Powerful terahertz emission from $Bi_2Sr_2CaCu_2O_{8+\delta}$ mesa arrays, Appl. Phys. Lett. **103**, 022602 (2013).

[34] T. M. Benseman, A. E. Koshelev, W.-K. Kwok, U. Welp, V. K. Vlasko-Vlasov, K. Kadowaki, H. Minami, and C. Watanabe, Direct imaging of hot spots in $Bi_2Sr_2CaCu_2O_{8+\delta}$ mesa terahertz sources, J. Appl. Phys. **113**, 133902 (2013).

[35] B. Gross, J. Yuan, D. Y. An, M. Y. Li, N. V. Kinev, X. J. Zhou, M. Ji, Y. Huang, T. Hatano, R. G. Mints, V. P. Koshelets, P. H. Wu, H. B. Wang, D. Koelle, and R. Kleiner, Modeling the linewidth dependence of coherent terahertz emission from intrinsic Josephson junction stacks in the hot-spot regime, Phys. Rev. B **88**, 014524 (2013).

[36] D. Y. An *et al.*, Terahertz emission and detection both based on high-T_c superconductors: Towards an integrated receiver, Appl. Phys. Lett. **102**, 092601 (2013).

[37] F. Turkoglu, L. Ozyuzer, H. Koseoglu, Y. Demirhan, S. Preu, S. Malzer, Y. Simsek, H. B. Wang, and P. Müller, Emission of the THz waves from large area mesas of superconducting $Bi_2Sr_2CaCu_2O_{8+\delta}$ by the injection of spin polarized current, Physica (Amsterdam) **491C**, 7 (2013).

[38] K. Kadowaki, M. Tsujimoto, K. Delfanazari, T. Kitamura, M. Sawamura, H. Asai, T. Yamamoto, K. Ishida, C. Watanabe, and S. Sekimoto, Quantum terahertz electronics

(QTE) using coherent radiation from high temperature superconducting $Bi_2Sr_2CaCu_2O_{8+\delta}$ intrinsic Josephson junctions, Physica (Amsterdam) **491C**, 2 (2013).

[39] H. Minami, C. Watanabe, K. Sato, S. Sekimoto, T. Yamamoto, T. Kashiwagi, R. A. Klemm, and K. Kadowaki, Local SiC photoluminescence evidence of hot spot formation and sub-THz coherent emission from a rectangular $Bi_2Sr_2CaCu_2O_{8+\delta}$ mesa, Phys. Rev. B **89**, 054503 (2014).

[40] T. Kashiwagi, K. Nakade, B. Markovi, Y. Saiwai, H. Minami, T. Kitamura, C. Watanabe, K. Ishida, S. Sekimoto, K. Asanuma, T. Yasui, Y. Shibano, M. Tsujimoto, T. Yamamoto, J. Mirkovi, and K. Kadowaki, Reflection type of terahertz imaging system using a high-T_c superconducting oscillator, Appl. Phys. Lett. **104**, 022601 (2014).

[41] T. Kashiwagi, K. Nakade, Y. Saiwai, H. Minami, T. Kitamura, C. Watanabe, K. Ishida, S. Sekimoto, K. Asanuma, T. Yasui, Y. Shibano, M. Tsujimoto, T. Yamamoto, B. Markovi, J. Mirkovi, R. A. Klemm, and K. Kadowaki, Computed tomography image using subterahertz waves generated from a high-T_c superconducting intrinsic Josephson junction oscillator, Appl. Phys. Lett. **104**, 082603 (2014).

[42] A. Grib and P. Seidel, The influence of external separate heating on the synchronization of Josephson junctions, Phys. Status Solidi B **251**, 1040 (2014).

[43] M. Ji, J. Yuan, B. Gross, F. Rudau, D. Y. An, M. Y. Li, X. J. Zhou, Y. Huang, H. C. Sun, Q. Zhu, J. Li, N. Kinev, T. Hatano, V. P. Koshelets, D. Koelle, R. Kleiner, W. W. Xu, B. B. Jin, H. B. Wang, and P. H. Wu, $Bi_2Sr_2CaCu_2O_8$ intrinsic Josephson junction stacks with improved cooling: Coherent emission above 1 THz, Appl. Phys. Lett. **105**, 122602 (2014).

[44] M. Tsujimoto, H. Kambara, Y. Maeda, Y. Yoshioka, Y. Nakagawa, and I. Kakeya, Dynamic Control of Temperature Distributions in Stacks of Intrinsic Josephson Junctions in $Bi_2Sr_2CaCu_2O_{8+\delta}$ for Intense Terahertz Radiation, Phys. Rev. Applied **2**, 044016 (2014).

[45] T. Kitamura, T. Kashiwagi, T. Yamamoto, M. Tsujimoto, C. Watanabe, K. Ishida, S. Sekimoto, K. Asanuma, T. Yasui, K. Nakade, Y. Shibano, Y. Saiwai, H. Minami, R. A. Klemm, and K. Kadowaki, Broadly tunable, high-power terahertz radiation up to 73 K from a stand-alone $Bi_2Sr_2CaCu_2O_{8+\delta}$ mesa, Appl. Phys. Lett. **105**, 202603 (2014).

[46] S. S. Andrews and S. G. Boxer, A liquid nitrogen immersion cryostat for optical measurements, Rev. Sci. Instrum. **71**, 3567 (2000).

[47] H. J. M. ter Brake and G. F. M. Wiegerinck, Low-power cryocooler survey, Cryogenics **42**, 705 (2002).

[48] O. Mitrofanov, T. Tan, P. R. Mark, B. Bowden, and J. A. Harrington, Waveguide mode imaging and dispersion analysis with terahertz near-field microscopy, Appl. Phys. Lett. **94**, 171104 (2009).

[49] O. Mitrofanov, R. James, F. A. Fernández, T. K. Mavrogordatos, and J. A. Harrington, Reducing transmission losses in hollow THz waveguides, IEEE Trans. THz Sci. Technol. **1**, 124 (2011).

[50] H. Eisele, M. Naftaly, and J. R. Fletcher, A simple interferometer for the characterization of sources at terahertz frequencies, Meas. Sci. Technol. **18**, 2623 (2007).

[51] T. Watanabe, T. Fujii, and A. Matsuda, Anisotropic Resistivities of Precisely Oxygen Controlled Single-Crystal $Bi_2Sr_2CaCu_2O_{8+\delta}$: Systematic Study on "Spin Gap" Effect, Phys. Rev. Lett. **79**, 2113 (1997).

Publication 9

Terahertz Spectroscopy of Dilute Gases Using $Bi_2Sr_2CaCu_2O_{8+\delta}$ Intrinsic Josephson-Junction Stacks

Hancong Sun,[1,2] Zhibao Yang,[1] Nickolay V. Kinev,[3] Oleg S. Kiselev,[3] Yangyang Lv,[1] Ya Huang,[1,2] Luyao Hao,[1,2] Xianjing Zhou,[1,2] Min Ji,[1,2] Xuecou Tu,[1] Caihong Zhang,[1] Jun Li,[1] Fabian Rudau,[4] Raphael Wieland,[4] Johannes S. Hampp,[4] Olcay Kizilaslan,[4,5] Dieter Koelle,[4] Biaobing Jin,[1] Jian Chen,[1] Lin Kang,[1] Weiwei Xu,[1] Reinhold Kleiner,[4,†] Valery P. Koshelets,[3] Huabing Wang,[1,*] and Peiheng Wu[1]

[1]*Research Institute of Superconductor Electronics, Nanjing University, Nanjing 210023, China*
[2]*National Institute for Materials Science, Tsukuba 305-0047, Japan*
[3]*Kotelnikov Institute of Radio Engineering and Electronics, Moscow 125009, Russia*
[4]*Physikalisches Institut and Center for Quantum Science in LISA$^+$, Universität Tübingen, D-72076 Tübingen, Germany*
[5]*Department of Biomedical Engineering, Faculty of Engineering, Inonu University, 44280 Malatya, Turkey*

(Received 30 July 2017; published 3 November 2017)

We report on spectrometric gas detection using terahertz waves radiated from $Bi_2Sr_2CaCu_2O_{8+\delta}$ (BSCCO) intrinsic Josephson-junction stacks. The emission frequency is varied by changing the bias current through and thus the voltage across the emitter. For the terahertz detection, both bolometric and heterodyne detection methods are employed. Clear absorption dips of water and ammonia vapor on the terahertz spectrum are obtained with both detection methods. With the bolometric scheme, we achieve a frequency resolution of about 1 GHz, which is on the order of the frequency resolution of systems employing terahertz time-domain spectroscopy. With the more stable heterodyne detection scheme, the minimum detectable gas pressure is around 0.001 mbar for H_2O and about 0.07 mbar for NH_3. The smallest observable absorption linewidths are in the range of 4 to 5 MHz. Our results suggest that the frequency-tunable BSCCO emitters can be convenient sources for potential terahertz applications in spectroscopy for frequencies between roughly 0.4 and 2 THz.

DOI: 10.1103/PhysRevApplied.8.054005

I. INTRODUCTION

Terahertz science and technology has been a hot topic for decades due to potential applications in detection and imaging, such as environmental monitoring, high-bandwidth communication technologies, medical diagnostics, public security, and food quality control [1,2]. A variety of sources of terahertz radiation have been reported [1]. For example, in terms of compact solid-state devices, there are powerful quantum cascade lasers for frequencies above 1.5 THz [3,4]. For frequencies between 0.5 and 1.5 THz, resonant-tunneling diodes look promising, reaching power levels in the microwatt range [5,6]. In this paper, we focus on terahertz emitters based on the high-critical-temperature (T_c) superconductor $Bi_2Sr_2CaCu_2O_{8+\delta}$ (BSCCO) operating at frequencies of between 0.4 and 2.4 THz [7–9]. These oscillators are based on the ac Josephson effect.

A unit cell of BSCCO consists of superconducting CuO_2 layers and insulating BiO and SrO layers, resulting in natural (intrinsic) Josephson junctions along the c axis [10]. A single crystal of 1.5 μm thickness forms a stack of $N \sim 1000$ of such intrinsic Josephson junctions (IJJs). If the voltage across all IJJs is the same, the junctions oscillate at a frequency $f_J = 2eV/hN$, where e is the elementary charge, h is the Planck constant, and V is the voltage across the whole stack. Coherent off-chip terahertz emission is first demonstrated for 1-μm-thick BSCCO stacks, with an extrapolated output power of up to 0.5 μW for frequencies of between 0.5 and 0.85 THz [11]. Phase synchronization of the IJJs is reached through cavity resonances excited in the stack. Terahertz emission from BSCCO stacks is under intensive experimental [11–41] and theoretical [42–65] research and has led to several demonstrations of applications, such as terahertz absorption and reflection imaging [25,33,40] or an all-high-T_c integrated receiver [26]. IJJ stacks have been patterned as mesas on top of BSCCO base crystals, as bare IJJ stacks contacted by Au layers [gold-BSCCO-gold (GBG) structures] [24,26,29,31] and as all-superconducting Z-shaped structures [21]. For the best stacks, an emission power P_e in the range of tens of microwatts has been achieved [26,28,29,35], and arrays of mesas showed emission with P_e values of up to 0.61 mW [28]. Emission frequencies range from 0.4 to 2.4 THz [9,31,34,35]; however, above about 2 THz, the emission power decreases strongly.

*hbwang@nju.edu.cn
†kleiner@uni-tuebingen.de

The IJJ stacks are affected by Joule heating. For sufficiently low bias currents, the temperature rises only slightly to values above the bath temperature T_b, and the voltage V across the stack increases with an increasing bias current I. With increasing I values and input power, the current-voltage characteristics (IVC) starts to backbend and, at a certain bias current in the backbending region, a hot spot forms in the stack, creating a region which is heated to temperatures above T_c. In the IJJ stacks, one can thus distinguish a low-bias regime where the temperature in the stack varies only weakly and a high-bias regime where the hot spot has formed. Terahertz emission can be observed in both regimes. While the reported linewidth of radiation is not smaller than 0.5 GHz at low bias [22,24], in the high-bias regime it can be as narrow as 7 MHz [22,66].

It is of interest to study to what extent IJJ stacks can be used for spectroscopy purposes. Thus, in this work, sweeping the emission frequency of BSCCO emitters by varying the bias current, we measure terahertz absorption spectra of water and ammonia vapor. In a first, proof-of-principle experiment, we detect the terahertz radiation bolometrically. In a second and more elaborate experiment, we monitor the terahertz absorption characteristics of the two gases by a heterodyne-mixing detection method. Here, a 5-MHz (4-MHz) linewidth of the absorption signal of ammonia vapor is observed at a pressure p of 0.23 mbar (0.07 mbar).

II. MEASUREMENTS

The emitter is fabricated as a GBG structure from a BSCCO single crystal which is annealed at 650 °C, 18 Pa Ar, and 2 Pa O_2 for 48 h. After annealing, the critical temperature T_c is approximately 89 K. The microfabrication process is described in Ref. [26]. The resulting rectangular IJJ stack has an in-plane size of $(300 \times 50)\ \mu m^2$ and a thickness of 1.1 μm, corresponding to approximately 730 IJJs in series. The emitter is shown schematically in Fig. 1(a). For electrical contact, two gold wires are connected to the electrodes by silver epoxy.

In a first and very simple experiment, we use the gas-detection system shown in Fig. 1. Using GE varnish, the MgO substrate hosting the BSCCO emitter is glued onto a hemispheric sapphire lens. No special measures are taken into account for thermal management or impedance mismatch between the sample, the substrate, and the lens. Then the emitter is placed in a Stirling cryocooler (RICOR K535) which can cool down to 30 K from room temperature. The temperature is detected by a DT-670 silicon diode. The emission is directed to a 52-cm-long gas cell via an off-axis parabolic mirror, where both windows of the cell are made of 2-mm-thick terahertz-transparent Teflon. The terahertz beam is modulated by a mechanical chopper (with a modulation frequency of 14 Hz) and detected with a TYDEX GC-1P Golay cell. This cell is read out by a lock-in amplifier and calibrated against the response of a Si bolometer that is calibrated using a blackbody radiation source. The gas

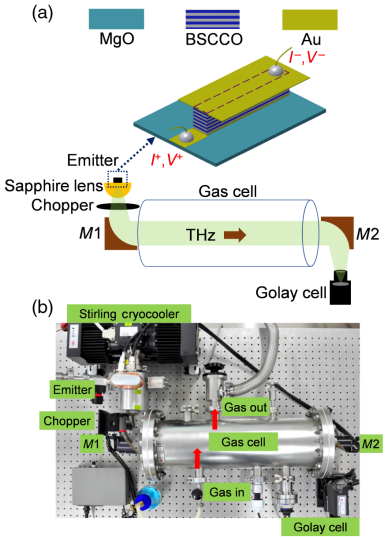

FIG. 1. (a) Sketch and (b) photograph of the terahertz gas-detection system with BSCCO intrinsic Josephson junctions as a tunable terahertz emitter. $M1$ and $M2$ denote parabolic mirrors. The IJJ stack forming a GBG structure is shown at the top of the sketch.

chamber is initially pumped out to a pressure of 3×10^{-5} mbar, and the target gas is then directed into the chamber via a gas valve. Here, we should note that the ammonia vapor used for the experiment volatilizes from ammonia water and contains additional water vapor with a proportion of less than 10%. The terahertz beam goes partially through air, also causing absorption due to water. The environmental humidity is about 40%. To change the emission frequency of the terahertz source, we simply vary the bias current through the IJJ stack, leading to a change in voltage V and, consequently, in f_J. To determine the frequency of the emitted radiation, a homemade Fourier spectrometer [67] is inserted into the beam path. For further evaluation, V is monitored and converted to frequency using this calibration and the proportionality of f_J and V. In a second experiment, we operate the emitter in a helium-cooled optical cryostat and use a helium-cooled superconducting integrated receiver instead of the Golay cell to directly detect the emission power and frequency by heterodyne mixing. The setup is similar to the one shown in Ref. [68].

III. RESULTS

Figure 2 shows the IVC of the stack, as measured at a bath temperature $T_b = 30$ K. The contact resistance

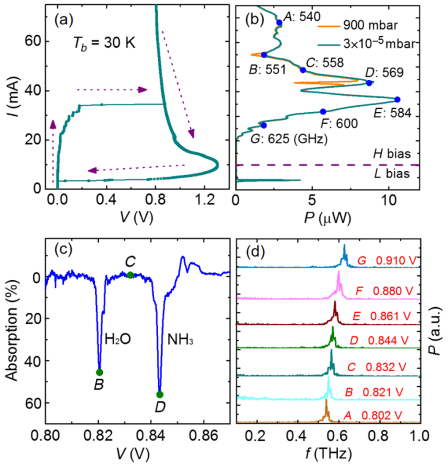

FIG. 2. (a) IVC of the emitter, as measured at a bath temperature $T_b = 30$ K. Dashed lines indicate the current sweep sequence. (b) Emission power detected by the Golay cell as a function of I for the evacuated gas cell ($p = 3 \times 10^{-5}$ mbar) and for the cell filled with ammonia vapor at a pressure of 900 mbar. (c) Absorption, as calculated from a ratio of the spectra at $p =$ 900 mbar and $p = 3 \times 10^{-5}$ mbar, as a function of voltage V across the stack. (d) Fourier spectra of the emitted radiation for the bias points (A) to (G) indicated in (b). The emission peaks of these spectra are indicated by the numbers in (b). The labels "H bias" and "L bias" in (b) indicate the high-bias and low-bias regimes.

between the IJJ stack and the contacting gold layers is subtracted. Dashed lines in the graph indicate the current sweep sequence. All junctions switch to their resistive states when the bias current exceeds 34.5 mA. By further increasing I to 75 mA and then back to zero, the IVC in the fully resistive state is obtained, exhibiting the typical heating-induced S shape. The highest voltage across the stack is 1.31 V. Figure 2(b) shows—as a function of I, by the dark-cyan line—the emission power, as detected by the Golay cell, for the case of an evacuated gas cell ($p = 3 \times 10^{-5}$ mbar).

In the high-bias regime, where the differential resistance of the IVC is negative, the stack emits in the current range 20–75 mA, covering a voltage range of 0.805 to 0.956 V. The highest detected emission power occurs at $I =$ 36.76 mA [point E in Fig. 2(b)] and amounts to about 10.6 μW. The emission observed is stable over time but exhibits several peaks as a function of I, presumably because different resonant modes are excited at different currents [11,12,17,18,24]. There is also an emission peak at low bias, at a current near 5 mA. We do not evaluate this peak further since our focus is on the high-bias regime, providing a much broader and more stable regime to tune our device by current. The orange line in Fig. 2(b) displays the detected terahertz emission for an ammonia pressure of 900 mbar. While, over large current ranges, this curve coincides with the background curve measured at 3×10^{-5} mbar gas pressure, at currents near 40 and 55 mA, the two curves deviate. To show this difference more clearly, we plot in Fig. 2(c) the absorption, calculated from the ratio of the two curves of Fig. 2(b), as a function of V. Two absorption dips are clearly visible, where, in fact, one is from the water vapor and the other from ammonia.

Note that there is also an "emission" peak between 0.85 and 0.86 V. This is actually an artifact arising from the steep gradients in the terahertz emission spectra visible in Fig. 2(b) between bias points D and E. In principle, the voltage V across the stack could be directly converted to frequency if the number of IJJs participating in radiation and the contact resistance were known exactly. As this is not the case, we measure, for the evacuated gas cell, emission spectra using our homemade Fourier spectrometer. Some spectra, as detected for the bias points A–G in Fig. 2(b), are shown in Fig. 2(d). The widths of the emission peaks seen here are resolution limited by the maximum displacement of the two split mirrors used in the spectrometer. The peak positions vary from 540 to 625 GHz, which covers the range of the rotational frequencies of interest of ammonia and water molecules. From these data, we also find a number N of 710 ± 10 IJJs contributing to the emission peaks, which roughly corresponds to the number of IJJs estimated from the thickness of the stack.

Figure 3 shows the terahertz absorption spectra of ammonia and water vapor at different gas pressures, calculated from the ratio of the various P-vs-V curves to the P-vs-V background curve obtained for the evacuated gas cell. At the highest pressures, the widths of the absorption lines of the two gases are very large (about 2 mV), which is expected due to collisional broadening. However, for lower pressures, the linewidths decrease mildly, reaching values of around 1.2–1.4 mV for pressures below 20 mbar and showing that the resolution (in voltage) of the absorption lines is limited by noise in the setup. For ammonia vapor, as shown in Fig. 3(a), the absorption center of the curves is at $V = 0.843$ V, where the frequency, measured with our interferometer, is about 569 GHz. This is close to the well-known rotational-transition frequency ($f = 572.5$ GHz) of ammonia molecules. We use this value and the Josephson relation to recalibrate the frequency axis in Fig. 3(a) and to obtain a more precise value for the number of emitting IJJs, $N = 712$.

For water-vapor absorption, as shown in Fig. 3(b), the same calculation also yields $N = 712$, confirming that we can perform gas spectroscopy—at least in principle—by sweeping the current and monitoring the voltage of the

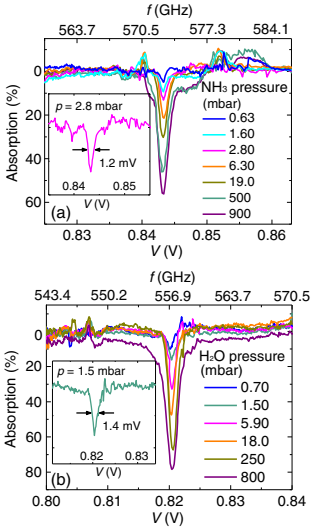

FIG. 3. Terahertz absorption signal vs voltage across the stack for different pressures of (a) ammonia vapor and (b) water vapor. The frequency displayed at the upper abscissa is calculated via the Josephson relation $f = 2eV/hN$, with $N = 712$. The inset in (a) shows the NH_3 absorption spectrum at $p = 2.8$ mbar, and the inset in (b) the H_2O absorption spectrum at $p = 1.5$ mbar.

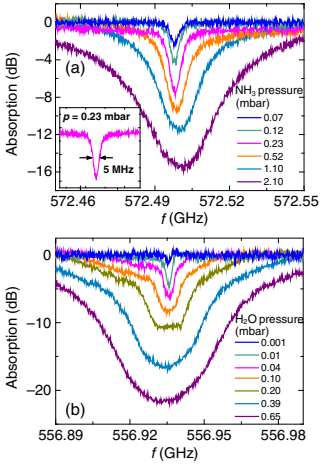

FIG. 4. (a) Terahertz absorption spectra of ammonia (mixed with water; 10% solution) and (b) water vapor at different pressures by a BSCCO emitter and a SIR terahertz detector. The emitter and the SIR are operated at $T_b = 4.2$ K. The empty-cell curve is subtracted from the data. (Inset) An absorption spectrum of ammonia vapor at $p = 0.23$ mbar, with an absorption linewidth of 5 MHz.

BSCCO emitter. The minimum pressure of the ammonia vapor where we can still observe the absorption dip is 0.63 mbar. The inset in Fig. 3(a) shows the absorption signal vs V at $p = 2.8$ mbar, with a maximum absorption of about 13.1%. Here, the measured linewidth of the absorption curves is 1.2 mV, corresponding to about 0.82 GHz. For water [see the inset in Fig. 3(b)], we can safely detect the absorption line down to $p = 0.7$ mbar, and the minimal linewidth is about 1.4 mV (0.95 GHz), which is already comparable to the frequency resolution of systems used in time-domain spectroscopy [69].

For further improvement, in our second experiment, to accurately measure the terahertz absorption spectra of ammonia and water vapor, a Nb-AlN-NbN superconducting integrated receiver (SIR) [66], with an effective frequency detection range of 450 to 700 GHz and a confirmed frequency resolution well below 100 kHz is employed as a detector [66,70]. The SIR was used previously to study terahertz emission from IJJ stacks [22] and to perform gas detection [66,68,71,72]. In the present experiment, the bias current through the BSCCO emitter is kept at a constant value, tuned to the respective gas-line frequency, and intermediate-frequency spectra are taken using the SIR. Measurements are done at $T_b = 4.2$ K, where the linewidth of radiation of the emitter is 60 MHz at 572.5 GHz (NH_3) and 57 MHz at 557 GHz (H_2O). With this setup, high-resolution terahertz absorption spectra of ammonia and water vapor are, as in Ref. [68], achieved in a narrow frequency band lower than the linewidth of the BSCCO emitter; see Fig. 4 [73]. The emitter, operated in a free-running mode, is stable enough to permit this kind of measurement. As in Fig. 3, the absorption lines of ammonia and water are highly broadened at large gas pressures, with the linewidth decreasing with decreasing pressure. For ammonia, at $p = 0.23$ mbar, which is the order of the concentration of trace gases, a clear absorption dip with an absorption linewidth of about 5 MHz is observed, as shown in the inset of Fig. 4(a). At $p = 0.07$ mbar, the measured linewidth is 4 MHz (although affected by Doppler broadening, which we do not further analyze here).

The observed rotation frequencies of ammonia (572.498 GHz) and water (556.936 GHz) coincide with literature values. Further improvement of the lowest resolvable linewidth is possible by using proper feedback techniques for the oscillator [70].

IV. CONCLUSIONS

In this work, using terahertz waves generated from BSCCO IJJ stacks, we record terahertz absorption spectra

of ammonia vapor near 572 GHz and water vapor near 557 GHz using two different setups. The first experiment uses a very simple terahertz transmission gas-detection system based on the bolometric detection of the terahertz emission signal. The emitter is cooled by a Stirling cryocooler. Clear absorption dips at different gas pressures are observed by simply sweeping the bias current and monitoring the voltage across the stacks; however, the setup is not stable enough to resolve the absorption linewidths at low pressures.

In the second experiment, we measure terahertz absorption characteristics of the two gases using a superconducting integrated receiver for detecting the terahertz power and frequency. The emitter and the receiver are mounted in different helium-cooled cryostats. With this setup, we achieve minimum absorption linewidths of 4 to 5 MHz at pressures well below 0.1 mbar. Of course, the performance is still far below the sensitivity and frequency resolution of the most sophisticated detection schemes based on chirped-pulse Fourier-transform spectroscopy [74]. However, it is not so different from quantum-cascade-laser-based schemes realized for gas sensing in the 2- to 3-THz range [75]. BSCCO emitters are suitable candidates for terahertz spectroscopy for frequencies of between about 0.4 and 2 THz and can be used for applications in environmental monitoring.

ACKNOWLEDGMENTS

We gratefully acknowledge financial support from the National Natural Science Foundation of China (Grants No. 11234006, No. 61611130069, No. 11227904, No. 61371036, No. 61521001, and No. 61501220), the Fundamental Research Funds for the Central Universities and Jiangsu Key Laboratory of Advanced Techniques for Manipulating Electromagnetic Waves, the Priority Academic Program Development of Jiangsu Higher Education Institutions (PAPD), the Jiangsu Provincial Natural Science Fund (Grant No. BK20150561), RFBR Grant No. 17-52-12051, and the Deutsche Forschungsgemeinschaft via Project No. KL930-13/2.

[1] M. Tonouchi, Cutting-edge terahertz technology, Nat. Photonics **1**, 97 (2007).
[2] B. Ferguson and X. C. Zhang, Materials for terahertz science and technology, Nat. Mater. **1**, 26 (2002).
[3] B. S. Williams, Terahertz quantum-cascade lasers, Nat. Photonics **1**, 517 (2007).
[4] S. Kumar, Recent progress in terahertz quantum cascade lasers, IEEE J. Sel. Top. Quantum Electron. **17**, 38 (2011).
[5] M. Feiginov, H. Kanaya, S. Suzuki, and M. Asada, Operation of resonant-tunneling diodes with strong back injection from the collector at frequencies up to 1.46 THz, Appl. Phys. Lett. **104**, 243509 (2014).
[6] S. Suzuki, M. Asada, A. Teranishi, H. Sugiyama, and H. Yokoyama, Fundamental oscillation of resonant tunneling diodes above 1 THz at room temperature, Appl. Phys. Lett. **97**, 242102 (2010).
[7] U. Welp, K. Kadowaki, and R. Kleiner, Superconducting emitters of THz radiation, Nat. Photonics **7**, 702 (2013).
[8] I. Kakeya and H. B. Wang, Terahertz-wave emission from Bi2212 intrinsic Josephson junctions: A review on recent progress, Supercond. Sci. Technol. **29**, 073001 (2016).
[9] T. Kashiwagi, H. Kubo, K. Sakamoto, T. Yuasa, Y. Tanabe, C. Watanabe, T. Tanaka, Y. Komori, R. Ota, G. Kuwano, K. Nakamura, T. Katsuragawa, M. Tsujimoto, T. Yamamoto, R. Yoshizaki, H. Minami, K. Kadowaki, and R. A. Klemm, The present status of high-T_c superconducting terahertz emitters, Supercond. Sci. Technol. **30**, 074008 (2017).
[10] R. Kleiner, F. Steinmeyer, G. Kunkel, and P. Müller, Intrinsic Josephson Effects in $Bi_2Sr_2CaCu_2O_8$ Single Crystals, Phys. Rev. Lett. **68**, 2394 (1992).
[11] L. Ozyuzer, A. E. Koshelev, C. Kurter, N. Gopalsami, Q. Li, M. Tachiki, K. Kadowaki, T. Yamamoto, H. Minami, H. Yamaguchi, T. Tachiki, K. E. Gray, W.-K. Kwok, and U. Welp, Emission of coherent THz radiation from superconductors, Science **318**, 1291 (2007).
[12] H. B. Wang, S. Guénon, J. Yuan, A. Iishi, S. Arisawa, T. Hatano, T. Yamashita, D. Koelle, and R. Kleiner, Hot Spots and Waves in $Bi_2Sr_2CaCu_2O_8$ Intrinsic Josephson Junction Stacks: A Study by Low Temperature Scanning Laser Microscopy, Phys. Rev. Lett. **102**, 017006 (2009).
[13] H. Minami, I. Kakeya, H. Yamaguchi, T. Yamamoto, and K. Kadowaki, Characteristics of terahertz radiation emitted from the intrinsic Josephson junctions in high-T_c superconductor $Bi_2Sr_2CaCu_2O_{8+\delta}$, Appl. Phys. Lett. **95**, 232511 (2009).
[14] K. E. Gray, L. Ozyuzer, A. E. Koshelev, C. Kurter, K. Kadowaki, T. Yamamoto, H. Minami, H. Yamaguchi, M. Tachiki, W.-K. Kwok, and U. Welp, Emission of terahertz waves from stacks of intrinsic Josephson junctions, IEEE Trans. Appl. Supercond. **19**, 886 (2009).
[15] S. Guénon, M. Grünzweig, B. Gross, J. Yuan, Z. G. Jiang, Y. Y. Zhong, M. Y. Li, A. Iishi, P. H. Wu, T. Hatano, R. G. Mints, E. Goldobin, D. Koelle, H. B. Wang, and R. Kleiner, Interaction of hot spots and THz waves in $Bi_2Sr_2CaCu_2O_8$ intrinsic Josephson junction stacks of various geometry, Phys. Rev. B **82**, 214506 (2010).
[16] C. Kurter, L. Ozyuzer, T. Proslier, J. F. Zasadzinski, D. G. Hinks, and K. E. Gray, Counterintuitive consequence of heating in strongly-driven intrinsic junctions of $Bi_2Sr_2CaCu_2O_{8+\delta}$ mesas, Phys. Rev. B **81**, 224518 (2010).
[17] H. B. Wang, S. Guénon, B. Gross, J. Yuan, Z. G. Jiang, Y. Y. Zhong, M. Grünzweig, A. Iishi, P. H. Wu, T. Hatano, D. Koelle, and R. Kleiner, Coherent Terahertz Emission of Intrinsic Josephson Junction Stacks in the Hot Spot Regime, Phys. Rev. Lett. **105**, 057002 (2010).
[18] M. Tsujimoto, K. Yamaki, K. Deguchi, T. Yamamoto, T. Kashiwagi, H. Minami, M. Tachiki, K. Kadowaki, and R. A. Klemm, Geometrical Resonance Conditions for THz Radiation from the Intrinsic Josephson Junctions in $Bi_2Sr_2CaCu_2O_{8+\delta}$, Phys. Rev. Lett. **105**, 037005 (2010).
[19] H. Koseoglu, F. Turkoglu, Y. Simsek, and L. Ozyuzer, The fabrication of THz emitting mesas by reactive ion-beam

etching of superconducting Bi2212 with multilayer masks, J. Supercond. Novel Magn. **24**, 1083 (2011).

[20] T. M. Benseman, A. E. Koshelev, K. E. Gray, W.-K. Kwok, U. Welp, K.Kadowaki, M. Tachiki, and T. Yamamoto, Tunable terahertz emission from $Bi_2Sr_2CaCu_2O_{8+\delta}$ mesa devices, Phys. Rev. B **84**, 064523 (2011).

[21] J. Yuan, M. Y. Li, J. Li, B. Gross, A. Ishii, K. Yamaura, T. Hatano, K. Hirata, E. Takayama Muromachi, P. H. Wu, D. Koelle, R. Kleiner, and H. B. Wang, Terahertz emission from $Bi_2Sr_2CaCu_2O_{8+\delta}$ intrinsic Josephson junction stacks with all-superconducting electrodes, Supercond. Sci. Technol. **25**, 075015 (2012).

[22] M. Y. Li, J. Yuan, N. Kinev, J. Li, B. Gross, S. Guénon, A. Ishii, K. Hirata, T. Hatano, D. Koelle, R. Kleiner, V. P. Koshelets, H. B. Wang, and P. H. Wu, Linewidth dependence of coherent terahertz emission from $Bi_2Sr_2CaCu_2O_8$ intrinsic Josephson junction stacks in the hot-spot regime, Phys. Rev. B **86**, 060505(R) (2012).

[23] I. Kakeya, Y. Omukai, T. Yamamoto, K. Kadowaki, and M. Suzuki, Effect of thermal inhomogeneity for terahertz radiation from intrinsic Josephson junction stacks of $Bi_2Sr_2CaCu_2O_{8+\delta}$, Appl. Phys. Lett. **100**, 242603 (2012).

[24] T. Kashiwagi, M. Tsujimoto, T. Yamamoto, H. Minami, K. Yamaki, K. Delfanzari, K. Deguchi, N. Orita, T. Koike, R. Nakayama, T. Kitamura, M. Sawamura, S. Hagino, K. Ishida, K. Ivancovic, H. Asai, M. Tachiki, R. A. Klemm, and K. Kadowaki, High temperature superconductor terahertz emitters: Fundamental physics and its applications, J. Appl. Phys. **51**, 010113 (2012).

[25] M. Tsujimoto, H. Minami, K. Delfanazari, M. Sawamura, R. Nakayama, T. Kitamura, T. Yamamoto, T. Kashiwagi, T. Hattori, and K. Kadowaki, Terahertz imaging system using high-T_c superconducting oscillation devices, J. Appl. Phys. **111**, 123111 (2012).

[26] D. Y. An *et al.*, Terahertz emission and detection both based on high-T_c superconductors: Towards an integrated receiver, Appl. Phys. Lett. **102**, 092601 (2013).

[27] T. M. Benseman, A. E. Koshelev, W.-K. Kwok, U. Welp, V. K. Vlasko-Vlasov, K. Kadowaki, H. Minami, and C. Watanabe, Direct imaging of hot spots in $Bi_2Sr_2CaCu_2O_{8+\delta}$ mesa terahertz sources, J. Appl. Phys. **113**, 133902 (2013).

[28] T. M. Benseman, K. E. Gray, A. E. Koshelev, W.-K. Kwok, U. Welp, H. Minami, K. Kadowaki, and T. Yamamoto, Powerful terahertz emission from $Bi_2Sr_2CaCu_2O_{8+\delta}$ mesa arrays, Appl. Phys. Lett. **103**, 022602 (2013).

[29] S. Sekimoto, C. Watanabe, H. Minami, T. Yamamoto, T. Kashiwagi, R. A. Klemm, and K. Kadowaki, Continuous 30 μW terahertz source by a high-T_c superconductor mesa structure, Appl. Phys. Lett. **103**, 182601 (2013).

[30] H. Minami, C. Watanabe, K. Sato, S. Sekimoto, T. Yamamoto, T. Kashiwagi, R. A. Klemm, and K. Kadowaki, Local SiC photoluminescence evidence of hot spot formation and sub-THz coherent emission from a rectangular $Bi_2Sr_2CaCu_2O_{8+x}$ mesa, Phys. Rev. B **89**, 054503 (2014).

[31] M. Ji *et al.*, $Bi_2Sr_2CaCu_2O_8$ intrinsic Josephson junction stacks with improved cooling: Coherent emission above 1 THz, Appl. Phys. Lett. **105**, 122602 (2014).

[32] T. Kashiwagi, K. Nakade, Y. Saiwai, H. Minami, T. Kitamura, C. Watanabe, K. Ishida, S. Sekimoto, K. Asanuma, T. Yasui, Y. Shibano, M. Tsujimoto, T. Yamamoto, B. Markovic, J. Mirkovic, R. A. Klemm, and K. Kadowaki, Computed tomography image using sub-terahertz waves generated from a high-T_c superconducting intrinsic Josephson junction oscillator, Appl. Phys. Lett. **104**, 082603 (2014).

[33] T. Kashiwagi, K. Nakade, B. Markovic, Y. Saiwai, H. Minami, T. Kitamura, C. Watanabe, K. Ishida, S. Sekimoto, K. Asanuma, T. Yasui, Y. Shibano, M. Tsujimoto, T. Yamamoto, J. Mirkovic, and K. Kadowaki, Reflection type of terahertz imaging system using a high-T_c superconducting oscillator, Appl. Phys. Lett. **104**, 022601 (2014).

[34] T. Kashiwagi, T. Yamamoto, T. Kitamura, K. Asanuma, C. Watanabe, K. Nakade, T. Yasui, Y. Saiwai, Y. Shibano, H. Kubo, K. Sakamoto, T. Katsuragawa, M. Tsujimoto, K. Delfanazari, R. Yoshizaki, H. Minami, R. A. Klemm, and K. Kadowaki, Generation of electromagnetic waves from 0.3 to 1.6 terahertz with a high-T_c superconducting $Bi_2Sr_2CaCu_2O_{8+\delta}$ intrinsic Josephson junction emitter, Appl. Phys. Lett. **106**, 092601 (2015).

[35] T. Kashiwagi, K. Sakamoto, H. Kubo, Y. Shibano, T. Enomoto, T. Kitamura, K. Asanuma, T. Yasui, C. Watanabe, K. Nakade, Y. Saiwai, T. Katsuragawa, M. Tsujimoto, R. Yoshizaki, T. Yamamoto, H. Minami, R. A. Klemm, and K. Kadowaki, A high-T_c intrinsic Josephson junction emitter tunable from 0.5 to 2.4 terahertz, Appl. Phys. Lett. **107**, 082601 (2015).

[36] X. J. Zhou, Q. Zhu, M. Ji, D. Y. An, L. Y. Hao, H. C. Sun, S. Ishida, F. Rudau, R. Wieland, J. Li, D. Koelle, H. Eisaki, Y. Yoshida, T. Hatano, R. Kleiner, H. B. Wang, and P. H. Wu, Three-terminal stand-alone superconducting terahertz emitter, Appl. Phys. Lett. **107**, 122602 (2015).

[37] L. Y. Hao, M. Ji, J. Yuan, D. Y. An, M. Y. Li, X. J. Zhou, Y. Huang, H. C. Sun, Q. Zhu, F. Rudau, R. Wieland, N. Kinev, J. Li, W. W. Xu, B. B. Jin, J. Chen, T. Hatano, V. P. Koshelets, D. Koelle, R. Kleiner, H. B. Wang, and P. H. Wu, Compact Superconducting Terahertz Source Operating in Liquid Nitrogen, Phys. Rev. Applied **3**, 024006 (2015).

[38] T. Kashiwagi *et al.*, Efficient Fabrication of Intrinsic-Josephson-Junction Terahertz Oscillators with Greatly Reduced Self-Heating Effects, Phys. Rev. Applied **4**, 054018 (2015).

[39] C. Watanabe, H. Minami, T. Kitamura, K. Asanuma, K. Nakade, T. Yasui, Y. Saiwai, Y. Shibano, T. Yamamoto, T. Kashiwagi, R. A. Klemm, and K. Kadowaki, Influence of the local heating position on the terahertz emission power from high-T_c superconducting $Bi_2Sr_2CaCu_2O_{8+\delta}$ mesas, Appl. Phys. Lett. **106**, 042603 (2015).

[40] K. Nakade, T. Kashiwagi, Y. Saiwai, H. Minami, T. Yamamoto, R. A. Klemm, and K. Kadowaki, Applications using high-T_c superconducting terahertz emitters, Sci. Rep. **6**, 23178 (2016).

[41] M. Tsujimoto, Y. Maeda, A. Elarabi, Y. Yoshioka, Y. Nakagawa, Y. Wen, T. Doi, H. Saito, and I. Kakeya, Cavity mode identification for coherent terahertz emission from high-T_c superconductors, Opt. Express **24**, 4591 (2016).

[42] L. N. Bulaevskii and A. E. Koshelev, Radiation due to Josephson Oscillations in Layered Superconductors, Phys. Rev. Lett. **99**, 057002 (2007).

[43] A. E. Koshelev, Alternating dynamic state self-generated by internal resonance in stacks of intrinsic Josephson junctions, Phys. Rev. B **78**, 174509 (2008).

[44] S. Lin and X. Hu, Possible Dynamic States in Inductively Coupled Intrinsic Josephson Junctions of Layered High-T_c Superconductors, Phys. Rev. Lett. **100**, 247006 (2008).
[45] V. M. Krasnov, Nonlinear Nonequilibrium Quasiparticle Relaxation in Josephson Junctions, Phys. Rev. Lett. **103**, 227002 (2009).
[46] R. A. Klemm and K. Kadowaki, Output from a Josephson stimulated terahertz amplified radiation emitter, J. Phys. Condens. Matter **22**, 375701 (2010).
[47] N. F. Pedersen and S. Madsen, THz generation using fluxon dynamics in high temperature superconductors, IEEE Trans. Appl. Supercond. **19**, 726 (2009).
[48] X. Hu and S. Z. Lin, Cavity phenomena in mesas of cuprate high-T_c superconductors under voltage bias, Phys. Rev. B **80**, 064516 (2009).
[49] T. Koyama, H. Matsumoto, M. Machida, and K. Kadowaki, In-phase electrodynamics and terahertz wave emission in extended intrinsic Josephson junctions, Phys. Rev. B **79**, 104522 (2009).
[50] V. M. Krasnov, Coherent flux-flow emission from stacked Josephson junctions: Nonlocal radiative boundary conditions and the role of geometrical resonances, Phys. Rev. B **82**, 134524 (2010).
[51] A. E. Koshelev, Stability of dynamic coherent states in intrinsic Josephson-junction stacks near internal cavity resonance, Phys. Rev. B **82**, 174512 (2010).
[52] A. A. Yurgens, Temperature distribution in a large $Bi_2Sr_2CaCu_2O_{8+\delta}$ mesa, Phys. Rev. B **83**, 184501 (2011).
[53] V. M. Krasnov, Terahertz electromagnetic radiation from intrinsic Josephson junctions at zero magnetic field via breather-type self-oscillations, Phys. Rev. B **83**, 174517 (2011).
[54] M. Tachiki, K. Ivanovic, K. Kadowaki, and T. Koyama, Emission of terahertz electromagnetic waves from intrinsic Josephson junction arrays embedded in resonance LCR circuits, Phys. Rev. B **83**, 014508 (2011).
[55] H. Asai, M. Tachiki, and K. Kadowaki, Three-dimensional numerical analysis of terahertz radiation emitted from intrinsic Josephson junctions with hot spots, Phys. Rev. B **85**, 064521 (2012).
[56] S. Z. Lin and X. Hu, In-plane dissipation as a possible synchronization mechanism for terahertz radiation from intrinsic Josephson junctions of layered superconductors, Phys. Rev. B **86**, 054506 (2012).
[57] Yu. O. Averkov, V. M. Yakovenko, V. A. Yampol'skii, and F. Nori, Conversion of Terahertz Wave Polarization at the Boundary of a Layered Superconductor due to the Resonance Excitation of Oblique Surface Waves, Phys. Rev. Lett. **109**, 027005 (2012).
[58] B. Gross, S. Guénon, J. Yuan, M. Y. Li, J. Li, A. Ishii, R. G. Mints, T. Hatano, P. H. Wu, D. Koelle, H. B. Wang, and R. Kleiner, Hot-spot formation in stacks of intrinsic Josephson junctions in $Bi_2Sr_2CaCu_2O_8$, Phys. Rev. B **86**, 094524 (2012).
[59] B. Gross, J. Yuan, D. Y. An, M. Y. Li, N. Kinev, X. J. Zhou, M. Ji, Y. Huang, T. Hatano, R. G. Mints, V. P. Koshelets, P. H. Wu, H. B. Wang, D. Koelle, and R. Kleiner, Modeling the linewidth dependence of coherent terahertz emission from intrinsic Josephson junction stacks in the hot-spot regime, Phys. Rev. B **88**, 014524 (2013).
[60] H. Asai and S. Kawabata, Intense terahertz emission from intrinsic Josephson junctions by external heat control, Appl. Phys. Lett. **104**, 112601 (2014).
[61] A. Grib and P. Seidel, The influence of external separate heating on the synchronization of Josephson junctions, Phys. Status Solidi B **251**, 1040 (2014).
[62] F. Rudau *et al.*, Thermal and electromagnetic properties of $Bi_2Sr_2CaCu_2O_8$ intrinsic Josephson junction stacks studied via one-dimensional coupled sine-Gordon equations, Phys. Rev. B **91**, 104513 (2015).
[63] F. Rudau, R. Wieland, J. Langer, X. J. Zhou, M. Ji, N. Kinev, L. Y. Hao, Y. Huang, J. Li, P. H. Wu, T. Hatano, V. P. Koshelets, H. B. Wang, D. Koelle, and R. Kleiner, Three-Dimensional Simulations of the Electrothermal and Terahertz Emission Properties of $Bi_2Sr_2CaCu_2O_8$ Intrinsic Josephson Junction Stacks, Phys. Rev. Applied **5**, 044017 (2016).
[64] D. P. Cerkoney, C. Reid, C. M. Doty, A. Gramajo, T. D. Campbell, M. A. Morales, K. Delfanazari, M. Tsujimoto, T. Kashiwagi, T. Yamamoto, C. Watanabe, H. Minami, K. Kadowaki, and R. A Klemm, Cavity mode enhancement of terahertz emission from equilateral triangular microstrip antennas of the high-T_c superconductor $Bi_2Sr_2CaCu_2O_{8+\delta}$, J. Phys. Condens. Matter **29**, 015601 (2017).
[65] R. A. Klemm, A. E. Davis, and Q. X. Wang, Terahertz emission from thermally managed square intrinsic Josephson junction microstrip antennas, IEEE J. Sel. Top. Quantum Electron. **23**, 1 (2017).
[66] V. P. Koshelets, P. N. Dmitriev, M. I. Faley, L. V. Filippenko, K. V. Kalashnikov, N. V. Kinev, O. S. Kiselev, A. A. Artanov, K. I. Rudakov, A. De Lange, G. De Lange, V. L. Vaks, M. Y. Li, and H. B. Wang, Superconducting integrated terahertz spectrometers, IEEE Trans. Terahertz Sci. Technol. **5**, 687 (2015).
[67] H. Eisele, M. Naftaly, and J. R. Fletcher, A simple interferometer for the characterization of sources at terahertz frequencies, Meas. Sci. Technol. **18**, 2623 (2007).
[68] E. Sobakinskaya, V. L. Vaks, N. Kinev, M. Ji, M. Y. Lia, H. B. Wang, and V. P. Koshelets, High-resolution terahertz spectroscopy with a noise radiation source based on high-T_c superconductors, J. Phys. D **50**, 035305 (2017).
[69] T. Uno and H. Tabata, *In situ* measurement of combustion gas using terahertz time domain spectroscopy setup for gas phase spectroscopy and measurement of solid sample, Jpn. J. Appl. Phys. **49**, 04DL17 (2010).
[70] V. P. Koshelets and S. V. Shitov, Integrated superconducting receivers, Supercond. Sci. Technol. **13**, R53 (2000).
[71] G. de Lange *et al.*, Development and characterization of the superconducting integrated receiver channel of the TELIS atmospheric sounder, Supercond. Sci. Technol. **23**, 045016 (2010).
[72] N. V. Kinev, L. V. Filippenko, K. V. Kalashnikov, O. S. Kiselev, V. L. Vaks, E. G. Domracheva, and V. P. Koshelets, Superconducting integrated terahertz receiver for spectral analysis of gas compounds, J. Phys. Conf. Ser. **741**, 012169 (2016).
[73] Note that the amplitudes of the signals detected in experiments 1 and 2 (Figs. 3 and 4) are difficult to compare

since the measurements are done with very different receiver input bandwidths. The wideband receiver of experiment 1 integrates the power emitted by the BSCCO emitter at different frequencies; thus, the absorption is much lower than the calculations and measurements associated with the SIR, having a spectral resolution well below the gas lines at all gas pressures displayed.

[74] E. Gerecht, K. O. Douglass, and D. F. Plusquellic, Chirped-pulse terahertz spectroscopy for broadband trace gas sensing, Opt. Express **19**, 8973 (2011).

[75] L. Consolino, S. Bartalini, H. E. Beere, D. A. Ritchie, M. Serena Vitiello, and P. De Natale, THz QCL-based cryogen-free spectrometer for *in situ* trace gas sensing, Sensors **13**, 3331 (2013).